

24 JUL 2000

Contract Report on
**Steady and Unsteady Heat Transfer in a Film-Cooled
Transonic Turbine Cascade**

AFOSR F49620-96-1-0465

for the period
September 1, 1996 to December 31, 1999

submitted to

Program Manager
Dr. Tom Beutner
AFOSR/NA
801 N Randolph St, Rm 732
Arlington VA 22203-1977

submitted by

Wing Ng, Tom Diller, Oliver Popp
Mechanical Engineering Department
Virginia Tech, MC 0238
Blacksburg VA 24061

July 2000

20000908 060

DTIC QUALITY INSPECTED 4

Public reporting burden for this collection of information is estimated to average 1 hour per response, including the time for review of data needed, and completing and reviewing this collection of information. Send comments regarding this burden estimate or any other aspect of this collection of information, including suggestions for reducing this burden to Washington Headquarters Services, Directorate for Information Operations and Reports (0402-0002). Respondents should be aware that notwithstanding any other provision of law, no person shall be subject to any penalty for failing to provide information if it does not contain a control number. PLEASE DO NOT RETURN YOUR FORM TO THE ABOVE ADDRESS.

using the
reducing
3202.

Standard Form 298 (Rev. 8-98)
Prescribed by ANSI Std. Z39-18

Steady and Unsteady Heat Transfer in a Film Cooled Transonic Turbine Cascade

Oliver Popp, Ph.D.

Virginia Polytechnic Institute and State University, 1999

Advisor: Dr. Wing F. Ng, Chair

ABSTRACT

The unsteady interaction of shock waves emerging from the trailing edge of modern turbine nozzle guide vanes and impinging on downstream rotor blades is modeled in a linear cascade. The Reynolds number based on blade chord and exit conditions ($5 \cdot 10^6$) and the exit Mach number (1.2) are representative of modern engine operating conditions. The relative motion of shocks and blades is simulated by sending a shock wave along the leading edges of the linear cascade instead of moving the blades through an array of stationary shock waves. The blade geometry is a generic version of a modern high turning rotor blade with transonic exit conditions. The blade is equipped with a showerhead film cooling scheme. Heat flux, surface pressure and surface temperature are measured at six locations on the suction side of the central blade. Pressure measurements are taken with *Kulite XCQ-062-50a* high frequency pressure transducers. Heat flux data is obtained with *Vatell HFM-7/L* high speed heat flux sensors. High speed heat flux and pressure data are recorded during the time of the shock impact with and without film cooling. The data is analyzed in detail to find the relative magnitudes of the shock effect on the heat transfer coefficient and the recovery temperature or adiabatic wall temperature (in the presence of film cooling). It is shown that the variations of the heat transfer coefficient and the film

effectiveness are less significant than the variations of recovery temperature. The effect of the shock is found to be similar in the cases with and without film cooling. In both cases the variation of recovery temperature induced by the shock is shown to be the main contribution to the overall unsteady heat flux.

The unsteady heat flux is compared to results from different prediction models published in the literature. The best agreement of data and prediction is found for a model that assumes a constant heat transfer coefficient and a temperature difference calculated from the unsteady surface pressure assuming an isentropic compression.

Acknowledgments

This work was supported by the Air Force Office of Scientific Research (AFOSR) under grant F08671-9601062, monitored by Dr. Jim M. McMichael, Dr. Mark Glauser and Dr. Tom Beunter. I would like to thank Mr. Scott Hunter, Mr. Monty Shelton and Mr. Mark Pearson of General Electric Aircraft Engines for their collaboration on this project.

I would like to express my gratitude to the members of my committee. Dr. Ng has taught me economical thinking which will be invaluable for my future career. Dr. Diller has given me great insight in convective heat transfer and the measurement thereof. He has shown me how to stay focused on a long term goal and not to give in to the temptations of short-lived mood-swings. Dr. Schetz has always helped me out with practical suggestions from his immense vault of real-world experience. Dr. Wicks knowledge of the issue of gauge frequency response and signal processing has helped me greatly in achieving confidence in my measurements.

My particular appreciation goes to the graduate students directly involved with this project. Dwight Smith, Hank Grabowski and Jim Bubb have made this project not only successful but also very enjoyable. Thank you for the hard work and the fun we had. Also, I would like to thank the entire team of Dr. Ng's graduate students for their suggestions and discussions. Especially, Nikhil Rao and John Watts deserve my gratitude for their help with practical and theoretical matters.

For the first year of this project the Mechanical Engineering workshop was booked solid with bits and pieces of the new setup. I thank Johnny Cox for handling this overwhelming amount of work. A special thanks goes to James Dowdy for his advice, quality of work and selfless support.

The guys from the Aerospace and Ocean Engineering machine shop did something unbelievable. Throughout this project they supported me generously with hardware and advice even though there was no reason for them to do so. Thanks a lot.

None of this would have happened without the loving support of my wife Kerstin. She sacrificed a lot for this to come to a successful ending. Most importantly, I want to thank her for giving birth to our son Sebastian Boris. His presence is all the motivation I need.

OLIVER POPP

Virginia Polytechnic Institute and State University

June 1999

Contents

Abstract	ii
Acknowledgments	iv
List of Tables	x
List of Figures	xii
Nomenclature	xix
Chapter 1 Introduction	1
1.1 Problem Statement: Turbine Blade Heat Transfer	1
1.2 Literature Review	6
1.2.1 Research at Texas A & M University	7
1.2.2 Research at Iwate University	8
1.2.3 Research at NASA Lewis Research Center	8
1.2.4 Research at Calspan-UB Research Center	9
1.2.5 Research at MIT	10
1.2.6 Research at Oxford University	11
1.2.7 Research at Virginia Tech	14
1.3 This Work	15
1.4 Overview	17
Chapter 2 Steady Heat Transfer	19

2.1	Introduction and Problem Statement	19
2.2	Experimental Setup for Steady Experiments	20
2.3	Data Reduction Technique	26
2.3.1	Analysis of Uncooled Experiments	26
2.3.2	Results from Uncooled Experiments	29
2.3.3	Analysis of Cooled Experiments	32
2.3.4	Results from Cooled Experiments	34
Chapter 3	Unsteady Heat Transfer	38
3.1	Experimental Setup for Investigation of Unsteady Heat Flux	38
3.1.1	Shock Apparatus	39
3.2	Test Matrix	44
3.3	Instrumentation and Data Acquisition for Unsteady Measurements	47
3.3.1	Unsteady Pressure Measurements for Test Series "Unsteady De- composition"	47
3.3.2	Unsteady Heat Flux Measurements for Test Series "Unsteady Decomposition"	50
3.3.3	Unsteady Pressure Measurements for "Direct Comparison" . .	53
3.3.4	Unsteady Heat Flux Measurements for "Direct Comparison" .	55
3.3.5	Shadowgraph Flow Visualization	56
3.4	Signal Processing	57
3.4.1	Pressure	57
3.4.2	Heat Transfer	61
3.5	Results and Discussion	64
3.5.1	General Observations	65
3.5.2	"Unsteady Decomposition" of Heat Flux	72
3.5.2.1	Analytical Model without Film Cooling	72
3.5.2.2	Effect of Shock Passing without Film Cooling	75
3.5.2.3	Analytical Model with Film Cooling	88

3.5.2.4	Effect of Shock Passing with Film Cooling	91
3.5.2.5	Conclusion from the Unsteady Decomposition Tech- nique	113
3.5.3	"Direct Comparison" of Predicted and Measured Heat Flux .	114
3.5.3.1	Moss' Model	114
3.5.3.2	Johnson's Model	123
3.5.3.3	Rigby's Model	134
3.5.4	Comparison with Reid's Numerical Model	145
Chapter 4 Conclusions from the Investigation of Unsteady Heat Flux		149
4.1	Summary	149
4.2	Application to Turbine Design	151
4.3	Outlook	151
Bibliography		153
References		153
Appendix A Shock Progression Details		158
Appendix B Investigation of the Transfer Function of Different <i>Kulite</i>		
Pressure Transducers		163
B.1	Problem Statement and Approach	163
B.2	Experimental Setup	164
B.3	Results and Discussion	169
B.3.1	Determination of Transfer Functions	174
B.4	Conclusions	179
Appendix C Investigation of the Transfer Function of a <i>Vatell HFM</i>		
7/L Heat Flux Sensor		180
C.1	Problem Statement and Approach	180
C.2	Experimental Setup	181
C.3	Theoretical Heat Flux and Gauge Response	182

C.4 Results and Discussion	185
Appendix D Transfer Functions of the <i>Measurements Group 2310</i> Strain Gauge Conditioner and Signal Amplifier at Different Gain Settings	188
Appendix E Measurement Error	195
E.1 Measurement Uncertainty	195
E.2 Measurement Repeatability	200
Appendix F Discussion of the Surface Heat Flux Equations and their Discretization	204
F.1 Derivation of the Basic Equation	205
F.2 Comparison of Different Ways to Obtain Heat Flux from Discrete Tem- perature Data	212
Appendix G Steady and Unsteady Heat Transfer in a Transonic Film Cooled Turbine Cascade	224
Appendix H Comparison of Radiation versus Convection Calibration of Thin-Film Heat Flux Gauges	234
Vita	241

List of Tables

2.1	Mean Heat Transfer Coefficients for all Gauges and All Uncooled Experiments for "Unsteady Decomposition" Technique (Section 3.5.2.2)	29
2.2	$T_d = T_t - T_r$ for all Gauges and All Uncooled Experiments for "Unsteady Decomposition" Technique (Section 3.5.2.2)	30
2.3	h and $T_d = T_t - T_r$ for Gauges 1 and 2. Uncooled Run # 3 for "Direct Comparison" (Sections 3.5.3)	31
2.4	Mean Heat Transfer Coefficients for all Gauges and All Cooled Experiments for "Unsteady Decomposition" Technique (Section 3.5.2.4)	35
2.5	Mean Film Cooling Effectiveness for all Gauges and All Cooled Experiments for "Unsteady Decomposition" Technique (Section 3.5.2.4)	36
2.6	h_c and η for Gauges 1 and 2. Cooled Runs # 1 and #2 for "Direct Comparison" (Sections 3.5.3)	37
3.1	Shock Strength and Total Temperatures at Shock Impact for All Uncooled Experiments	76
3.2	Recovery Temperatures at Shock Impact for All Gauges and All Uncooled Experiments	76
3.3	Wall Temperatures at Shock Impact for All Gauges and All Uncooled Experiments	76
3.4	Mean Heat Transfer Coefficients for all Gauges and All Uncooled Experiments	77
3.5	Test Matrix, Total Temperature and Coolant Temperature Before Shock Impact for All Cooled Experiments	92

3.6	Recovery Temperature Before Shock Impact for All Gauges and All Cooled Experiments	92
3.7	Adiabatic Wall Temperature Before Shock Impact for All Gauges and All Cooled Experiments	93
3.8	Wall Temperature Before Shock Impact for All Gauges and All Cooled Experiments	93
3.9	Heat Transfer Coefficient for All Gauges and All Cooled Experiments	94
3.10	Film Effectiveness for All Gauges and All Cooled Experiments	94
3.11	Test Matrix and Parameters for All Runs and Gauges 1 and 2 for "Direct Comparison"	115
3.12	Conditions at Shock Impact for All Runs and Gauges 1 and 2 for "Direct Comparison"	115
B.1	Coefficients A_i and B_i Describing the Transfer Function of the <i>Kulite Pressure Transducer XCO-062-50a</i> with B-screen	178
D.1	Coefficients A_i and B_i Describing the Transfer Function of the <i>Measurements Group 2310 Strain Gauge Conditioner and Signal Amplifier</i> according to Equation D.1	189
E.1	HFM Gauge Uncertainties	196
E.2	Precision Uncertainties	199
E.3	Measurement Repeatability For Uncooled Runs	200
E.4	Measurement Repeatability for Cooled Runs	203
F.1	Corresponding Variables in Equations F.12 and F.15	209

List of Figures

1.1	Advance of Materials and Cooling Technology. Source: Royal Aeronautical Society / Aerospace - 1994.	2
1.2	Schematical Depiction of the Non-Uniformity of the Flowfield Downstream of a Modern NGV Row.	5
2.1	Transonic Blowdown Windtunnel at Virginia Tech, from Smith (1999).	20
2.2	Instrumented Film Cooled Blade, from Bubb (1999).	24
2.3	Coolant Supply Schematic.	25
2.4	Time History From Uncooled Experiment.	26
2.5	Determination of h and T_d	28
2.6	Time History From Experiment with Film Cooling.	32
2.7	Determination of h_c and η	34
3.1	Overview of the Shock Apparatus.	40
3.2	Shock Shaper Design.	43
3.3	Test Matrix for Experiments With and Without Film Cooling for Test Series "Unsteady Decomposition".	44
3.4	Test Matrix for Experiments With and Without Film Cooling for Test Series "Direct Comparison".	45
3.5	Measurement Chain for Unsteady Pressure Measurements for Test Series "Unsteady Decomposition" in Section 3.5.2.	48
3.6	Measurement Chain for Unsteady Heat Flux Measurements for Test Series "Unsteady Decomposition" in Section 3.5.2.	51

3.7 Measurement Chain for Unsteady Pressure Measurements for "Direct Comparison"	53
3.8 Measurement Chain for Unsteady Heat Flux Measurements for "Direct Comparison".	55
3.9 Optical Setup for Shadowgraph Flow Visualization	56
3.10 Sample Shadowgraph of Shock Passing Event with Film Cooling.	65
3.11 Sample Time Histories of Pressure Ratio for Gauges 2,3,4,5 from one of the Experiments without Film Cooling.	66
3.12 Sample Time Histories of Unsteady Heat Flux for Gauges 1,2,3,4,5 from one of the Experiments without Film Cooling.	67
3.13 Schematic Depiction of Shock Expansion Process. States 1, 2 and 3 Represent the Shock At Different Successive Times.	68
3.14 Sample Time Histories of Pressure Ratio for Gauges 2,4,5,6 from Experiment with Film Cooling.	70
3.15 Sample Time Histories of Unsteady Heat Flux for Gauges 1,2,3,4,5 from Experiment with Film Cooling.	71
3.16 Shock Passing Events for Gauge # 2 at Increased Shock Strength without Film Cooling. Three Experiments at Different Levels of Initial Heat Flux	79
3.17 Shock Passing Events for Gauge # 2 at Increased Shock Strength without Film Cooling. Three Experiments at Different Levels of Initial Heat Flux. Initial Level of Heat Flux Removed	80
3.18 Shock Passing Events for Gauge # 2 at Increased Shock Strength without Film Cooling. Three Experiments at Different Levels of Initial Heat Flux. Initial Level of Heat Flux Removed. Converted to Temperature Variation.	81
3.19 Shock Passing Events for Gauge # 1 at Different Shock Conditions without Film Cooling. Three Experiments at Different Levels of Initial Heat Flux for Each Shock Strength. Top Graphs: Absolute Values. Bottom Graph: Initial Value Subtracted.	83

3.20 Shock Passing Events for Gauge # 2 at Different Shock Conditions without Film Cooling. Three Experiments at Different Levels of Initial Heat Flux for Each Shock Strength. Top Graphs: Absolute Values. Bottom Graph: Initial Value Subtracted	84
3.21 Shock Passing Events for Gauge # 3 at Different Shock Conditions without Film Cooling. Three Experiments at Different Levels of Initial Heat Flux for Each Shock Strength. Top Graphs: Absolute Values. Bottom Graph: Initial Value Subtracted	85
3.22 Shock Passing Events for Gauge # 4 at Different Shock Conditions without Film Cooling. Three Experiments at Different Levels of Initial Heat Flux for Each Shock Strength. Top Graphs: Absolute Values. Bottom Graph: Initial Value Subtracted	86
3.23 Shock Passing Events for Gauge # 5 at Different Shock Conditions without Film Cooling. Three Experiments at Different Levels of Initial Heat Flux for Each Shock Strength. Top Graphs: Absolute Values. Bottom Graph: Initial Value Subtracted	87
3.24 Shock Passing Events for Gauge # 1 at Increased Shock Strength with Strong Film Cooling. Three Experiments at Different Levels of Initial Heat Flux	96
3.25 Shock Passing Events for Gauge # 1 at Increased Shock Strength with Strong Film Cooling. Three Experiments at Different Levels of Initial Heat Flux. Initial Level of Heat Flux Removed	97
3.26 Shock Passing Events for Gauge # 1 at Increased Shock Strength with Strong Film Cooling. Three Experiments at Different Levels of Initial Heat Flux. Initial Level of Heat Flux Removed. Converted to Temperature Variation.	98
3.27 Shock Passing Events for Gauge # 1 at Different Shock Conditions with Film Cooling. Three Experiments at Different Levels of Initial Heat Flux for Each Shock and Cooling Strength. Top Graphs: Absolute Values. Bottom Graph: Initial Value Subtracted	100

3.28 Shock Passing Events for Gauge # 2 at Different Shock Conditions with Film Cooling. Three Experiments at Different Levels of Initial Heat Flux for Each Shock and Cooling Strength. Top Graphs: Absolute Values. Bottom Graph: Initial Value Subtracted.	101
3.29 Shock Passing Events for Gauge # 3 at Different Shock Conditions with Film Cooling. Three Experiments at Different Levels of Initial Heat Flux for Each Shock and Cooling Strength. Top Graphs: Absolute Values. Bottom Graph: Initial Value Subtracted.	102
3.30 Shock Passing Events for Gauge # 4 at Different Shock Conditions with Film Cooling. Three Experiments at Different Levels of Initial Heat Flux for Each Shock and Cooling Strength. Top Graphs: Absolute Values. Bottom Graph: Initial Value Subtracted.	103
3.31 Shock Passing Events for Gauge # 5 at Different Shock Conditions with Film Cooling. Three Experiments at Different Levels of Initial Heat Flux for Each Shock and Cooling Strength. Top Graphs: Absolute Values. Bottom Graph: Initial Value Subtracted.	104
3.32 Comparison of T'_{aw} from Run #2 Gauge #1 with Film Cooling and $T_r \cdot (1 - \eta)$ from Run #2 Gauge #1 without Film Cooling.	107
3.33 Comparison between T'_{aw} and $T_r \cdot (1 - \eta)$ for all Experiments with Film Cooling. Results from Gauge #1.	108
3.34 Comparison between T'_{aw} and $T_r \cdot (1 - \eta)$ for all Experiments with Film Cooling. Results from Gauge #2.	109
3.35 Comparison between T'_{aw} and $T_r \cdot (1 - \eta)$ for all Experiments with Film Cooling. Results from Gauge #3.	110
3.36 Comparison between T'_{aw} and $T_r \cdot (1 - \eta)$ for all Experiments with Film Cooling. Results from Gauge #4.	111
3.37 Comparison between T'_{aw} and $T_r \cdot (1 - \eta)$ for all Experiments with Film Cooling. Results from Gauge #5.	112
3.38 Shock Passing Event for Gauge # 2 from Uncooled Run #3. Raw Signals of Pressure Ratio and Unsteady Heat Flux.	117

3.39 Shock Passing Event for Gauge # 2 from Uncooled Run #3. Processed Signals of Pressure Ratio and Unsteady Heat Flux	118
3.40 Shock Passing Event for Gauge # 2 from Uncooled Run #3. Predicted and Measured Unsteady Heat Flux.	119
3.41 Shock Passing Event from Run #1 with Film Cooling. Moss' Model And Comparison with Data.	120
3.42 Shock Passing Event from Run #2 with Film Cooling. Moss' Model And Comparison with Data.	121
3.43 Shock Passing Event from Run #3 without Film Cooling. Moss' Model And Comparison with Data.	122
3.44 Shock Passing Event for Gauge # 1 from Uncooled Run #3. Pressure Ratios and Isentropic Gas Temperature. Pressure Signal Corrected According to Section "Signal Processing" 3.4.	125
3.45 Shock Passing Event for Gauge # 1 from Uncooled Run #3. q_u Accord- ing to Johnson et al. (1988). Heat Flux Signal Corrected According to Section "Signal Processing" 3.4.	127
3.46 Shock Passing Event for Gauge # 1 from Uncooled Run #3. q_m Ac- cording to Johnson et al. (1988). Heat Flux Signal Corrected Accord- ing to Section "Signal Processing" 3.4.	128
3.47 Shock Passing Event for Gauge # 1 from Uncooled Run #3. Compar- ison Between $q_u + q_m$ and q' . Heat Flux Signal Corrected According to Section "Signal Processing" 3.4.	129
3.48 Shock Passing Event from Run #1 With Film Cooling. Johnson's Model And Comparison with Data. Pressure and Heat Flux Signals Corrected According to Section "Signal Processing" 3.4.	131
3.49 Shock Passing Event from Run #2 With Film Cooling. Johnson's Model And Comparison with Data. Pressure and Heat Flux Signals Corrected According to Section "Signal Processing" 3.4.	132

3.50 Shock Passing Event from Run #3 Without Film Cooling. Johnson's Model And Comparison with Data. Pressure and Heat Flux Signals Corrected According to Section "Signal Processing" 3.4	133
3.51 Change in Laminar Sublayer Temperature Profile from T_0 to T Due to Compression and Heating Induced by Pressure Change. From Rigby et al. (1989).	134
3.52 Shock Passing Event from Run #1 With Film Cooling. Rigby's Model And Comparison with Data. Pressure and Heat Flux Signals Corrected According to Section "Signal Processing" 3.4	142
3.53 Shock Passing Event from Run #2 With Film Cooling. Rigby's Model And Comparison with Data. Pressure and Heat Flux Signals Corrected According to Section "Signal Processing" 3.4	143
3.54 Shock Passing Event from Run #3 Without Film Cooling. Rigby's Model And Comparison with Data. Pressure and Heat Flux Signals Corrected According to Section "Signal Processing" 3.4	144
3.55 Reid's and Johnson's Simplified Depictions of the Shock Impingement Process.	145
A.1 Shock Progression: Still # 1, time $\approx 450\mu s$	159
A.2 Shock Progression: Still # 2, time $\approx 520\mu s$	159
A.3 Shock Progression: Still # 3, time $\approx 525\mu s$	160
A.4 Shock Progression: Still # 4, time $\approx 562\mu s$	160
A.5 Shock Progression: Still # 5, time $\approx 585\mu s$	161
A.6 Shock Progression: Still # 6, time $\approx 600\mu s$	161
A.7 Shock Progression: Still # 7, time $\approx 622\mu s$	162
A.8 Shock Progression: Still # 8, time $\approx 640\mu s$	162
B.1 Shock Tube with <i>Kulite</i> Pressure Sensors.	165
B.2 Transfer Function of the Measurements Group 2310 Strain Gauge Conditioner and Signal Amplifier at a gain of 1.	166

B.3	Transfer Function of the <i>Ithaco 4302</i> low-pass filter at a cut-off frequency of 1 MHz.	167
B.4	Combined Transfer Function of <i>Measurements Group 2310 Strain Gauge Conditioner and Signal Amplifier</i> at a gain of 1 and the <i>Ithaco 4302</i> low-pass filter at a cut-off frequency of 1 MHz.	168
B.5	Raw Data from Both Transducers.	170
B.6	Traces after Truncation, Padding of Downslope, Zeroing of Initial Value. Also Shown is the "Ideal" Step Input. Upper Graph a): Entire Traces. Lower Graph b): Time Window Around Shock Event.	172
B.7	Data Corrected for the Influence of the Amplifier and the Filter. Upper Graph a): Unscreened Sensor: Raw Signal, Corrected Signal and Ideal Step. Lower Graph b): Sensor with B-Screen: Raw Signal, Corrected Signal and Ideal Step.	173
B.8	Bode Plot of Fourier Transforms of the Ideal Step Input, the Unscreened Sensor and the Sensor with the B-Screen.	174
B.9	Bode Plot of Transfer Function of Unscreened Sensor.	176
B.10	Bode Plot of Transfer Function of Sensor with B-Screen.	177
C.1	Shock Tube with <i>Vatell</i> Heat Flux Sensor.	181
C.2	Comparison of theoretical heat flux, theoretical gauge response and experimental data.	186
D.1	Experimental and Approximated Transfer Function of the <i>2310 Amplifier</i> at a Gain of 1.	190
D.2	Experimental and Approximated Transfer Function of the <i>2310 Amplifier</i> at a Gain of 10.	191
D.3	Experimental and Approximated Transfer Function of the <i>2310 Amplifier</i> at a Gain of 100.	192
D.4	Experimental and Approximated Transfer Function of the <i>2310 Amplifier</i> at a Gain of 1000.	193

E.1	Measurement Repeatability of Heat Transfer Coefficient at $PR=1.04$.	201
E.2	Measurement Repeatability of Effectiveness at $PR=1.04$	202

Nomenclature

Symbols

A	Constant in Solution for $T_h(y, s)$, Section 3.5.3.3
B	Constant in Solution for $T_h(y, s)$, Section 3.5.3.3
c_p	Specific heat at constant pressure of air in Section 3.5.3.2
d	Thickness of Laminar Sublayer, Section 3.5.3.3
h	Heat transfer coefficient, mean value of heat transfer coefficient before shock impact
H_{2310}	Transfer Function of the <i>Measurements Group 2310 Strain Gauge Conditioner and Signal Amplifier</i> , see equation (3.2), page 59
h_c	Heat transfer coefficient with film cooling, mean value of heat transfer coefficient before shock impact with film cooling
$h_{c1} \dots h_{c6}$	Mean value of heat transfer coefficient before shock impact for gauges 1 through 6
H_c	Unsteady component of heat flux with film cooling
$h_1 \dots h_6$	Mean value of heat transfer coefficient before shock impact for gauges 1 through 6

H_{Kulite}	Transfer function of <i>Kulite XCQ-062-50a</i> pressure transducer, see Appendix B, see equation (3.3), page 60
H	Unsteady component of heat transfer coefficient
j	$\sqrt{-1}$, see equation (3.4), page 62
k	Thermal conductivity of air in Section 3.5.3.2
\bar{x}	Laplace transform of x
m	Counter for time step t_m , see equation (3.36), page 124
N	Number of data points in trace, see equation (3.1), page 58
n	Counting variable, see equation (3.1), page 58
p	Mean value of static freestream pressure before shock impact
p_1, p_2	Two arbitrary pressure traces, see equation (3.1), page 58
p_{av}	Static pressure before shock impact in Section 3.5.1
$P_{corr2310}$	Fourier Transform of Pressure Signal Corrected for the Amplifier Transfer Function, see equation (3.2), page 59
P_{final}	Fourier transform of pressure signal after all corrections, see equation (3.3), page 60
p_{∞}	Freestream total pressure
p'	Unsteady component of static freestream pressure, in Sections 3.5.3.1 and 3.5.3.2
P_{raw}	Fourier Transform of Pressure Signal, see equation (3.2), page 59
q	Heat flux, mean heat flux before shock impact
q_c	Surface Heat Flux Due to Compression Heating, Section 3.5.3.3

$q_{corr,n}$	n-th value of corrected heat flux, see equation (3.5), page 62
Q_{final}	Fourier transform of the corrected heat flux signal , see equation (3.4), page 62
q_h	Heat Flux Due to Transient Conduction, Section 3.5.3.3
q_m	Unsteady component of heat flux in Section 3.5.3.2, see equation (3.42), page 128
q'	Unsteady component of heat flux
$q_{raw,n}$	n-th value of raw heat flux data, see equation (3.5), page 62
Q_{raw}	Fourier transform of the raw heat flux signal , see equation (3.4), page 62
q_u	Unsteady component of heat flux in Section 3.5.3.2
r	Pearson product moment correlation coefficient, see equation (3.1), page 58
s	Variable in Laplace domain
T_{aw}	Adiabatic wall temperature, mean value of adiabatic wall temperature before shock impact
T'_{aw}	Unsteady component of adiabatic wall temperature
$T_{aw1} \dots T_{aw6}$	Mean value of adiabatic wall temperature before shock impact for gauges 1 through 6
T_c	Coolant temperature
$T_c(y,t)$	Temperature Induced by Compression, Section 3.5.3.3
T_g	Unsteady component of freestream temperature, see equation (3.33), page 123
$T_h(y,t)$	Temperature Induced by Transient Conduction, Section 3.5.3.3
$T_o(y)$	Temperature Distribution in the Laminar Sublayer, Section 3.5.3.3

T_r	Recovery temperature, mean value of recovery temperature before shock impact
$T_{r1} \dots T_{r6}$	Mean value of recovery temperature before shock impact for gauges 1 through 6
T'_r	Unsteady component of recovery temperature
T_s	Mean value of static freestream temperature before shock impact, in Section 3.5.3.1
T'_s	Unsteady component of static freestream temperature in Section 3.5.3.1
T_t	Freestream total temperature
T_w	Wall temperature
$T_{w1} \dots T_{w6}$	Mean value of wall temperature before shock impact for gauges 1 through 6
T'_w	Unsteady component of wall temperature
v	Vertical Velocity, Section 3.5.3.3
y	Boundary Layer Coordinate, Section 3.5.3.3
y_0	Boundary Layer Coordinate Prior to Disturbance, Section 3.5.3.3

Greek Symbols

β_g	$\sqrt{k \cdot \rho \cdot c_p}$, thermal product of air
Δt	Sampling period, see equation (3.1), page 58
ΔT	Step change of gas temperature induced by incoming and reflected shock, see equation (3.73), page 146
γ	Ratio of specific heats

η	Film effectiveness, mean value of film effectiveness before shock impact, see equation (3.19), page 89
$\eta_1 \dots \eta_6$	Mean value of film effectiveness before shock impact for gauges 1 through 6
η'	Unsteady component of film effectiveness, see equation (3.20), page 90
Π	Isentropic Compression Coefficient, Section 3.5.3.3
ρ	Density of air in Section 3.5.3.2
ρ'	Varying Component of Density, Section 3.5.3.3
τ	Time constant of heat flux gauge
ω	$2 \cdot \pi$ frequency in Section 3.4.2

Chapter 1

Introduction

1.1 Problem Statement: Turbine Blade Heat Transfer

Economic as well as ecological demands have driven the progress in gas turbine development over the past 60 years. The two goals most relevant to the aero-thermal designer have always been:

1. Higher cycle efficiencies
2. Higher thrust to weight ratios

A simple analysis of a standard Brayton cycle reveals the two most influential parameters in the quest for higher efficiencies:

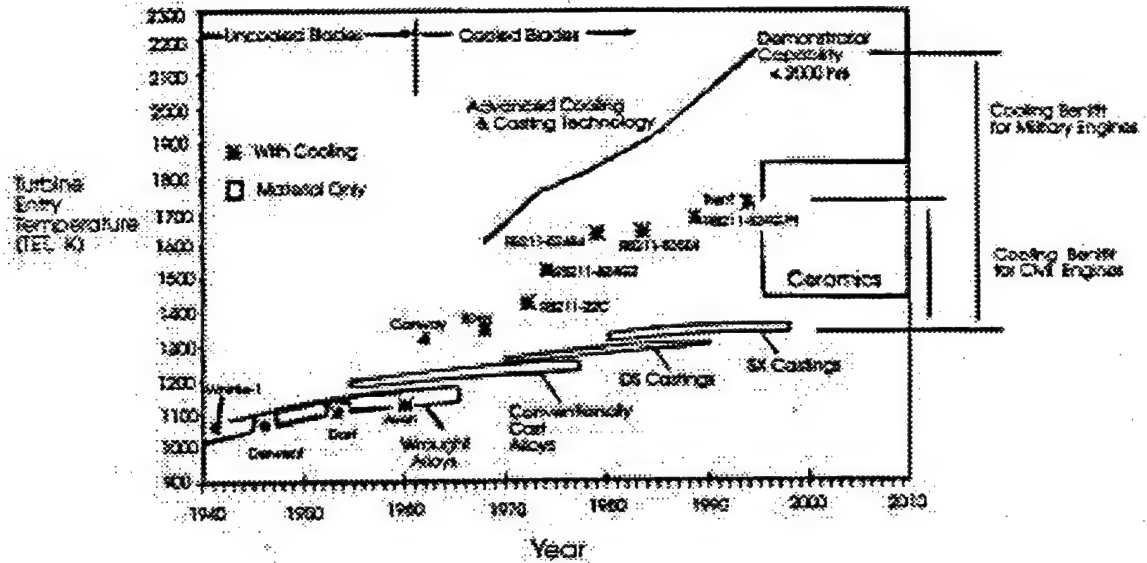


Figure 1.1: Advance of Materials and Cooling Technology. Source: Royal Aeronautical Society / Aerospace - 1994.

$$\eta = 1 - \frac{\Theta \cdot \left(1 - \eta_t \cdot \left(1 - \Pi^{-\frac{\gamma-1}{\gamma}}\right)\right) - 1}{\Theta - \frac{\Pi^{\frac{\gamma-1}{\gamma}} - 1 + \eta_c}{\eta_c}} \quad (1.1)$$

Besides the turbine and compressor efficiency η_t and η_c respectively, the two governing parameters are the ratio of highest to lowest cycle temperature Θ and the compression ratio Π . An increase in both will increase the overall efficiency η . Consequently, turbine inlet temperatures and compression ratios have increased dramatically in the last decades. Until the early sixties the limiting factor for a further increase of turbine inlet temperature was the availability of materials that could withstand the thermal and mechanical loads. The improvement in cooling techniques, such as internal cooling using impinging jets or simple convective cooling, continuously extended the range of feasible turbine inlet temperatures (see Figure 1.1). A quantum leap was achieved when external cooling techniques such as transpiration cooling, evaporation cooling and film cooling were introduced in the late sixties and early seventies. Of all the external cooling techniques only film cooling found a broad

acceptance. The best definition of film cooling was given by Goldstein (1976) as the "introduction of a secondary fluid (coolant) at one or more discrete locations along a surface exposed to a high temperature environment to protect that surface not only in the immediate region of injection but also in the downstream region." Film cooling today is very commonly used in engines in a wide variety of applications.

While a high pressure ratio is a desirable goal for the design of high efficiency engines, its side effects are high Reynolds Numbers in the turbine and larger overall engine size and weight. The higher Reynolds numbers translate into high heat transfer coefficients and, therefore, higher heat transfer rates. With the reduction of adiabatic wall temperature by film cooling the increase in heat transfer coefficient is of secondary significance. The increase of weight, on the other hand, is undesirable. This leads to the demand for higher thrust to weight ratios. The same amount of work is to be added to or extracted from the flow with the smallest number of stages and the smallest overall size possible. While it has been known for a long time that the extraction or addition of work in the engine is inherently related to the unsteadiness of the flow in the engine (Dean (1959)), it has also been shown that higher loading causes higher levels of unsteadiness in the engine (Greitzer (1979)). To increase the amount of work extracted from the flow in an axial turbine three relevant parameters have to be increased: radius, rotational speed and circumferential flow velocity components. The choice of radius and rotational speed are governed by mechanical constraints and overall design decisions (number of spools, overall engine size, radial stresses, etc.). Flow velocities, on the other hand, are a parameter to be decided upon by the aerodynamic designer. To increase the circumferential velocity components, the turning angles in stators and rotors have been increased significantly. Also, the absolute velocities have exceeded the sonic limit. The flow then features trailing edge shocks emerging from the trailing edge of the stators and/or rotors. On the other hand, the requirement for small dimensions has decreased the spacing between blade rows. The flowfield upstream of the rotor blade row has, therefore, become very non-uniform. It features trailing edge shocks, distinct wakes (little spacing between

blade rows) and strong pressure gradients (due to the high turning in the nozzle guide vanes). The situation is depicted schematically in Figure 1.2. For a rotor blade row passing through a flow field of this kind, the non-uniformity presents itself in the form of high frequency unsteadiness. The concern has since then been the prediction of heat transfer under these unsteady conditions. Analytical, computational and experimental efforts have been made to approach this task.

The work presented in this dissertation is an experimental attempt to assess the heat transfer effect of a shock wave passing over a blade with and without film cooling. Of all the unsteady events, the shock wave is expected to have the strongest effect on the turbine blade heat transfer since it presents a distinct discontinuity of all flow parameters (velocity, temperature and, most importantly, pressure).

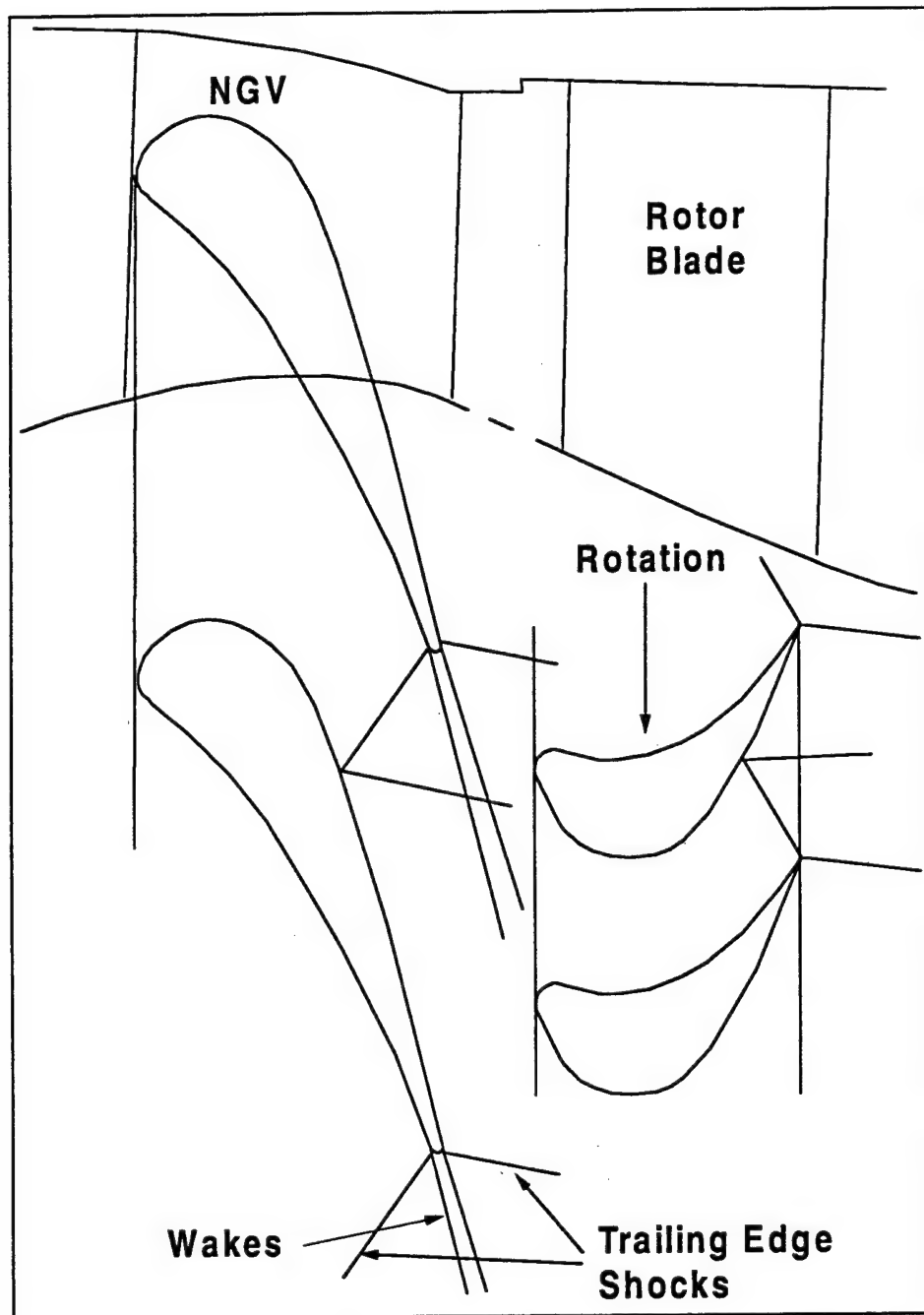


Figure 1.2: Schematic Depiction of the Non-Uniformity of the Flowfield Downstream of a Modern NGV Row.

1.2 Literature Review

Unsteady phenomena in gas turbines have been under investigation since the early fifties. The focus of these early efforts was to determine the effects of unsteady phenomena on the time-averaged profile losses and the overall effect on gas turbine operation. The problem of unsteady heat transfer in a turbine due to the interaction between NGV shocks and wakes and the rotor blade boundary layer has been under detailed investigation approximately since the mid-eighties and was initiated by the work of Doorly et al. (1985) at the University of Oxford. Since then, a wide variety of research institutes have contributed to the understanding and prediction of unsteady heat flux on a rotor blade. These activities do not present a well concerted effort in terms of their chronological succession. It is for this reason that an overview over the last fifteen years of research will not be given in a chronological order. Instead, a paragraph will be dedicated to each institute that has contributed significantly to the topic. The order of these paragraphs will be in accordance with their degree of relevance to the work presented in this dissertation.

In the discussion two physical parameters will be of primary interest. The heat transfer coefficient h defined as:

$$q = h \cdot (T_{aw} - T_w) \quad (1.2)$$

In this Equation q is the heat flux, $(T_{aw} - T_w)$ is the driving temperature difference. The second parameter of importance is the film effectiveness η defined as:

$$\eta = \frac{T_{aw} - T_c}{T_r - T_c} \quad (1.3)$$

Here T_c is the temperature of the coolant and T_r is the recovery temperature of the freestream.

1.2.1 Research at Texas A & M University

Ou et al. (1994) and Mehendale et al. (1994) first published results from a low speed linear turbine cascade with and without film cooling. They produced wakes using a spoked wheel rotating in front of the cascade. Air and CO_2 at freestream temperatures were used by Ou et al. (1994) to vary the density ratio between 0.97 (Air) and 1.48 (CO_2). The increase in heat transfer coefficient observed when introducing the wake disturbances on a blade without film cooling was very significant on the downstream suction side. It was attributed to an earlier transition and a longer transition length caused by the wake passing on the suction side. On a film cooled blade this effect could not be observed. The introduction of film cooling increased the heat transfer coefficient significantly when compared to the case without film cooling, probably due to the early tripping of the boundary layer. The additional introduction of the wake disturbances did not affect the heat transfer coefficient severely. Mehendale et al. (1994) investigated the film effectiveness under the same conditions. The influence of the wake passing on the film effectiveness was small (largest values around ± 5 percent) and not easily explicable.

Du et al. (1997) used liquid crystals instead of surface thermocouples to determine the film effectiveness and heat transfer coefficients for the same conditions and were able to replicate the results. The conclusion from the experiments seems to be that the main mechanism for the wakes to influence the heat transfer coefficient is by affecting the transitional behaviour of the suction side boundary layer. In areas free of transitional features the effects of the passing wakes were rather small.

1.2.2 Research at Iwate University

Funazaki et al. (1996) investigated the effect of wake passing on the time and span averaged film effectiveness on a film cooled blunt body model in a low speed wind tunnel. The wakes were again generated by a rotating bar mechanism. The effect of wake passing on the time and span averaged film effectiveness was miniscule except for the lowest blowing rate condition, where the presence of wakes decreased the film effectiveness on the downstream part of the suction side by about eight percent. It is unclear what the motivation behind the research could have been since actually it is a further simplification compared to the experiments done at Texas A & M three years earlier. The use of liquid crystals for the determination of film effectiveness may have been an incentive. Texas A & M used this technique one year later on their setup.

1.2.3 Research at NASA Lewis Research Center

Heidmann et al. (1997) presented experimental work on a somewhat more realistic model. An annular stationary cascade with an inlet Mach Number of 0.27 was used to investigate the effect of wake passing on a film cooled turbine blade. The wakes were generated using a rotating bar mechanism rotating upstream of the cascade annulus. Showerhead film cooling was applied through two rows of holes on both the pressure and suction side and one row in the stagnation line. There was no transition on the suction side with or without wake passing. The effects produced by the wake generator were twofold. On the one hand, the presence of the wakes generally increased mixing and therefore decreased the film cooling effectiveness all along the blade. On the other hand, the wake generator also generated flow swirl. This flow swirl caused the stagnation line on the rotor blades to move toward the suction side, thereby causing the amount of coolant flow to decrease on the suction side and to increase on the pressure side. This effect attenuated the effect of increased

mixing on the pressure side. The decrease of film effectiveness was therefore smaller on the pressure side. On the suction side the decrease was more pronounced due to this shift of coolant flow. Neglecting the effect of the swirl introduced by the wake generator, the decrease of film effectiveness was not very significant. The effects of the wake passing on the time averaged heat transfer were not reported. It can be expected, though, that the effect will be minor since the wakes do not affect transition on the suction side.

1.2.4 Research at Calspan-UB Research Center

In the late seventies, M.G. Dunn and other researchers at the Calspan-UB Research Center began a long series of experiments in a full-stage rotating turbine driven by a shock tube. An extensive list of publications has resulted from these experiments. Film cooling has so far not been implemented. Also, no shocks were present in the flowfield since the turbine stage was designed for a relatively low overall pressure drop. In 1982, Dunn et al. (1982) reported on time averaged heat transfer data obtained on the stator vane and rotor blade. After comparison with predictions for a stand alone stator vane, they found that the presence of the rotor increases the heat transfer on the stator vane. With increasing frequency response of the thin-film heat flux gauges, it became possible for them to obtain time-resolved heat flux measurements. A first attempt of analyzing this high-speed data was published in Dunn et al. (1986). It was found that the magnitudes of the unsteady heat flux variations decrease towards the trailing edge of the rotor blade. In 1989 Dunn et al. (1989) finally published fully phase-locked heat transfer data taken on the rotor blade and the shroud. For the shroud measurements it was shown that pressure and heat flux time histories are in phase and similar in shape. The presence of trailing-edge cooling ejection from the NGV had a major impact on the unsteady heat transfer in the stagnation region of the rotor blade in that it increased the magnitudes of the fluctuations by a large factor. Unfortunately, no attempts were made to model

or explain the unsteady heat transfer. The fact that no pressure measurements were done on the rotor makes it hard to correlate the heat transfer data to flowfield features.

1.2.5 Research at MIT

In 1984, Epstein et al. (1984) presented the new MIT Blowdown Turbine Facility. In 1989, Guenette et al. (1989) published a first set of on rotor time-resolved heat transfer data. The mid span section of this rotor was tested in a linear cascade at the University of Oxford (see Section 1.2.6). Steady as well as unsteady pressure and heat flux data from the full scale MIT turbine and the Oxford linear cascade were compared with reasonable success. While the flow field of the turbine inherently featured shock waves and wakes, these had to be modeled with a rotating bar mechanism in the cascade experiments (see Section 1.2.6). The conclusion from this early work was that data from the full stage turbine is comparable to results from the linear cascade with modeled unsteadiness. At this point there was no film cooling involved with either the cascade or the rotating rig. Film cooling was introduced in Oxford in 1990 (Rigby et al. (1990)) and at MIT in 1992 by Abhari et al. (1994). A time averaged pressure distribution over the blade was used to numerically calculate the steady-state heat flux to the blade. The time averaged heat flux measured on the suction side was 12 % lower than the one calculated with the steady code. On the pressure side the measured heat flux was 5% higher than predicted. Specifically, the decrease of heat transfer on the suction side is a surprising finding. The effects of unsteady phenomena were linked to the time history of the blowing ratio affected by the varying static pressure at the coolant exits.

Abhari (1996) later developed an injection model to be implemented with a numerical solver for time-accurate resolution of the stator-rotor interaction process. The code was validated with steady-state film cooled cascade data obtained at the VKI and unsteady data obtained by Abhari et al. (1994). Then a direct comparison

between a steady calculation and an unsteady calculation was done. It showed that the time mean heat transfer on the suction side did not change considerably with the introduction of unsteady phenomena. On the pressure side, on the other hand, the film effectiveness decreased by as much as 64%. A reduction of time mean coolant massflow due to pulsations and strong interactions with the freestream flow were identified as the primary causes for this decrease of film effectiveness on the pressure side.

1.2.6 Research at Oxford University

The most comprehensive body of research on the unsteady heat transfer on a rotor blade due to shock waves and wakes has been established at the University of Oxford. It spans from early cascade experiments with a rotating bar and without film cooling (Doorly et al. (1985)) to full scale experiments in a rotating rig (Moss et al. (1997)).

Doorly et al. (1985) were the first to report on high speed heat transfer data in the linear cascade blowdown windtunnel on a rotor blade without film cooling. A combination of shocks and wakes was created with a rotating bar mechanism rotating upstream of the cascade at transonic speeds relative to the freestream flow. Each bar created a small bow shock wave, a recompression shock wave and a wake impinging on the rotor blades in the cascade. The weak bow shock and the recompression shock wave showed almost no signature in the heat flux recorded on the suction side because of their very low strength. The recompression shock wave created a small separation bubble that traveled downstream along the suction side. It caused a large spike of heat flux on its path. The second contribution to unsteady heat flux was the wake influence on the boundary layer. The turbulence associated with this wake rendered large portions of the boundary layer transitional, if not turbulent, for the duration of the wake interaction. It was speculated that these turbulent patches may eventually

merge and that finally, the entire boundary layer may become turbulent. The way the shock wake combination influences the heat transfer is by affecting the transitional behavior of the boundary layer. Even though the shock strength was very low and the effects of shocks and wakes were strongly interrelated, the study showed that the modeling of the unsteady effects of shocks and wakes was possible in a linear cascade.

In 1988 Johnson et al. (1988) published data acquired with the same setup but different blades and higher speeds of the rotating bar. The blades were a cascade model of the midspan section used in the full scale turbine experiments done by Guenette et al. (1989) at MIT (see Section 1.2.5). The speed of the rotating bars was increased from $M = 0.98$ to $M = 1.23$ relative to the freestream flow. This increased the strength of the bow shock and the recompression shock significantly. The heat transfer due to the actual shock impingement now became the major contribution to the overall unsteady heat transfer. The effects of the separation bubble were not discussed any further. In this paper a model is developed for the unsteady heat transfer. The basic equation of this model — derived from the boundary layer energy equation — is identical to the one-dimensional unsteady heat conduction equation. The gas temperature change is calculated from the static surface pressure measurement assuming an isentropic compression. This temperature history is used in the solution of the 1-D unsteady heat conduction equation to obtain the heat flux on the surface. The heat transfer predicted by this method and the measured heat transfer matched fairly well.

In 1989 Rigby et al. (1989) published a modified version of the model first presented in Johnson et al. (1988). In this publication they also provide a detailed derivation of the model equation. The basic assumptions behind Rigby et al. (1989) and Johnson et al. (1988) are identical, and the results of the predictions are similar. The experiments used for comparison were done in the same cascade.

In 1990 Johnson et al. (1990) extended their investigation to the pressure

side of the same cascade. Although the agreement between the model developed in Johnson et al. (1988) in 1988 matched the measured data fairly well on the suction side, it underpredicted heat transfer on the pressure side. The phenomenon found to explain this discrepancy was a "Vortical Bubble" traveling down the pressure side. It is the same phenomenon that Doorly et al. (1985) had described as a "Separation Bubble" found to travel down the suction side.

Rigby et al. (1990) first included film cooling in the research done in the linear cascade at Oxford University. The effects of shocks and wakes on the heat transfer with film cooling was investigated. The values of film effectiveness obtained with the different cooling configurations were so low that the actual heat flux increased in some regions on the blade with the introduction of film cooling. The heat flux signatures of both shocks and wakes that are visibly different with and without film cooling are implying the presence of heat transfer modes different than assumed in the compression/unsteady conduction model.

After this last attempt to model the unsteady heat transfer in a linear cascade a new transonic turbine stage was put in service. In 1995 Moss et al. (1995) reported the first set of unsteady heat transfer and pressure data measured on the rotor of this facility. No film cooling was used at that time and no time average data was presented. The NGV exit velocity of the new facility was slightly subsonic so that no shocks are present in the flowfield. The unsteady heat flux data was compared to the heat flux predicted using Johnson's compression/unsteady conduction model. The agreement was relatively poor. Assuming a constant heat transfer coefficient and calculating a temperature change from the surface pressure data using an isentropic compression model resulted in a predicted unsteady heat transfer that compared far better with the measured heat flux data. The time mean heat transfer with and without the presence of unsteady phenomena was then expected to be similar since the unsteady heat transfer was shown to be mostly driven by a variation in temperature, which in the presence of unsteady phenomena will vary around its mean.

In 1997 Moss et al. (1997) provided the proof for this argument by presenting time averaged heat transfer data with and without the presence of wakes. The way the "clean" inlet flowfield was established was by removing the NGV's and spinning the rotor in the direction opposite to its design turning direction. The time averaged heat flux data was nearly identical for both cases. This was highly unexpected given the wide variety of different observations mentioned above.

1.2.7 Research at Virginia Tech

At Virginia Tech, research began to focus on unsteady phenomena in turbines around 1992. The intention was to separate the effects of shock waves and wakes for detailed analysis. Doughty et al. (1994) developed a system to expose a linear turbine rotor cascade to multiple incident shock waves. The work was then published in Doughty et al. (1995). Nix et al. (1997) measured in detail the pressure and heat flux signature of a single passing shock wave on several locations on the blade. It became clear that unsteady pressure and heat flux correlated in strength and shape on all measurement locations. Reid (1998) developed a numerical code to apply the quasi-2D Navier-Stokes equations to the problem of a normal shock wave impinging normally on a surface with boundary layer. He compared his numerical results with experimental data from Nix et al. (1997) and found good agreement for the case of air at rest. The agreement between data taken with the crossflow present and the numerical results was somewhat less satisfactory.

In Popp et al. (1999) film cooling was introduced in a similar setup with large scale blades. In an attempt to determine the influence of variations of heat transfer coefficient and film effectiveness during shock impingement, it was found that neither of them seemed to contribute significantly to the unsteady heat transfer. The heat transfer was found to be driven mostly by a variation of temperature. The origin of this temperature variation was not explained.

1.3 This Work

While the experimental researchers mentioned above are forced to investigate either only wakes or a combination of wakes and shocks, the setup at Virginia Tech allows for the investigation of the shock interaction in isolation. Therefore, it can be seen as a necessary completion of the research efforts described in Section 1.2. The possibility of measuring heat flux directly using *Vatell HFM-7/L* high speed heat flux transducers allows a very detailed and accurate analysis of the effects of the shock-blade interaction. In combination with *Kulite XCQ-062-50a* high speed pressure transducers it is possible to link the unsteady heat flux to aerodynamic flow field phenomena. With the introduction of film cooling the size of the blades had to be increased from earlier experiments to accommodate all the sensors necessary. Other advantages of this up-scaling were the reduction of the relative footprint of the heat flux and pressure sensors and a more realistic Reynolds Number level. It was decided to only investigate the suction side of the blade since the effect of the shock wave was expected to be most significant at this location. Preliminary results were obtained with only one set of gauges on the suction side. They are not reported here but are summarized in Popp et al. (1999) in Appendix G. The conclusions from this set of experiments were surprising. The heat transfer coefficient and the film effectiveness were not significantly affected by the shock impact. In order to validate this conclusion, more measurement locations and different physical parameters had to be investigated.

In order to be able to investigate the unsteady heat transfer, some physical parameters from a steady analysis had to be known. Section 2 refers to the Master's Theses by Bubbs (1999) and Smith (1999) for an in-depth description of the steady state experiments without shock interference. Only the very basic information necessary to the understanding of the unsteady investigation will be given.

Section 3 presents in detail the investigation of the unsteady heat transfer due to shock passing.

1.4 Overview

This thesis is divided into two major parts: "Steady Heat Transfer" (Section 2) and "Unsteady Heat Transfer" (Section 3). The Section on "Steady Heat Transfer" has been added for completeness; the focus of this work is clearly on the unsteady heat transfer. In the Section "Unsteady Heat Transfer", two different ways of analyzing the unsteady heat transfer due to shock passing are presented. They are referred to as "Unsteady Decomposition" and "Direct Comparison".

The basic idea behind the analysis of unsteady heat transfer according to the technique labeled "Unsteady Decomposition" is the comparison of heat flux traces initiated at different levels of heat flux. This comparison combined with a mathematical decomposition of all physical parameters involved provides insight in the relative magnitude of different contributions to the overall unsteady heat flux. This method does not require the measurement of static surface pressure on the blade, since only heat flux traces are needed. The pressure data was used only as a redundant monitor of the shock passing event. Using this technique, a wide variety of experiments were analyzed. The level of heat flux before shock impingement was varied in three steps, the strength of the passing shock wave in two steps and the ratio of the total pressure of the coolant and the freestream total pressure in two steps as well. This resulted in twelve overall experiments with film cooling and six experiments without film cooling. Heat flux data from five heat flux sensors was used in the analysis.

The method labeled "Direct Comparison" was applied only to two different sets of experiments. Two experiments with and one without film cooling. Only one shock strength and one level of initial heat flux were chosen for this type of analysis. Also, only data from two measurement locations was used. The models for predicting unsteady heat flux evaluated in this direct comparison all use static surface pressure to predict the heat flux. Therefore, more care had to be applied in acquiring and

processing pressure and heat flux data.

Each of these methods required different sets of experiments, different instrumentation and data acquisition and different strategies of signal processing. Therefore, Sections "Steady Heat Transfer" 2, "Instrumentation and Data Acquisition" 3.3 and "Signal Processing" 3.4 refer to the two different analytical methods even though they will not be introduced in detail before Section "Results and Discussion" 3.5.

Chapter 2

Steady Heat Transfer

2.1 Introduction and Problem Statement

The analysis of the unsteady heat transfer due to the shock passing event required the establishment of a cascade with well defined heat transfer characteristics with and without film cooling. In order to analyze the unsteady heat transfer due to shock impingement, the following parameters had to be known:

- The heat transfer coefficient before the shock impact without film cooling.
- The heat transfer coefficient and the film effectiveness before shock impact for the case with the film cooled blade.

In this Chapter the experimental setup and the procedure used to determine these parameters will be described briefly. For more detailed information the reader is referred to Bubb (1999) and Smith (1999).

2.2 Experimental Setup for Steady Experiments

The transonic blowdown windtunnel of Virginia Tech is shown in Figure 2.1. A four stage reciprocating compressor is loading outside storage tanks with high pressure air. Upon opening of the on/off valve, the air is allowed through the system of pipes and the test section and exhausted to the atmosphere. The heater loop is used to heat up a stack of copper tubes in the main flow path prior to the tunnel run. During the tunnel run the air takes this stored heat from the copper tubes which act like a passive heat exchanger. This way the air will be significantly hotter than the blades in the test section. This temperature difference is needed to obtain reasonably high heat flux readings on the blade. The instrumented blade is shown in Figure 2.2.

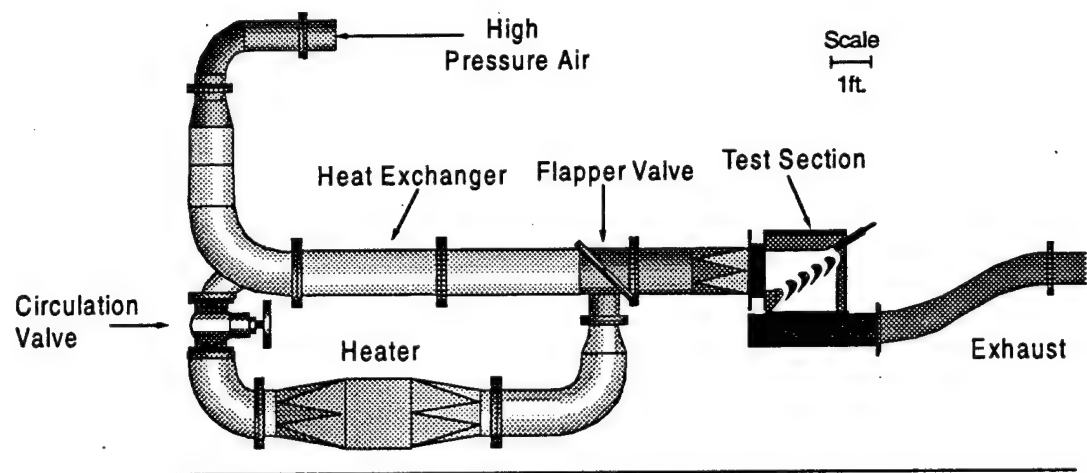


Figure 2.1: Transonic Blowdown Windtunnel at Virginia Tech, from Smith (1999).

Six measurement locations are staggered chordwise and spanwise along the suction side (1 through 6 in the upper right figure). The reasons for this arrangement are twofold:

1. The measurement locations were chosen to be on the suction side because the

passing shock was expected to have the most significant impact there.

2. The gauges were staggered in the spanwise direction to avoid the gauges from affecting the reading of the downstream sensors by disturbing the boundary layer. It was determined by oil flow visualization that the flow over the instrumented area is two-dimensional (see Bubb (1999)).

As seen in the Figure, each measurement location consists of three sensors: A *Kulite XCQ-062-50a* pressure transducer ((a) in lower right schematic), a surface thermocouple built in house ((c) in lower right schematic) and a *Vatell HFM-7/L* heat flux microsensor consisting of a heat flux sensor and a surface temperature thermistor ((b) in lower right schematic). The *Kulite XCQ-062-50a* pressure transducers provide low and high speed measurements of static surface pressure. The dynamic characteristic of these transducers was investigated in detail and is presented in Appendix B. The *Vatell HFM-7/L* heat flux microsensor consists of two independent sensors. One of them provides a direct reading of surface heat flux up to high frequencies. The dynamic behavior of this sensor was investigated. Details of the investigation are shown in Appendix C. The second part of the sensor is a surface resistance temperature device (RTD). The surface thermocouple is used as a backup and calibration device for this RTD. The outputs from the thin-film RTD's were zeroed before a set of experiments when the blade was considered to be at thermal equilibrium. A mean temperature reading from the surface thermocouples before the experiments was used as the reference temperature for the determination of the RTD temperature during the run. The difference between the temperature readings of the RTDs and the thermocouples at one location can be as large as 2°C for certain experiments, which has to be attributed to drift in the amplifier and a difference between the actual thermocouple reading and the average thermocouple reading before the experiments. The transient temperature histories of the surface thermocouple and the RTD during the tunnel run are similar in shape and magnitude. The difference in the transient component of the temperature histories is usually less than 0.8°C. The temperature difference be-

tween the thermocouples and the RTDs is caused by the difference in thickness of the two surface temperature measurements. Since the surface thermocouple penetrates deeper into the surface it lags behind the surface temperature history as measured by the RTD.

The cooling scheme consists of six rows of cooling holes (7 through 12 in upper left figure). Their diameter is 0.041 in. and the ratio of hole spacing to diameter is about nine. The rows are staggered half the pitch with respect to the neighboring rows. Only three rows of cooling holes actually provide cooling to the suction side (7,8,9). Rows 8 and 9 are inclined 30° from the spanwise direction and are normal to the chordwise tangent. Row 7 is in the chordwise plane and forms an angle of 30° with the chordwise tangent. For a more detailed explanation see Smith (1999). The holes labeled (a) in the lower left schematic are used for surface pressure measurements at the exit location of each row. The next column labeled (b) is equipped with a thermocouple to measure the coolant exit temperature for each row of cooling holes. For a more detailed description of the instrumentation around the showerhead see Bubb (1999).

The blade was supplied with coolant air by the system depicted schematically in Figure 2.3. A 5 horse power *Ingersoll-Rand* compressor in combination with a filter and dryer supplies clean and dry (less than 5% relative humidity) air to a large (2.92 m^3) storage tank. A control valve lowers the pressure in order to maintain a preset pressure difference between the coolant plenum in the blade and the freestream in the cascade. The coolant mass flow is then metered by an orifice plate. It is chilled in a simple heat exchanger. The heat exchanger consists of copper coils immersed in liquid nitrogen. The coolant then enters the coolant plenum in the blade. A differential pressure transducer measures the difference between the total pressure in the plenum and the total pressure in the cascade. The voltage from this transducer is compared to a voltage set by the user. The difference between the two voltages is integrated with respect to time in an analog circuit. The resulting output voltage is

fed to a electro-pneumatic converter which outputs a pressure signal to the control valve, thereby closing the control loop. This control loop will keep the difference between total pressure in the coolant plenum and the freestream total pressure in the cascade constant. A pressure difference set by means of the objective voltage prior to the run will be maintained during the run and under changing freestream conditions. For more details on the pressure control, the reader is referred to Bubb (1999).

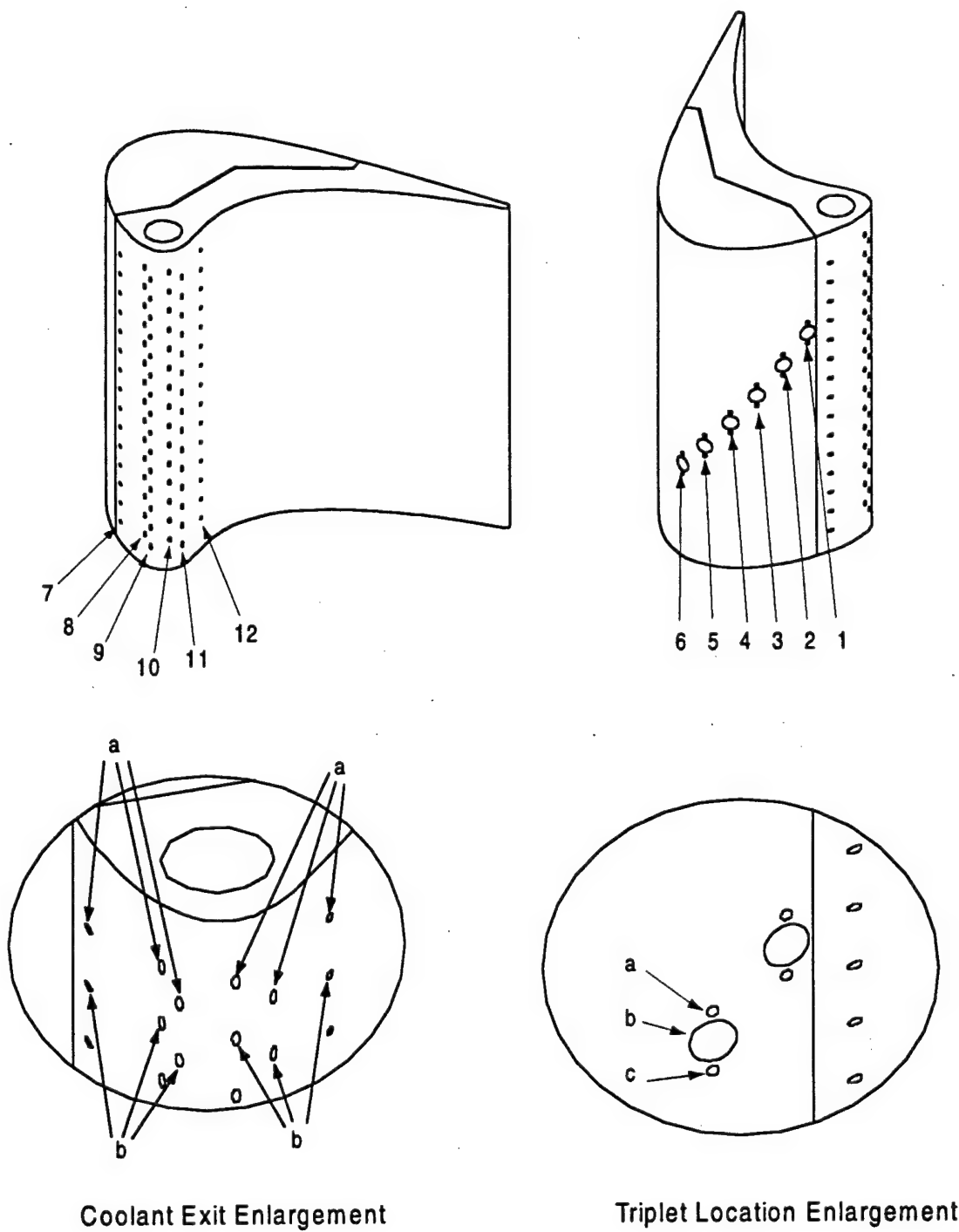


Figure 2.2: Instrumented Film Cooled Blade, from Bubb (1999).

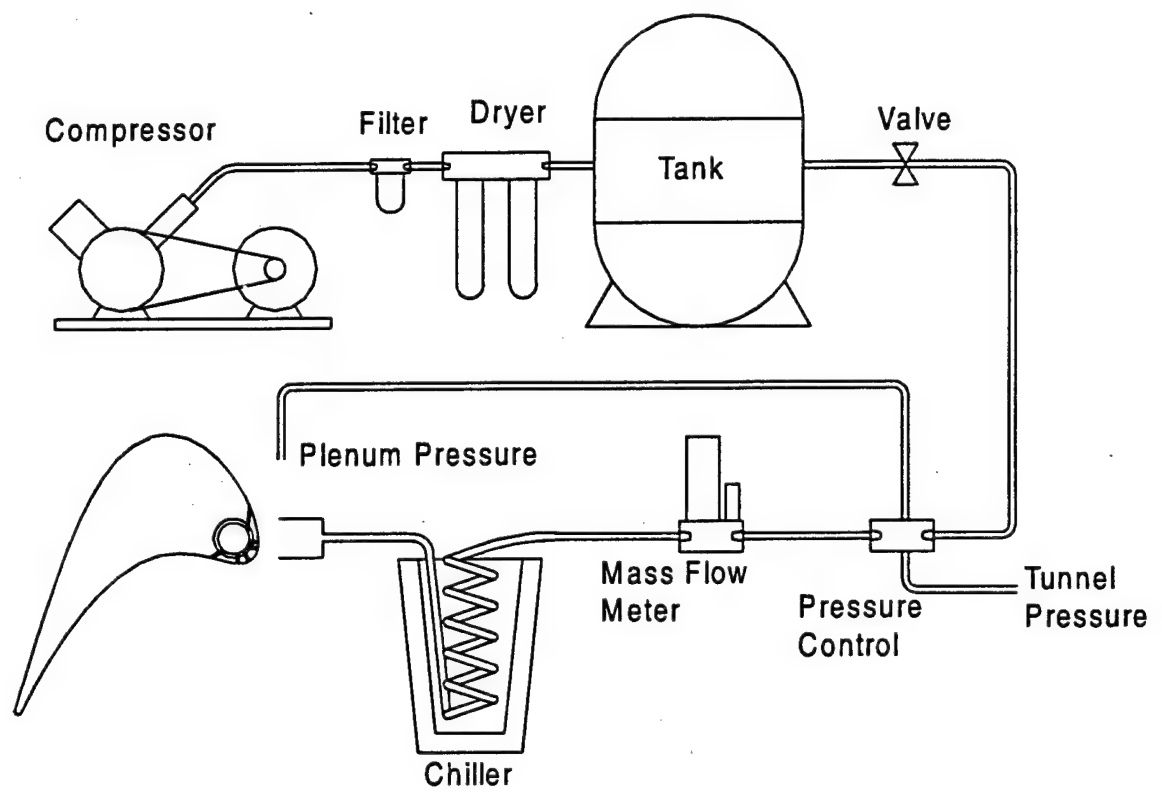


Figure 2.3: Coolant Supply Schematic.

2.3 Data Reduction Technique

2.3.1 Analysis of Uncooled Experiments

Figure 2.4 shows the time history of a tunnel run without film cooling. Shown are the traces of upstream total temperature and the heat flux and surface temperature measured on gauge location 3. It is clear that the experiments are not "steady"

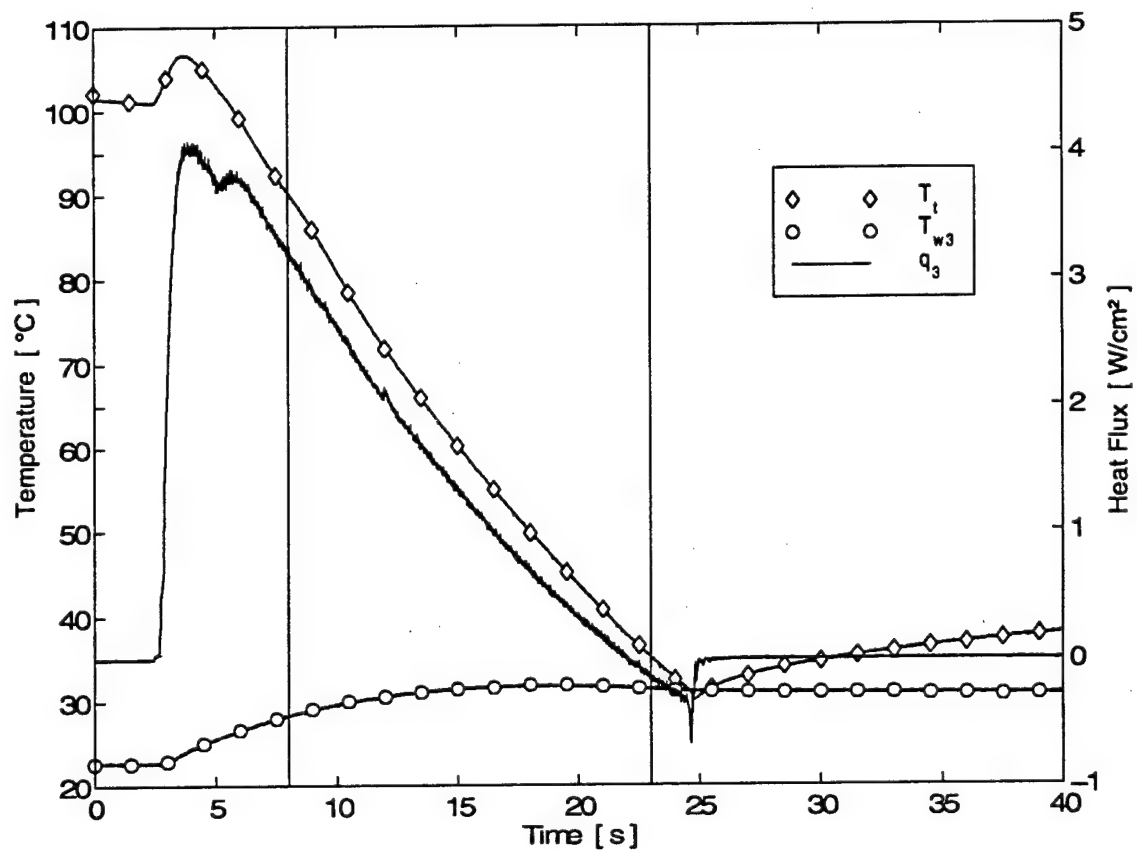


Figure 2.4: Time History From Uncooled Experiment.

in the true sense. The temperature and heat flux levels vary significantly with time. The reason these experiments are referred to as "steady" lies in the fact that the changes are so slow that each data point can be considered a steady state. Any time

scale related to the boundary layer or core flow will be orders of magnitude smaller than the rate of change of the properties shown in Figure 2.4.

The basic Equation defining the heat transfer coefficient can be stated as follows:

$$q = h \cdot (T_{aw} - T_w) \quad (2.1)$$

Without film cooling, the adiabatic wall temperature T_{aw} can be replaced by the recovery temperature for high speed flows T_r :

$$q = h \cdot (T_r - T_w) \quad (2.2)$$

The difference between freestream total temperature T_t and recovery temperature T_r is a constant according to:

$$T_d \equiv T_t - T_r = (1 - r) \cdot \frac{u^2}{2 \cdot c_p} \quad (2.3)$$

where u is the local freestream velocity and r is the local recovery factor. Replacing T_r in Equation 2.2 yields after rearrangement:

$$q = h \cdot ((T_t - T_w) - T_d) \quad (2.4)$$

Assuming that the heat transfer coefficient h is a constant throughout the run, this Equation is a linear relationship between q as the dependent variable and $(T_t - T_w)$ as the independent variable. The heat transfer coefficient h is the slope and T_d is the x-axis intercept. Plotting the data shown in Figure 2.4 with q on the y-axis and $(T_t - T_w)$ on the x-axis, the value of h can be found as the slope of the resulting curve and T_d as the x-axis intercept. The result is shown in Figure 2.5. This illustrates how

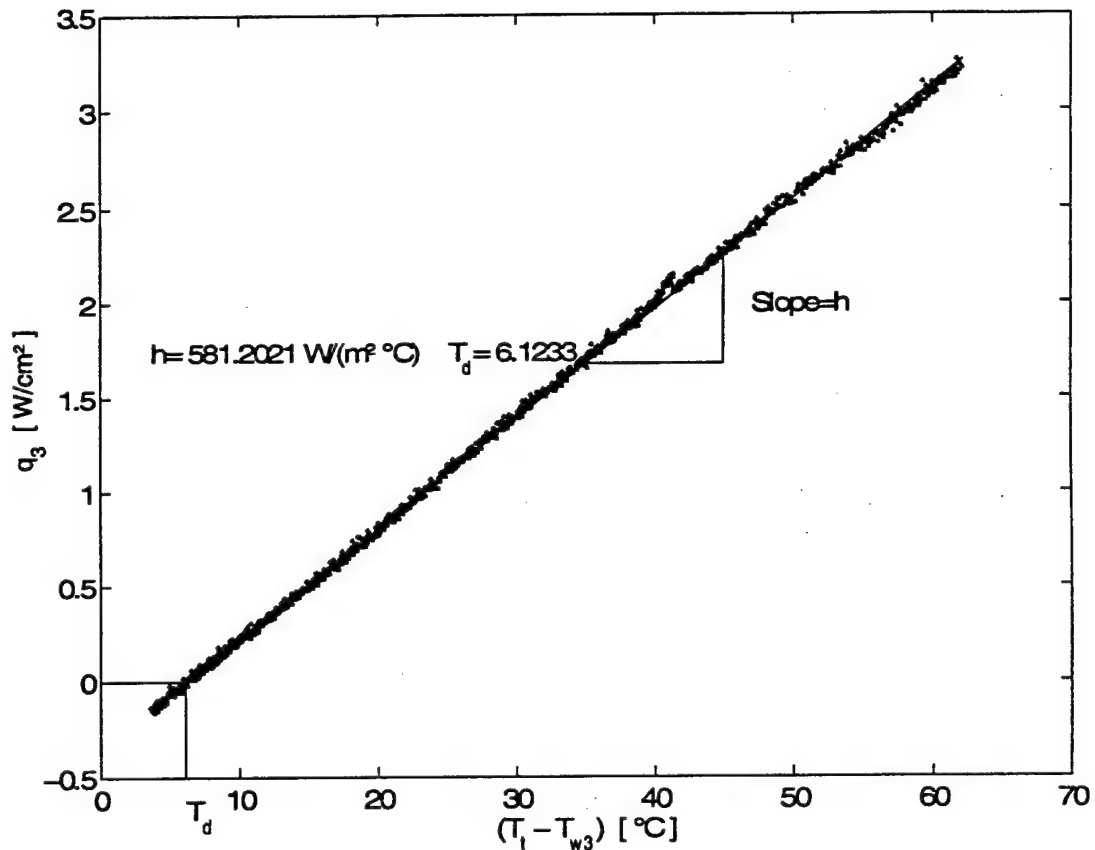


Figure 2.5: Determination of h and T_d .

T_d (difference between total freestream temperature and recovery temperature) and the heat transfer coefficient without film cooling were determined. All of them need to be known for all gauges and experiments in the investigation of heat transfer due to shock passing. For more detailed information on this technique see Smith (1999) and Bubb (1999).

Table 2.1: Mean Heat Transfer Coefficients for all Gauges and All Uncooled Experiments for “Unsteady Decomposition” Technique (Section 3.5.2.2)

Run #	h_1 $[\frac{W}{m^2 \cdot K}]$	h_2 $[\frac{W}{m^2 \cdot K}]$	h_3 $[\frac{W}{m^2 \cdot K}]$	h_4 $[\frac{W}{m^2 \cdot K}]$	h_5 $[\frac{W}{m^2 \cdot K}]$	h_6 $[\frac{W}{m^2 \cdot K}]$
1	1085.9	787.5	702.6	904.3	871.1	1069.1
2	1103.2	795.4	712.0	917.8	901.3	1131.0
3	1104.5	804.1	707.1	901.7	881.0	1112.3
4	1126.8	818.7	724.0	933.8	911.9	1143.6
5	1097.5	797.7	708.4	914.4	894.8	1119.3
6	1100.5	798.7	707.5	914.4	896.0	1131.5

2.3.2 Results from Uncooled Experiments

The results from these experiments are the heat transfer coefficient without film cooling and the difference between total temperature and recovery temperature T_d needed in both experiments with and without film cooling. They are listed in this Section for completeness.

Steady Data for Experiments without Film Cooling and “Unsteady Decomposition” Technique (Section 3.5.2.2)

The results for heat transfer coefficients are listed in Table 2.1. For a discussion of bias, precision and uncertainty estimates see Appendix E taken from Bubb (1999).

The values obtained for the difference between freestream total temperature and recovery temperature T_d are listed in Table 2.2. For the calculation of recovery temperature in the experiments with and without film cooling the mean $T_{d,i}$ will be used for consistency. Uncertainties on $T_{d,i}$ are discussed in Appendix E.

Table 2.2: $T_d = T_i - T_r$ for all Gauges and All Uncooled Experiments for “Unsteady Decomposition” Technique (Section 3.5.2.2)

Run #	T_{d1} [°C]	T_{d2} [°C]	T_{d3} [°C]	T_{d4} [°C]	T_{d5} [°C]	T_{d6} [°C]
1	5.0	4.4	5.5	8.8	10.0	16.5
2	5.7	5.0	5.8	8.6	9.7	16.2
3	6.2	5.3	5.9	9.4	10.5	16.5
4	7.1	6.1	6.3	9.3	10.5	16.8
5	5.1	4.4	5.1	8.8	9.9	15.4
6	6.6	5.7	6.1	9.3	10.5	16.6
mean	5.95	5.15	5.78	9.03	10.18	16.33

Table 2.3: h and $T_d = T_i - T_r$ for Gauges 1 and 2. Uncooled Run # 3 for “Direct Comparison” (Sections 3.5.3)

Gauge#	h_i [$\frac{W}{m^2.K}$]	T_{di} [$^{\circ}C$]
1	660.0	6.7
2	680.0	6.2

Steady Data for Experiments without Film Cooling and “Direct Comparison”(Section 3.5.3)

Only three experiments were done for the test series compared to analytical models by Moss et al. (1995), Johnson et al. (1988) and Rigby et al. (1989). The first two runs were with film cooling and only the last experiment was uncooled. Also only gauge locations 1 and 2 were used. The results for h and T_d are listed in Table 2.3. For consistency, the mean values of T_d were used for the calculation of T_r for both the cooled experiments Run #1 and Run #2 as well as the uncooled Run #3.

2.3.3 Analysis of Cooled Experiments

Figure 2.6 shows a sample time history for an experiment with film cooling. The traces shown are freestream total temperature, coolant temperature (mass averaged over the three rows of coolant affecting the suction side) and surface temperature as well as heat flux measured at location # 3. The basic equation defining the heat

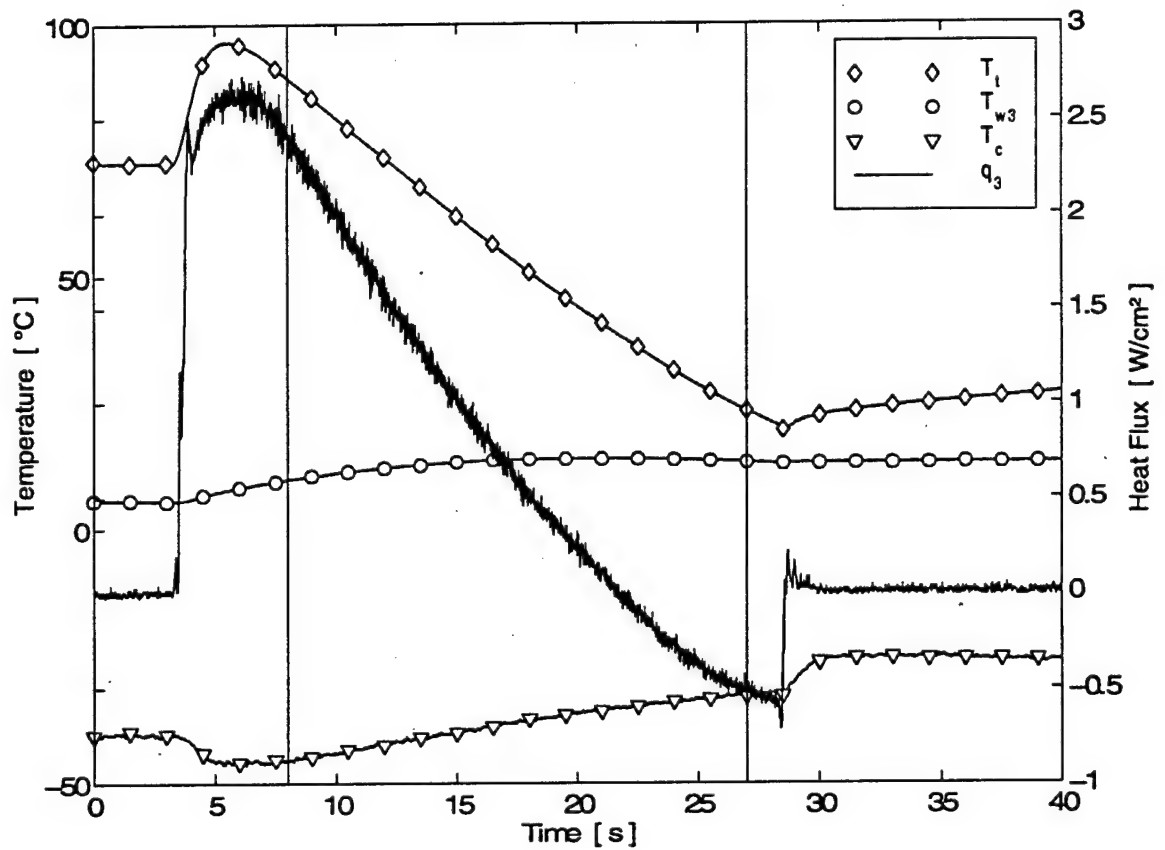


Figure 2.6: Time History From Experiment with Film Cooling.

transfer coefficient is again:

$$q = h_c \cdot (T_{aw} - T_w) \quad (25)$$

The adiabatic wall temperature is usually expressed in terms of the non-dimensional film effectiveness:

$$\eta = \frac{T_{aw} - T_r}{T_c - T_r} \quad (2.6)$$

Rearranging and substituting into the first Equation yields:

$$q = h_c \cdot ((T_r - T_w) - \eta \cdot (T_r - T_c)) \quad (2.7)$$

Dividing by $(T_r - T_w)$ yields:

$$\frac{q}{T_r - T_c} = h_c \cdot \left(\frac{T_r - T_w}{T_r - T_c} - \eta \right) \quad (2.8)$$

Assuming that h_c and η are constant throughout the run this Equation is a linear relation between the independent variable $\frac{T_r - T_w}{T_r - T_c}$ and the dependent variable $\frac{q}{T_r - T_c}$. Plotting the data shown in Figure 2.6 in this manner one obtains the heat transfer coefficient h_c as the slope of the curve and the film effectiveness η as the x-axis intercept. This is shown in Figure 2.7. Note that the recovery temperature T_r was calculated from T_t by subtracting T_d determined from uncooled runs as described in Section 2.3.1. The values of film effectiveness η and heat transfer coefficient h_c are necessary for the analysis of the unsteady heat transfer due to shock passing. For more detailed information on this technique and an uncertainty analysis the reader is referred to Bubb (1999).

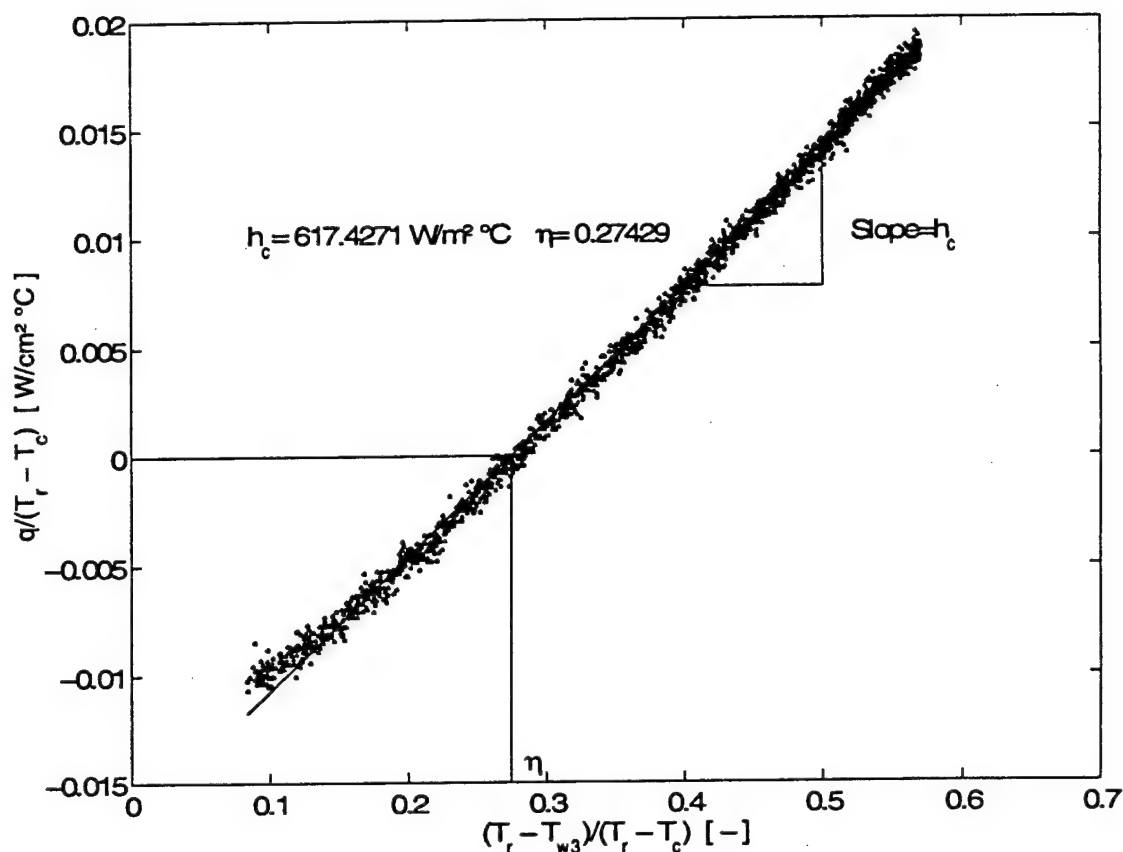


Figure 2.7: Determination of h_c and η .

2.3.4 Results from Cooled Experiments

The results from these experiments are the heat transfer coefficient with film cooling h_c and the film effectiveness η . They are listed in this Section for completeness.

Steady Data for Experiments with Film Cooling and "Unsteady Decomposition" Technique

The results for heat transfer coefficients are listed in Table 2.4. The results for the film effectiveness are listed in Table 2.5. The values for Run # 8 could not be

Table 2.4: Mean Heat Transfer Coefficients for all Gauges and All Cooled Experiments for “Unsteady Decomposition” Technique (Section 3.5.2.4)

Run #	h_{c1} $[\frac{W}{m^2 \cdot K}]$	h_{c2} $[\frac{W}{m^2 \cdot K}]$	h_{c3} $[\frac{W}{m^2 \cdot K}]$	h_{c4} $[\frac{W}{m^2 \cdot K}]$	h_{c5} $[\frac{W}{m^2 \cdot K}]$	h_{c6} $[\frac{W}{m^2 \cdot K}]$
1	1512.5	956.7	755.2	1014.4	1028.2	1373.0
2	1403.3	940.2	752.9	997.7	969.9	1341.9
3	1302.0	859.1	784.2	1022.1	983.7	1203.4
4	1375.2	887.5	776.5	1021.3	1014.8	1256.7
5	1354.4	920.1	768.2	914.6	969.1	1248.2
6	1374.0	919.6	752.2	965.3	953.9	1254.6
7	867.8	875.8	654.9	1098.2	988.5	1200.0
8	NaN	NaN	NaN	NaN	NaN	NaN
9	1332.9	919.5	718.1	984.1	954.9	1329.1
10	1318.3	899.3	770.4	989.7	979.7	1312.5
11	1218.8	869.1	763.0	993.9	998.1	1251.9
12	1318.9	844.8	762.6	952.9	988.3	1245.4

obtained since the low speed data acquisition failed to write to file. For an uncertainty analysis on the heat transfer coefficient and film cooling effectiveness see Appendix E. Runs 1,2,5,6,9,10 were done at a lower blowing rate ($\frac{p_c}{p_\infty} = 1.04$) and runs 3,4,7,8,11,12 were done at a higher blowing rate ($\frac{p_c}{p_\infty} = 1.20$). This contributes to the differences in h_c and η .

Table 2.5: Mean Film Cooling Effectiveness for all Gauges and All Cooled Experiments for “Unsteady Decomposition” Technique (Section 3.5.2.4)

Run #	η_1 [-]	η_2 [-]	η_3 [-]	η_4 [-]	η_5 [-]	η_6 [-]
1	0.309	0.181	0.347	0.226	0.188	0.269
2	0.296	0.184	0.327	0.223	0.176	0.279
3	0.174	0.154	0.194	0.235	0.159	0.188
4	0.231	0.176	0.200	0.237	0.172	0.216
5	0.332	0.184	0.353	0.221	0.204	0.274
6	0.310	0.190	0.341	0.221	0.193	0.274
7	0.256	0.201	0.190	0.215	0.178	0.247
8	NaN	NaN	NaN	NaN	NaN	NaN
9	0.289	0.164	0.325	0.210	0.179	0.293
10	0.331	0.181	0.345	0.225	0.198	0.278
11	0.201	0.177	0.209	0.220	0.167	0.217
12	0.151	0.148	0.188	0.204	0.145	0.219

Steady Data for Experiments with Film Cooling and "Direct Comparison"

The first two experiments done for the analysis by comparison with analytical models were with film cooling. Only data from gauge locations 1 and 2 are available. The steady-state values for h_c and η for these experiments and gauges are listed in Table 2.6. Both runs were done at a blowing pressure of $\frac{p_c}{p_\infty} = 1.04$.

Table 2.6: h_c and η for Gauges 1 and 2. Cooled Runs # 1 and #2 for "Direct Comparison" (Sections 3.5.3)

Run #	h_{c1} [$\frac{W}{m^2 \cdot K}$]	h_{c2} [$\frac{W}{m^2 \cdot K}$]	η_1 [-]	η_2 [-]
1	862	795	0.30	0.18
2	775	800	0.33	0.19

Chapter 3

Unsteady Heat Transfer

3.1 Experimental Setup for Investigation of Unsteady Heat Flux

Without the opportunity for performing experiments in a rotating cascade a method has to be found to model the relative motion of the shock wave and the blades in the cascade. A rotating bar mechanism was not an option since the effects of the shock wave were to be investigated separately. A rotating bar mechanism as designed and built by the University of Oxford is disadvantageous because it is problematic to separate the effects of wakes and shocks. The first successful attempt at creating an isolated shock wave to pass over a linear cascade was reported on by Collie (1991) from Virginia Tech. A shotgun was used to create a shock wave of desired strength. Doughty (1994) replaced the shotgun by a normal shock tube. This shock tube produces a normal shock wave that is guided it into the test section. As the normal shock wave expands into the open space of the cascade it transforms into a cylindrical detonation or blast wave. This blast wave represents the flow relative to the rotor

passage better than a normal shock would. The characteristics of the shock wave were calculated and described in detail in Doughty (1994). The shock apparatus used in the present investigation is essentially identical to the one developed by Doughty (1994)

3.1.1 Shock Apparatus

An overview over the entire shock apparatus is shown in Figure 3.1. The elements of the apparatus will be described in detail in the following paragraphs.

Pneumatic Valve to Operate the Shocktube

A pneumatic valve controls the flow of driver gas into the driven section of the shocktube. This control valve is actuated from a pneumatic switch mounted on the tunnel control desk. The valve will be in the open position as long as the switch is pressed down. After the release of the switch it will turn off. This setup is advantageous over a manual control of the driver fluid since the shock can be triggered by the person in charge of the tunnel control.

Shock Tube

The shock tube was originally designed and hydro-tested by Doughty. The mechanical details of the shock tube can be found in Doughty (1994) in Section 3.3.

The strength of the shock arriving at the instrumented blade depends directly on the strength of the normal shock wave created in the shock tube (see the cal-

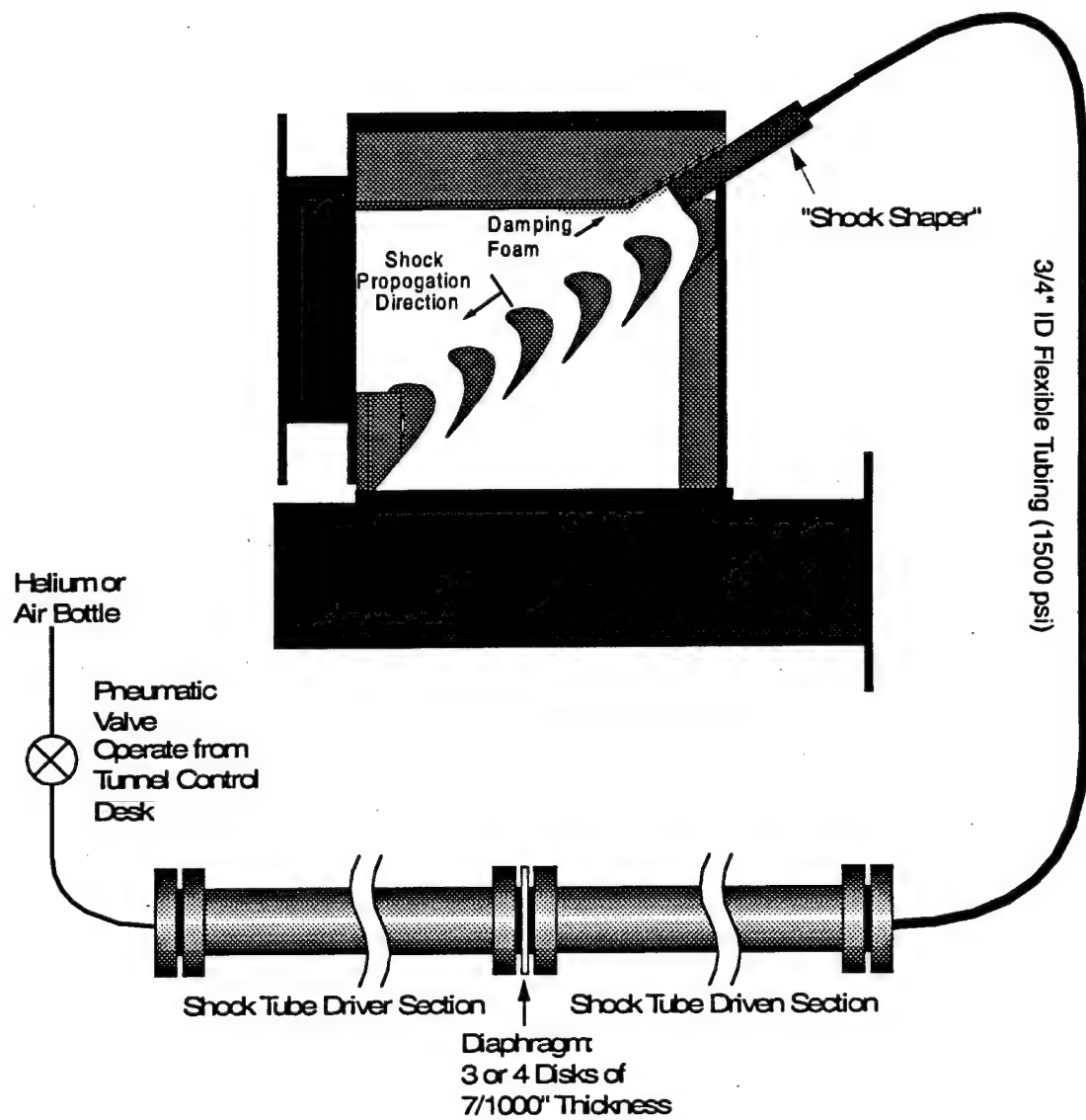


Figure 3.1: Overview of the Shock Apparatus.

culations in Doughty (1994)) for details). This strength is controlled by the overall thickness of diaphragms inserted between the flanges separating the driver section and the driven section. For the present study, two cases were investigated: 3 diaphragms (approximate shock strength on the blade is 1.23 in terms of static pressure ratio) and 4 diaphragms (resulting in shock strength of about 1.32). The diaphragms are cut from clear *Mylar* sheets of 0.007 in. thickness. Helium was used to create a stronger shock without higher driver pressure (see Chapman (1971) for a good description of shock tube fluid mechanics). The burst pressure in the driver section was around 350 psig for the experiments with three diaphragms (nominal shock strength) and slightly higher for the experiments with four diaphragms (higher shock strength).

Flexible Tubing

In the original setup used by Doughty, the distance between the shock shaper and the instrumented blade was significantly shorter than in the present setup. The shock strength at arrival on the test blade, therefore, was higher than observed in the preliminary experiments with the present setup. Increasing the number of diaphragms beyond six (0.042 in. overall thickness) was not feasible since the pressure induced by the shock wave reflected off the endcap would have exceeded the rating of the shock tube. Therefore, a larger diameter flexible tube had to be used to increase the overall energy passing into the test section. The original diameter was 1/2 in. nominal ID. It was replaced with a 3/4 in. flexible tube rated up to 1500 psi. The resulting shock strength was indeed significantly higher than the one measured when using the smaller diameter tubing.

Shock Shaper

The purpose of the shock shaper is to transition from the circular normal shock wave coming out of the flexible tube to a cylindrical blast wave stretching over the entire width of the test section. Doughty did extensive work on the design of the shock shaper as reported in Section 3.5 in Doughty (1994). A new shock shaper had to be built, because the diameter of the flexible tube was increased. The design for the new shock shaper is shown in Figure 3.2. Except for the height of the diverging duct, all dimensions were kept the same.

Damping Foam

It became clear after some preliminary tests that the shock emerging from the shock shaper creates a strong reflection off the upper surface of the cascade. The reflection then travels after the primary shock wave, slowly catching up to it. So instead of one shock wave two shock waves impinge on the blade. After several attempts to solve the problem a 1/2 in. layer of foam glued to the upper surface successfully decreased the strength of the reflected shock (see Figure 3.1).

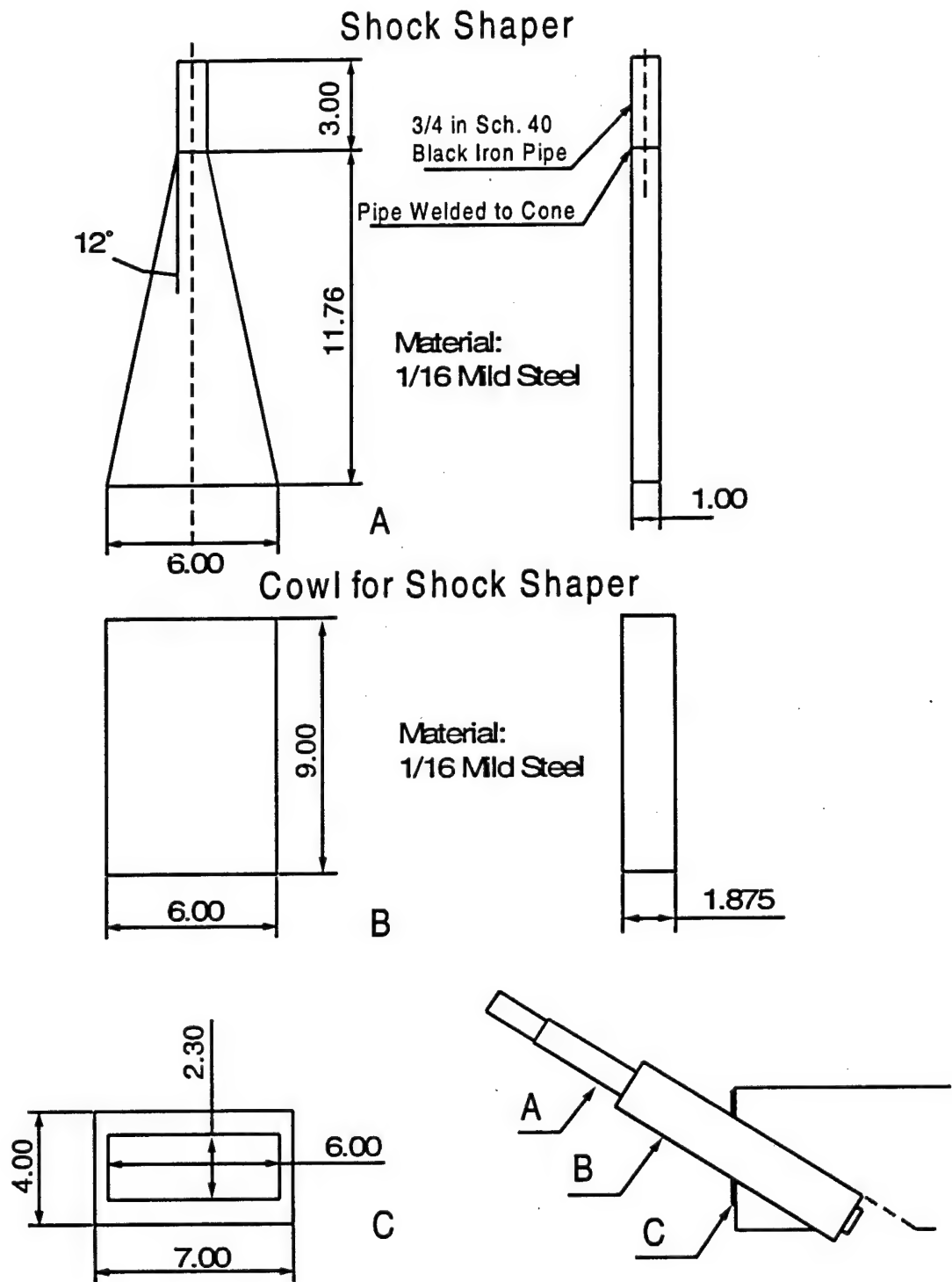


Figure 3.2: Shock Shaper Design.

3.2 Test Matrix

In Section 3.5 "Results and Discussion" two entirely different ways of analyzing the unsteady heat transfer data are presented. The first one is referred to as "Unsteady Decomposition" and the second one "Direct Comparison". The former was developed at Virginia Tech and will be of primary interest in the analysis. A wide variety of parameters were varied in order to generalize the conclusions. The three parameters varied are the initial level of heat flux, the shock strength and — for the case with film cooling — the ratio of total pressure of the coolant to the total pressure of the freestream. The schematic in Figure 3.3 shows the parameters and their corresponding values. The shock strength is expressed as the ratio of the peak static pressure over the static pressure before shock impact. The shock of the lower strength was created using three diaphragms of 0.007 in. thickness in the shock tube. For the higher shock strength four diaphragms of the same thickness were used.

Without Film Cooling		With Film Cooling	
Parameter	Values	Parameter	Values
Level of Heat Flux Before Shock Passing	Low Medium High	Level of Heat Flux Before Shock Passing	Low Medium High
Shock Strength (p_{max}/p)	1.23 (nominal) 1.32 (high)	Shock Strength (p_{max}/p)	1.23 (nominal) 1.32 (high)
		Total Pressure Ratio p_{tc}/p_{tf}	1.04 (nominal) 1.20 (high)

Number of Tests = 6

Number of Tests = 12

Heat Flux Gauges Used: Gauges #1, 2, 3, 4, 5
Pressure Sensors Used: Gauges #2, 4, 5, 6

Figure 3.3: Test Matrix for Experiments With and Without Film Cooling for Test Series "Unsteady Decomposition".

The second test series labeled "Direct Comparison" compares the results from predictive models published in the literature to actual heat flux data. It was not necessary or of interest to perform this comparison at different conditions. Therefore, only one value was chosen for each parameter and three experiments were performed, two with and one without film cooling. Also only pressure and heat flux data from gauge locations # 1 and #2 were analyzed. The short test matrix for this set of experiments is shown in Figure 3.4. The value of shock strength in terms of the static pressure ratio is higher in this figure than the number in Figure 3.3. The reason for this is that the pressure signal was recorded and processed differently for the two test series as explained in detail in Sections 3.3 and 3.4. The actual shock was of the same strength as the stronger shock in test matrix 3.3. Both were created using four diaphragms of 0.007 in. thickness in the shock tube.

Without Film Cooling		With Film Cooling	
Parameter	Values	Parameter	Values
Level of Heat Flux Before Shock Passing	Medium	Level of Heat Flux Before Shock Passing	Medium
Shock Strength (P_{max}/P)	1.5 (high)	Shock Strength (P_{max}/P)	1.5 (high)
		Total Pressure Ratio P_{tc}/P_{tf}	1.04 (nominal)

Number of Tests = 1 Number of Tests = 2 (one repeat)

Heat Flux Gauges Used: Gauges #1, 2
Pressure Sensors Used: Gauges #1, 2

Figure 3.4: Test Matrix for Experiments With and Without Film Cooling for Test Series "Direct Comparison".

The instrumentation, data acquisition and signal processing procedure for both the "Unsteady Decomposition" and the "Direct Comparison" will be described in

detail in the following Sections.

3.3 Instrumentation and Data Acquisition for Unsteady Measurements

In measuring high speed events like a passing shock, the dynamic behavior of the entire measurement chain is of utmost importance. The dynamic characteristics of each and every component has to be known in order to clearly establish how well a measurement represents the real event. Theoretically, it is impossible to obtain a "correct" representation of a shock wave. A shock wave is represented mathematically by a discontinuity. The frequency content of a discontinuity is infinitely wide. It can only be the goal in this investigation to obtain as wide a frequency range as possible and be content with the representation of the real event in this frequency band. The effort has to be to obtain the best possible representation of the event in this frequency band.

3.3.1 Unsteady Pressure Measurements for Test Series "Unsteady Decomposition"

In the test series for the "Unsteady Decomposition" technique presented in Section 3.5.2 the pressure measurement is not crucial in terms of the analysis. The data is analyzed by mere comparison of heat flux traces from different runs. Still, it was desired to have a second measurement to monitor the unsteady shock event. As a result the *Kulite XCQ-062-50a* pressure sensors were used in the frequency range below 25 kHz where the sensors show little phase shift and signal attenuation.

The entire measurement chain for the unsteady pressure measurements in this particular test series is shown in Figure 3.5.

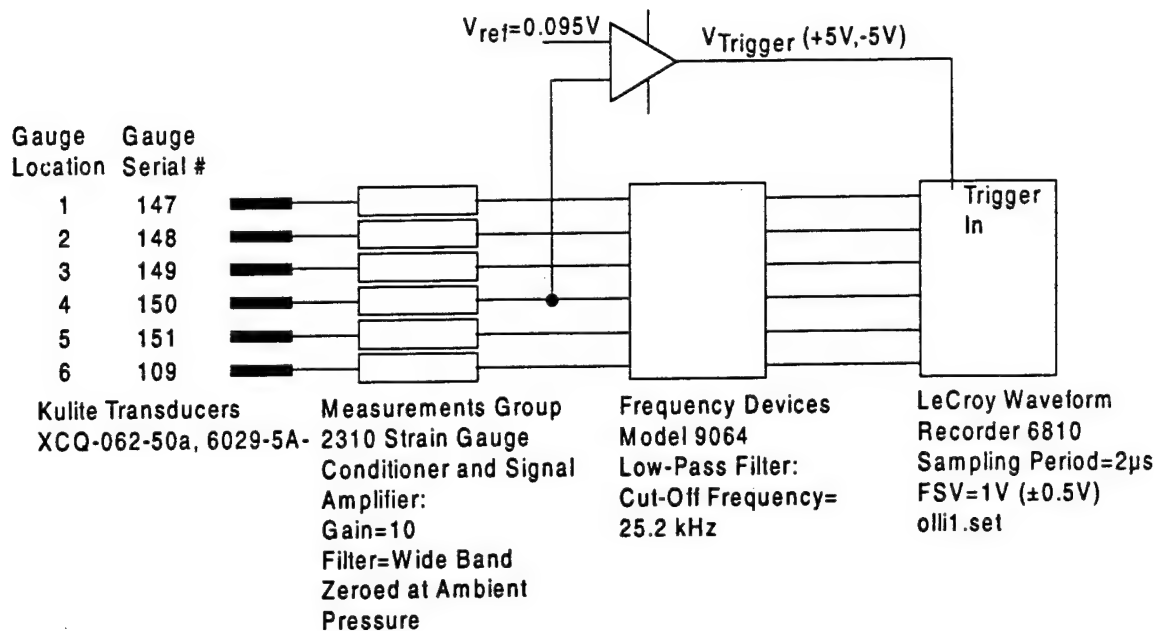


Figure 3.5: Measurement Chain for Unsteady Pressure Measurements for Test Series “Unsteady Decomposition” in Section 3.5.2.

Kulite XCQ-062-50a Pressure Transducers

The dynamic behaviour of the *Kulite XCQ-062-50a* pressure transducers is studied in detail in Appendix B. The fact that the transducers are protected by a *B-Screen* reduces the frequency response significantly. In the frequency range up to 25 kHz the transfer function is relatively flat in terms of magnitude and phase.

Measurements Group 2310 Strain Gauge Conditioner and Signal Amplifier

The “wide band” setting on the amplifier provides the widest range of usable frequency band. Nevertheless, the transfer function of this device is still dependent on the gain setting. The transfer functions of the *Measurements Group 2310 Strain Gauge Conditioner and Signal Amplifier* at different gain settings is shown in Appendix D. Since the pressure transducers will only be used up to 25 kHz, the amplifier

is not going to interfere with the signal content at a gain of 10 (see appendix D).

Frequency Devices Model 9064 Low-Pass Filter

The 8-Pole Butterworth Low-Pass filters were set to a cut-off frequency of 25.2 kHz in order to avoid a misrepresentation of the shock due to the strong phase shift and signal attenuation by the pressure transducers. This frequency range is not wide enough to provide a good approximation of the actual event. Since the pressure measurements were not used in the analysis other than for timing purposes, no realistic measurements were needed.

LeCroy Waveform Recorder 6810

Two *Le Croy* systems had to be used for the data acquisition since 12 channels had to be recorded (six heat flux signals and six pressure signals). A new version of the driver software had to be installed to run both modules at the same time (E:\catlyst\catlst). The sampling frequency for this particular set of tests was set to 500 kHz. The data acquisition was triggered by a very simple comparator circuit shown in Figure 3.5. The trigger was dc coupled at a level of 0.196 Volts and set to a delay of $-1/8$ (about $500\mu s$). The full scale voltage was set to 1 V (± 0.5 V, resolution of 0.2 mV) to ensure good resolution with the 12-bit acquisition system.

3.3.2 Unsteady Heat Flux Measurements for Test Series "Unsteady Decomposition"

For the data and analysis presented in Section 3.5.2 the heat flux measurements were of higher importance than the pressure measurements. Mainly, it was necessary to obtain data from different experiments and gauges recorded with a sufficiently wide frequency band to gather enough information about the shock passing process. It was also necessary to record all gauges and experiments the same way in order to compare different traces.

The dynamic behaviour of the *Vatell HFM-7* Heat Flux was assumed to be a first order system with a time constant of about $6\mu s$. However, later this assumption appeared to be not quite correct (see Appendix C). For the direct comparison of two different heat flux time histories this does not present a major drawback. Basically, it is still possible to compare two representations of an event which are inadequate in the same way.

The entire measurement chain for the unsteady heat flux measurements in this particular test series is shown in Figure 3.6.

Vatell HFM-7/L Heat Flux Sensors

The dynamic behavior of the *Vatell HFM-7/L* heat flux sensors was studied in detail in Appendix C. Unfortunately, this work was done after the test series for the "Unsteady Decomposition" analysis was completed. It showed that the gauge responded like a first order system with a time constant of about $17\mu s$. Since in this investigation the direct comparison between different runs was important, no correction for this first order characteristic was done.

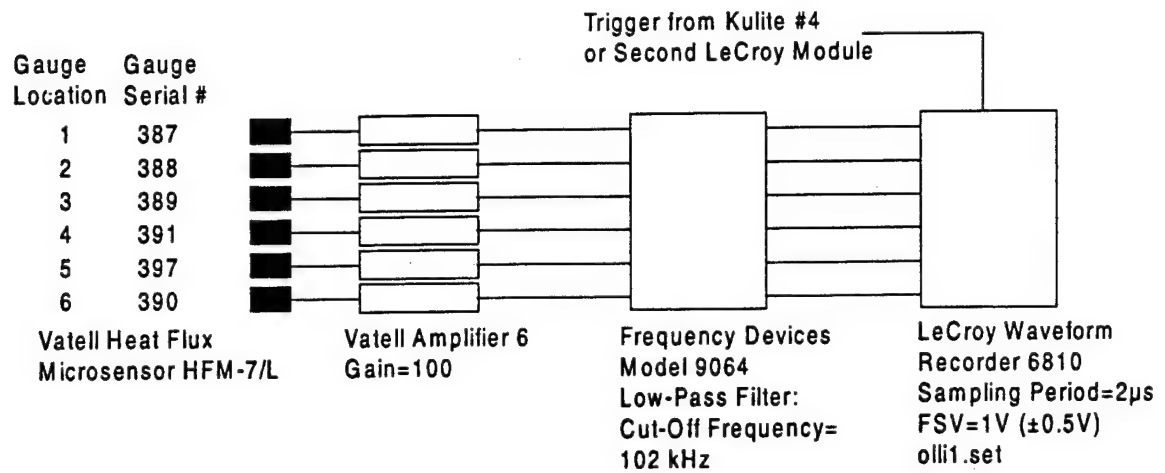


Figure 3.6: Measurement Chain for Unsteady Heat Flux Measurements for Test Series “Unsteady Decomposition” in Section 3.5.2.

Vatell Amplifier 6

The Gain-Bandwidth Product of the *Analog Devices* Op-Amp used in the *Vatell Amplifier 6* is given as 25 MHz. It was therefore decided that at a gain setting of 100 the frequency band of the amplifier would not interfere with the gauge response up to the cut-off frequency of 102 kHz.

Frequency Devices Model 9064 Low-Pass Filter

The 8-Pole Butterworth Low-Pass filters were set to a cut-off frequency of 102 kHz. The magnitude of the gauge transfer function has already reached a very low value at this frequency (0.25 for $\tau = 6\mu s$, 0.09 for $\tau = 17\mu s$) so no significant information will be lost. But aliasing and noise will be suppressed by this filter setting.

LeCroy Waveform Recorder 6810

The settings on the *LeCroy* Waveform Recorder were identical to the settings described in Section 3.3.1.

3.3.3 Unsteady Pressure Measurements for "Direct Comparison"

In Sections 3.5.3.1, 3.5.3.2 and 3.5.3.3 the unsteady heat transfer is predicted from the static pressure measured on the blade. This means that an accurate representation of the shock event in terms of pressure and heat flux is absolutely necessary. The matter is very complex since the *Kulite XCQ-062-50a* transducers and the *Vatell HFM-7/L* heat flux sensors show very different dynamic characteristics. Also, the influence of the measurement chains have to be known in order to avoid interference from different transfer functions. All components of the pressure measurement chain were investigated thoroughly and the setup shown in Figure 3.7 was found to be adequate for the goals of the investigation according to Moss' Model. The two main

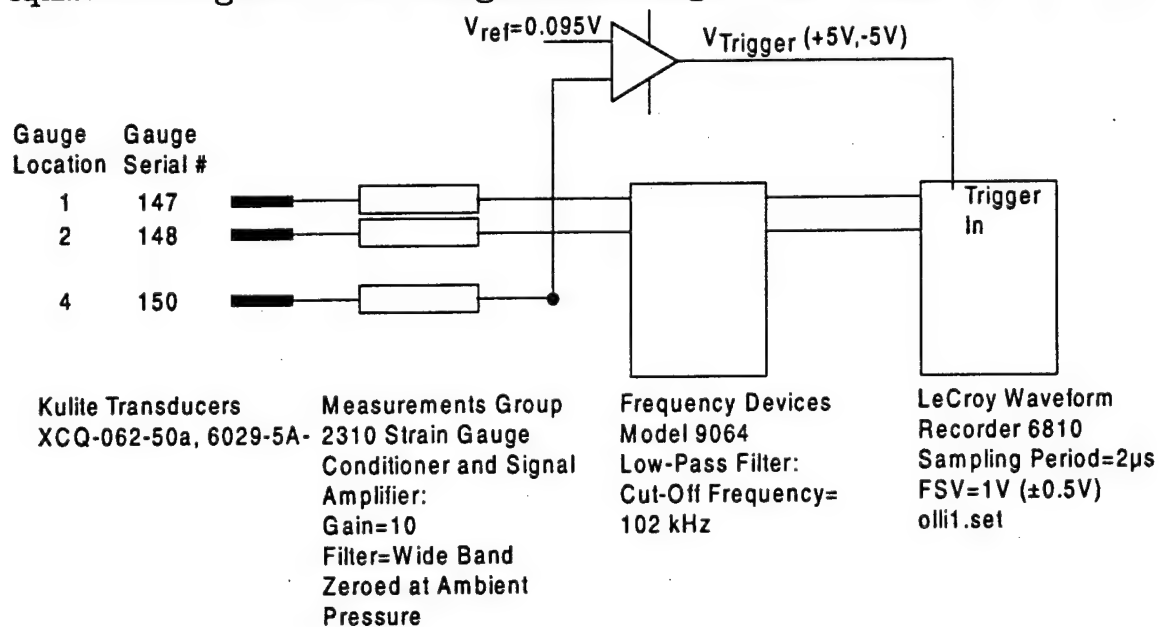


Figure 3.7: Measurement Chain for Unsteady Pressure Measurements for "Direct Comparison."

differences between this setup and the one shown in Figure 3.5 in Section 3.3.1 are that only data from the first two locations are recorded and that the cut-off frequency on the *Frequency Devices Model 9064* Low-Pass Filters is set to 102 kHz instead of

25 kHz in the test series for the "Unsteady Decomposition" analysis. It was necessary to extend the frequency range acquired with the pressure sensors in order to obtain a better representation of the physical event since a direct comparison with the results from the heat flux sensors was to be accomplished. The transfer function of the *Kulite XCQ-062-50a* pressure sensors shown in Appendix B show very strong signal attenuations and phase shifts in the frequency range of up to 102 kHz. Also the *Measurements Group 2310 Strain Gauge Conditioner and Signal Amplifier* shows some influence in the frequency range measured (see Appendix D). The signal from the pressure sensors will have to be corrected for these characteristics. This process is presented in Section 3.4.1.

3.3.4 Unsteady Heat Flux Measurements for “Direct Comparison”

The measurement of unsteady heat flux for the investigation according to the models by Moss, Johnson and Rigby (sections 3.5.3.1, 3.5.3.2 and 3.5.3.3 respectively) was essentially identical to the setup used in the analysis according to the “Unsteady Decomposition” technique. The measurement chain is shown in Figure 3.8. The

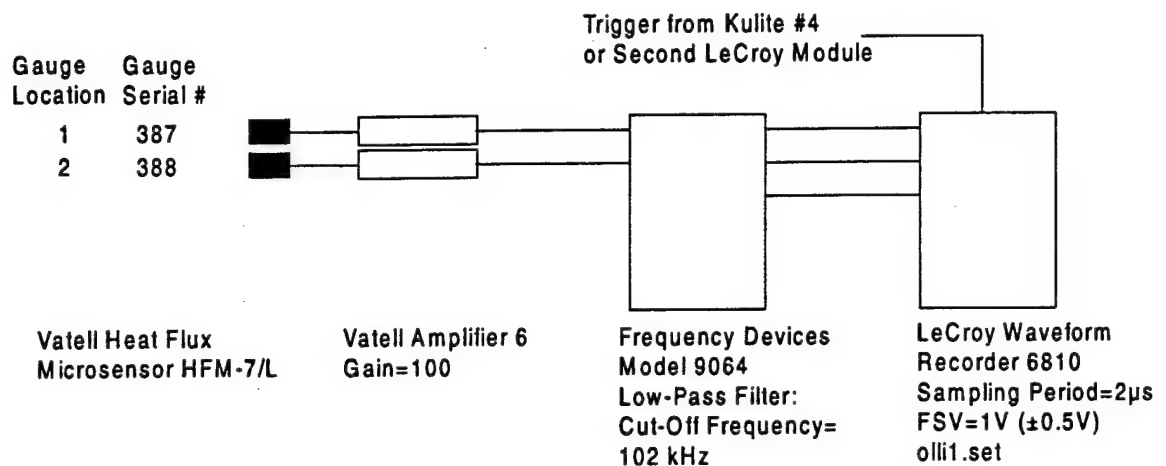


Figure 3.8: Measurement Chain for Unsteady Heat Flux Measurements for “Direct Comparison”.

sampling frequency and most importantly the cut-off frequency are identical to the the settings for the pressure transducers. The dynamic characteristics of the *Vatell HFM-7/L* heat flux sensors are investigated in detail in Appendix C. According to the transfer function determined there, the signals will be corrected. Only then is it possible to compare signals from the pressure and the heat flux sensors.

3.3.5 Shadowgraph Flow Visualization

In order to optically analyze the shock passing process a Shadowgraph setup was used (see Figure 3.9). The light source was a 15 mW Helium-Neon Laser. The High-Speed Camera was a Hadland Photonics high speed digital camera with four CCD receptors. It is capable of taking pictures at a frequency of up to 8 MHz. All pictures shown in Sections 3.5.1 and A were taken with this setup. The camera was triggered by an upstream *Kulite* pressure transducer and the timing for the camera was set in the control software.

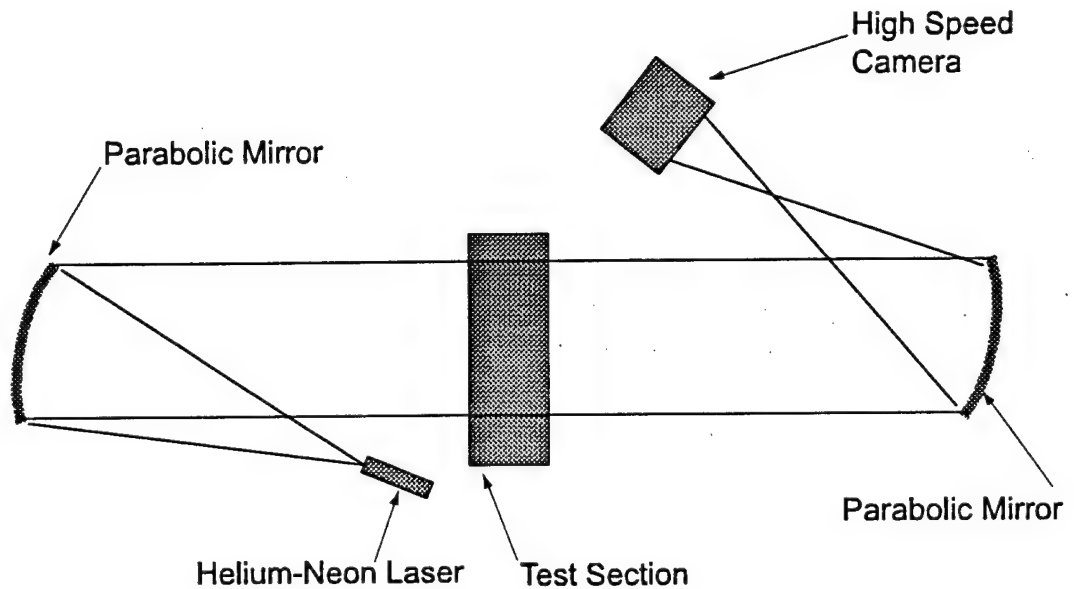


Figure 3.9: Optical Setup for Shadowgraph Flow Visualization

3.4 Signal Processing

This Section explains the post-processing procedure for the pressure and heat flux data after processing. Section 3.4.1 shows the data processing for the pressure measurements and different test series. The manipulation of the heat flux data for the different test series is demonstrated in Section 3.4.2.

3.4.1 Pressure

Signal Processing for Pressure Measurements for "Unsteady Decomposition"

Section 3.5.2 presents an analysis of the unsteady data referred to as "Unsteady Decomposition." The very core of this technique consists of a comparison of heat flux traces representing the shock impact initiated at different levels of heat flux before the shock event. This comparison provides understanding of the relative magnitudes of different contributions to the overall unsteady heat transfer. The pressure traces are only needed for a consistency check and for alignment of traces recorded in different experiments. It would also be impossible to expect a reasonable representation of the shock since the pressure data was recorded with a cut-off frequency of only 25 kHz (see Section 3.3.1). This cut-off frequency was chosen in order to avoid recording the frequency range in which the *Kulite Pressure Transducer XCQ-062-50a* shows strong phase shifts and begins to attenuate the signal (see Appendix B).

The alignment of traces recorded in different experiments was done in the following way:

Since the pressure data is much less affected by noise (fluctuations of tempera-

ture and mixing do affect the heat flux measurements but not the pressure data), all the traces of heat flux and pressure were aligned by shifting them by a certain time obtained from an analysis of the pressure traces. To illustrate this technique, the data from one heat flux sensor and one pressure transducer recorded during two different experiments will be used. The result will be two pairs of traces each consisting of a heat flux and a pressure time history referred to as q_1, p_1 (from first experiment) and q_2, p_2 (from second experiment). q_1 and p_1 are aligned with respect to time since they were recorded over the same sampling time. So are q_2 and p_2 . On the other hand, the two pairs do not necessarily have the same relation to the physical event. The trigger setting or the overall sampling time may have been different, and so the same physical event does not necessarily happen at the same point in the sampling time. In order to compare the two heat flux traces their relative position with respect to the physical event needs to be known. Since the pressure histories have the same time reference as the corresponding heat flux traces and are less affected by noise, this time shift can be obtained by comparison of the pressure traces. To obtain the "delay" between the two traces the following procedure was applied. One of the pressure traces (say p_2) is shifted in time by a certain number of sampling periods $n \cdot \Delta t$. Now the Pearson product moment correlation coefficient, r , is calculated for p_1 and the shifted time history p_2 :

$$r(n \cdot \Delta t) = \frac{N \cdot (p_1 \cdot p_2) - \sum p_1 \cdot \sum p_2}{\sqrt{(N \cdot (p_1 \cdot p_1) - \sum p_1^2) \cdot (N \cdot (p_2 \cdot p_2) - \sum p_2^2)}} \quad (3.1)$$

The products of time histories are the vector products of the vectors with time being the index. This correlation coefficient reflects the extent of a linear relationship between two data sets. This coefficient is calculated for a large range of n -values. The n -value at which $r(n \cdot \Delta T)$ shows a maximum was then used to shift q_2 and p_2 for comparison with q_1 and p_1 . Since all experiments were done with nearly identical data acquisition settings, these n -values were usually very small (on the order of

±4). All the traces shown in Sections 3.5.2.2 and 3.5.2.4 were aligned in the manner described here.

Signal Processing for Pressure Measurements for "Direct Comparison"

In Sections 3.5.3.1, 3.5.3.2 and 3.5.3.3, unsteady heat flux due to shock passing is predicted in different ways from the static pressure measurement. Therefore, it was necessary to:

1. Record both signals at the same high cut-off frequency. The settings of the data acquisition chain are shown in Section 3.3.3.
2. Correct both pressure and heat flux readings to obtain comparable readings

The way the pressure data was corrected is presented in this paragraph. The raw data was first corrected for the influence of the *Measurements Group 2310 Strain Gauge Conditioner and Signal Amplifier* at a gain setting of 10 (see Figure 3.7). The transfer functions of this amplifier and the way they were obtained are shown in Appendix D.

$$P_{corr2310}(\omega) = \frac{P_{raw}(\omega)}{H_{2310}(\omega)} \quad (3.2)$$

In this Equation $P_{corr2310}$ is the corrected signal before the amplifier, P_{raw} is the signal as recorded and H_{2310} is the transfer function of the amplifier as shown in Appendix D. Capital letters indicate the Fourier Transform of the signal or transfer function.

This improved signal was then corrected for the dynamic behavior of the *Kulite Pressure Transducer XCQ-062-50a*. The transfer function of these sensors was deter-

mined in a shock tube experiment presented in Appendix B.

$$P_{final}(\omega) = \frac{P_{corr2310}(\omega)}{H_{Kulite}(\omega)} \quad (3.3)$$

This way it was possible to obtain a better estimate of the "real" frequency and phase information up to the cut-off frequency.

3.4.2 Heat Transfer

Signal Processing for Heat Transfer Measurements for "Unsteady Decomposition"

Section 3.5.2 presents an analysis of the unsteady data referred to as "Unsteady Decomposition." The very core of this technique consists of a comparison of heat flux traces representing the shock impact initiated at different levels of heat flux before the shock event. The heat flux traces are different from the "real" heat flux histories, since the gauges have a certain dynamic behavior. It can be expected, though, that all gauges have the same transfer function. Therefore, each trace of unsteady heat flux has the same relation to the "real" time history of unsteady heat flux. A comparison between different traces is, therefore, possible even without a correction for the dynamic behavior of the gauges. Still, it has to be acknowledged that the time histories analyzed in Section 3.5.2 are not the best possible representations of the physical event.

Since heat flux time histories from different experiments had to be compared, the data had to be aligned with respect to the shock passing event. The procedure used to align the data was explained in Section 3.4.1. The settings of the data acquisition chain are shown in Section 3.3.2.

Signal Processing for Heat Flux Measurements for "Direct Comparison"

In Sections 3.5.3.1, 3.5.3.2 and 3.5.3.3 a direct comparison is presented between heat flux predicted from pressure measurements and measured unsteady heat flux due to shock impingement. In order to be able to make this comparison it was necessary to obtain a realistic representation of the shock event in terms of pressure and heat

flux. The way the pressure data was processed is explained in Section 3.4.1. This Section explains the data reduction of the heat flux signals.

The dynamic behavior of the heat flux gauges was investigated in order to determine its transfer function (see Appendix C). It was shown that the *Vatell Heat Flux Microsensor HFM-7/L* could be modeled as a first order system with a time constant of about $17\mu s$. The amplifiers were set to a gain of 100 and were expected not to have a significant influence on the transfer function of the measurement chain (see Section 3.3.2). Therefore the only correction to be applied to the data was the transfer function of the heat flux gauge itself. This could be done in one of two ways. The first option is to use the transfer function itself:

$$Q_{final}(\omega) = \frac{Q_{aw}(\omega)}{j\omega \cdot \tau + 1} \quad (3.4)$$

In this Equation τ is the time constant of the sensor. In the case of the specific sensors used here it equals about $17\mu s$. Another way to correct for the characteristic dynamic behavior of the sensor would be to apply it point by point:

$$q_{corr,n} = q_{aw,n} + \frac{\tau}{\Delta t} \cdot (q_{aw,n-1} - 2 \cdot q_{aw,n} + q_{aw,n+1}) \quad (3.5)$$

Here Δt is the sampling period and n is the time index. The results of the two procedures are nearly identical.

After applying the corrections to the pressure traces (Section 3.4.1) and the heat flux traces the comparisons presented in Sections 3.5.3.1, 3.5.3.2 and 3.5.3.3 are possible.

It needs to be stated that the physical size of the active surface of the heat flux microsensor (about 4 mm) has an effect on the frequency response of the gauge. Heat flux fluctuations caused by any perturbation passing tangentially over the gauge will be smoothed out because the gauge is spatially integrating over the sensing surface. The shock waves produced by the shock apparatus shown in Section 2.2 pass nearly tangentially over the gauges on the upstream suction side. It takes the shock front approximately $10\ \mu s$ to pass tangentially over a sensor. This is not a negligible amount of time compared to the time scales measured. No attempt was made in the frame of the work presented to correct for this spatial averaging.

3.5 Results and Discussion

The results of the shock passing experiments will be presented and analyzed in this Section. Different analytical methods will be applied and comparison will be made with the data.

To introduce the reader to the experimental results, Section 3.5.1 will show the data taken in a qualitative way. Some general observations will be made to lead into a more in depth analysis. Section 3.5.2 analyzes the results using a decomposition technique. The different contributions to the unsteady heat transfer will be identified by an analytical separation of the physical parameters involved.

Three different attempts to predict the unsteady heat flux from surface pressure measurements will be applied to the data in Section 3.5.3:

1. A model recently developed by Moss et al. (1995) at the University of Oxford will be compared with the experimental data in Section 3.5.3.1.
2. An earlier analytical approach to unsteady heat transfer developed by Johnson et al. (1988) at the same institute will be compared with the data and discussed in detail in Section 3.5.3.2.
3. Rigby et al. (1989) published a modified version of this model in 1989 and added a thorough derivation. The model will be presented and compared to the data in Section 3.5.3.3.

A numerical approach to the problem stated by Johnson et al. (1988) was recently developed by Reid (1998) at Virginia Tech. The conclusions from his research will be discussed in the context of Johnson's and Moss' model and the data presented here (Section 3.5.4).

3.5.1 General Observations

In this Section, the data will be presented in a qualitative way. This will also serve to help the reader physically understand the flow to be analyzed.

Figure 3.10 shows a shadowgraph of the shock passing. It was taken with a high speed digital camera. The attached cooling film is visible on the blade surface. The direction of the flow and the progression of the shock are shown schematically. Also shown are the locations of the gauges # 1 through 3 counting in the flow direction. A whole series of eight such shadowgraphs were taken (all of them are shown in Appendix A). The surprising conclusion from these shadowgraphs is that there is

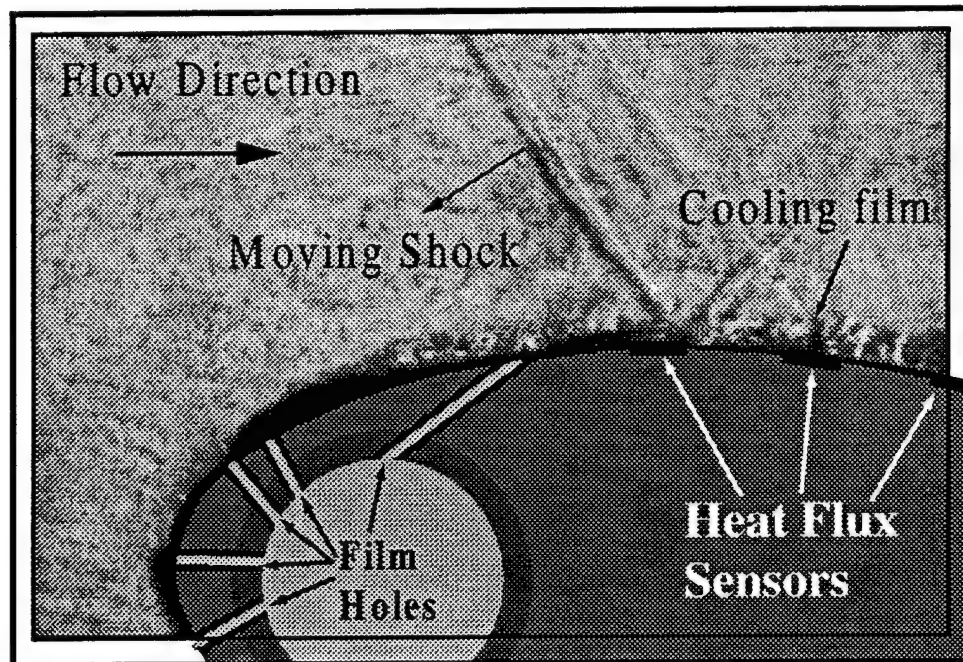


Figure 3.10: Sample Shadowgraph of Shock Passing Event with Film Cooling.

no strong interaction between the cooling film and the shock. No film separation or detachment nor a "Separation Bubble" (as reported by Doorly et al. (1985) and Johnson et al. (1988)) behind the shock can be detected.

In Figure 3.11, all available pressure traces from one of the uncooled experiment are shown. The pressure sensors in locations 1 and 3 did not work properly; therefore they did not provide useful time histories. In Figure 3.12, the heat flux data corresponding to the pressure traces shown in Figure 3.11 are plotted. In both figures, the time axes are identical to illustrate the shock propagation along the suction surface of the blade toward the leading edge. Also, the y-axes are identical for all graphs on the figures for a better comparison of the relative magnitudes of pressure and heat flux histories respectively. The pressure histories are normalized with the steady pressure before shock impact p_{av} to show the shock strength rather than absolute values. Only the unsteady component of heat flux is shown. The absolute value of heat flux before shock impact was removed for ease of comparison.

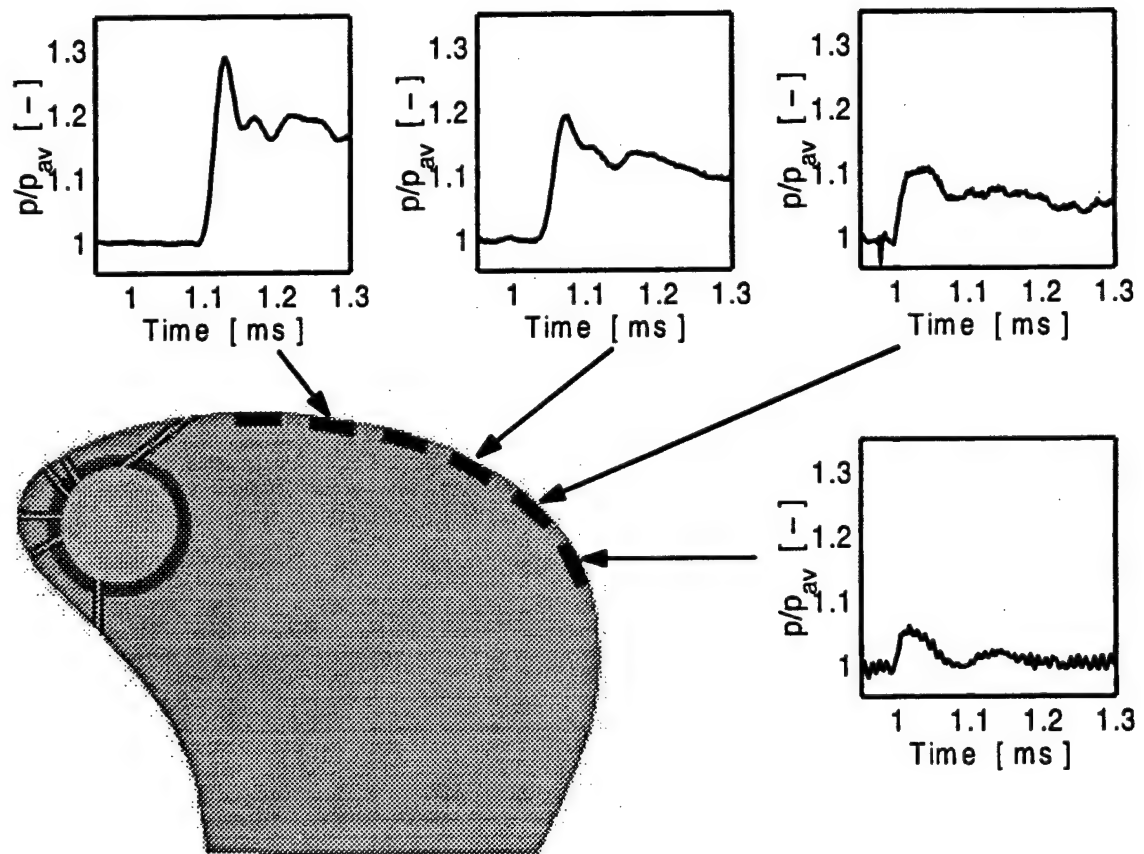


Figure 3.11: Sample Time Histories of Pressure Ratio for Gauges 2,3,4,5 from one of the Experiments without Film Cooling.

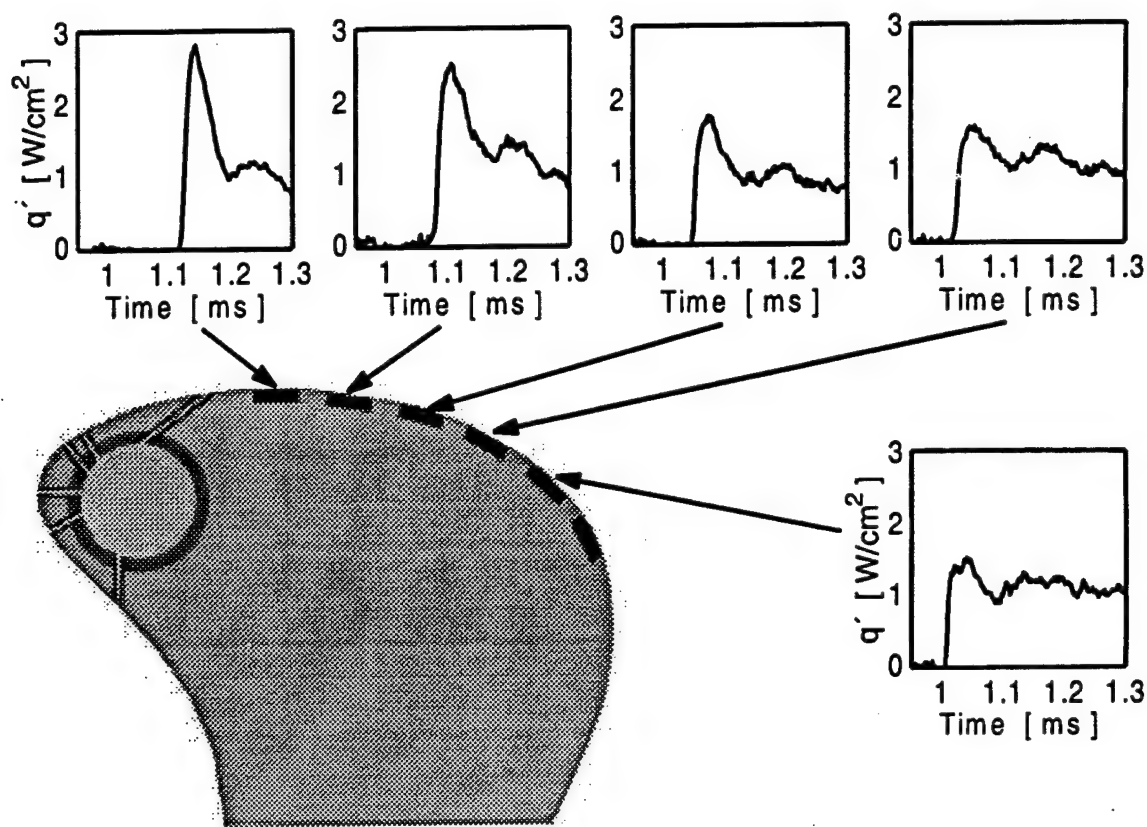


Figure 3.12: Sample Time Histories of Unsteady Heat Flux for Gauges 1,2,3,4,5 from one of the Experiments without Film Cooling.

The shape of the pressure traces observed in Figure 3.11 show the typical features of blast waves as described and calculated in Doughty (1994). It becomes clear from Figures 3.11 and 3.12 that the gauges further downstream see a weaker shock in terms of pressure ratio and unsteady heat flux than the upstream gauges. The reason for this is qualitatively depicted in Figure 3.13. The shock wave has to expand into the passage after passing over the upper blade. Since energy has to be preserved, this expansion leads to a weakening of the shock. The relation between the shock pressure ratio and heat flux due to shock impingement was expected and is demonstrated experimentally in Figures 3.11 and 3.12. A more in-depth analysis of this correlation will be presented in the following Sections.

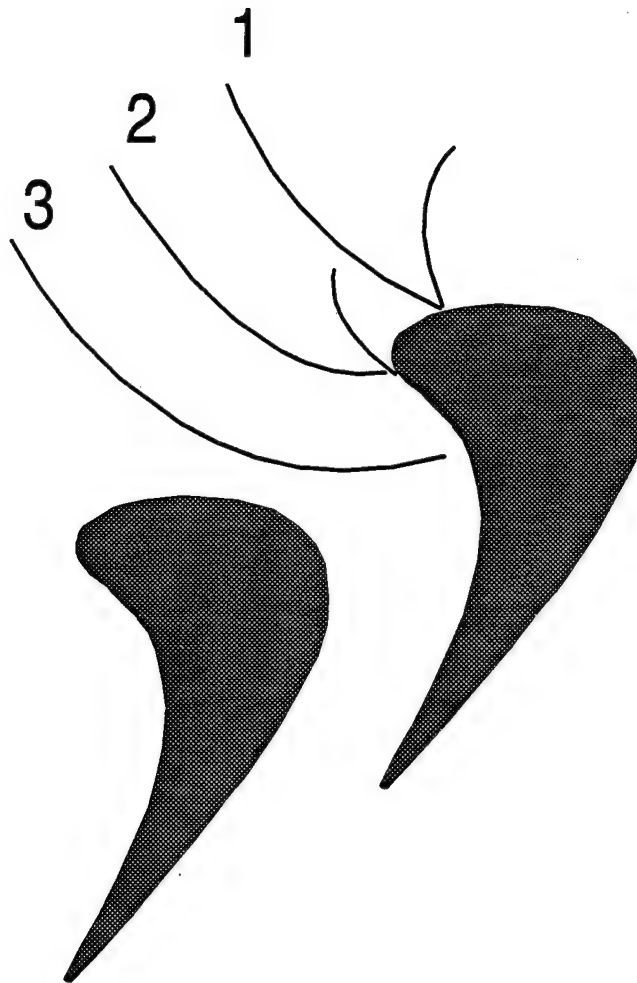


Figure 3.13: Schematic Depiction of Shock Expansion Process. States 1, 2 and 3 Represent the Shock At Different Successive Times.

For completeness, a sample time history of pressure ratio for gauges 2,4,5 and 6 from an experiment with film cooling is shown in Figure 3.14. The corresponding time histories of unsteady heat flux are shown in Figure 3.15. The same conclusions that were drawn from the Figures without film cooling can be drawn from these figures with film cooling. The major difference between the two sets of Figures is the fact that the heat flux traces with film cooling contain significantly more noise than the corresponding time histories without film cooling. The reason lies in the presence of inherently unsteady mixing processes in the boundary layer in the case with film cooling. The pressure traces with and without film cooling are nearly identical. Even the heat flux traces in Figures 3.12 and 3.15 are remarkably similar. That indicates that the core flow field is not affected significantly by the presence of the cooling film.

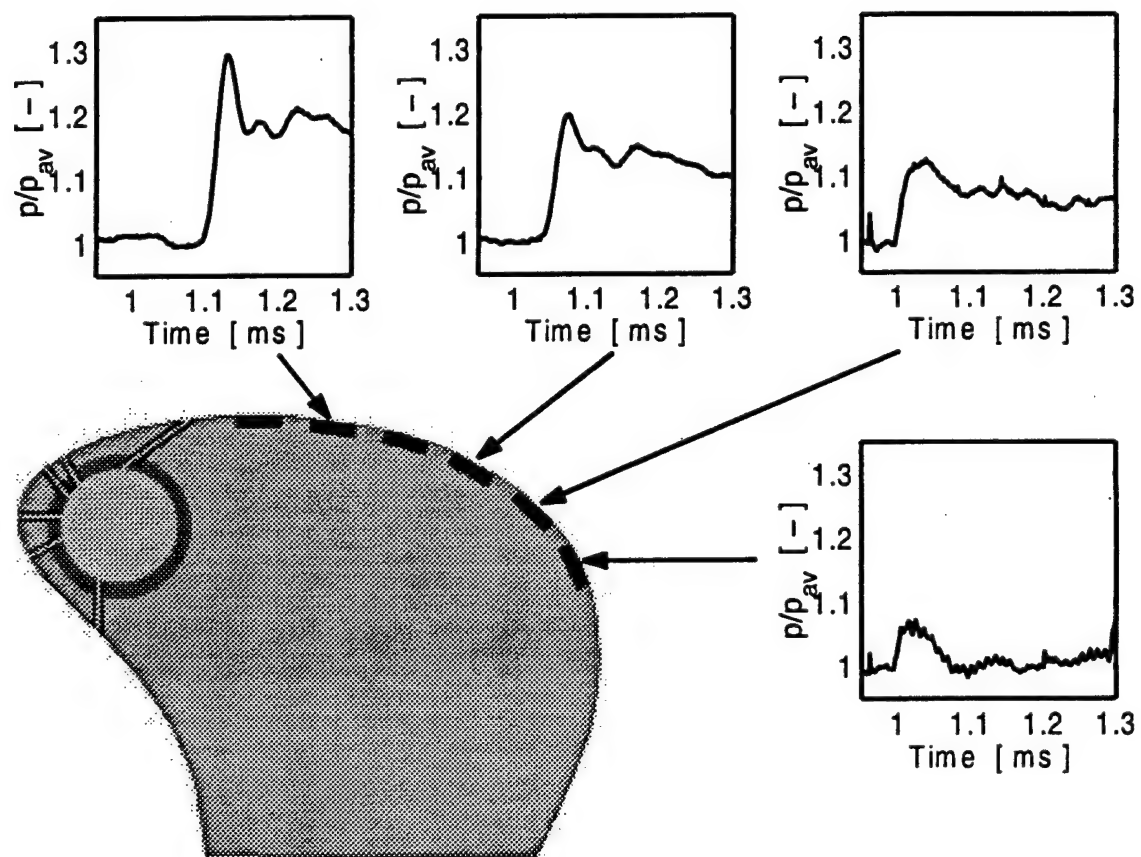


Figure 3.14: Sample Time Histories of Pressure Ratio for Gauges 2,4,5,6 from Experiment with Film Cooling.

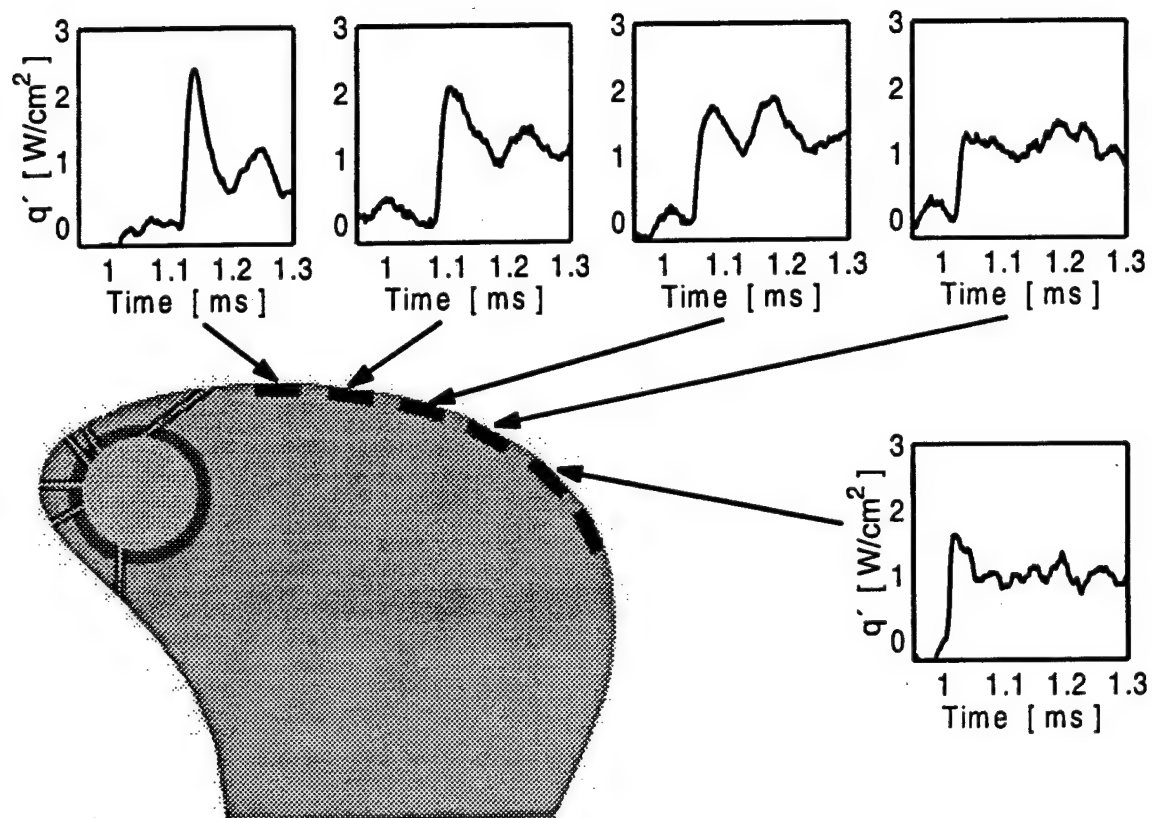


Figure 3.15: Sample Time Histories of Unsteady Heat Flux for Gauges 1,2,3,4,5 from Experiment with Film Cooling.

3.5.2 "Unsteady Decomposition" of Heat Flux

The underlying idea in this Section is the mathematical and physical decomposition of the heat flux due to the passing shock. This decomposition will be the instrument for the analysis of the contributions of different physical parameters during the shock passing event. Since the analytical model looks somewhat different for cooled and uncooled cases, this Section will be divided into two major parts. In the first part, the analytical model for the uncooled case will be developed (Section 3.5.2.1) and compared to the measured results (Section 3.5.2.2). In the second part the analogous model is derived for the case with film cooling (Section 3.5.2.3) and compared to actual data (Section 3.5.2.4). The qualitative conclusions derived using the unsteady decomposition technique will be given in Section 3.5.2.5.

3.5.2.1 Analytical Model without Film Cooling

In this Section, the concept of the unsteady decomposition of heat flux will be introduced. In order to analyze the contributions of different physical parameters during the shock impact, these parameters will be split up into their time mean component before the shock impact (no superscript) and the unsteady component during the shock impact (superscript '). From the basic definition of the heat transfer coefficient

$$q = h \cdot (T_{aw} - T_w) \quad (3.6)$$

follows the definition of the heat transfer coefficient in the uncooled case by replacing T_{aw} by the recovery temperature T_r . In the conventional notation:

$$q = h \cdot (T_r - T_w) \quad (3.7)$$

Now all the properties will be replaced by the sum of their time mean value before shock impact and their unsteady component during shock impact:

$$q + q' = (h + h') \cdot (T_r + T_r' - T_w - T_w') \quad (3.8)$$

The wall temperature T_w does not vary during the short time of the shock impact, therefore, T_w' is set to zero in Equation 3.8. The basic Equation that is going to be used in this Section and Section 3.5.2.4 can then be written as:

$$q + q' = (h + h') \cdot (T_r + T_r' - T_w) \quad (3.9)$$

In order to separate the different contributions of unsteady parameters, the right hand side of Equation 3.9 can be expanded to:

$$q + q' = h \cdot (T_r - T_w) + h' \cdot (T_r - T_w) + h \cdot T_r' + h' \cdot T_r' \quad (3.10)$$

The first term on the right hand side of this Equation, $h \cdot (T_r - T_w)$, represents the steady value of heat flux before the shock impact, or q . Subtracting this time mean component from both sides yields:

$$q = H \cdot (T_r - T_w) + h \cdot T_r + h' \cdot T_r \quad (3.11)$$

The result is an expression for the unsteady component of heat flux as a function of all time-varying components. The first term on the right hand side of Equation 3.11, $H \cdot (T_r - T_w)$, represents the first order contribution of the time-varying heat transfer coefficient to the unsteady heat transfer. The second term, $h \cdot T_r$, is the first order contribution of the time-varying recovery temperature to q' . The last term on the right hand side of Equation 3.11 is the combined effect of the fluctuating components of the heat transfer coefficient and recovery temperature.

The purpose of this decomposition is to identify the relative magnitudes of the three terms on the right hand side of Equation 3.11 or, more specifically, the contribution of H and T_r to the unsteady heat transfer. The importance of this analysis will be explained in detail in Section 3.5.2.2.

3.5.2.2 Effect of Shock Passing without Film Cooling

In this Section, a comparison will be made between the model developed in Section 3.5.2.1 and measured heat flux data. This comparison will yield the relative magnitudes of the different contributions to the unsteady heat flux. More specifically, the analysis will show how much the variation in heat transfer and recovery temperature add to the overall unsteady heat flux.

The experiments that this analysis refers to and all important properties before shock impact are listed in Tables 3.1 through 3.4. The values for recovery temperatures are calculated from the freestream total temperature before the shock impact by subtracting the local T_{di} value determined in the steady state experiments (see Section 2.3.1). Since several values of T_{di} were determined — one from each experiment — a mean value of T_{di} was used for every gauge. The recovery temperatures listed in Table 3.2 are then calculated according to:

$$T_{ri} = T_t - T_{di} \quad (3.12)$$

The index i refers to the six gauge locations. The mean heat transfer coefficient in Table 3.4 is evaluated over the entire run as explained in detail in Section 2.3.1.

Table 3.1: Shock Strength and Total Temperatures at Shock Impact for All Uncooled Experiments

Run #	Shock Strength $\frac{p+p'_{max}}{p}$	T_t [°C]
1	1.23	71.7
2	1.32	71.7
3	1.23	69.9
4	1.32	55.9
5	1.23	61.4
6	1.32	53.2

Table 3.2: Recovery Temperatures at Shock Impact for All Gauges and All Uncooled Experiments

Run #	T_{r1} [°C]	T_{r2} [°C]	T_{r3} [°C]	T_{r4} [°C]	T_{r5} [°C]	T_{r6} [°C]
1	65.8	66.6	65.9	62.7	61.5	55.4
2	65.8	66.6	65.9	62.7	61.5	55.4
3	63.9	64.7	64.0	60.8	59.6	53.5
4	49.9	50.7	50.0	46.8	45.6	39.5
5	55.4	56.2	55.5	52.3	51.1	45.0
6	47.2	48.0	47.3	44.1	42.9	36.8

Table 3.3: Wall Temperatures at Shock Impact for All Gauges and All Uncooled Experiments

Run #	T_{w1} [°C]	T_{w2} [°C]	T_{w3} [°C]	T_{w4} [°C]	T_{w5} [°C]	T_{w6} [°C]
1	29.7	31.2	30.5	30.5	30.2	27.1
2	35.2	36.7	36.2	36.2	35.9	33.0
3	26.2	27.8	27.1	27.1	26.7	23.7
4	34.4	36.0	35.4	35.4	35.1	32.1
5	26.5	28.1	27.4	27.4	27.1	24.0
6	34.4	35.8	35.3	35.3	34.9	31.9

Table 3.4: Mean Heat Transfer Coefficients for all Gauges and All Un-cooled Experiments

Run #	h_1 $[\frac{W}{m^2 \cdot K}]$	h_2 $[\frac{W}{m^2 \cdot K}]$	h_3 $[\frac{W}{m^2 \cdot K}]$	h_4 $[\frac{W}{m^2 \cdot K}]$	h_5 $[\frac{W}{m^2 \cdot K}]$	h_6 $[\frac{W}{m^2 \cdot K}]$
1	1085.9	787.5	702.6	904.3	871.1	1069.1
2	1103.2	795.4	712.0	917.8	901.3	1131.0
3	1104.5	804.1	707.1	901.7	881.0	1112.3
4	1126.8	818.7	724.0	933.8	911.9	1143.6
5	1097.5	797.7	708.4	914.4	894.8	1119.3
6	1100.5	798.7	707.5	914.4	896.0	1131.5

The governing Equation for the following comparison was developed in Section 3.5.2.1:

$$q = h' \cdot (T_r - T_w) + h \cdot T_r + h' \cdot T_r \quad (3.13)$$

The unsteady variation of heat transfer coefficient h is multiplied by the overall temperature difference before the shock impact ($T_r - T_w$) to yield the first order contribution of the time varying heat transfer coefficient to the unsteady heat flux. This overall temperature difference is equivalent to the time mean heat flux level before the shock impact. This implies that the contribution of the fluctuating heat transfer coefficient should depend on the heat flux level before the shock passing. In order to quantify this component, it was, therefore, necessary to initiate the shock at different levels of heat flux. According to the time histories of heat flux described in detail in Section 2.3.1, this is possible by triggering the shock at different times during the tunnel run. Early triggering will provide a high initial level of heat flux. The later the shock is released the lower the level of heat flux will be.

Figure 3.16 shows the data from runs 2,4 and 6 at the higher shock strength as listed in Table 3.1. For the argument about to be proposed, only results from gauge #2 will be presented at these conditions (Run #2, Run #4, Run #6). At the end of this Section, Figures 3.19 to 3.22 will include all test results without film cooling from all available gauges and different shock conditions. It can be seen that the three traces of heat flux shown in Figure 3.16 start from different levels of heat flux before shock impact (Run #2: $2 \frac{W}{cm^2}$, Run #4: $1 \frac{W}{cm^2}$, Run #6: $0.7 \frac{W}{cm^2}$). Analogous to Equation 3.13, the mean heat flux before shock impact will be removed to obtain only the unsteady component of heat flux: Figure 3.17 shows very clearly that the three time histories of unsteady heat transfer are very much alike in terms of magnitude and general shape even though the initial levels of heat flux were quite different. This

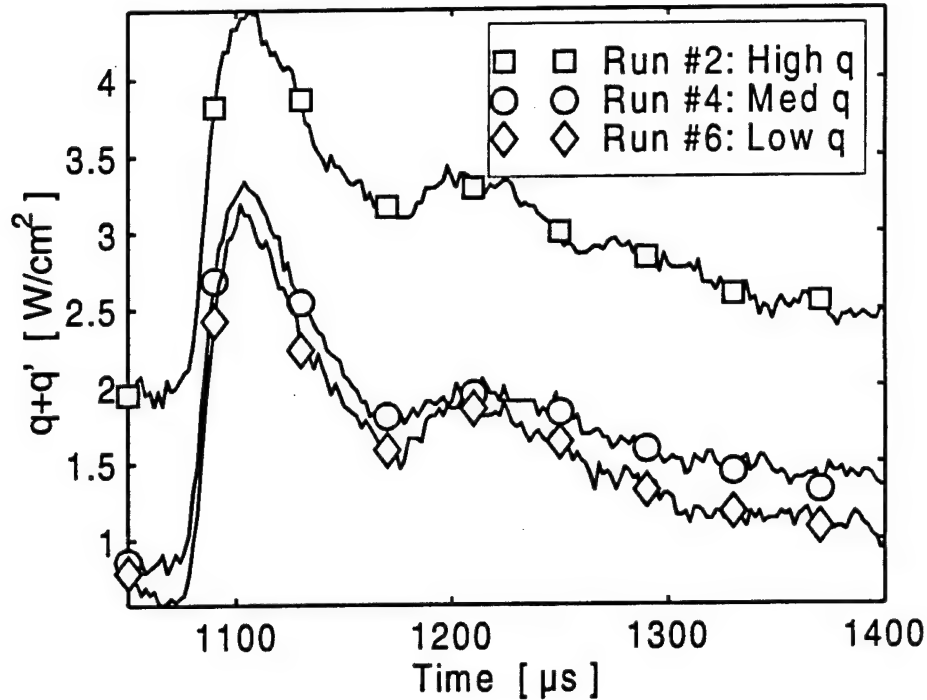


Figure 3.16: Shock Passing Events for Gauge # 2 at Increased Shock Strength without Film Cooling. Three Experiments at Different Levels of Initial Heat Flux.

will lead to a far-reaching conclusion.

The first term on the right hand side of Equation 3.13 states that the first order contribution of the variation of heat transfer coefficient h to the overall unsteady heat flux is scaled by the driving temperature difference before shock impact ($T_r - T_w$). This temperature difference is proportional to the initial level of heat flux before shock impact. The unsteady heat transfer was shown to be independent of this heat flux level (see Figure 3.17). This means that the unsteady component of the heat transfer coefficient is not contributing significantly to the overall unsteady heat flux. If h was of the same order of magnitude as h , the unsteady contribution of h would have to be of the same order as the initial heat flux level. For all experiments it can be shown that the unsteady component of heat flux does not scale with this initial value of heat flux. Therefore, it can be concluded that the order of h is much smaller than the

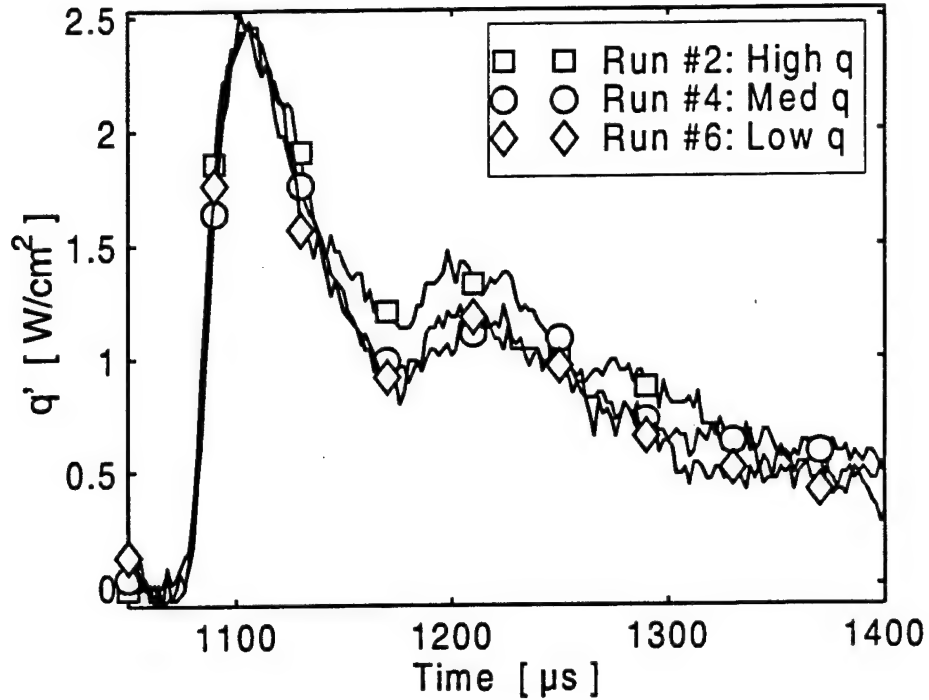


Figure 3.17: Shock Passing Events for Gauge # 2 at Increased Shock Strength without Film Cooling. Three Experiments at Different Levels of Initial Heat Flux. Initial Level of Heat Flux Removed.

order of h . Neglecting all terms containing h and rearranging Equation 3.13, yields an expression for the unsteady variation of recovery temperature T_r :

$$T_r = \frac{q}{h} \quad (3.14)$$

This expression states that the variation of the recovery temperature is proportional to the unsteady variation of heat transfer. Therefore, the traces of T_r will look exactly like the traces in Figure 3.17 scaled by the steady heat transfer coefficient. For completeness these traces are shown in Figure 3.18. Based on the traces of T_r in Figure 3.18 one can make an order of magnitude argument to estimate the relative magnitude of h . T_r in Figure 3.18 takes values up to about 35° . $T_r - T_w$ takes on

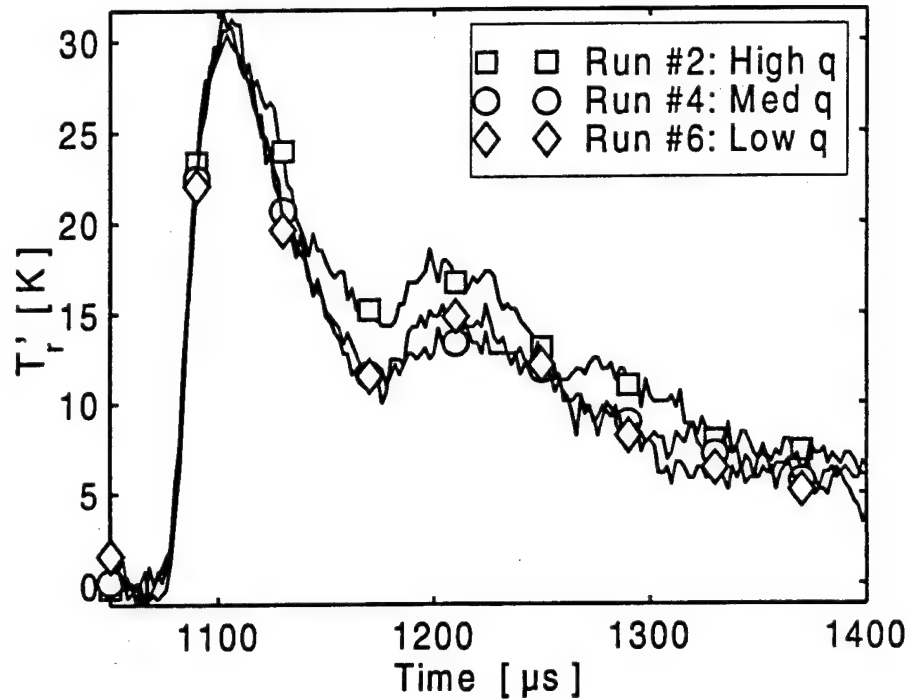


Figure 3.18: Shock Passing Events for Gauge # 2 at Increased Shock Strength without Film Cooling. Three Experiments at Different Levels of Initial Heat Flux. Initial Level of Heat Flux Removed. Converted to Temperature Variation.

similar values as seen in Tables 3.2 and 3.3. Then $h \cdot (T_r - T_w)$ should take on similar values as $h \cdot (T_r - T_w)$ or q if h was of the same order of magnitude as h . The traces of unsteady heat flux would then have to differ by about $1 \frac{W}{cm^2}$ since the initial values of heat flux differ by that amount. Such differences can not be observed in Figure 3.17. The significance of this observation will be pointed out more specifically in Section 3.5.2.5.

Figures 3.19 through 3.23 show all experiments from gauges 1 through 5 in comparison. An inspection of these Figures provides convincing evidence that the observations made in this Section are repeatable for all gauges and conditions. The results from gauge #6 are erroneous due to a problem with the amplifier and are not shown here. The two plots on the left hand side show the heat flux at nominal

conditions while the two plots on the right show the results for a higher shock strength. The top graphs show the absolute values while the bottom graphs show the same traces with the initial value of heat flux removed.

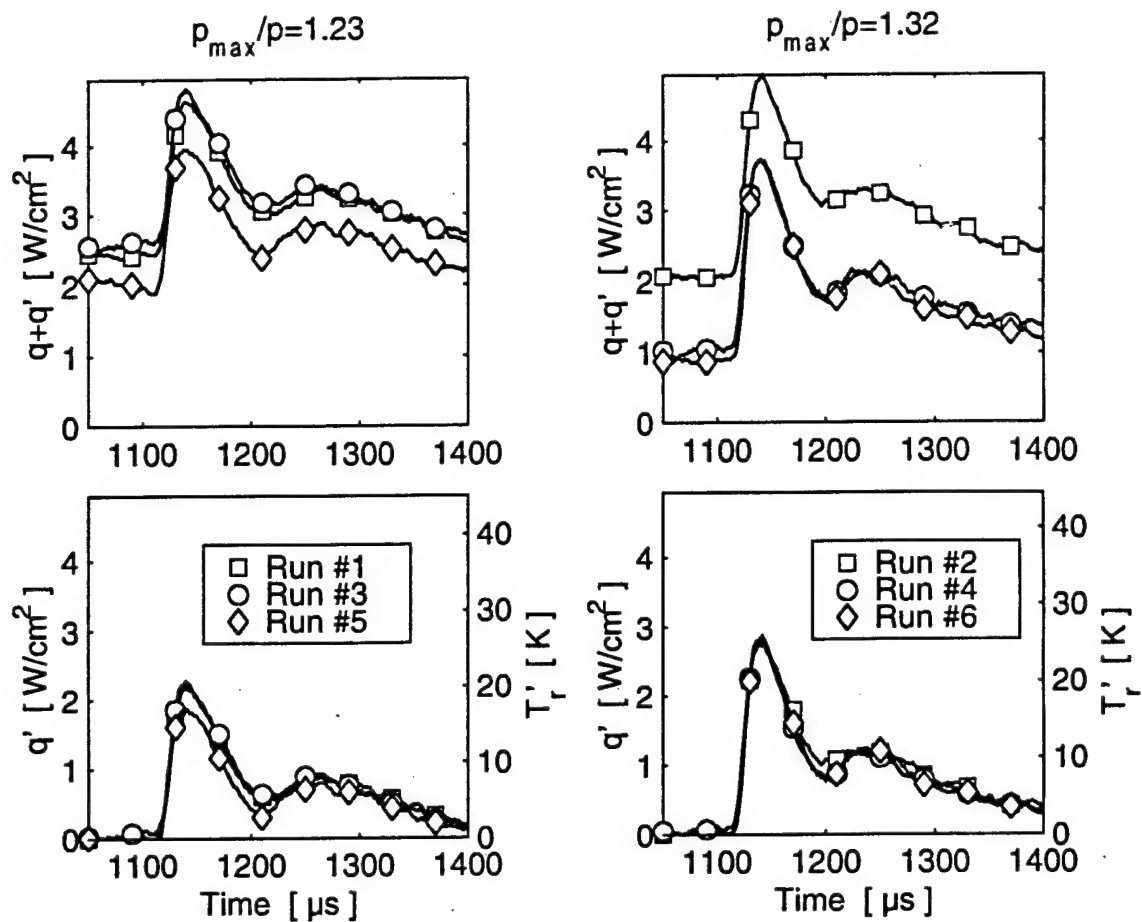


Figure 3.19: Shock Passing Events for Gauge # 1 at Different Shock Conditions without Film Cooling. Three Experiments at Different Levels of Initial Heat Flux for Each Shock Strength. Top Graphs: Absolute Values. Bottom Graph: Initial Value Subtracted.

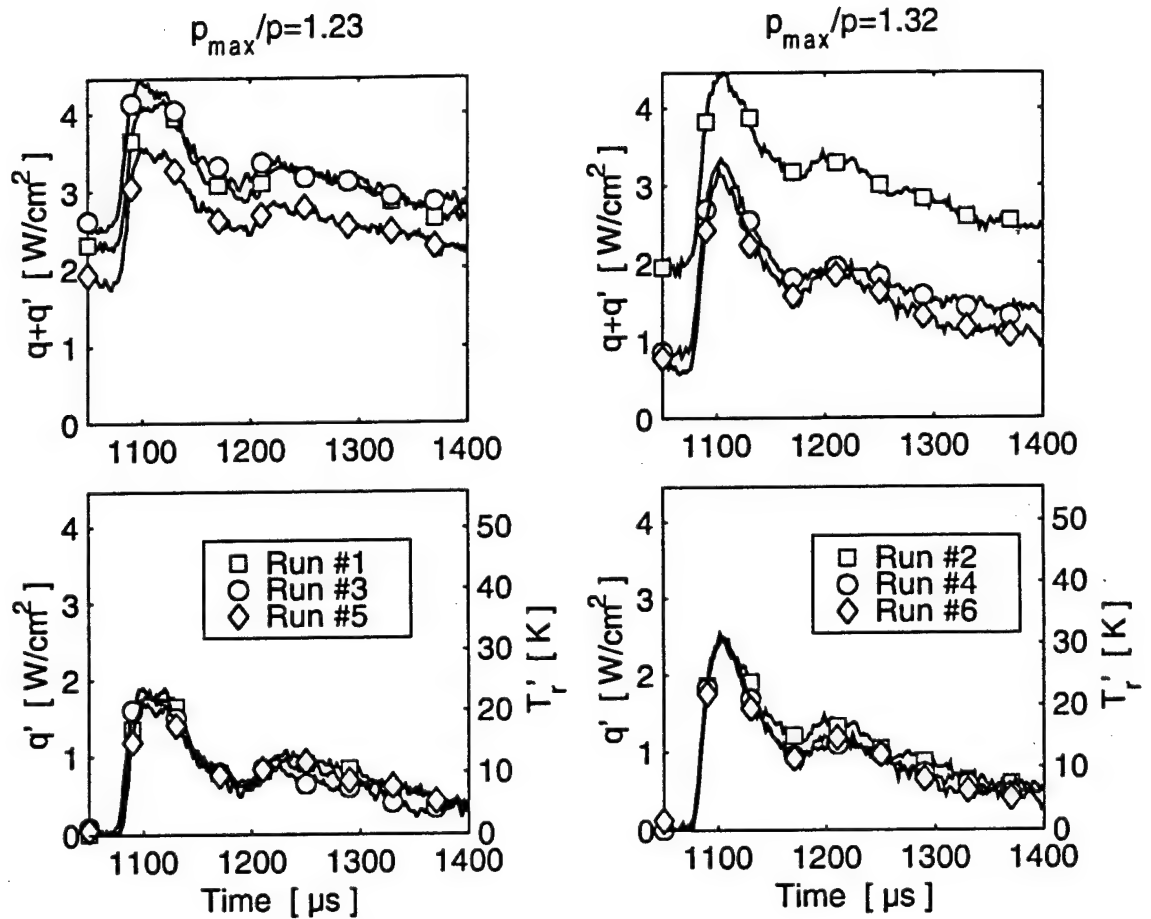


Figure 3.20: Shock Passing Events for Gauge # 2 at Different Shock Conditions without Film Cooling. Three Experiments at Different Levels of Initial Heat Flux for Each Shock Strength. Top Graphs: Absolute Values. Bottom Graph: Initial Value Subtracted.

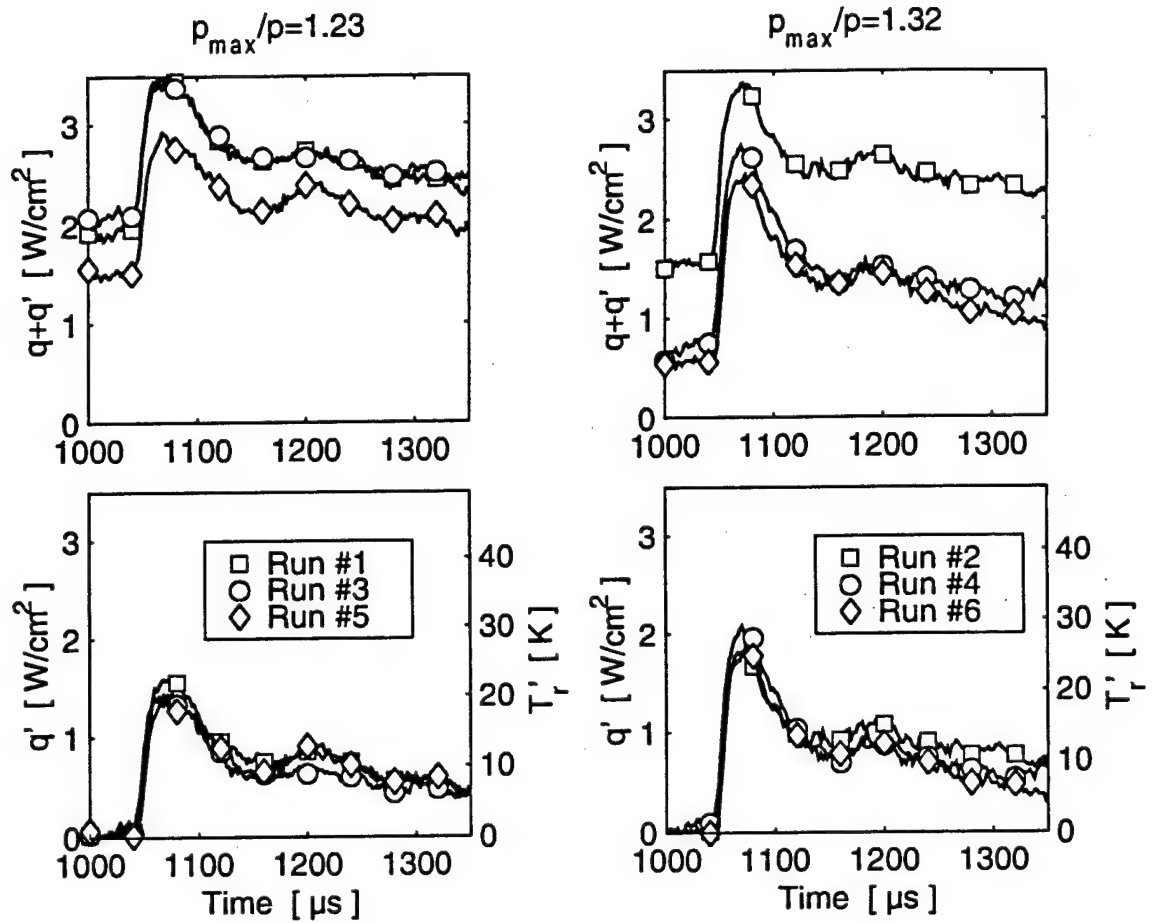


Figure 3.21: Shock Passing Events for Gauge # 3 at Different Shock Conditions without Film Cooling. Three Experiments at Different Levels of Initial Heat Flux for Each Shock Strength. Top Graphs: Absolute Values. Bottom Graph: Initial Value Subtracted.

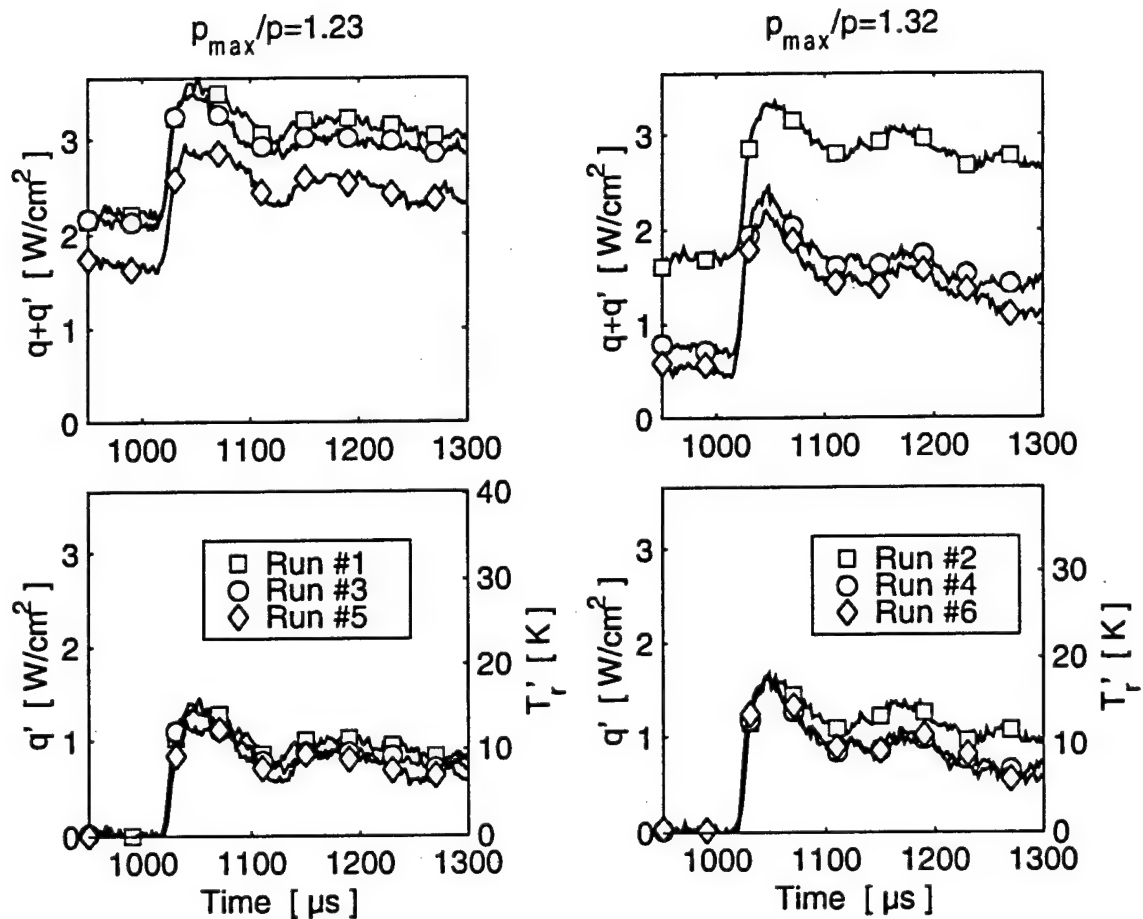


Figure 3.22: Shock Passing Events for Gauge # 4 at Different Shock Conditions without Film Cooling. Three Experiments at Different Levels of Initial Heat Flux for Each Shock Strength. Top Graphs: Absolute Values. Bottom Graph: Initial Value Subtracted.

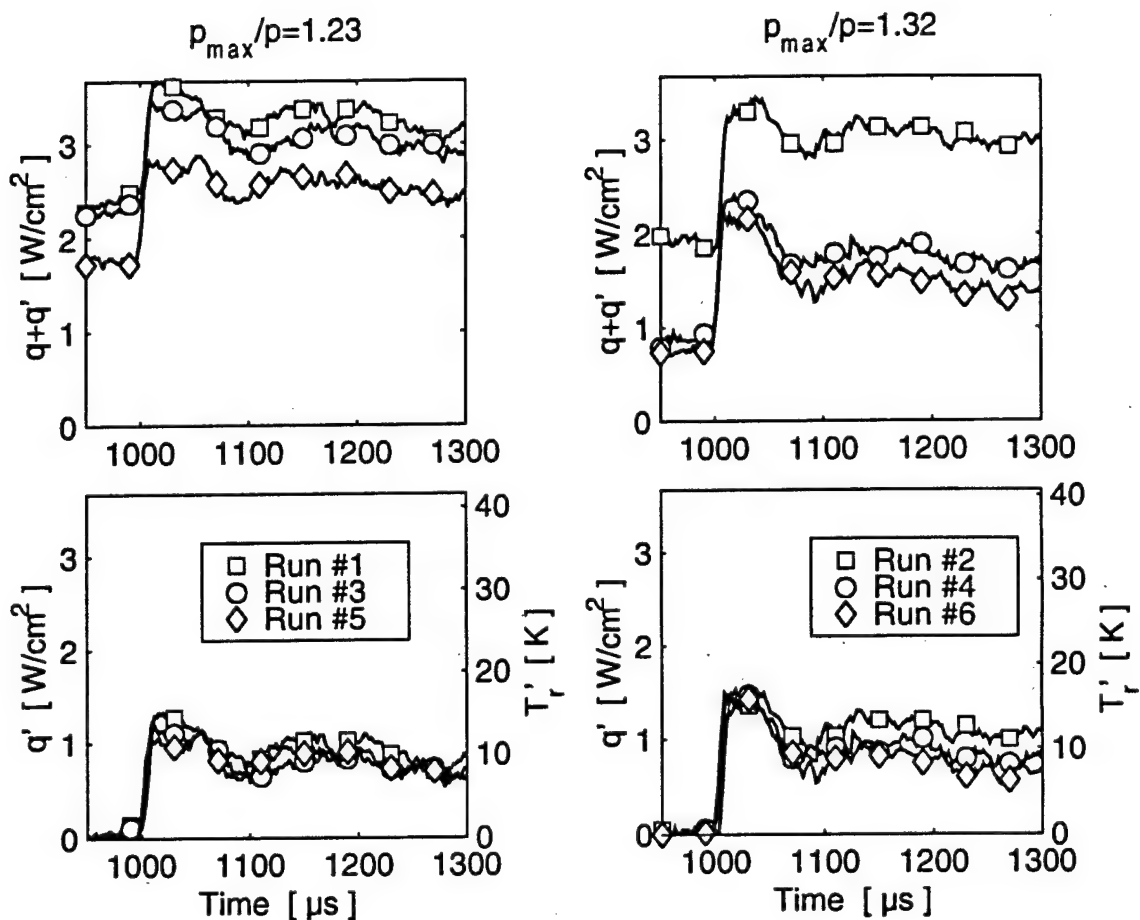


Figure 3.23: Shock Passing Events for Gauge # 5 at Different Shock Conditions without Film Cooling. Three Experiments at Different Levels of Initial Heat Flux for Each Shock Strength. Top Graphs: Absolute Values. Bottom Graph: Initial Value Subtracted.

3.5.2.3 Analytical Model with Film Cooling

The decomposition of heat flux for the case with film cooling is somewhat different from the analysis without film cooling. That is why a separate Section is dedicated to the derivation. The definition of heat transfer coefficient is the same for the cooled case as it was in the case without film cooling (in the old notation):

$$q = h_c \cdot (T_{aw} - T_w) \quad (3.15)$$

Analogous to the derivation in Section 3.5.2.1, the physical variables are now replaced by the sum of the time mean value before shock impact and a fluctuating component during the shock passing:

$$q + q' = (h_c + h'_c) \cdot (T_{aw} + T'_{aw} - T_w) \quad (3.16)$$

Equation 3.16 considers the fact that the wall temperature does not vary during the short time period of the shock passing event. Again the right hand side of Equation 3.16 is multiplied out to obtain:

$$q + q' = h_c \cdot (T_{aw} - T_w) + h'_c \cdot (T_{aw} - T_w) + h_c \cdot T'_{aw} + h'_c \cdot T_{aw} \quad (3.17)$$

The first term on the right hand side of Equation 3.17, $h_c \cdot (T_{aw} - T_w)$, represents the time mean value of heat transfer before the shock impact, q . After subtracting

these time mean values on both sides of Equation 3.17, an expression for the unsteady component of heat flux is obtained:

$$q' = h'_t \cdot (T_{aw} - T_w) + h_c \cdot T'_{aw} + h'_t \cdot T'_{aw} \quad (3.18)$$

The first term on the right hand side of Equation 3.18, $h'_t \cdot (T_{aw} - T_w)$, constitutes the first order contribution of the fluctuating heat transfer coefficient to the overall unsteady heat transfer. The second term on the right hand side, $h_c \cdot T'_{aw}$, describes the first order contribution of the time varying component of the adiabatic wall temperature to the overall heat flux. The combined effect of the two varying properties, heat transfer coefficient and adiabatic wall temperature, is represented by the last term on the right hand side of Equation 3.18.

The first step of the analysis will be to determine the relative magnitudes of these three terms or, more specifically, the relative magnitude of the contributions of h and T_{aw} to the unsteady heat flux. A second step for further analysis is the decomposition of the adiabatic wall temperature expressed in terms of the film effectiveness (in the conventional notation):

$$T_{aw} = T_r - \eta \cdot (T_r - T_c) \quad (3.19)$$

Again, all the variables involved are replaced by the sum of their time mean value before shock impact and their unsteady component during the shock passing:

$$T_{aw} + T'_{aw} = T_r + T'_r - (\eta + \eta') \cdot (T_r + T'_r - T_c) \quad (3.20)$$

In Equation 3.20 it is assumed that the coolant exit temperature does not change during the short time of the shock impact. It is arguable, though, whether the coolant exit temperature will change sometime later as the shock travels upstream and reaches the coolant exit locations. This hypothesis will be investigated in a future effort.

The right hand side of Equation 3.20 is multiplied out and rearranged for convenient analysis to yield:

$$T_{aw} + T'_{aw} = T_r - \eta \cdot (T_r - T_c) + T_r' \cdot (1 - \eta) - \eta' \cdot (T_r - T_c) - \eta' \cdot T_r' \quad (3.21)$$

The time mean value of adiabatic wall temperature is found as the first term on the right hand side of Equation 3.21, $T_r - \eta \cdot (T_r - T_c)$. After subtracting the time mean value of heat transfer from both sides of Equation 3.21, an expression for the unsteady variation of adiabatic wall temperature is obtained:

$$T'_{aw} = T_r' \cdot (1 - \eta) - \eta' \cdot (T_r - T_c) - \eta' \cdot T_r' \quad (3.22)$$

The contributions of the unsteady variation of recovery temperature T_r' , the varying film effectiveness η' and their combined effect are found in the respective order on the right hand side of Equation 3.22. It is of interest to analyze the relative magnitudes of these contributions to the overall fluctuation of the adiabatic wall temperature.

3.5.2.4 Effect of Shock Passing with Film Cooling

The first step in the analysis will be the comparison of actual heat flux data to the model developed in 3.5.2.3. The goal is to determine the contributions of the unsteady component of heat transfer coefficient h and adiabatic wall temperature T_{aw} to the overall unsteady heat transfer q' . The method will be similar to the analysis of the heat transfer without film cooling in Section 3.5.2.2. The observations will be verified for different conditions. The parameters varied were the shock strength, the ratio of coolant to freestream total pressure, and the heat flux levels (or overall temperature difference $(T_{aw} - T_w)$) before shock impact. Two values were chosen for the shock strength: the nominal value of $\frac{p+p_{max}}{p} = 1.23$ and a higher value of 1.32. For the coolant to freestream total pressure ratio the design value of 1.04 and a much higher value of 1.2 were chosen for the parameter variation. As described in Section 3.5.2.2, it was attempted to achieve three different levels of initial heat flux. This test matrix resulted in twelve experiments overall. The conditions at shock impact are listed in Tables 3.5 through 3.10 for all twelve experiments with film cooling and all gauges. All values from run #8 were lost due to a problem with the low speed data acquisition system. The recovery temperatures listed in Table 3.6 were calculated from the total temperature by subtracting the mean T_i as determined from the steady state experiments described in Section 2.3.1. The adiabatic wall temperatures listed in Table 3.7 were calculated using this recovery temperature and the film effectiveness determined using low speed data from the entire run as described in Section 2.3.3 and listed in Table 3.10:

$$T_{awi} = T_{ri} - \eta_i \cdot (T_{ri} - T_c) \quad (3.23)$$

The index i refers to the gauges 1 through 6.

Table 3.5: Test Matrix, Total Temperature and Coolant Temperature Before Shock Impact for All Cooled Experiments

Run #	Shock Strength $\frac{p+p'_{max}}{p}$	$\frac{p_c}{p_{oc}}$ [-]	T_t [°C]	T_c [°C]
1	1.23	1.04	71.7	-118.7
2	1.32	1.04	79.1	-99.4
3	1.23	1.20	83.7	-68.5
4	1.32	1.20	77.3	-80.9
5	1.23	1.04	60.1	-127.8
6	1.32	1.04	59.6	-95.4
7	1.23	1.20	58.2	-99.7
8	1.32	1.20	NaN	NaN
9	1.23	1.04	45.3	-67.0
10	1.32	1.04	40.9	-122.8
11	1.23	1.20	42.1	-67.1
12	1.32	1.20	41.5	-37.1

Table 3.6: Recovery Temperature Before Shock Impact for All Gauges and All Cooled Experiments

Run #	T_{r1} [°C]	T_{r2} [°C]	T_{r3} [°C]	T_{r4} [°C]	T_{r5} [°C]	T_{r6} [°C]
1	65.8	66.6	65.9	62.7	61.5	55.4
2	73.2	74.0	73.3	70.1	68.9	62.8
3	77.8	78.6	77.9	74.7	73.5	67.4
4	71.4	72.2	71.5	68.3	67.1	61.0
5	54.2	55.0	54.3	51.1	49.9	43.8
6	53.7	54.5	53.8	50.6	49.4	43.3
7	52.3	53.1	52.4	49.2	48.0	41.9
8	NaN	NaN	NaN	NaN	NaN	NaN
9	39.4	40.2	39.5	36.3	35.1	29.0
10	35.0	35.8	35.1	31.9	30.7	24.6
11	36.2	37.0	36.3	33.1	31.9	25.8
12	35.6	36.4	35.7	32.5	31.3	25.2

Table 3.7: Adiabatic Wall Temperature Before Shock Impact for All Gauges and All Cooled Experiments

Run #	T_{aw1} [°C]	T_{aw2} [°C]	T_{aw3} [°C]	T_{aw4} [°C]	T_{aw5} [°C]	T_{aw6} [°C]
1	8.75	33.02	1.85	21.68	27.64	8.54
2	22.08	42.05	16.84	32.28	39.29	17.52
3	52.30	55.90	49.51	41.02	50.94	41.82
4	36.18	45.21	41.03	32.91	41.66	30.32
5	-6.26	21.32	-9.97	11.54	13.66	-3.24
6	7.44	25.98	2.93	18.31	21.47	5.27
7	13.35	22.35	23.51	17.16	21.72	6.90
8	NaN	NaN	NaN	NaN	NaN	NaN
9	8.61	22.58	4.90	14.58	16.84	0.85
10	-17.27	7.05	-19.36	-2.93	0.32	-16.40
11	15.40	18.53	14.70	11.03	15.38	5.61
12	24.58	25.48	22.03	18.28	21.40	11.53

Table 3.8: Wall Temperature Before Shock Impact for All Gauges and All Cooled Experiments

Run #	T_{w1} [°C]	T_{w2} [°C]	T_{w3} [°C]	T_{w4} [°C]	T_{w5} [°C]	T_{w6} [°C]
1	1.7	3.8	4.3	4.3	4.5	2.5
2	-1.1	0.5	1.1	1.1	1.1	-1.1
3	-4.1	-2.3	-2.1	-2.1	-1.9	-4.2
4	3.1	5.1	5.1	5.1	5.2	2.7
5	3.2	5.0	5.7	5.7	6.1	4.2
6	2.5	4.3	4.6	4.6	4.9	2.5
7	-1.0	0.9	1.5	1.5	1.9	-0.1
8	NaN	NaN	NaN	NaN	NaN	NaN
9	6.1	7.9	7.8	7.8	7.8	5.5
10	-1.8	-0.1	0.3	0.3	0.9	-0.8
11	9.0	10.6	10.4	10.4	10.5	8.6
12	11.8	13.6	13.1	13.1	12.8	10.2

Table 3.9: Heat Transfer Coefficient for All Gauges and All Cooled Experiments

Run #	h_{c1} $[\frac{W}{m^2 \cdot K}]$	h_{c2} $[\frac{W}{m^2 \cdot K}]$	h_{c3} $[\frac{W}{m^2 \cdot K}]$	h_{c4} $[\frac{W}{m^2 \cdot K}]$	h_{c5} $[\frac{W}{m^2 \cdot K}]$	h_{c6} $[\frac{W}{m^2 \cdot K}]$
1	1512.5	956.7	755.2	1014.4	1028.2	1373.0
2	1403.3	940.2	752.9	997.7	969.9	1341.9
3	1302.0	859.1	784.2	1022.1	983.7	1203.4
4	1375.2	887.5	776.5	1021.3	1014.8	1256.7
5	1354.4	920.1	768.2	914.6	969.1	1248.2
6	1374.0	919.6	752.2	965.3	953.9	1254.6
7	867.8	875.8	654.9	1098.2	988.5	1200.0
8	NaN	NaN	NaN	NaN	NaN	NaN
9	1332.9	919.5	718.1	984.1	954.9	1329.1
10	1318.3	899.3	770.4	989.7	979.7	1312.5
11	1218.8	869.1	763.0	993.9	998.1	1251.9
12	1318.9	844.8	762.6	952.9	988.3	1245.4

Table 3.10: Film Effectiveness for All Gauges and All Cooled Experiments

Run #	η_1 [-]	η_2 [-]	η_3 [-]	η_4 [-]	η_5 [-]	η_6 [-]
1	0.309	0.181	0.347	0.226	0.188	0.269
2	0.296	0.184	0.327	0.223	0.176	0.279
3	0.174	0.154	0.194	0.235	0.159	0.188
4	0.231	0.176	0.200	0.237	0.172	0.216
5	0.332	0.184	0.353	0.221	0.204	0.274
6	0.310	0.190	0.341	0.221	0.193	0.274
7	0.256	0.201	0.190	0.215	0.178	0.247
8	NaN	NaN	NaN	NaN	NaN	NaN
9	0.289	0.164	0.325	0.210	0.179	0.293
10	0.331	0.181	0.345	0.225	0.198	0.278
11	0.201	0.177	0.209	0.220	0.167	0.217
12	0.151	0.148	0.188	0.204	0.145	0.219

The basic Equation for the analysis is Equation 3.18 from Section 3.5.2.3 which is repeated here:

$$q' = h'_t \cdot (T_{aw} - T_w) + h_c \cdot T'_{aw} + h'_t \cdot T'_{aw} \quad (3.24)$$

The contribution of the unsteady component of the heat transfer coefficient h'_t to the overall unsteady heat flux due to shock impingement is the first term on the right hand side of Equation 3.24. It is multiplied by the overall temperature difference before the shock impact. This means that its contribution is proportional to the heat flux level before shock impact. To analyze its relative magnitude the experiments were done at three different levels of initial heat flux.

For the argument about to be suggested, data from gauge # 1 and runs # 4, #8 and #12 will be used. This set of data illustrates the conclusions to be drawn relatively well. In the concluding Figures 3.27 through 3.31 all data from all experiments will be shown. In Figure 3.24 the three traces of heat transfer are shown prior to any manipulation. The traces before the shock impact show a very unsteady behavior. This is true for all experiments with film cooling. The unsteadiness is introduced by the presence of inherently unsteady film mixing processes and the motion of the cooling jets. This poses two problems:

1. A point in time or a window of time before the the shock impact has to be chosen to find the mean value of heat flux before shock impact q . This choice is necessarily arbitrary. To best capture the effect of the passing shock a time window of $5\mu s$ just before the shock impact was used for the determination of q . This problem was not present in the analysis without film cooling. For the case without film cooling the heat transfer before the shock impact was a steady value without significant fluctuations.

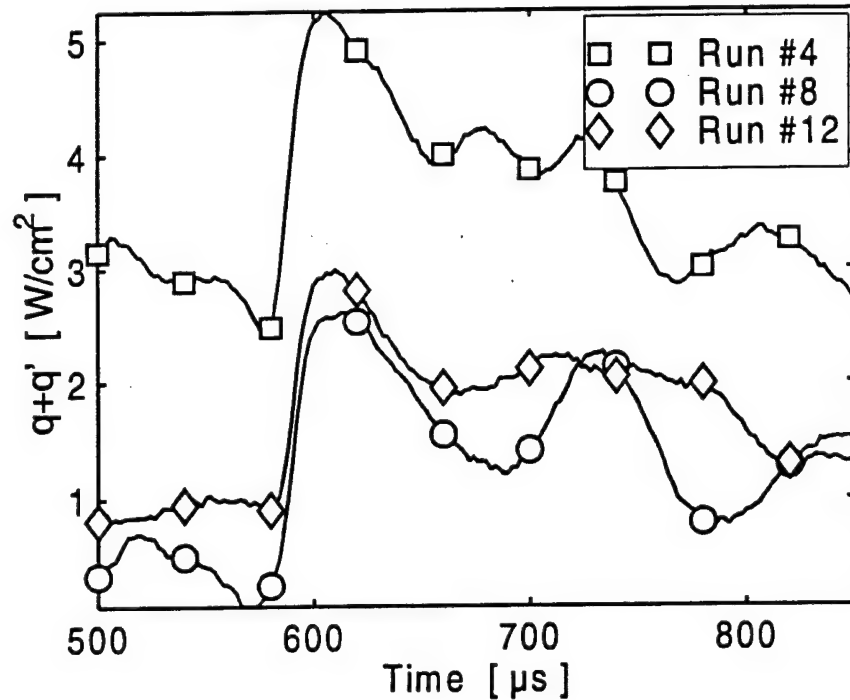


Figure 3.24: Shock Passing Events for Gauge # 1 at Increased Shock Strength with Strong Film Cooling. Three Experiments at Different Levels of Initial Heat Flux.

2. The fluctuations due to the presence of the film cooling superimpose with the unsteady heat transfer caused by the passing shock. This superimposed random signal blurs the effect of the passing shock somewhat. Still the effect of the passing shock is distinctly visible and an analysis is possible.

Figure 3.25 shows the traces with the “mean” heat flux level before shock impact removed. The three traces do not coincide as closely as was the case in Section 3.5.2.2. Also, there is more variation between the traces before and after the shock impact. Still, it can be observed that the magnitudes of the unsteady heat transfer do not correlate with the initial level of heat flux. This observation is essentially true for all experiments. Even though the variations in unsteady heat transfer from experiment to experiment are significant, they do not correlate with the initial level

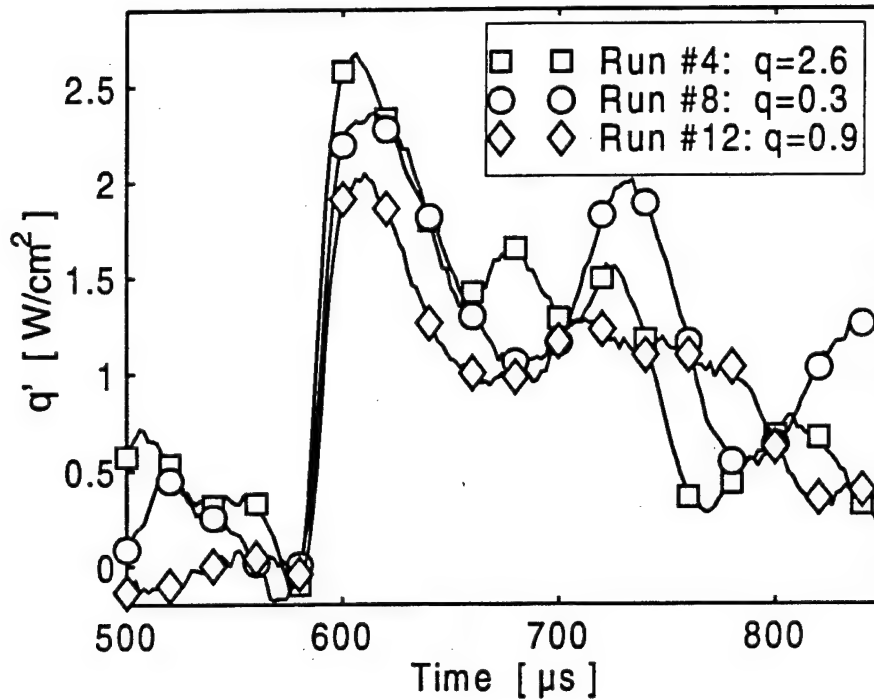


Figure 3.25: Shock Passing Events for Gauge # 1 at Increased Shock Strength with Strong Film Cooling. Three Experiments at Different Levels of Initial Heat Flux. Initial Level of Heat Flux Removed.

of heat flux before shock impact.

The unsteady variation of heat transfer coefficient is multiplied by the overall temperature difference before shock impact to yield the contribution of \dot{h} to the unsteady heat transfer. This implies that the unsteady component of heat transfer would depend on the heat flux before shock impact which is equivalent to the overall temperature difference before shock impact. Figure 3.25 shows that there is no correlation between the unsteady component of heat flux and the initial heat flux level. This can only be the case if h_t is not significantly large. So it can be concluded that the variation of heat transfer coefficient h_t is of minor importance in the heat transfer due to shock impact. Based on this conclusion, all terms containing h_t in Equation 3.24 will be dropped. After rearranging, this yields an expression for the variation of adiabatic wall temperature:

$$T_{aw} = \frac{q}{h_c} \quad (3.25)$$

The traces of the variation of adiabatic wall temperature obtained from this expression are scaled images of the traces of q of Figure 3.25. For completeness they are shown in Figure 3.26. To convert q from run #8 to temperature a mean heat transfer

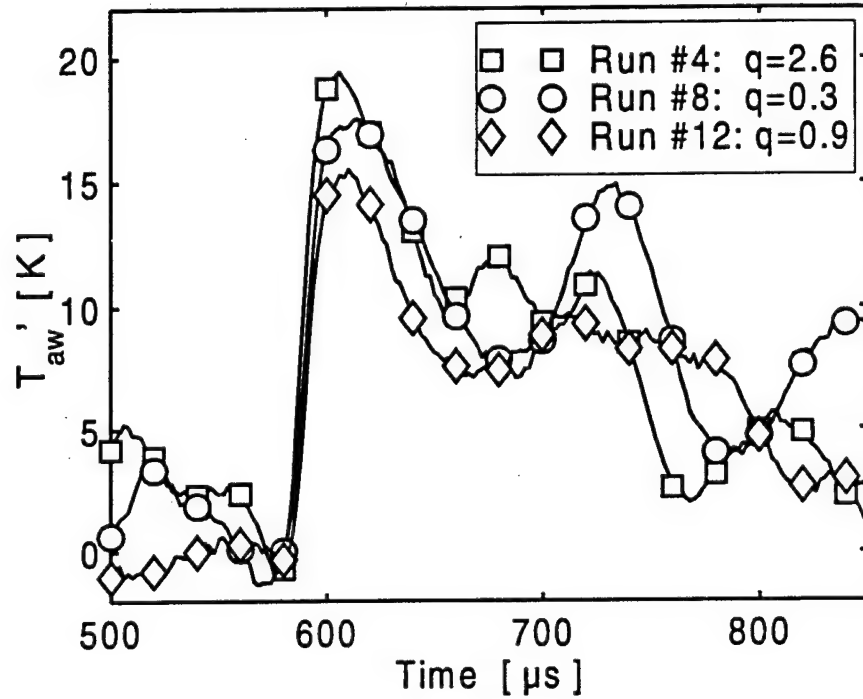


Figure 3.26: Shock Passing Events for Gauge # 1 at Increased Shock Strength with Strong Film Cooling. Three Experiments at Different Levels of Initial Heat Flux. Initial Level of Heat Flux Removed. Converted to Temperature Variation.

coefficient of $1347W/(m^2 K)$ was used.

With the traces of adiabatic wall temperature in Figure 3.26, another supporting argument for the conclusion that h_c is negligible can be found. The order of magnitude of T_{aw} is about the same as $(T_{aw} - T_w)$. Then, if h_c was of the same order

of magnitude as h_c , the contribution of $h'_c \cdot (T_{aw} - T_w)$ would have to be of the same order as the initial heat flux level q . This cannot be observed from the data in figure 3.25. It has to be concluded that $h'_c \ll h_c$.

This observation is essentially true for all experiments. A comparative summary of all these experiments is given in Figures 3.27 through 3.31. To convert q in these Figures to T'_{aw} a mean heat transfer coefficient from each set of three runs was used. Since the variation of heat transfer coefficient within those sets is relatively small (see Table 3.9), this procedure is justified. Compared to the data without film cooling this data shows more imperfections. For example, run #1 appears erroneous on gauges 1 and 2 while it seems absolutely reasonable on gauges 3, 4 and 5. Another "bad" example is run #2. A spike of sorts appears at a time around $580\mu s$, and the data of gauge 3 from this run is unusable. Apart from these glitches, the data supports the conclusions drawn above.

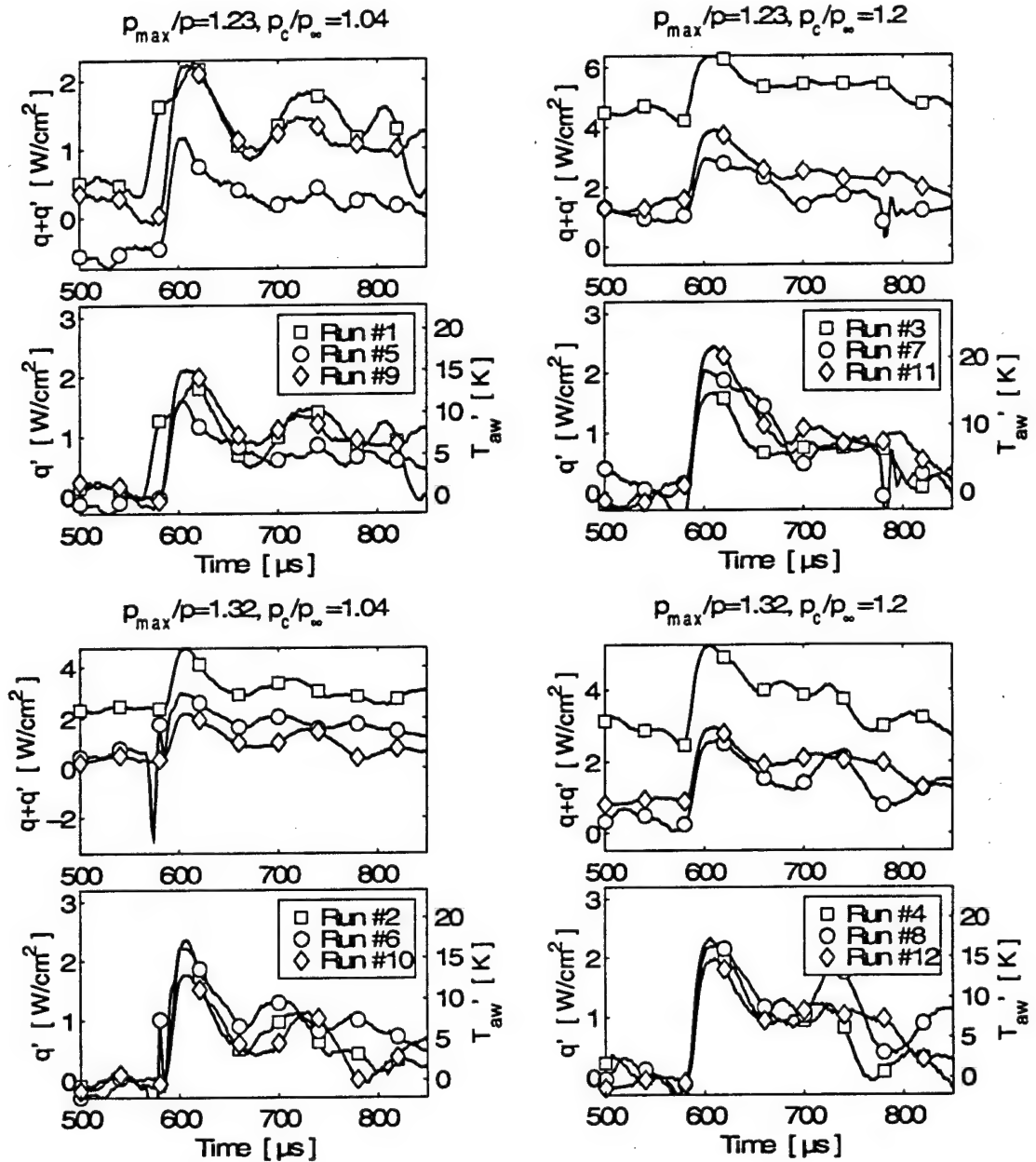


Figure 3.27: Shock Passing Events for Gauge # 1 at Different Shock Conditions with Film Cooling. Three Experiments at Different Levels of Initial Heat Flux for Each Shock and Cooling Strength. Top Graphs: Absolute Values. Bottom Graph: Initial Value Subtracted.

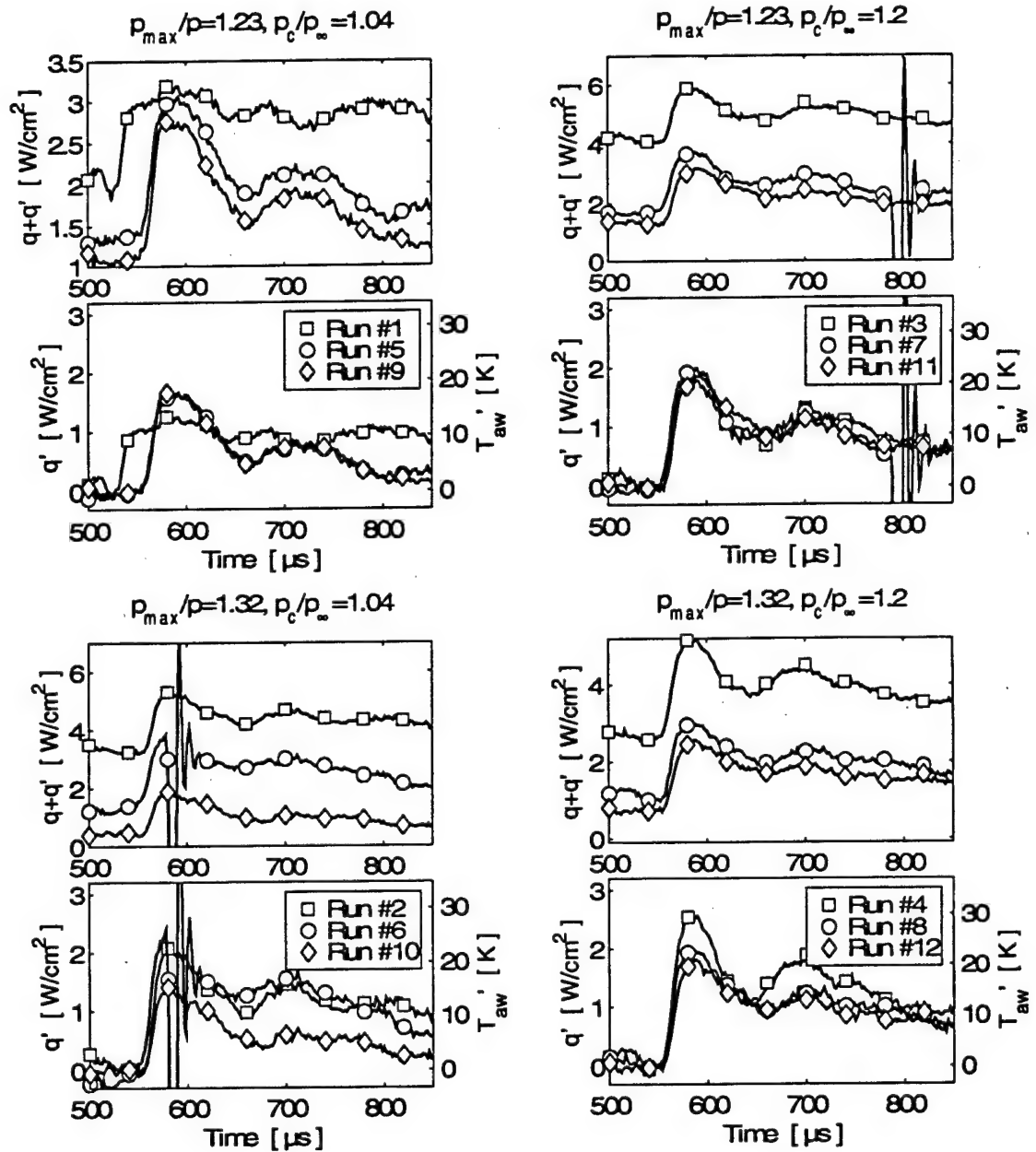


Figure 3.28: Shock Passing Events for Gauge # 2 at Different Shock Conditions with Film Cooling. Three Experiments at Different Levels of Initial Heat Flux for Each Shock and Cooling Strength. Top Graphs: Absolute Values. Bottom Graph: Initial Value Subtracted.

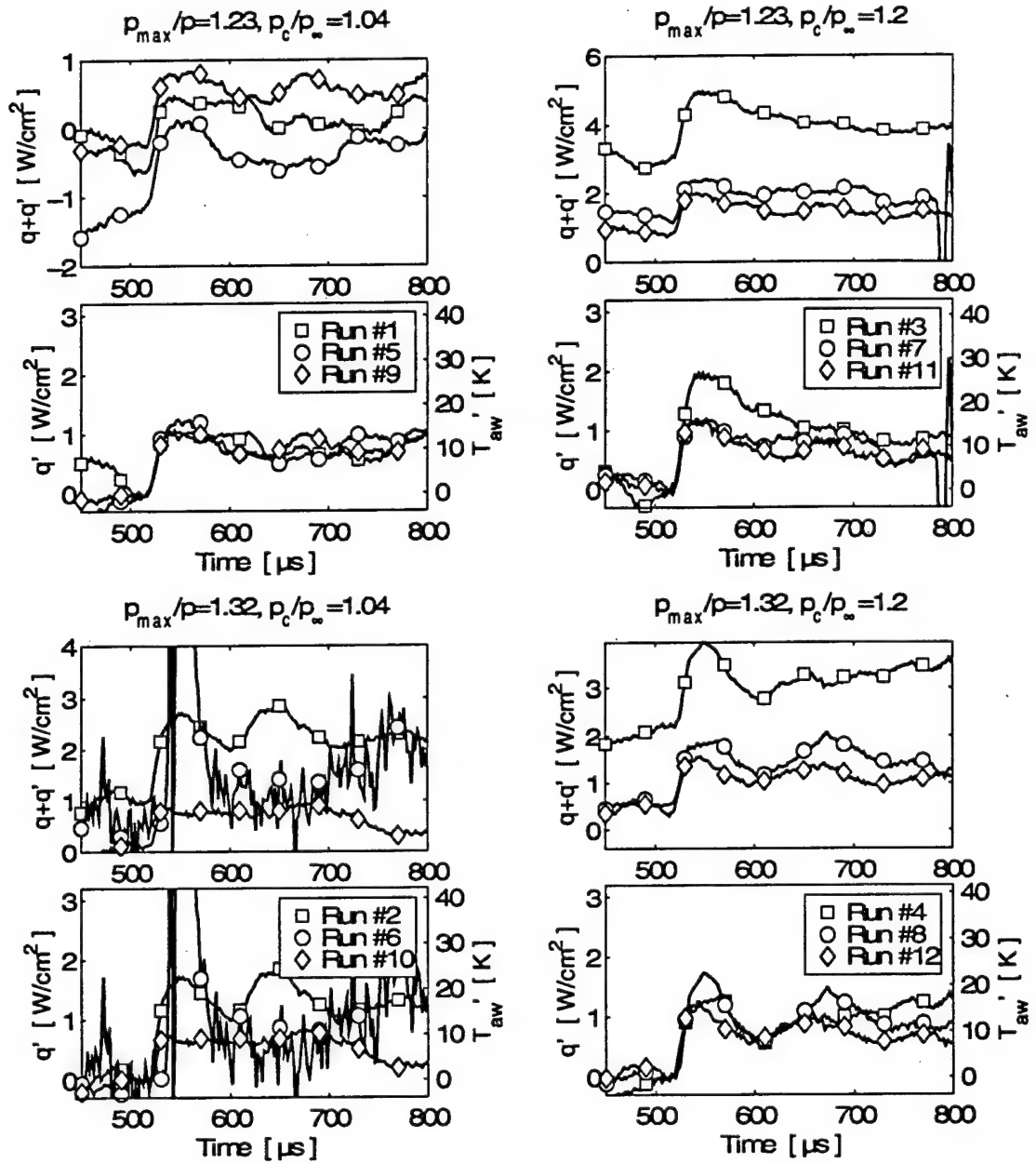


Figure 3.29: Shock Passing Events for Gauge # 3 at Different Shock Conditions with Film Cooling. Three Experiments at Different Levels of Initial Heat Flux for Each Shock and Cooling Strength. Top Graphs: Absolute Values. Bottom Graph: Initial Value Subtracted.

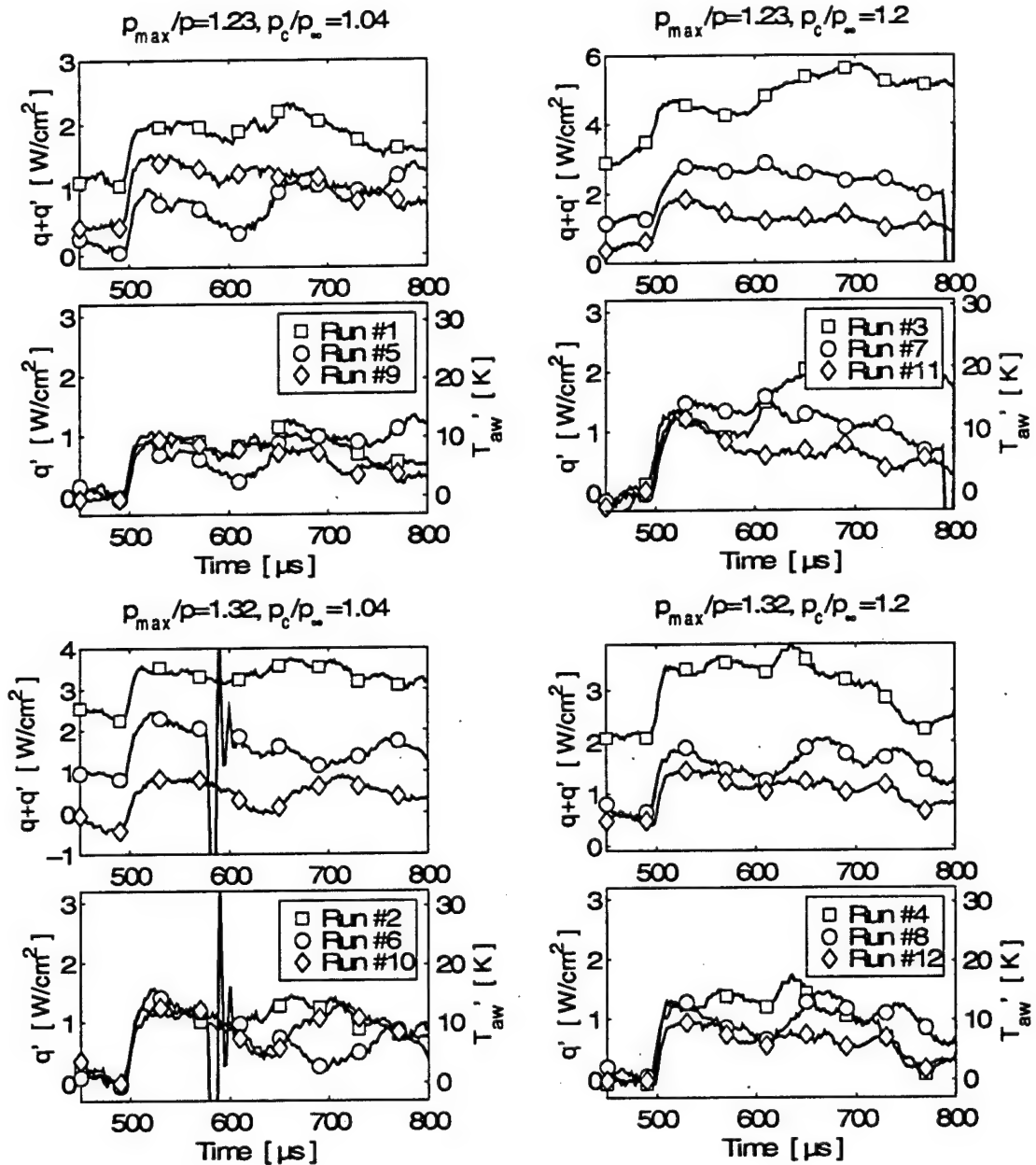


Figure 3.30: Shock Passing Events for Gauge # 4 at Different Shock Conditions with Film Cooling. Three Experiments at Different Levels of Initial Heat Flux for Each Shock and Cooling Strength. Top Graphs: Absolute Values. Bottom Graph: Initial Value Subtracted.

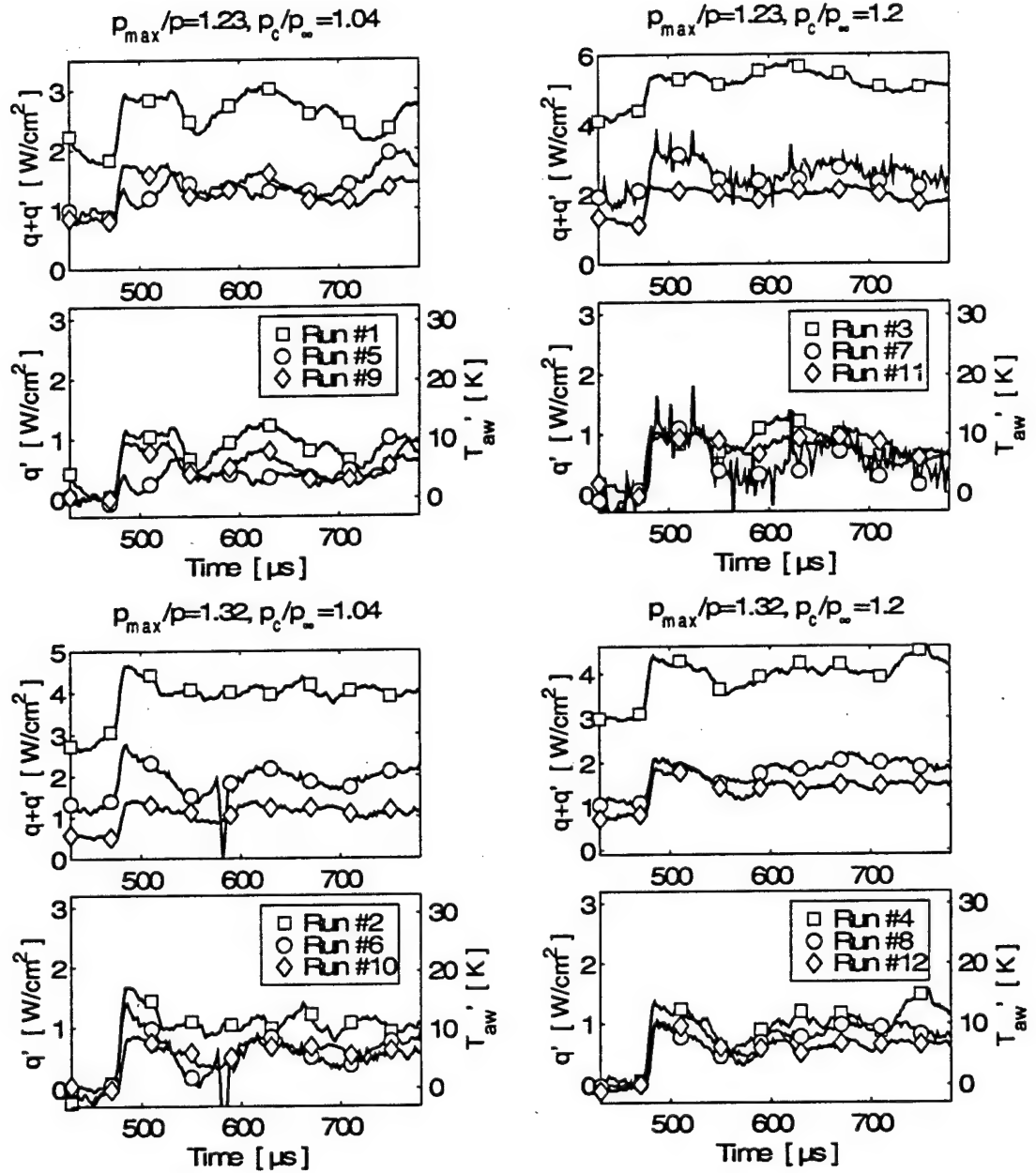


Figure 3.31: Shock Passing Events for Gauge # 5 at Different Shock Conditions with Film Cooling. Three Experiments at Different Levels of Initial Heat Flux for Each Shock and Cooling Strength. Top Graphs: Absolute Values. Bottom Graph: Initial Value Subtracted.

To complete the investigation of unsteady heat flux due to shock passing, the relative magnitude of the unsteady variation of film effectiveness will be investigated according to the decomposition technique layed out in Section 3.5.2.3. To illustrate the argument, results from only one set of data will be used. In the concluding Section all data will be shown subjected to the same analysis.

The unsteady variation of adiabatic wall temperature was analytically decomposed in Equation 3.22 in Section 3.5.2.3:

$$T'_{aw} = T'_r \cdot (1 - \eta) - \eta' \cdot (T_r - T_c) - \eta' \cdot T'_r \quad (3.26)$$

Basically, this Equation states that the fluctuation of adiabatic wall temperature is composed of three contributions. The first term on the right hand side contains the first order contribution of the fluctuation of the recovery temperature T'_r . Its influence is attenuated by the film effectiveness before shock impact $(1 - \eta)$. The second term on the right hand side contains the first order contribution of the fluctuation of film effectiveness scaled by the temperature difference before shock impact $\eta' \cdot (T_r - T_c)$.

The fluctuation of adiabatic wall temperature was determined in the first part of this Section to be proportional to the unsteady heat flux since the variation in heat transfer coefficient was shown to be small.

$$T'_{aw} = \frac{q}{h_c} \quad (3.27)$$

The fluctuation of recovery temperature can be assumed to be the one determined in Section 3.5.2.2 from the uncooled experiments. There is no reason to suggest that the

recovery temperature would behave differently for a film cooled or an uncooled blade when exposed to the same physical phenomenon. Therefore, it can be expressed by Equation 3.14 from Section 3.5.2.2:

$$T_r = \frac{q}{h} \quad (3.28)$$

For the purpose of the argument about to be made, all except the first term on the right hand side of 3.26 will be dropped. Then the fluctuating component of adiabatic wall temperature is expressed by:

$$T'_{aw} = T'_r \cdot (1 - \eta) \quad (3.29)$$

A comparison is shown in Figure 3.32 between the fluctuating component of the adiabatic wall temperature from the cooled run #2 gauge #1 and the fluctuating component of the recovery temperature from the uncooled run #2 gauge #1 multiplied by $(1 - \eta)$, which takes on the value of 0.704. The good agreement of the traces in Figure 3.32 suggests that the correlation between the fluctuating component of the adiabatic wall temperature and the fluctuating component of recovery temperature is well predicted by Equation 3.29. Qualitatively, one may conclude that the fluctuation of the adiabatic wall temperature is related mostly to the variation of recovery temperature. Figures 3.33 through 3.37 show all data from all gauges treated the same way as in figure 3.32.

To back up the conclusion drawn above, one may also consider an order of magnitude argument. $(T_r - T_c)$ in Equation 3.22 takes on values between 70°C and

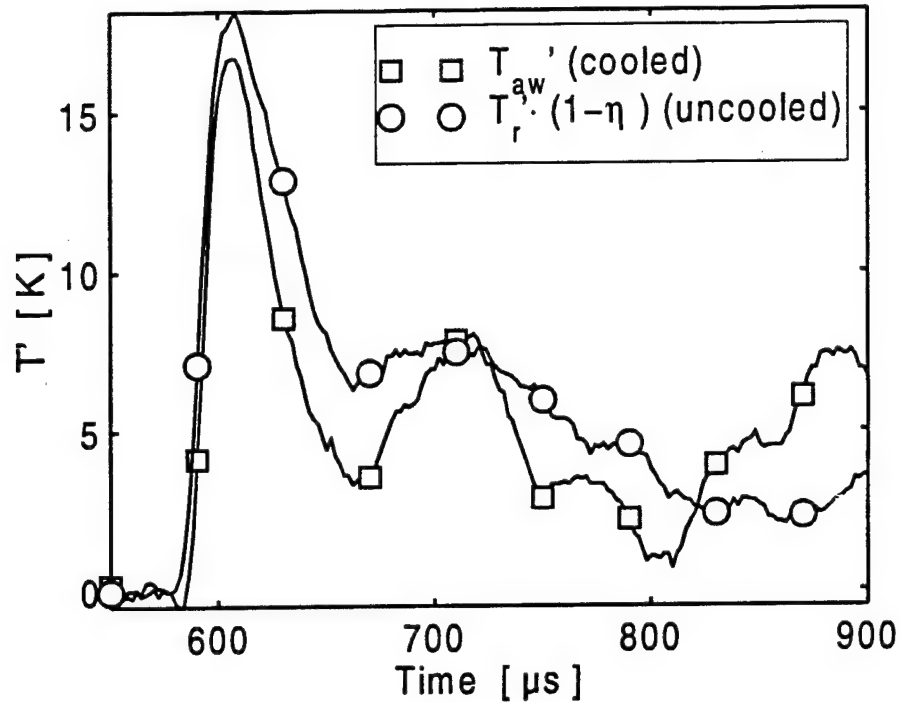


Figure 3.32: Comparison of T_{aw}' from Run #2 Gauge #1 with Film Cooling and $T_r \cdot (1 - \eta)$ from Run #2 Gauge #1 without Film Cooling.

190°C (as can be obtained from Tables 3.5 through 3.10). If the variation of film effectiveness η' was of the same order of magnitude as η , the variations of adiabatic wall temperature would have to be of the order of 10°C to 60°C above or below $T_r \cdot (1 - \eta)$. That is clearly not the case as can be seen from Figures 3.32 and 3.33 through 3.37. The variation of T_{aw}' from $T_r \cdot (1 - \eta)$ does not exceed about 5°C. Also, the difference does not show any specific pattern comparing different runs. It can be concluded that the variation of film effectiveness does not contribute significantly to the variation in unsteady heat transfer. It is significantly smaller in magnitude than the steady value of film effectiveness.

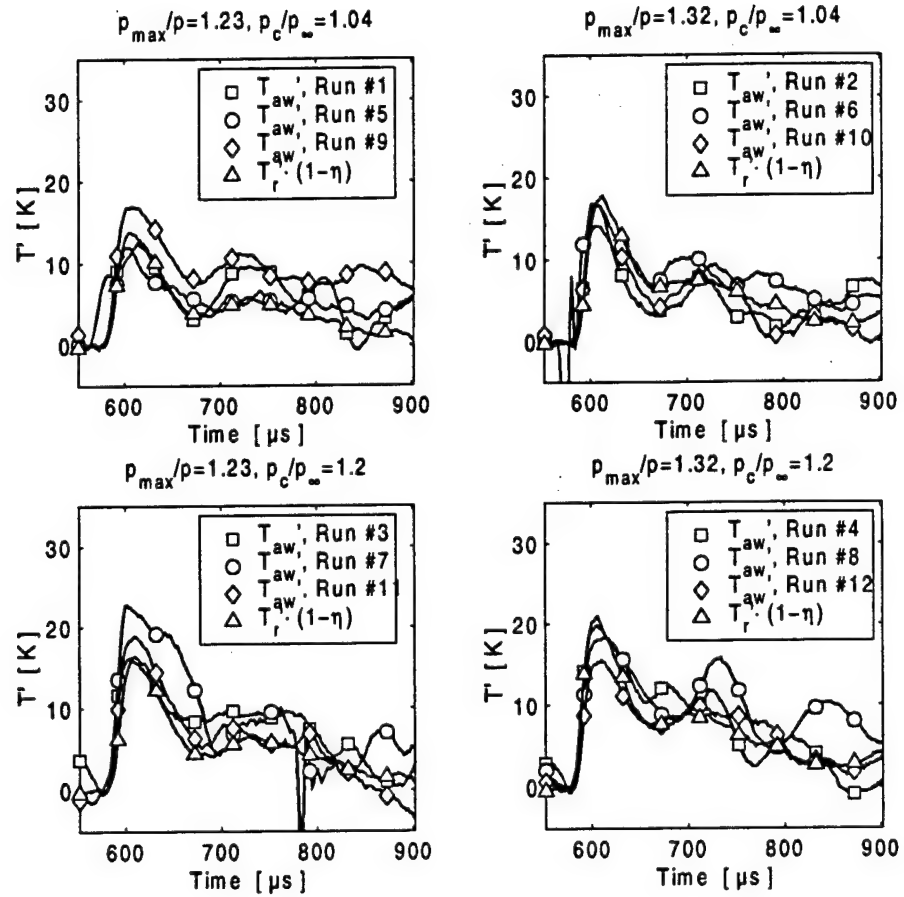


Figure 3.33: Comparison between T_{aw} and $T_r \cdot (1 - \eta)$ for all Experiments with Film Cooling. Results from Gauge #1.

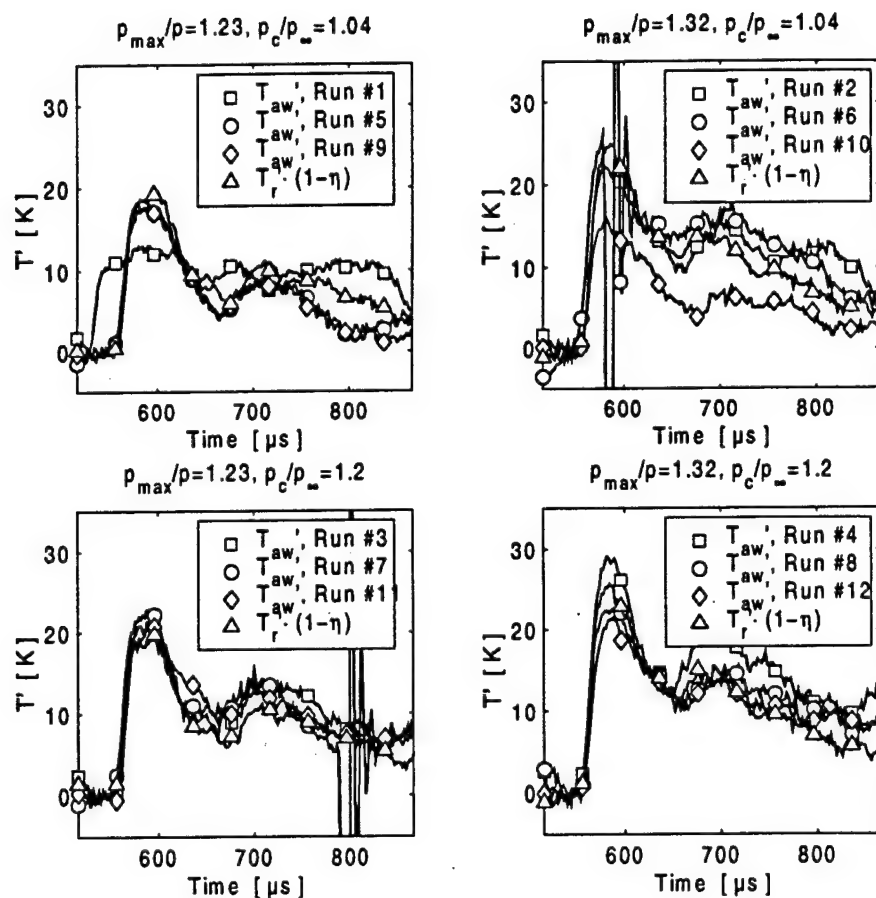


Figure 3.34: Comparison between T_{aw} and $T_r \cdot (1 - \eta)$ for all Experiments with Film Cooling. Results from Gauge #2.

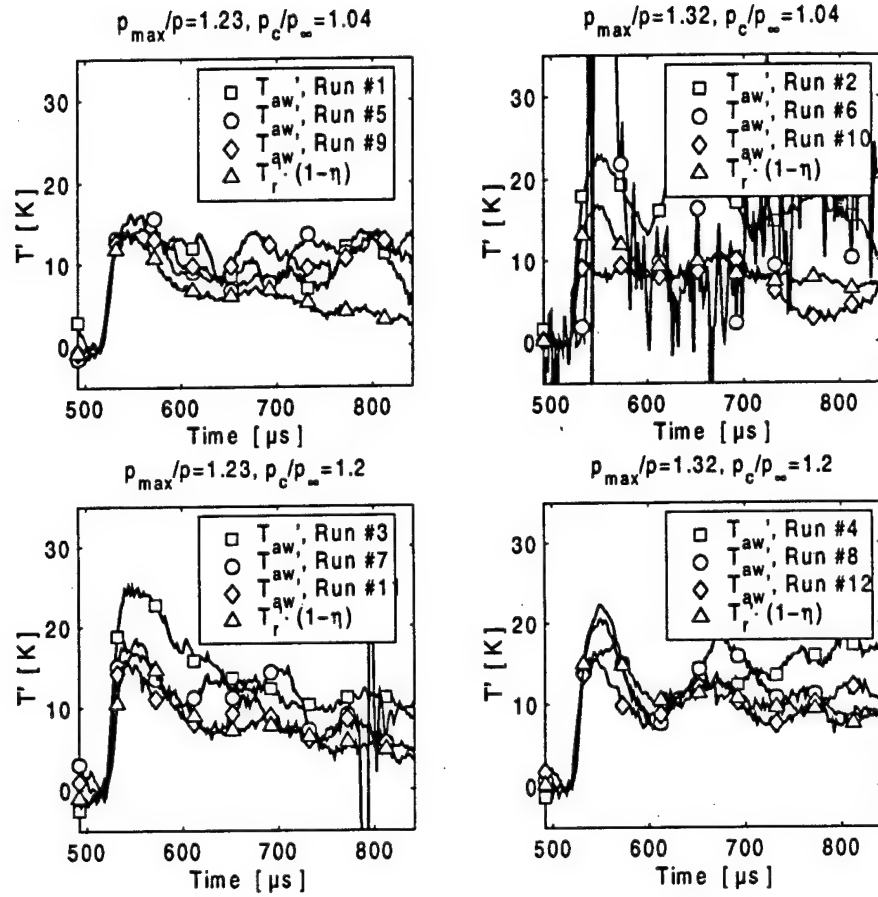


Figure 3.35: Comparison between T_{aw} and $T_r \cdot (1 - \eta)$ for all Experiments with Film Cooling. Results from Gauge #3.

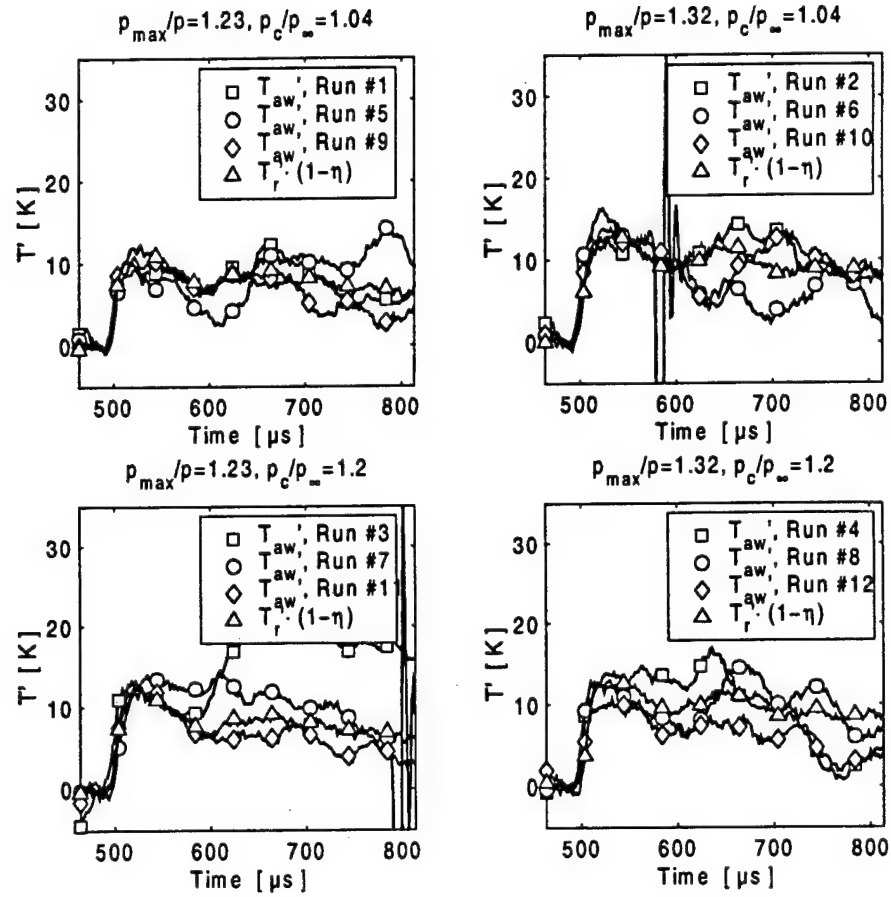


Figure 3.36: Comparison between T_{aw} and $T_r \cdot (1 - \eta)$ for all Experiments with Film Cooling. Results from Gauge #4.

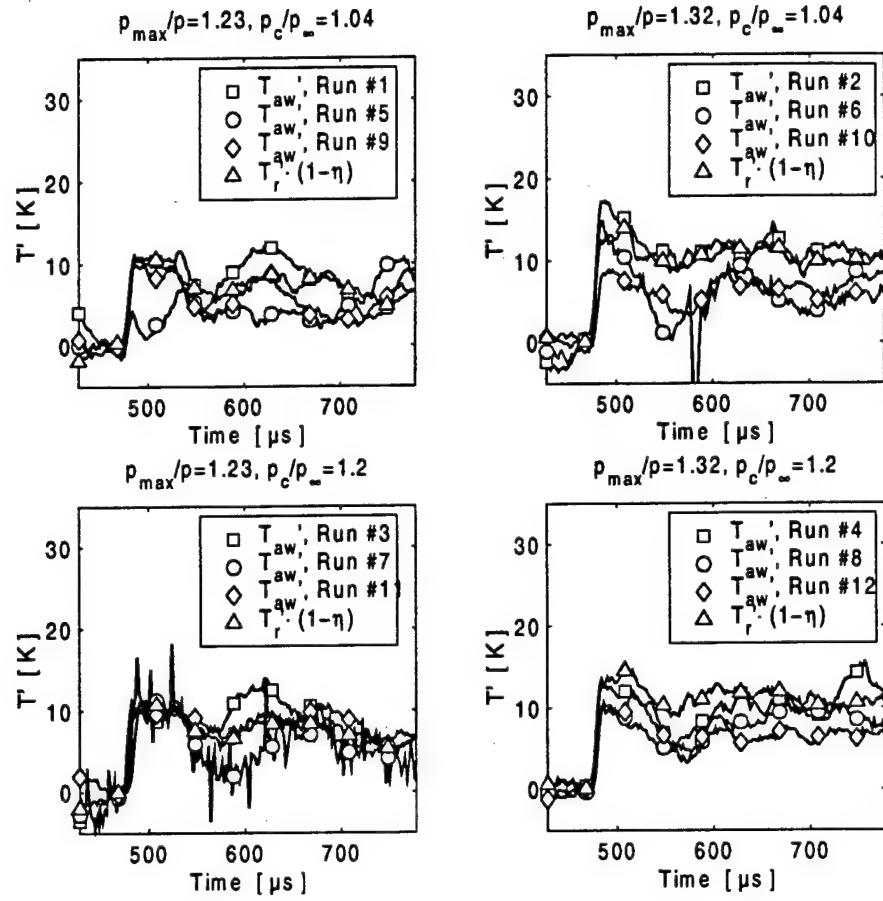


Figure 3.37: Comparison between T_{aw} and $T_r \cdot (1 - \eta)$ for all Experiments with Film Cooling. Results from Gauge #5.

3.5.2.5 Conclusion from the Unsteady Decomposition Technique

The conclusion from the four preceding Sections must be that the unsteady heat transfer with and without film cooling is driven mainly by a temperature variation induced by the compression associated with the passing shock wave. In the experiment, this temperature variation causes a very visible increase of heat transfer over a period of time of the same order of magnitude as the blade passing period. The shock adds energy to the flow field over this amount of time. In the engine, the situation is fundamentally different. The temperature field seen by the rotor blades varies periodically around its mean value. As the discussion of the unsteady decomposition technique indicated, the unsteady heat flux is primarily caused by temperature fluctuations. Since these vary around a mean value the heat flux will also. In other words, the time mean heat flux for a rotor blade that interacts with upstream shock waves will not be significantly different from the time mean heat flux the blade experiences with a uniform inlet flowfield.

This extrapolation of the experimental results has to be considered with care though. Several parameters that were not included in the parameter variation may affect the validity of the conclusions. For example it is possible that a turbulence level different than the one in these experiments (about 1%) will influence the reaction of the boundary to the shock impingement. Another influential parameter may be the state of the boundary layer in the experiments without film cooling. A completely turbulent or especially a transitional boundary layer might show different degrees of sensitivity to disturbances.

3.5.3 "Direct Comparison" of Predicted and Measured Heat Flux

3.5.3.1 Moss' Model

In this Chapter the data taken with and without film cooling will be compared to a model suggested by Moss et al. (1995) and in Moss et al. (1997). From heat transfer and static pressure measurements on the surface of rotor blades in a rotating turbine rig, Moss deduced that the unsteady component of heat flux could be predicted very well by simply assuming a constant heat transfer coefficient and isentropically predicting a temperature variation from the pressure variation. In those experiments, there were no shocks present, so only the effects of the wake on the rotor surface heat transfer were modeled. Also, the experiments did not involve film cooling. Here, the same procedure is going to be applied to the data taken with film cooling and shock passing in a stationary linear cascade. The predicted and the measured heat flux will be compared and conclusions will be drawn from this comparison.

When comparing measurements from different transducers directly, one has to know the dynamic behaviour of each of these transducers. It was because of this necessity that the dynamic behavior of both gauges was investigated in depth as reported in Appendices C and B.

From these investigations, it became clear that both signals (heat transfer and surface pressure) had to be recorded at the same sampling and cut-off frequency and that both signals had to be corrected for their dynamic behaviour in order to compare both signals directly. Because of the requirement for equal sampling and cut-off frequencies, it was not possible to use the data presented in Section 3.5.2 for the purpose of this investigation. The only way to use it would have been to digitally filter the heat flux signals to the cut-off frequency of the *Kulite* transducers (25 kHz)

and perform the comparison at this low level of frequency content. Since the frequency band from 0 to 25 kHz is not nearly adequate to obtain a good representation of the shock event, that procedure was decided against. Instead, a much shorter series of tests with less gauges was performed to verify Moss' conclusions with film cooling and shock passing. All signals were acquired at a sampling rate of 500 kHz and a cut-off frequency of 100 kHz. The gain setting on the 2310 Measurement Group strain gauge amplifier and signal conditioner was set to a value of 10 to avoid strong interference in the frequency range up to 100 kHz. The gain setting of the *Vatell Amplifiers 6* was 100 and was assumed not to have any significant influence in this frequency range. The data was treated according to the procedure presented in Sections 3.4.2 and 3.4.1.

Only signals from gauges 1 and 2 were recorded. Three experiments were done, run #1 and #2 with film cooling at nominal conditions and run #3 without film cooling. The conditions for the different runs are shown in Table 3.11 and the conditions at shock impact are shown in Table 3.12.

Table 3.11: Test Matrix and Parameters for All Runs and Gauges 1 and 2 for "Direct Comparison"

Run #	Shock Strength $\frac{p + p'_{max}}{p}$	$\frac{p_c}{p_\infty}$ [-]	h_1 $[\frac{W}{m^2 \cdot K}]$	h_2 $[\frac{W}{m^2 \cdot K}]$	η_1 [-]	η_2 [-]
1	1.32	1.04	862	795	0.30	0.18
2	1.32	1.04	775	800	0.33	0.19
3	1.32	na	666	690	na	na

Table 3.12: Conditions at Shock Impact for All Runs and Gauges 1 and 2 for "Direct Comparison"

Run #	T_i [°C]	T_c [°C]	T_{r1} [°C]	T_{r2} [°C]	T_{aw1} [°C]	T_{aw2} [°C]	T_{w1} [°C]	T_{w2} [°C]	T_{s1} [°C]	T_{s2} [°C]
1	70.0	-103.0	64.1	64.9	14.0	34.7	8.2	10.5	58.1	56.1
2	75.1	-139.0	69.2	70.0	0.5	30.3	-4.3	-1.0	60.0	58.5
3	79.3	na	73.4	74.2	73.4	74.2	27.4	27.1	64.2	62.5

If Moss' conclusion holds true for heat transfer with shock passing and film cooling, the following procedure should provide a good prediction of the unsteady

heat transfer:

1. From the ratio of unsteady static pressure over mean static pressure before shock impact, calculate a variation of unsteady temperature, assuming an isentropic compression. The temperature that this compression is applied to has to be the static freestream temperature (see in Table 3.12). Even though Moss does not specifically elaborate as to which temperature he is applying the compression to, it surely has to be the static temperature, since it is calculated using the static pressure.

$$\frac{T_s + T_i}{T_s} = \left(\frac{p + p'}{p} \right)^{\frac{\gamma-1}{\gamma}} \quad (3.30)$$

Or rearranged:

$$T_i = T_s \cdot \left(\left(\frac{p + p'}{p} \right)^{\frac{\gamma-1}{\gamma}} - 1 \right) \quad (3.31)$$

2. So the static freestream temperature is calculated from the freestream total temperature and the Mach Number derived from the ratio of mean local static pressure and freestream total pressure. Then the unsteady variation of static temperature is known.
3. This unsteady temperature variation is multiplied by the steady heat transfer coefficient to yield the predicted unsteady heat flux according to Moss' conclusion.

$$q = h \cdot T_s \cdot \left(\left(\frac{p + p'}{p} \right)^{\frac{\gamma-1}{\gamma}} - 1 \right) \quad (3.32)$$

In a sense, this method can be looked at as an extension of the decomposition technique layed out in Section 3.5.2. There, the unsteady heat flux was decomposed into its different components, and it was concluded that all components containing H were negligible. Then, Equations 3.11 and 3.18 were used to calculate the unsteady variation of temperature from the measured heat flux. No explanation was given for these temperature variations. Moss' conclusion leading to Equation 3.32 is an attempt to explain the temperature variation and predict the the unsteady heat transfer.

This technique will be illustrated using data from gauge # 2 and uncooled run # 3. The data from all three runs and two gauges will be presented in Figures 3.41 through 3.43. The raw traces of pressure and heat flux before any signal processing are shown in Figure 3.38. Both traces are shown in the same graph to facilitate comparison. In this graph, it seems that both traces are similar in shape, and a

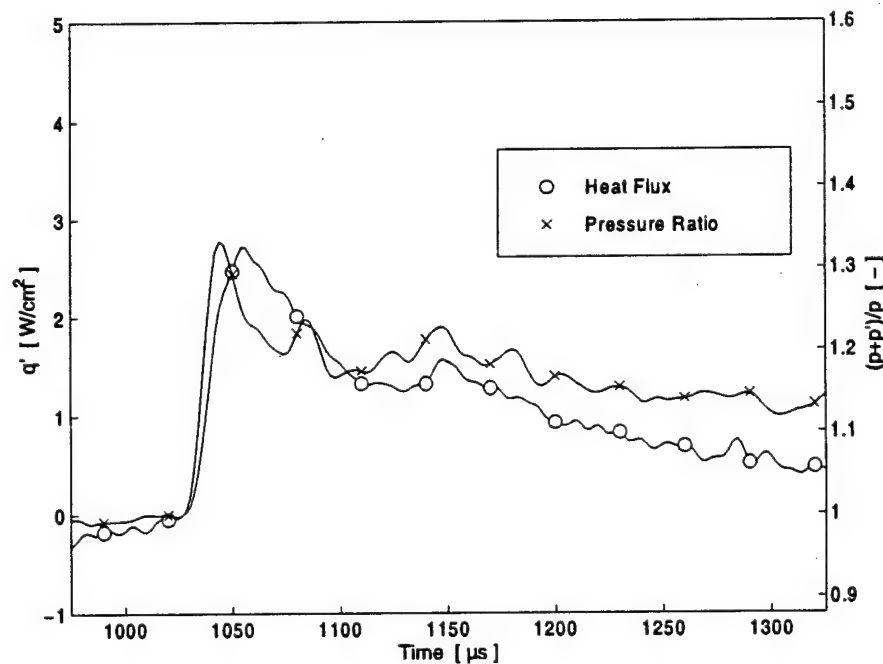


Figure 3.38: Shock Passing Event for Gauge # 2 from Uncooled Run #3. Raw Signals of Pressure Ratio and Unsteady Heat Flux.

prediction of heat flux from pressure may easily be possible. The data needs to

be treated according to the procedure explained in Sections 3.4.2 and 3.4.1. The influence of the transfer functions of both transducers is too significant to be ignored in this analysis. The traces after the correction are shown in Figure 3.39. The scales

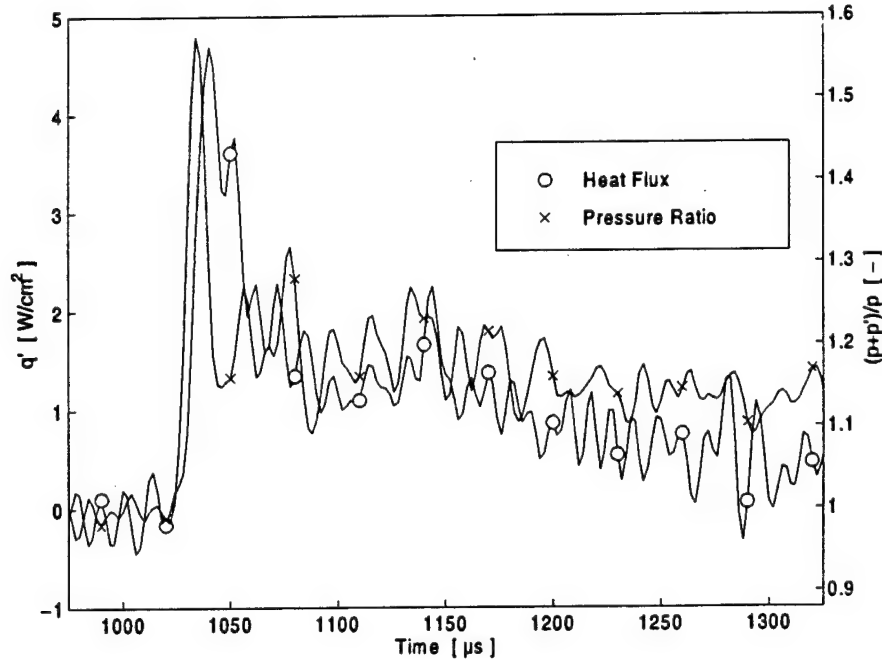


Figure 3.39: Shock Passing Event for Gauge # 2 from Uncooled Run #3. Processed Signals of Pressure Ratio and Unsteady Heat Flux.

in Figures 3.38 and 3.39 are identical in order to illustrate the significance of the data correction applied. The magnitudes and shapes differ strongly between the two figures. Still, the general shapes of the two curves seem comparable.

In Figure 3.40 the corrected measured heat flux and the predicted heat flux according to Equation 3.32 are compared. The order of magnitude of heat transfer is well predicted as is the general trend. On the other hand, the match is not close enough to attribute all the unsteady heat transfer to the temperature variation shown here. Figures 3.41 through 3.43 show different degrees of agreement between the prediction and the actual heat flux. The model works with varying degrees of success. This is certainly due in part to remaining uncertainties in the dynamic

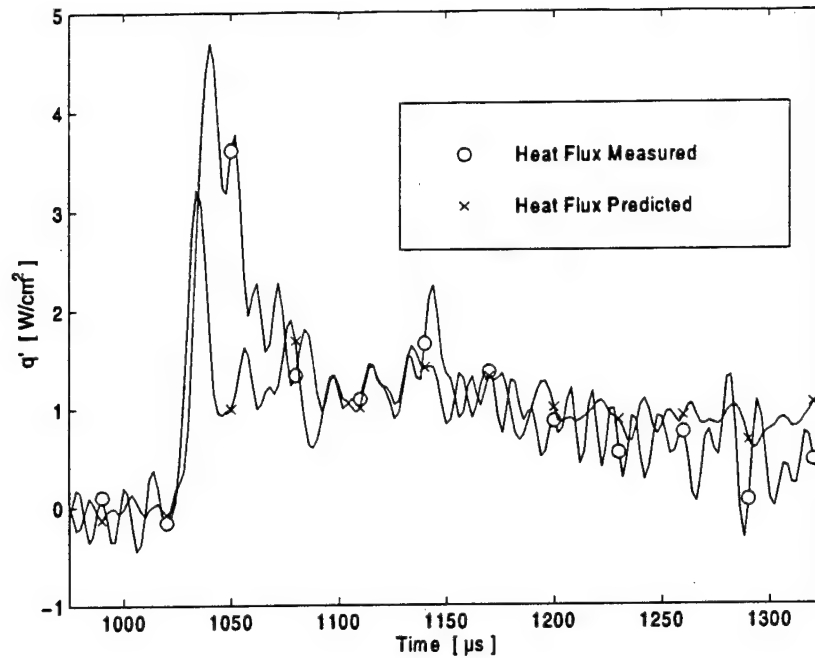


Figure 3.40: Shock Passing Event for Gauge # 2 from Uncooled Run #3. Predicted and Measured Unsteady Heat Flux.

characterization of the sensors.

Generally speaking, the model provides a good prediction of heat flux taking into account its simplicity. It is, therefore, valid to say that it supports the conclusions drawn in Section 3.5.2 in that it assumes a constant heat transfer coefficient. This coincides with the conclusion that h is negligible.

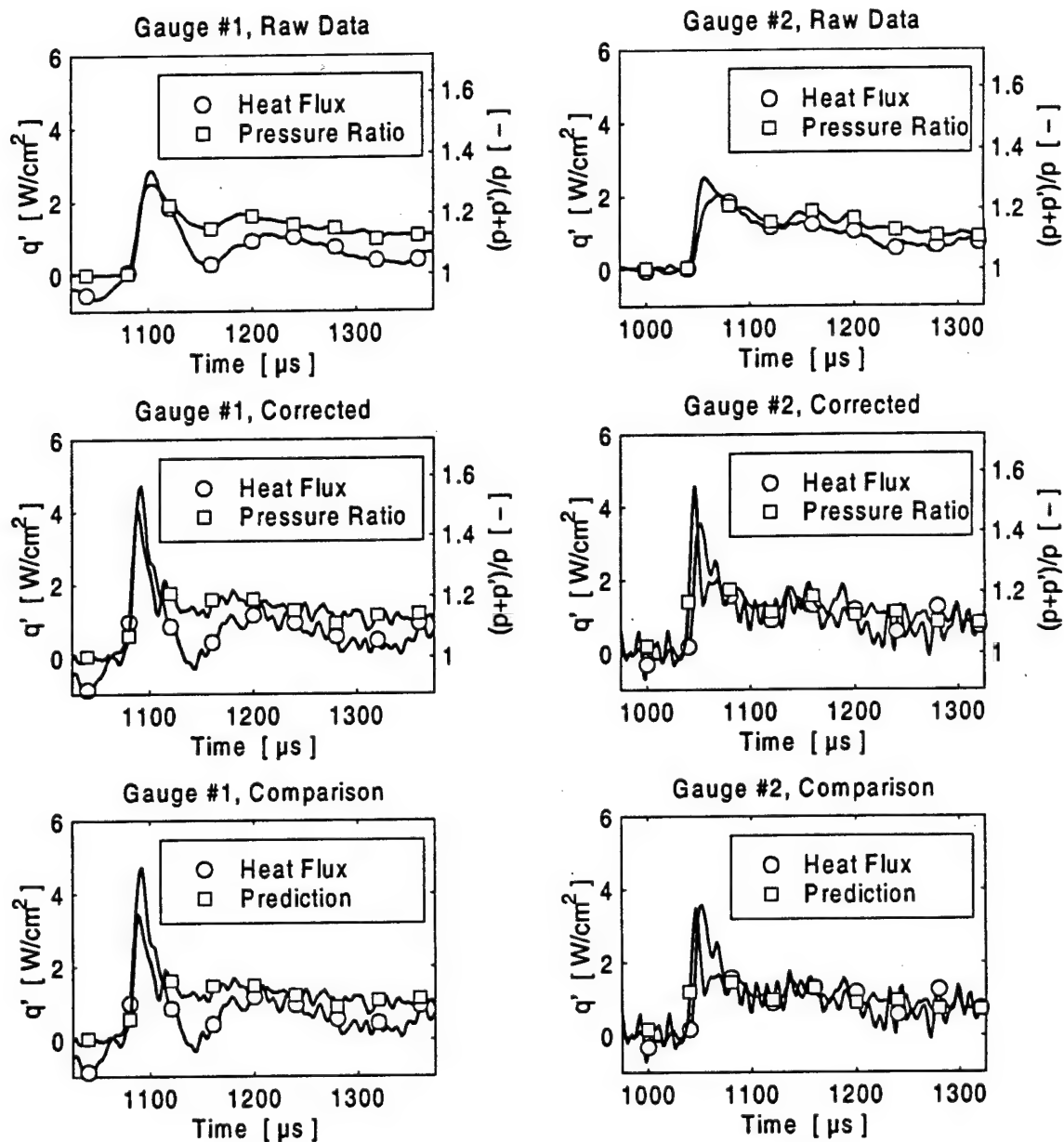


Figure 3.41: Shock Passing Event from Run #1 with Film Cooling. Moss' Model And Comparison with Data.

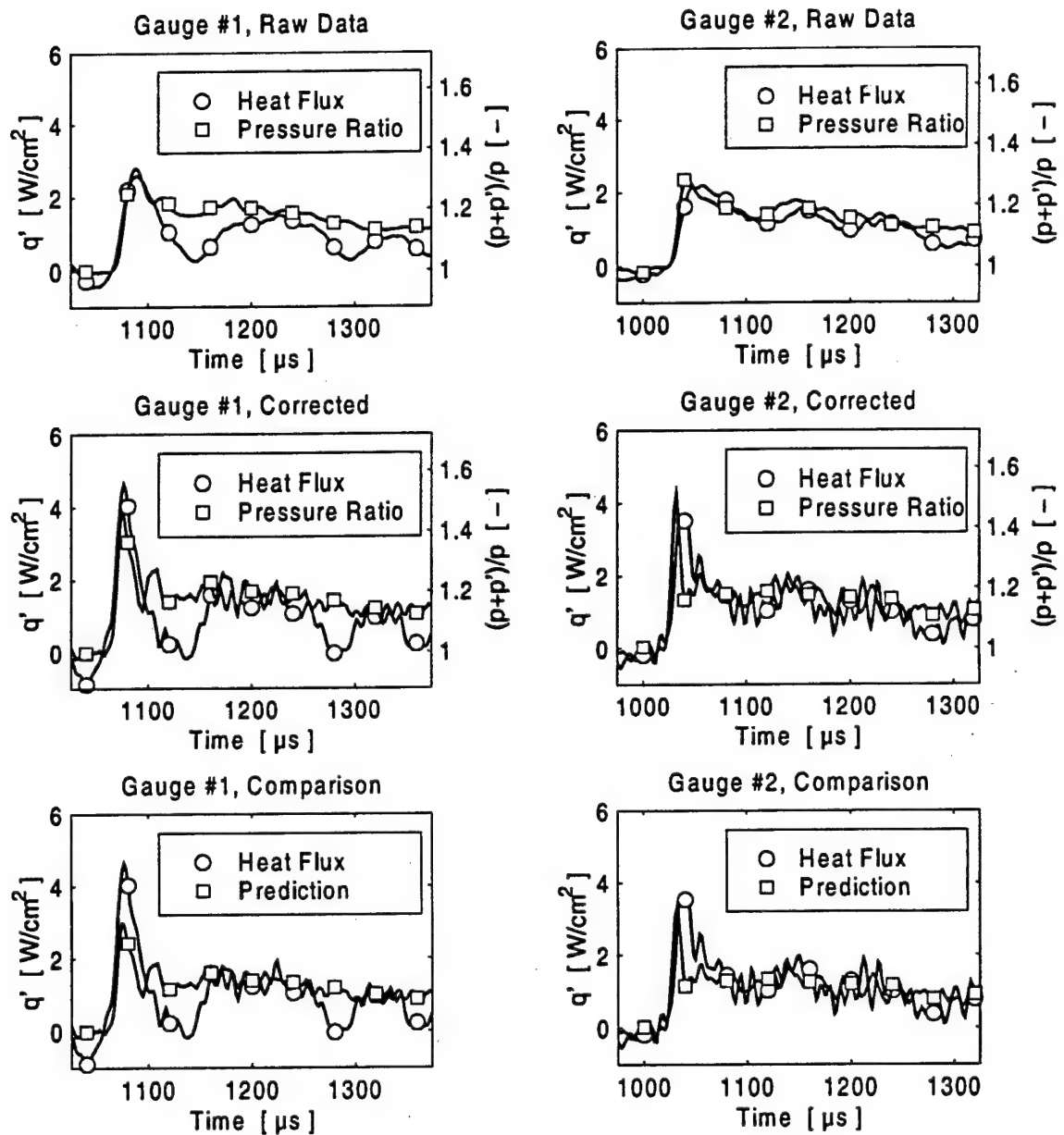


Figure 3.42: Shock Passing Event from Run #2 with Film Cooling. Moss' Model And Comparison with Data.

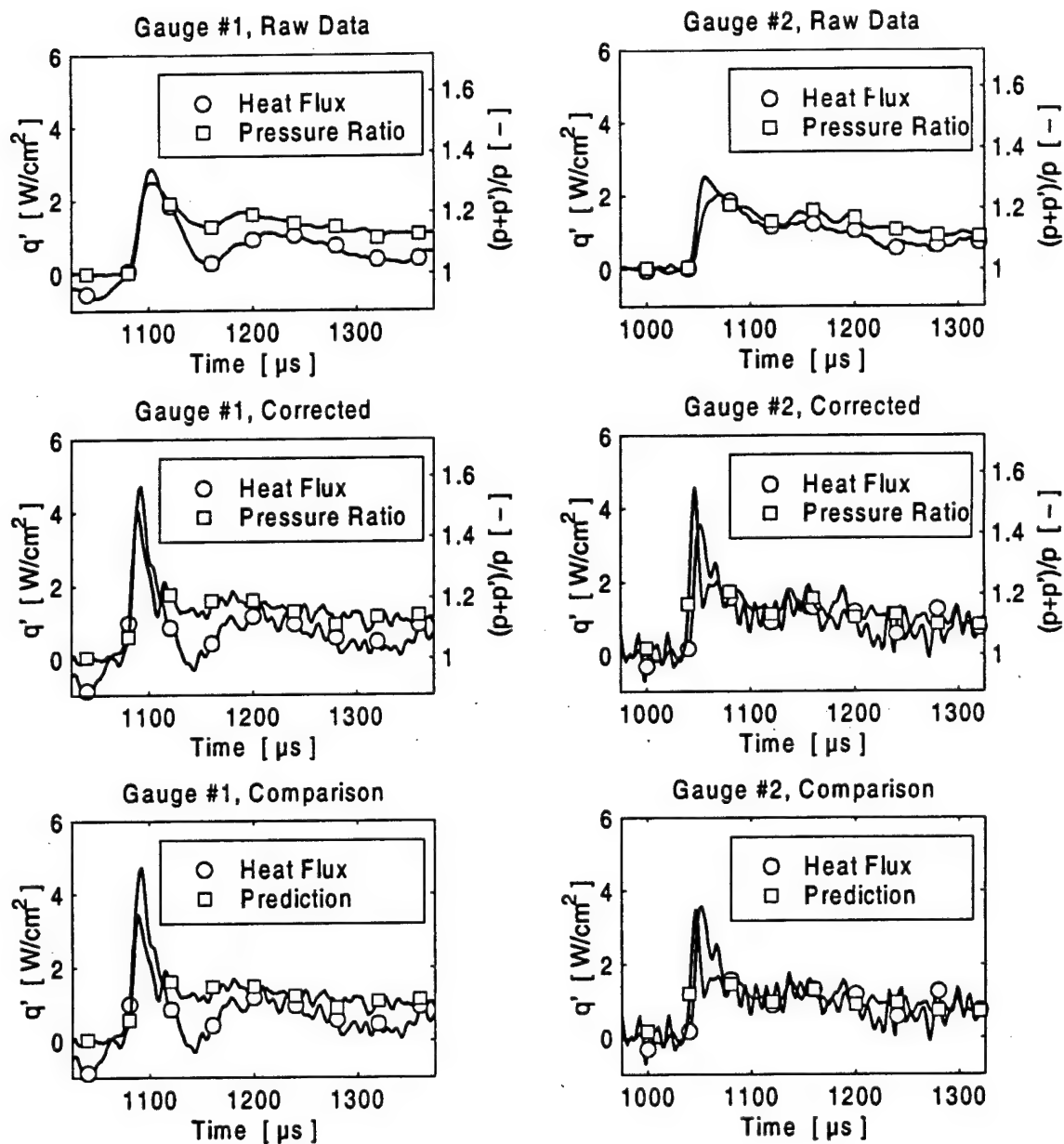


Figure 3.43: Shock Passing Event from Run #3 without Film Cooling. Moss' Model And Comparison with Data.

3.5.3.2 Johnson's Model

A large amount of work has been published by A.B. Johnson's team at Oxford University. They approached similar issues to the ones presented in this dissertation, but they do so in a quite different manner. Instead of the shock tube arrangement used here, they built a rotating bar mechanism to produce shock waves and wakes to interact with the rotor blades in a linear cascade. They measured the unsteady heat transfer and surface pressure. In Johnson et al. (1988) they published a theoretical model of the unsteady heat transfer and compared it to their data. This model will be applied to the data taken for this work. Even though the experiments done in Oxford did not involve film cooling, the model should still be applicable because of its many simplifications.

The data used for this comparison is the same that was used in Section 3.5.3.1 for comparison with Moss' Model and was treated the same way before use in the analysis.

After simplifying the energy equation including first order perturbations down to the one-dimensional heat conduction equation, Johnson finds the general solution of the surface heat flux in the Laplace domain to be:

$$\overline{q_u} = \sqrt{\rho \cdot c_p \cdot k_{equiv}} \cdot \overline{T_g} \cdot \sqrt{s} \quad (3.33)$$

This is Equation (14) in Johnson et al. (1988). The overline over a function denotes its Laplace transform, T_g denotes some kind of unsteady near wall temperature history and s is the Laplace variable. The term $\sqrt{\rho \cdot c_p \cdot k_{equiv}}$ refers to a weighted product taking into account the thermal product, β , of the gas and the surface material.

$$\sqrt{\rho \cdot c \cdot k_{equiv}} = \frac{\sqrt{\rho \cdot c \cdot k_s} \cdot \sqrt{\rho \cdot c_p \cdot k_g}}{\sqrt{\rho \cdot c \cdot k_s} + \sqrt{\rho \cdot c_p \cdot k_g}} \quad (3.34)$$

The subscript "g" describes the gas properties ($\beta_g = 6.98 \frac{kg}{K \cdot s^2 \cdot \sqrt{s}}$). The subscript "s" refers to the material of the surface that the heat flux is transferred to, in our case the *Vatell HFM-7/L* heat flux sensor ($\beta_s = 21551.4 \frac{kg}{K \cdot s^2 \cdot \sqrt{s}}$). Therefore, $\beta_{equiv} = \beta_g$ without any significant error. The gas temperature fluctuation is then calculated from the surface static pressure data assuming an isentropic compression. The assumption of an isentropic compression is valid for relatively weak shocks as the ones used in Johnson et al. (1988) and in this investigation. As the base temperature for the calculation of T_g , the freestream static temperature T_s will be used as determined in Section 3.5.3.1:

$$T_g = T_s \cdot \left(\left(\frac{p+p'}{p} \right)^{\frac{\gamma-1}{\gamma}} - 1 \right) \quad (3.35)$$

The method will be presented using the data from gauge #1 and uncooled run #3 according to Tables 3.11 and 3.12 in Section 3.5.3.1. The pressure trace from this experiment and gauge are shown again in Figure 3.44 along with the gas temperature calculated using the isentropic assumption. The discrete temperature history shown in Figure 3.44 can now be decomposed into linear components according to:

$$T(t) = \sum_{n=3}^m \frac{T_n - 2 \cdot T_{n-1} + T_{n-2}}{\Delta t} \cdot (t - t_{n-1}) \quad \text{with:} \quad t_{m-1} < t \quad (3.36)$$

Here, it is assumed that the time series starts at $n = 1$ and $t_1 = 0$. It is also assumed that the first two values of gas temperature are zero. T_g was replaced by T

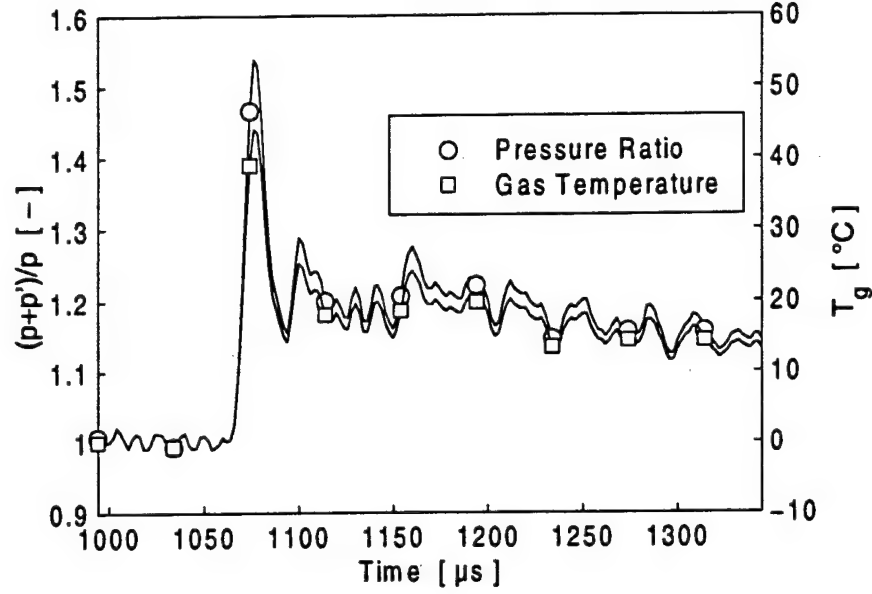


Figure 3.44: Shock Passing Event for Gauge # 1 from Uncooled Run #3. Pressure Ratios and Isentropic Gas Temperature. Pressure Signal Corrected According to Section "Signal Processing" 3.4.

for simplicity. Δt is the time interval between two data points. Equation 3.36 can be transformed into the Laplace domain:

$$\overline{T(t)} = \sum_{n=3}^m \frac{T_n - 2 \cdot T_{n-1} + T_{n-2}}{\Delta t} \cdot \frac{1}{s^2} \cdot e^{-t_{n-1} \cdot s} \quad \text{with: } t_{m-1} < t \quad (3.37)$$

By replacing $\overline{T_g}$ in Equation 3.33 by $\overline{T(t)}$ from Equation 3.37 an expression for the heat flux in the Laplace domain is found:

$$\overline{q_u} = \beta_g \cdot \sum_{n=3}^m \frac{T_n - 2 \cdot T_{n-1} + T_{n-2}}{\Delta t} \cdot \frac{1}{s \cdot \sqrt{s}} \cdot e^{-t_{n-1} \cdot s} \quad (3.38)$$

$\sqrt{\rho \cdot c_p \cdot k_g}$ was replaced by β_g for simplicity. Retransformation into the time domain yields the following expression for the heat flux:

$$q_u(t) = 2 \cdot \beta_g \cdot \sum_{n=3}^m \frac{T_n - 2 \cdot T_{n-1} + T_{n-2}}{\Delta t} \cdot \sqrt{\frac{t - t_{n-1}}{\pi}} \quad \text{with: } t_{m-1} < t \quad (3.39)$$

Or discretized:

$$q_u(t_m) = 2 \cdot \beta_g \cdot \sum_{n=3}^m \frac{T_n - 2 \cdot T_{n-1} + T_{n-2}}{\Delta t} \cdot \sqrt{\frac{t_m - t_{n-1}}{\pi}} \quad (3.40)$$

And simplified:

$$q_u(t_m) = \frac{2 \cdot \beta_g}{\sqrt{\pi} \cdot \Delta t} \sum_{n=3}^m (T_n - 2 \cdot T_{n-1} + T_{n-2}) \cdot \sqrt{m - n + 1} \quad (3.41)$$

This Equation is similar to Equation (18) of Johnson et al. (1988). The difference is that in Johnson's approach T_{i+1} is predicted from T_i and T_{i-1} while in the model developed here T_i is predicted from T_{i-1} and T_{i-2} . This slight change makes it easier to use with *Matlab* or *Mathematica* and gives the exact same results. For a more complete discussion of the different discretization schemes for Equation 3.33, refer to Appendix F.

Treating the data shown in Figure 3.44 according to Equation 3.41 and using $\beta_g = 6.98 \frac{\text{kg}}{\text{K} \cdot \text{s}^2 \cdot \sqrt{\text{s}}}$ yields the trace of heat flux q_u shown in Figure 3.45. The two traces

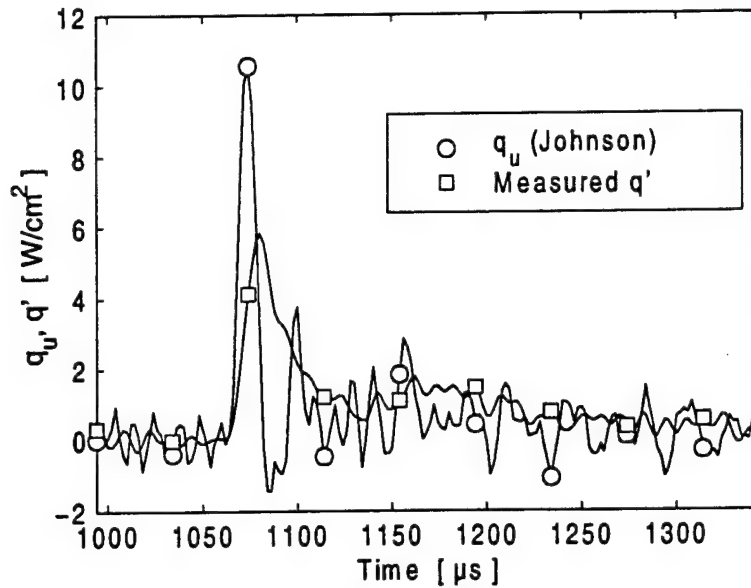


Figure 3.45: Shock Passing Event for Gauge # 1 from Uncooled Run #3. q_u According to Johnson et al. (1988). Heat Flux Signal Corrected According to Section "Signal Processing" 3.4.

do not compare well.

Johnson derives a second component of unsteady heat flux which is due to the change of thickness of the boundary layer. Even though this second component of unsteady heat flux was derived for a shock impinging normally to the surface, Johnson applied the method to locations on the blade where the shock passes tangentially rather than impinging normally. That justifies the use of this model in the present situation.

The second component of unsteady heat flux due to boundary layer compression is calculated according to Equation (16) of Johnson et al. (1988).

$$q_m = q \cdot \left(\frac{p+p'}{p} \right)^{\frac{1}{7}} \quad (3.42)$$

The underlying idea is that the thickness of the boundary layer scales proportionally with the change of density. Figure 3.46 shows the trace of q_m for the experiment presented here. q_m depends on the mean level of heat flux before the shock impact

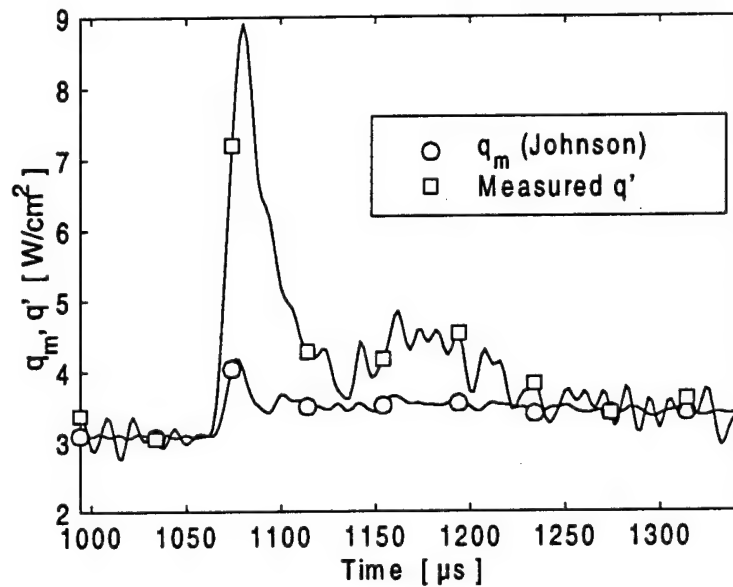


Figure 3.46: Shock Passing Event for Gauge # 1 from Uncooled Run #3. q_m According to Johnson et al. (1988). Heat Flux Signal Corrected According to Section "Signal Processing" 3.4.

q . The magnitudes of the unsteady component of q_m are small compared to the measured unsteady heat flux or compared to the heat flux due to the temperature change q_u . The reason for this lies in the fact that the boundary layer does not change significantly because the density does not vary much.

According to Johnson, the overall unsteady heat flux can be predicted by the sum of q_u and q_m . In Figure 3.47 this predicted heat flux and the measured

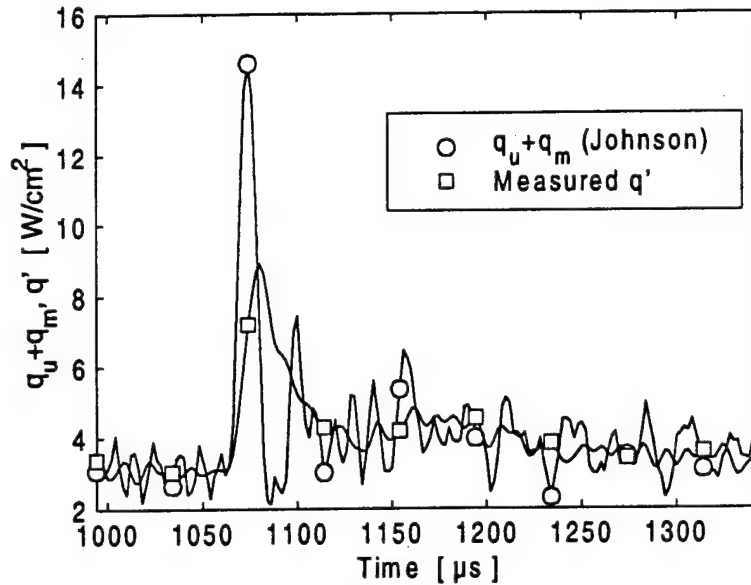


Figure 3.47: Shock Passing Event for Gauge # 1 from Uncooled Run #3. Comparison Between $q_u + q_m$ and q' . Heat Flux Signal Corrected According to Section "Signal Processing" 3.4

heat flux are shown on the same axis for comparison. Figure 3.47 shows that the prediction according to Johnson does not represent the measured data well. The prediction according to Moss et al. (1997) presented in Section 3.5.3.1 shows much better agreement. It must be stated that the agreement was not overwhelming even in the original publication by Johnson et al. (1988). Also, the data compared in Johnson et al. (1988) was filtered at 30 kHz, which brings with it a considerable loss of information and makes the comparison somewhat difficult.

The results of Johnson's prediction can be compared with the decomposition technique developed in Section 3.5.2. The pressure traces for each gauge are very much alike for all run conditions with the same shock strength. That means that q_u will look similar for all runs at a certain shock strength. The only scaling factor will be the freestream temperature. Since this temperature does not vary significantly on the Kelvin scale, the influence will be minor. In other words q_u represents the fraction

of unsteady heat flux not related to the initial level of heat flux, or:

$$q_u \approx h \cdot T_r \quad (3.43)$$

The component of predicted heat flux that does scale with the heat flux before shock impact is q_m . Therefore, it can be compared to $H \cdot (T_r - T_w)$ from the decomposition technique:

$$q_m \approx q + H \cdot (T_r - T_w) \quad (3.44)$$

Figure 3.46 shows that this component is relatively small compared to the overall unsteady heat flux and compared to the initial level of heat flux. This indicates that H is relatively small and the unsteady component of q_m can be neglected. In this case, q_u is the prediction for q' . According to Equation 3.43 this unsteady heat flux is linearly related to a variation of recovery temperature T_r . Then T_r would have to take the shape of q_u in Figure 3.45. It is not very likely that any temperature would vary in this way under the influence of a shock wave as seen in Figure 3.44. Therefore, it can be suggested that Johnson's Model does not reflect the physical event. Moss' model, on the other hand, does describe the physics of the shock passing with the assumption (and conclusion) that H is negligible. The resulting traces of T_r seemed physically reasonable.

Figures 3.48 through 3.50 present all data from all gauges and experiments treated according to the method presented in this Section. The comparison is similar for all the data taken and the same conclusions can be drawn.

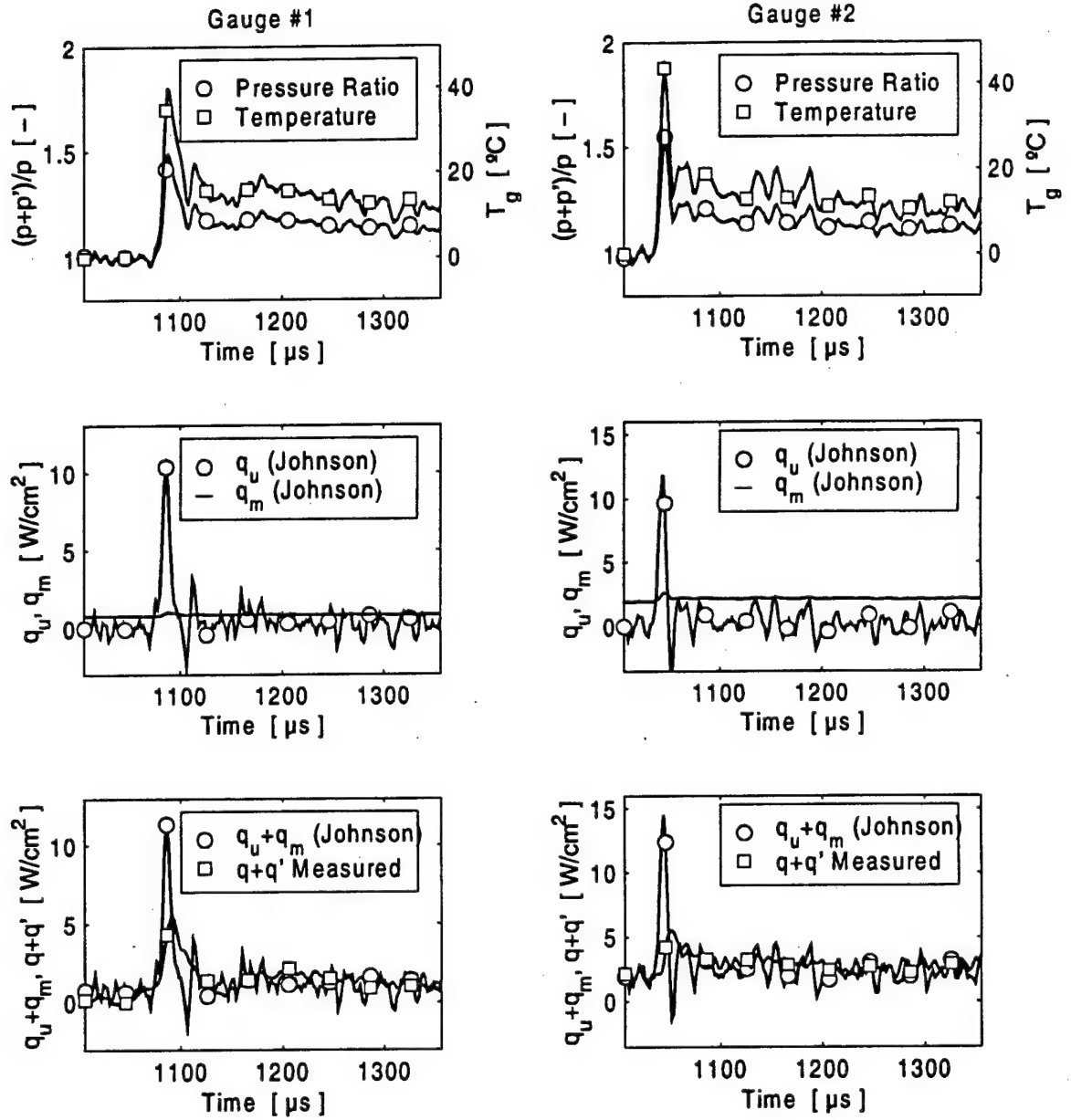


Figure 3.48: Shock Passing Event from Run #1 With Film Cooling. Johnson's Model And Comparison with Data. Pressure and Heat Flux Signals Corrected According to Section "Signal Processing" 3.4.

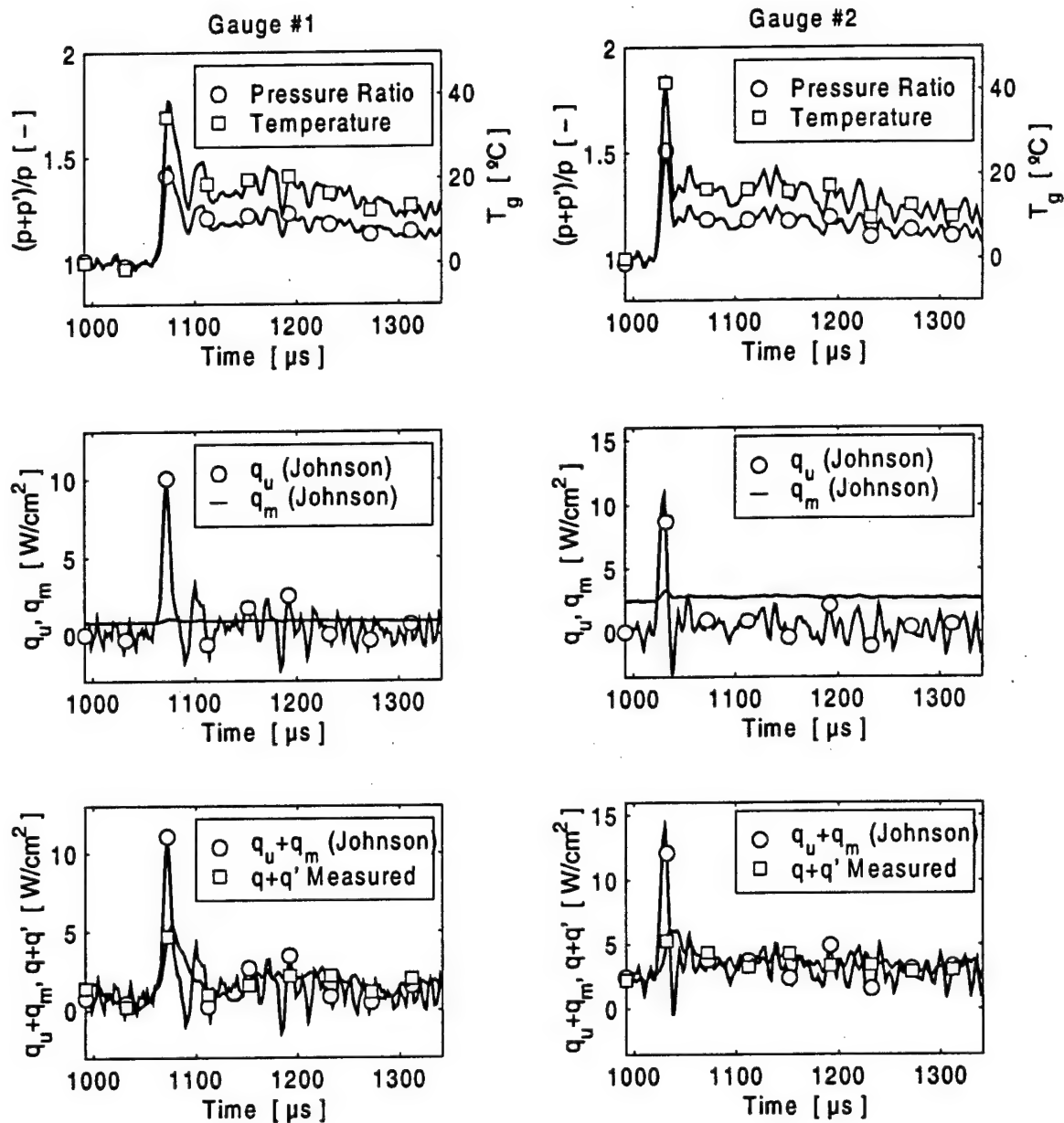


Figure 3.49: Shock Passing Event from Run #2 With Film Cooling. Johnson's Model And Comparison with Data. Pressure and Heat Flux Signals Corrected According to Section "Signal Processing" 3.4.

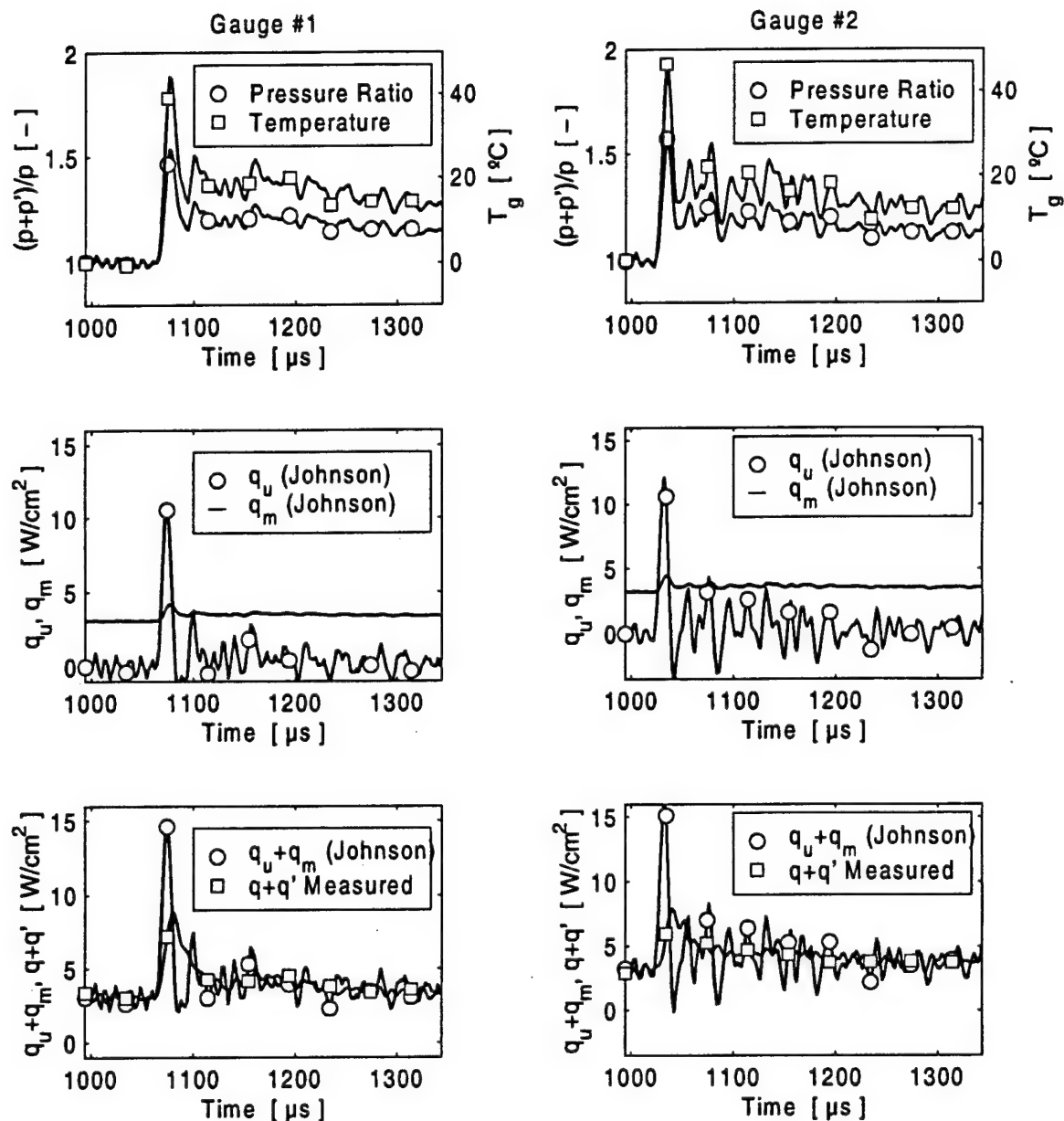


Figure 3.50: Shock Passing Event from Run #3 Without Film Cooling. Johnson's Model And Comparison with Data. Pressure and Heat Flux Signals Corrected According to Section "Signal Processing" 3.4.

3.5.3.3 Rigby's Model

In 1989 Rigby et al. (1989) published a modified version of Johnson's Model. In this publication, they provide a more thorough derivation of the equations. The final equations are slightly different from the ones published in Johnson et al. (1988). This model will be presented here and compared to the data. The derivation given in Rigby et al. (1989) will be presented for completeness.

The derivation refers to the situation depicted in Figure 3.51. The situation

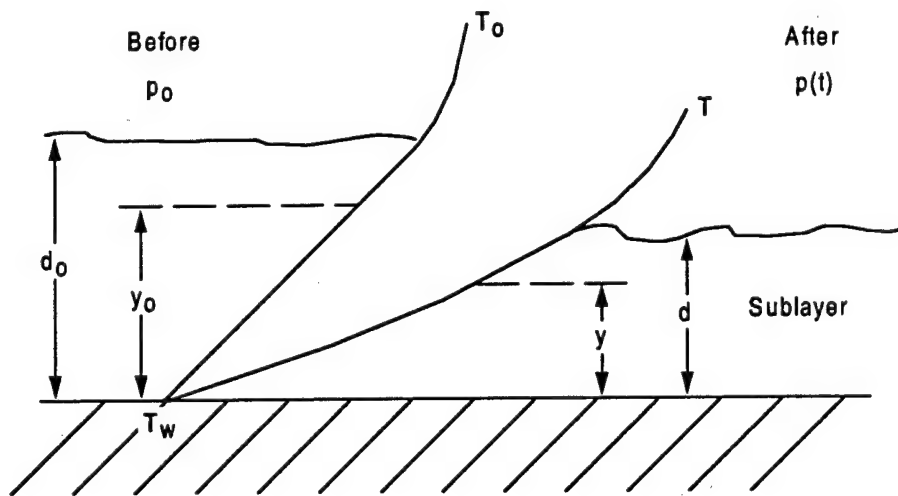


Figure 3.51: Change in Laminar Sublayer Temperature Profile from T_0 to T Due to Compression and Heating Induced by Pressure Change. From Rigby et al. (1989).

"Before" depicts an undisturbed flow field with a steady state boundary layer. The situation "After" shows an arbitrary point in time after the flow field has been disturbed by a pressure variation. The boundary layer thickness varies with the pressure and so is the position of any portion of fluid with respect to the wall ($d_0 \rightarrow d$ and $y_0 \rightarrow y$). The temperature profile is changed from T_0 to $T(y, t)$. The derivation is restricted to the laminar sub-layer shown in this Figure. The pressure fluctuations depicted in Figure 3.51 act simultaneously throughout the sub-layer. A linear

temperature profile is assumed prior to any perturbations:

$$T_o(y) = T_w + \frac{q}{k} \cdot y \quad (3.45)$$

The wall temperature is assumed to be constant. The temperature profile after a pressure perturbation $p(t)$ is now decomposed in two contributions:

$$T(y, t) = T_c(y, t) + T_h(y, t) \quad (3.46)$$

$T_c(y, t)$ is a temperature time history that is the result of the pressure fluctuation only. The pressure variation acts in the entire flow field as an isentropic compression.

$$T_c(y, t) = T_o(y) \cdot \left(\frac{p + p'}{p} \right)^{\frac{\gamma-1}{\gamma}} \quad (3.47)$$

The density in the sublayer changes according to:

$$\frac{\rho + \rho'}{\rho} = \left(\frac{p + p'}{p} \right)^{\frac{1}{\gamma}} \quad (3.48)$$

Therefore, the gas that is in a location y after the compression was originally at a position y_0 :

$$y_0 = y \cdot \left(\frac{p+p'}{p} \right)^{\frac{1}{\gamma}} \quad (3.49)$$

Replacing 3.49 in 3.45 and substituting the result in 3.47 yields for T_c :

$$T_c = T_w \cdot \left(\frac{p+p'}{p} \right)^{\frac{\gamma+1}{\gamma}} + \frac{q}{k} \cdot y \cdot \left(\frac{p+p'}{p} \right) \quad (3.50)$$

Therefore:

$$q = k \cdot \left. \frac{\partial T_c}{\partial y} \right|_{y=0} = q \cdot \left(\frac{p+p'}{p} \right) \quad (3.51)$$

$T_h(y, t)$ is the part of the temperature time history that is only due to transient conduction in the fluid. It is only significant close to the wall, where the conduction becomes important since the wall temperature stays constant. Outside of the sublayer, $T_h(y > d, t) = 0$. In order to determine the solution for this part of the temperature profile, Rigby et al. (1989) derive a differential temperature boundary layer equation from the unsteady Navier-Stokes viscous energy equation for the situation depicted in 3.51. They assume k to be constant and neglect viscous terms to arrive at:

$$\rho \cdot c_p \cdot v \cdot \frac{\partial T}{\partial y} + \rho \cdot c_p \cdot \frac{\partial T}{\partial t} = k \cdot \frac{\partial^2 T}{\partial y^2} + \frac{\partial p}{\partial t} \quad (3.52)$$

The velocity in the y-direction v is derived using Equation 3.49:

$$v = \frac{\partial y}{\partial t} = -\frac{1}{\gamma} \cdot \frac{y}{p+p'} \cdot \frac{\partial p'}{\partial t} \quad (3.53)$$

Substituting v and using the relations for a thermally and calorically perfect gas they arrive at:

$$\frac{\partial T}{\partial t} = \frac{1}{\alpha} \cdot \frac{\partial^2 T}{\partial y^2} + \frac{1}{\gamma \cdot (p+p')} \cdot \frac{\partial p'}{\partial t} \cdot \left[y \cdot \frac{\partial T}{\partial y} + (\gamma - 1) \cdot T \right] \quad (3.54)$$

The first term on the right hand side of Equation 3.54 is of the order of y^{-2} and outweighs the second term which is on the order of y^0 close to the wall. Then the second term may be dropped when stating the differential equation for $T_h(y, t)$ only ($T_c(y, t)$ and $T_h(y, t)$ superimpose linearly so each of them has to be a solution to the differential equation):

$$\frac{\partial^2 T_h(y, t)}{\partial y^2} = \frac{1}{\alpha} \cdot \frac{\partial T_h(y, t)}{\partial t} \quad (3.55)$$

This Equation is identical to the one-dimensional heat conduction equation (see discussion in Appendix F). Transforming 3.55 into the Laplace domain yields:

$$\frac{\partial^2 \bar{T}_h(y, s)}{\partial y^2} = \frac{s}{\alpha} \cdot \bar{T}_h(y, s) \quad (3.56)$$

The general solution to 3.56 is:

$$\bar{T}_h(y, s) = A \cdot e^{\sqrt{\frac{\gamma}{\alpha}} y} + B \cdot e^{-\sqrt{\frac{\gamma}{\alpha}} y} \quad (3.57)$$

The first boundary condition is that $T_h(y, t)$ becomes zero far away from the wall. Therefore A in Equation 3.57 has to be zero. The second boundary condition comes from Equation 3.46 at the wall:

$$\begin{aligned} T(0, t) &= T_c(0, t) + T_h(0, t) \\ T_w &= T_w \cdot \Pi(t) + T_h(0, t) \end{aligned} \quad (3.58)$$

Where:

$$\Pi(t) = \left(\frac{p+p'}{p} \right)^{\frac{\gamma-1}{\gamma}} \quad (3.59)$$

Then:

$$T_h(0, t) = T_w \cdot (1 - \Pi(t)) \quad (3.60)$$

or in the Laplace domain:

$$\bar{T}_h(0, s) = T_w \cdot \overline{(1 - \Pi(t))} \quad (3.61)$$

Using this boundary condition and expressing Equation 3.57 at $y = 0$ leads to an equation for B (noting that $A = 0$):

$$\bar{T}_h(0, s) = T_w \cdot \overline{(1 - \Pi(t))} = B \quad (3.62)$$

Now the constants in Equation 3.57 are known and so is the solution for $\bar{T}_h(y, s)$:

$$\bar{T}_h(y, s) = T_w \cdot \overline{(1 - \Pi(t))} \cdot e^{-\sqrt{\frac{k}{\alpha}} \cdot y} \quad (3.63)$$

The surface heat flux caused by this temperature variation can be expressed as:

$$q_h(t) = -k \cdot \left. \frac{\partial T_h(y, s)}{\partial y} \right|_{y=0} \quad (3.64)$$

Or in the Laplace domain:

$$\bar{q}_h(s) = -k \cdot \left. \frac{\partial \bar{T}_h(y, s)}{\partial y} \right|_{y=0} \quad (3.65)$$

Taking the derivative of $\bar{T}_h(y, s)$ at $y = 0$ and substituting into Equation 3.65 yields:

$$\bar{q}_h(s) = \sqrt{k \cdot \rho \cdot c_p} \cdot T_w \cdot \overline{(1 - \Pi(t))} \cdot \sqrt{s} \quad (3.66)$$

With the following redefinition

$$\bar{g}(s) \equiv \overline{(1 - \Pi(t))} \cdot \sqrt{s} \quad (3.67)$$

Equation 3.66 can be restated:

$$\bar{q}_h(s) = \sqrt{k \cdot \rho \cdot c_p} \cdot T_w \cdot \bar{g}(s) \quad (3.68)$$

The heat flux at the wall can now be calculated according to:

$$q + q' = q + q_h = q \cdot \frac{p + p'}{p} + \sqrt{k \cdot \rho \cdot c} \cdot T_w \cdot g(t) \quad (3.69)$$

The differences between this Equation and Johnson's equation, shown in the last Section, are subtle. The first term on the right hand side of Equation 3.69, q , is very similar to the expression for q_m given by Johnson:

$$\begin{array}{ll} \text{Rigby:} & q = q \cdot \frac{p + p'}{p} \\ \text{Johnson:} & q_m = q \cdot \left(\frac{p + p'}{p} \right)^{\frac{1}{\gamma}} \end{array} \quad (3.70)$$

The second term on the right hand side of Equation 3.69, q_h , closely resembles q from Johnson's analysis. The only difference here is that while Johnson did not specify the

base temperature for the calculation of T_g , Rigby's model clearly specifies the use of the wall temperature for the calculation of T_g . In the analysis according to Johnson's model in Section 3.5.3.2, the freestream static temperature was used for lack of a better choice.

The model developed by Rigby will be compared with the data presented in the two preceding Sections 3.5.3.1 and 3.5.3.2. The parameters for the different experiments and the conditions before shock impact were shown in Section 3.5.3.1. The same discretization scheme used in Section 3.5.3.2 will be used to calculate the heat flux due to transient conduction q_h :

$$q_h(t_m) = \frac{2 \cdot \beta_g}{\sqrt{\pi} \cdot \Delta t} \cdot \sum_{n=3}^m (T_n - 2 \cdot T_{n-1} + T_{n-2}) \cdot \sqrt{m-n+1} \quad (3.71)$$

The temperature history T_i is calculated from

$$T = T_{wi} \cdot \left(\frac{p+p'}{p} \right)^{\frac{\gamma-1}{\gamma}} \quad (3.72)$$

The index i refers to gauge 1 or 2. The comparison between the prediction and the measured data is similar for Johnson's and Rigby's model. The shape and the magnitude of the measured data is not predicted nearly as well as with Moss' assumption of a constant heat transfer coefficient.

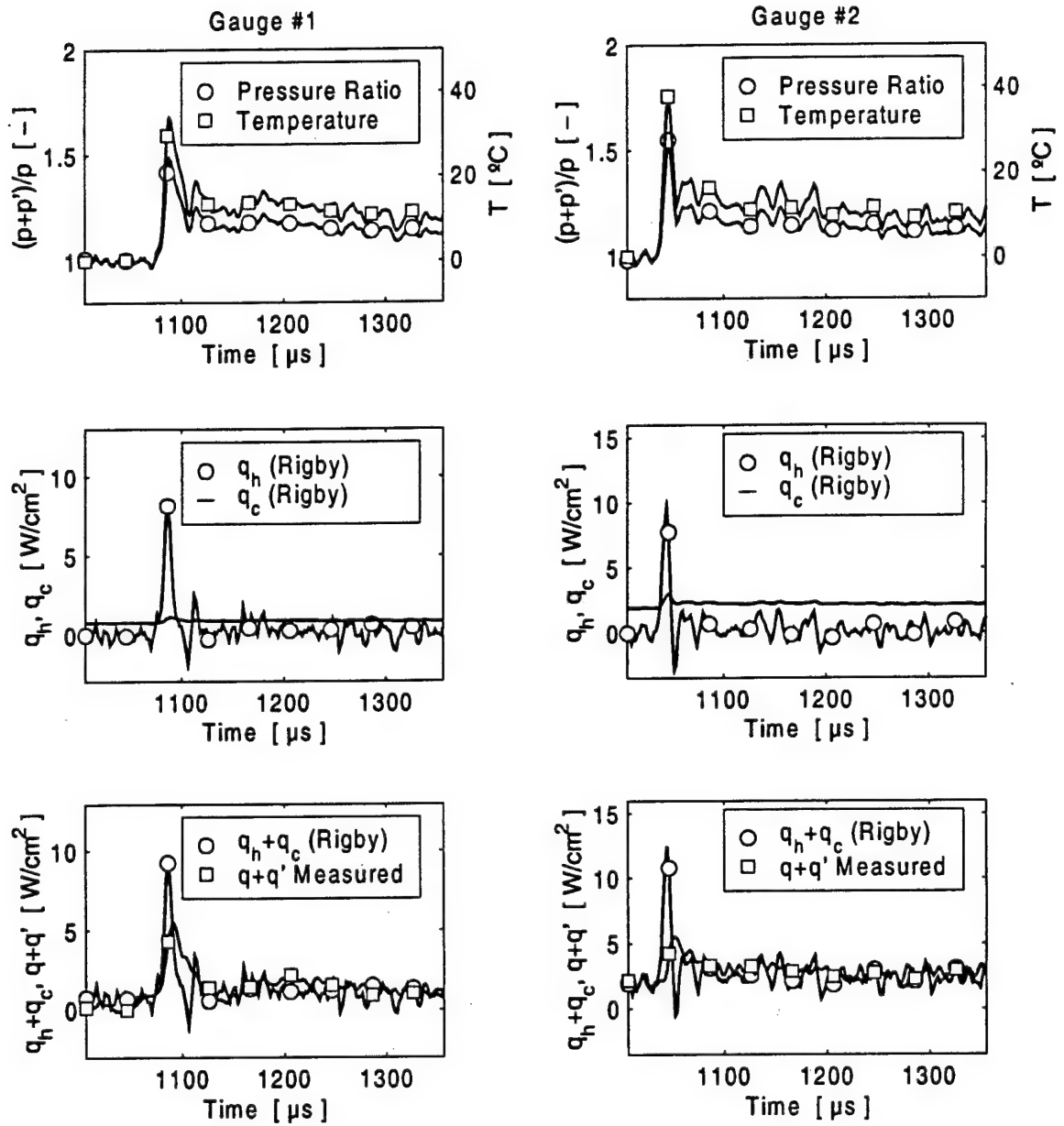


Figure 3.52: Shock Passing Event from Run #1 With Film Cooling. Rigby's Model And Comparison with Data. Pressure and Heat Flux Signals Corrected According to Section "Signal Processing" 3.4.

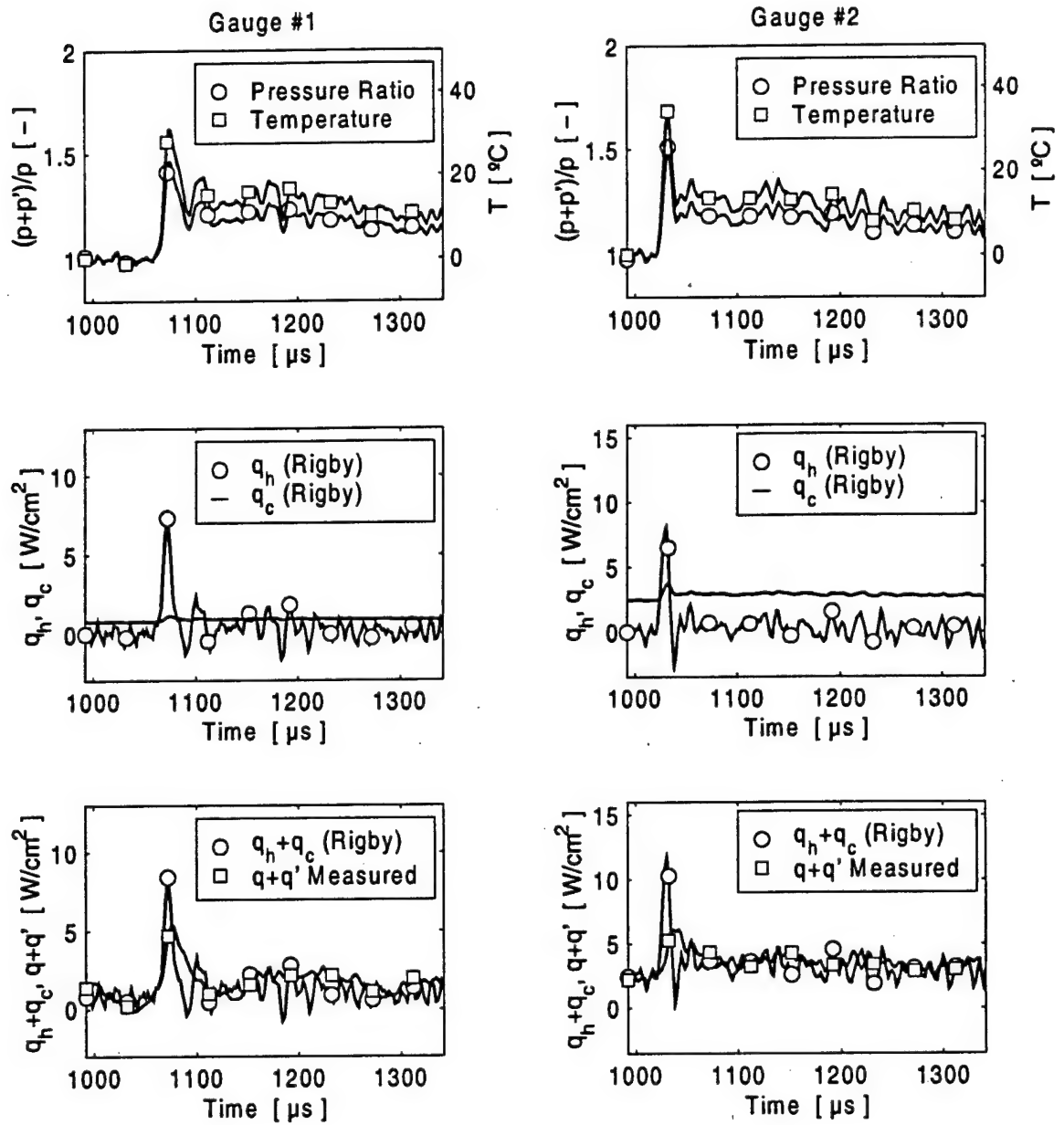


Figure 3.53: Shock Passing Event from Run #2 With Film Cooling. Rigby's Model And Comparison with Data. Pressure and Heat Flux Signals Corrected According to Section "Signal Processing" 3.4.

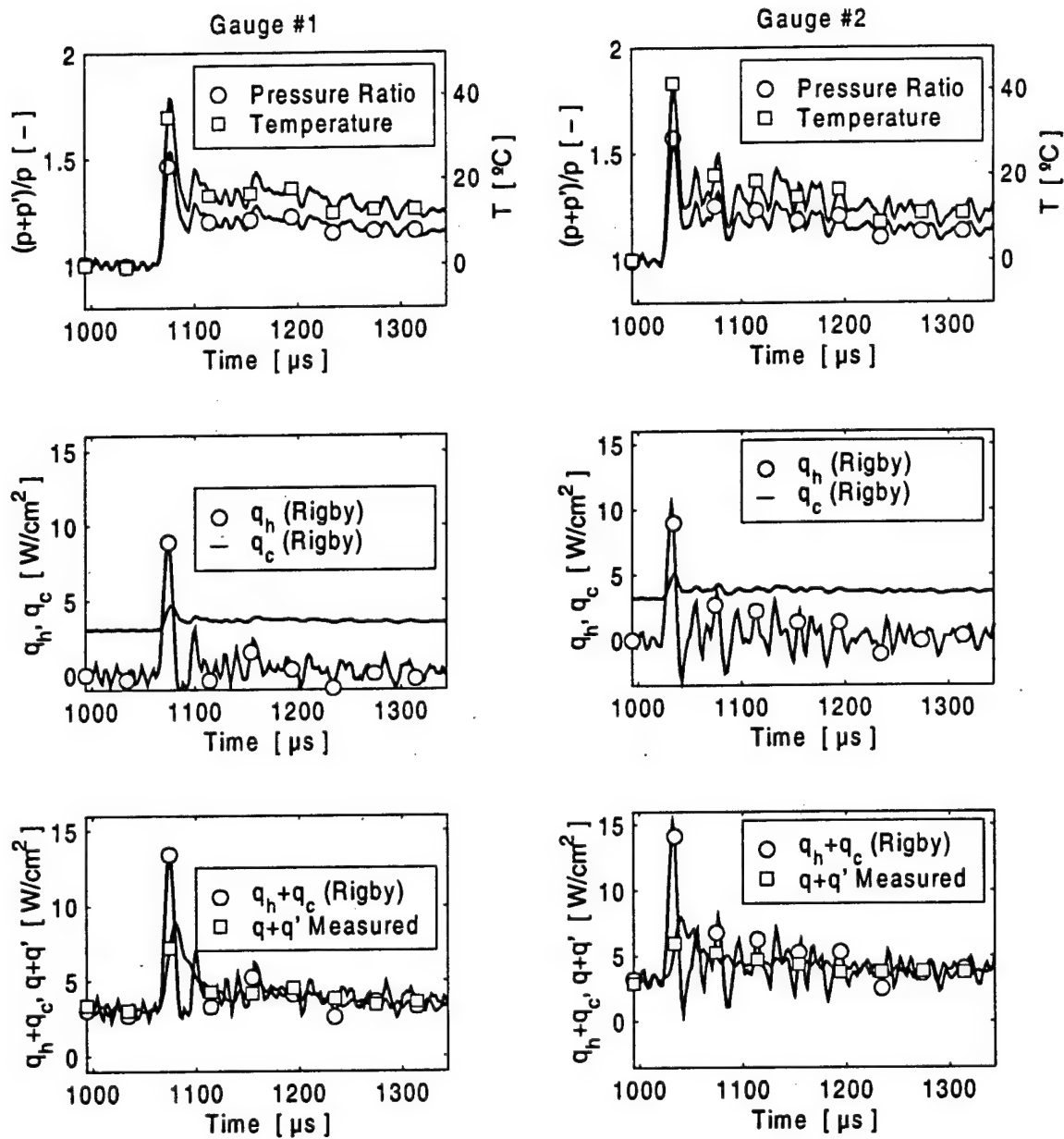


Figure 3.54: Shock Passing Event from Run #3 Without Film Cooling. Rigby's Model And Comparison with Data. Pressure and Heat Flux Signals Corrected According to Section "Signal Processing" 3.4.

3.5.4 Comparison with Reid's Numerical Model

In his Ph.D. thesis, Reid (1998) developed a numerical model for the unsteady heat transfer in the turbine cascade used in this investigation. He simplified the situation to the very same abstract model that Johnson et al. (1988) used to derive his equations described in Section 3.5.3.2 (see Figure 3.55). While Johnson simplifies

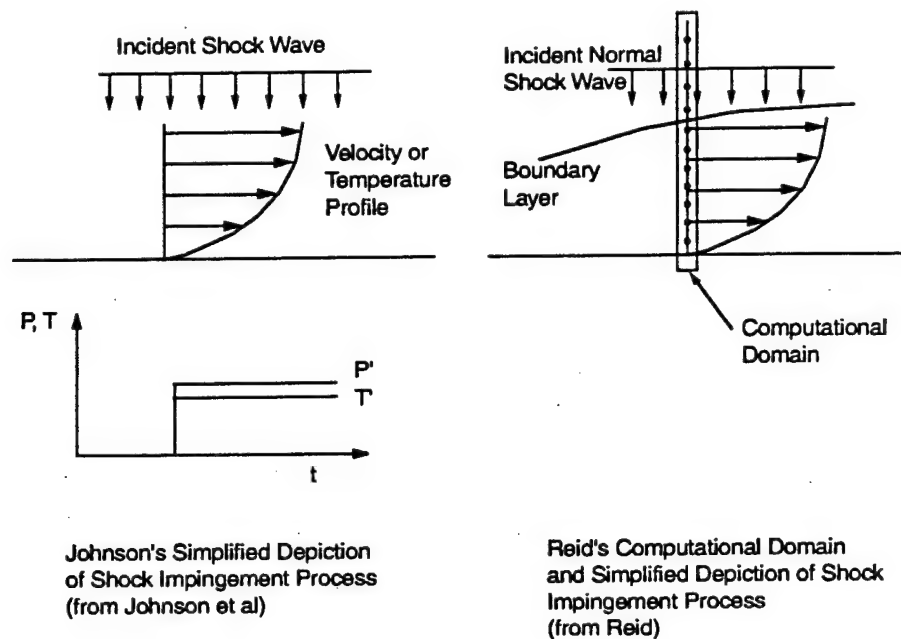


Figure 3.55: Reid's and Johnson's Simplified Depictions of the Shock Impingement Process.

the first order perturbation equations down to the one-dimensional heat conduction equation to obtain equations for the unsteady heat flux, Reid solves the problem numerically using the quasi-2D Navier-Stokes equation. And, while Johnson extends the model from a normal shock wave impinging normally to the surface to any fluctuating temperature history due to shocks, wakes and expansion waves, Reid numerically simulates only the case of the normal shock impinging normally on the surface.

Reid's numerical simulation yielded results virtually identical to the solution

of Johnson's simplified equations for the case of the normally impacting normal shock wave. In this way, Reid delivers proof that Johnson's simplifications in the simplified situation are valid. Reid's results for normal shock impingement with a preexisting thermal boundary layer can be summarized as follows:

$$q = \frac{\beta_g \cdot \Delta T}{\sqrt{\pi \cdot t}} + h \cdot (T_i - T_w + \Delta T) \cdot \left(\frac{p+p'}{p} \right)^{\frac{1}{\gamma}} - h \cdot (T_i - T_w) \quad (3.73)$$

Or simplified for better comparison with Johnson's results:

$$q = \frac{\beta_g \cdot \Delta T}{\sqrt{\pi \cdot t}} + q \cdot \left[\left(\frac{p+p'}{p} \right)^{\frac{1}{\gamma}} - 1 \right] + h \cdot \left(\frac{p+p'}{p} \right)^{\frac{1}{\gamma}} \cdot \Delta T \quad (3.74)$$

ΔT is the step in temperature induced by the normal shock and its reflection. p' in this case is the unsteady pressure seen on the surface and includes the pressure rise due to the impinging normal shock and its reflection. The equation for $q_u + q_n$ developed by Johnson applied to this special case yields:

$$q = \frac{\beta_g \cdot \Delta T}{\sqrt{\pi \cdot t}} + q \cdot \left[\left(\frac{p+p'}{p} \right)^{\frac{1}{\gamma}} - 1 \right] \quad (3.75)$$

The first term on the right hand side of Equations 3.74 and 3.75 is the solution of the one-dimensional heat conduction equation with a step input of temperature. The second term in both Equations represents the increase of heat flux due to the thinning of the boundary layer. This term will only contribute significantly to the overall unsteady heat transfer a long time after the shock impact. For short times

after shock impact, the heat flux expressed by the first terms is significantly higher. Reid's result contains an additional term on the right hand side, which contains the heat transfer due to both boundary layer thinning and the increase of temperature due to the shock. Johnson's Model does not include this component of heat transfer. Like the effect of the boundary layer thinning, this component of heat transfer will only be significant a long time after shock impact. It is also specific to the solution of the problem of a normal shock wave impacting normally on the surface. Since Johnson did not intend to model this particular problem but to establish a prediction model for a general pressure and time history, his model does not include this component of heat flux.

Despite this slight difference, the degree of agreement between the numerical and analytical model applied to this simplified situation is surprisingly high. In both models, the heat flux for short times after the shock impact is dominated by the solution to the one-dimensional heat conduction equation. Only long times after the shock impact do slight differences between the models show. Both models agree that most of the energy transfer is by one-dimensional conduction in the fluid which is relatively slow in air. The presence of the boundary layer does not change the heat transfer significantly. This is in contradiction with the results from this investigation. It was shown in Sections 3.5.2 and 3.5.3.1 that the heat transfer coefficient is not affected severely by the passing shock. The boundary layer reestablishes its original non-dimensional shape much faster than predicted with the one-dimensional conduction model. It was also shown that Johnson's model does not predict the unsteady heat transfer well (see Section 3.5.3.2).

One reason why Johnson's and Reid's models mutually agree but disagree with experimental data might be the fact that the reaction of the boundary layer to a sudden change in temperature includes not only conduction but also energy transport by convection in the boundary layer. It seems that the boundary layer reestablishes its original non-dimensional shape much quicker than predicted by the conduction-only

models. That is probably why the assumption of the time invariant heat transfer coefficient (Moss' model) yields so much better agreement with experimental data than Johnson's conduction model.

While Johnson's conduction model and Reid's numerical model predict that the boundary layer will never reestablish its original non-dimensional shape (and therefore heat transfer coefficient) once met with a sudden temperature change, Moss' model implies that the boundary layer never even changes its original shape, and the heat transfer coefficient stays constant. The experimental data suggests that Moss' model describes the boundary layer behavior far better than Johnson's and Reid's model. Since Rigby's model is almost identical to Johnson's model, it will not be compared to the numerical results separately.

Chapter 4

Conclusions from the Investigation of Unsteady Heat Flux

4.1 Summary

In Section 3.5.2 the unsteady heat transfer due to shock passing was investigated by use of the decomposition technique. By splitting all physical parameters into their time mean component before shock impact and their unsteady component during shock impact, a detailed analysis of the different contributions of different parameters was possible. The general conclusion was that neither the heat transfer coefficient nor the film effectiveness vary enough to significantly enhance or reduce unsteady heat transfer due to shock impingement. The major part of the unsteady heat transfer could be attributed to the increase in temperature induced by the passing shock wave. Considering the fact that in an engine the temperature is actually varying around a mean value, it was predicted that the time average heat transfer with and without passing shocks would have to be similar.

This prediction is exactly the result of the experimental work done by Moss et al. (1997). From these experiments it was concluded that the heat transfer coefficient is not affected strongly by pressure variations due to unsteady phenomena but that the heat transfer was driven mainly by an isentropic compression of the freestream air. By applying this assumption to the data, relatively good agreement between this model and the measurements could be obtained. This implies that the non-dimensional shape of the boundary layer is basically constant during the shock impact. The largest discrepancy between this model and the data is in the initial rise of heat flux. While Moss' Model is underpredicting the measured data in this time window, a model developed by Johnson et al. (1988) and Rigby et al. (1989) strongly overpredicts the initial rise. That could imply that the heat transfer coefficient is reacting to some extent short times after the shock impact. It has been mentioned that the physical gauge size influences the gauge frequency response. The shock rise times would probably be shorter and the peak levels of unsteady heat flux higher with a hypothetical point sensor. This would make the initial rise of the unsteady heat flux due to shock passing more similar to the prediction according to Rigby et al. (1989) and Johnson et al. (1988). Still, it can not be denied that the model by Moss et al. (1995) is closer to the data than the model by Johnson et al. (1988) and Rigby et al. (1989).

The overall conclusion to be drawn from the experimental observations and the comparison with existing models is the following: The variation of the heat transfer coefficient was shown to be of secondary significance in the unsteady heat transfer due to shock passing. This holds true for a film cooled blade and a blade without film cooling. Also, the film effectiveness could be proven to vary only insignificantly. The unsteady heat transfer is mainly due to a change in gas temperature induced by the passing shock wave. Since the gas temperature seen by the rotor blade in an actual engine varies around its mean, the time averaged heat transfer with the presence of shocks will not differ significantly from the time averaged heat flux without this flowfield disturbance.

4.2 Application to Turbine Design

Extrapolating from the above conclusion, recommendations for future turbine design applications are as follows:

1. The development of improved codes for the determination of steady state heat transfer data on blades with and without film cooling should be encouraged. According to the conclusions from Section 4.1, an accurate steady state prediction will provide a good estimate for the heat transfer in the presence of unsteady phenomena.
2. Convection has more influence on the unsteady behavior of the turbine blade boundary layer than assumed by conduction/unsteady compression models. It is not sufficient to reduce the problem of unsteady heat flux to a purely conductive phenomenon.

4.3 Outlook

Since the present investigation focused on the first part of the suction side of the blade, it is not certain that the conclusions will hold for other regions on the blade even though the investigation by Moss et al. (1997) indicates that an extrapolation to the entire blade surface is possible.

The freestream turbulence level is known to influence the boundary layer on the blade. In the present study the turbulence level was very low compared to engine conditions (about 1%). The effect of higher turbulence levels on the conclusions from this investigation will be interesting. The research done by Moss et al. (1997) was done at similar low turbulence levels, so an extrapolation to higher values of

turbulence cannot be done using their results.

Since the main mode of interaction between unsteady phenomena and the heat transfer coefficient seems to be the effect on the transitional behavior of the boundary layer on the suction side, it would be important to investigate the effect of a passing shock wave on the heat transfer on the later part of a turbine blade with transitional features. The cascade investigated here did not show any transitional behavior. The boundary layer is laminar all the way down to the passage shock where it immediately transitions to turbulent flow (shown in schlieren pictures presented in Bubb (1999)).

To summarize, recommendations for further research are as follows:

1. More locations on the blade should be investigated, especially on the downstream suction side.
2. The experiments should be repeated at higher turbulent intensities more representative of engine conditions.
3. Similar experiments should be done on a blade with a transitional suction side boundary layer.
4. It can be expected that at much higher pressure ratios there will be an effect of the shock on heat transfer coefficient and film effectiveness. Increasing the shock strength may, therefore, lead to different conclusions.
5. When modeling the passing shock wave with a shock tube setup or a rotating bar mechanism, the shock strength and speed are linked. It may well be that a shock of certain strength will have different effects when interacting with the surface at a different speed (see steady shock boundary layer interaction). An entirely different setup would have to be devised to make such an investigation possible.

References

- Abhari, R.S. 1996. Impact of Stator-Rotor Interaction on Turbine Blade Film Cooling. *Pages 123-133 of: ASME Journal of Turbomachinery*, vol. 118.
- Abhari, R.S., *et al.* 1994. An Experimental Study of Film Cooling in a Rotating Transonic Turbine. *Pages 63-70 of: ASME Journal of Turbomachinery*, vol. 116.
- Bubb, J.V. 1999. *The Influence of Pressure Ratio on Film Cooling Performance of a Turbine Blade*. MPhil. thesis, Virginia Polytechnic Institute and State University.
- Chapman, A.J., *et al.* 1971. *Introductory Gas Dynamics*. First edn. Holt, Rinehart and Winston, Inc.
- Collie, J. C. 1991. *Unsteady Shock Wave Effects on Transonic Turbine Cascade Performance*. MPhil. thesis, Virginia Polytechnic Institute and State University.
- Cook, W.J. 1970. Determination of Heat-Transfer Rates from Transient Surface Temperature Measurements. *Pages 1366-1368 of: AIAA Journal*, vol. 8.
- Cook, W.J., *et al.* 1966. Reduction of Data from Thin-Film Heat-Transfer Gauges: A Concise Numerical Technique. *Pages 561-562 of: AIAA Journal*, vol. 4.
- Dean, R. C. 1959. On the Necessity of Unsteady Flow in Fluid Machines. *Pages 24-28 of: Journal of Basic Engineering*, vol. 1.

- Diller, T.E. 1996. Methods of Determining Heat Flux from Temperature Measurements. Pages 251-262 of: *Proceedings of the 42nd International Instrumentation Symposium*, vol. 1.
- Doorly, D.J., *et al.* 1985. Simulation of the Effects of Shock Wave Passing on a Turbine Rotor Blade. *In: International Gas Turbine and Aeroengine Conference and Exhibit.*
- Doughty, R.L., *et al.* 1995. Multiple Shock wave Generation for Cascade Testing. *In: 33rd Aerospace Sciences Meeting and Exhibit.*
- Doughty, Roger L. 1994. *Effects of Shock Waves on the Flow in a Transonic Turbine Cascade.* Ph.D. thesis, Virginia Polytechnic Institute and State University.
- Du, H., *et al.* 1997. Effect of Unsteady Wake on Detailed Heat Transfer Coefficient and Film Effectiveness Distributions for a Gas Turbine Blade. *In: International Gas Turbine and Aeroengine Congress and Exposition.*
- Dunn, M.G. 1982. Measurement of Heat Flux and Pressure in a Turbine Stage. *In: ASME Journal of Turbomachinery*, vol. 104.
- Dunn, M.G. 1986. Heat-Flux Measurements for the Rotor of a Full-Stage Turbine: Part 2 - Description of Analysis Technique and Typical Time-Resolved Measurements. *In: ASME Journal of Turbomachinery*, vol. 108.
- Dunn, M.G. 1989. Phase and Time-Resolved Measurements of Unsteady heat Transfer and Pressure in a Full-Stage Rotating Turbine.
- Epstein, A.H., *et al.* 1984. The MIT Blowdown Turbine Facility. *In: International Gas Turbine and Aeroengine Congress and Exhibition.*
- Funazaki, K., *et al.* 1996. Effect of Periodic Wake Passing on Film Effectiveness of Inclined Discrete Cooling Holes Around the Leading Edge of a Blunt Body. *In: International Gas Turbine and Aeroengine Congress and Exhibition.*

- Goldstein, R.J. 1976. *Measurements in Heat Transfer*. Second edn. Hemisphere Pub. Corp.
- Greitzer, E. M. 1979. Introduction to Unsteady Flows in Turbomachines. *Pages 1-43 of: VKI Lecture Series 1979-3, Unsteady Flow in Turbomachines.*
- Guenette, G.R., *et al.* 1989. Fully Scaled Transonic Turbine Rotor Heat Transfer Measurements. *Pages 1-7 of: ASME Journal of Turbomachinery*, vol. 111.
- Heidmann, J.D., *et al.* 1997. An Experimental Study of the Effect of wake Passing on Turbine Blade Film Cooling. *In: International Gas Turbine and Aeroengine Congress and Exposition.*
- Johnson, A.B., *et al.* 1988. Surface Heat Transfer Fluctuations on a Turbine Rotor Blade Due to Upstream Shock Wave Passing. *In: ASME Journal of Turbomachinery.*
- Johnson, A.B., *et al.* 1990. Nozzle Guide Vane Shock Wave Propagation and Bifurcation in a Transonic Turbine Rotor. *In: Gas Turbine and Aeroengine Congress and Exposition.*
- Mehendale, A.B., *et al.* 1994. Unsteady Wake over a Linear Turbine Blade Cascade with Air and CO₂ Film Injection: Part 2- Effect on Film Effectiveness and Heat Transfer Distributions. *Pages 730-737 of: ASME Journal of Turbomachinery*, vol. 116.
- Moffat, R. J. 1988. Describing Uncertainties in Experimental Results. *In: Experimental Thermal and Fluid Science.* Elsevier Science Publishing Co., Inc.
- Moss, R.W., *et al.* 1995. Unsteady Pressure and Heat Transfer Measurements on a Rotating Blade Surface in a Transient Flow Facility. *Pages 22.1-22.9 of: AGARD Conference Proceedings CP-571.*
- Moss, R.W., *et al.* 1997. Effect of rotation on blade surface heat transfer: an experimental investigation. *In: ASME Journal of Turbomachinery.*

- Nix, A.C. 1997. *Effect of Shock Wave Passing on Turbine Blade Heat Transfer in a Transonic Turbine Cascade*. MPhil. thesis, Virginia Polytechnic Institute and State University.
- Nix, A.C., *et al.* 1997. Effects of Shock Wave Passing on Turbine Blade Heat Transfer in a Transonic Cascade. *In: 35th Aerospace Sciences Meeting and Exhibit*.
- Oldfield, M.L.G., *et al.* 1978. On-Line Computer for Transient Turbine Cascade Instrumentation. *Pages 669-679 of: IEEE Transactions on Aerospace and Electronic Systems*, vol. AES-14 No. 5.
- Ou, S., *et al.* 1994. Unsteady Wake over a Linear Turbine Blade Cascade with Air and CO₂ Film Injection: Part 1- Effect on Heat Transfer Coefficients. *Pages 721-729 of: ASME Journal of Turbomachinery*, vol. 116.
- Popp, O., *et al.* 1999. Steady and Unsteady Heat Transfer in a Transonic Film Cooled Turbine Cascade. *In: International Gas Turbine and Aeroengine Congress and Exhibition*.
- Reid, Terry Vincent. 1998. *A Computational Approach for Investigating Unsteady Turbine Heat Transfer Due to Shock Wave Impact*. Ph.D. thesis, Virginia Polytechnic Institute and State University.
- Rigby, M.J., *et al.* 1989. Temperature Scaling of Turbine Blade Heat Transfer with and without Shock Wave Passing. *Pages 669-679 of: International Symposium on Air Breathing Engines*, vol. 9.
- Rigby, M.J., *et al.* 1990. Gas Turbine Rotor Blade Film Cooling with and without Simulated NGV Shock Waves and Wakes. *In: Gas Turbine and Aeroengine Congress and Exposition*.
- Schultz, D.L., *et al.* 1973. Heat Transfer Measurements in Short-duration Hypersonic Facilities AGARD-AG-165. *In: AGARD-AGARDOGRAPH-165*.

- Smith, D.E. 1999. *Investigation of Heat Transfer Coefficient and Film Cooling Effectiveness in a Transonic Turbine Cascade*. M.Phil. thesis, Virginia Polytechnic Institute and State University.
- Smith, Dwight, *et al.* 1999. A Comparison of Radiation Versus Convection Calibration of Thin-Film Heat Flux Gauges. *In: The ASME Ad-Hoc Committee on Heat Flux Measurement*.
- Vidall, R.J. 1962. Transient Surface Temperature Measurements. *Pages 90-99 of: Symposium on Measurement in Unsteady Flow*, vol. 1.

Appendix A

Shock Progression Details

Shown here are eight shadowgraph images of the shock passing process. The eight pictures are composed of two sets of four pictures taken with the high speed camera. The timing shown in the captions must be considered with care. They are calculated from the camera settings but do not seem to accurately represent the time history of the event. As pointed out in Section 3.5.1 the interaction of the shock and the cooling film layer is not clearly visible. No film detachment or significant thinning or thickening is observed.

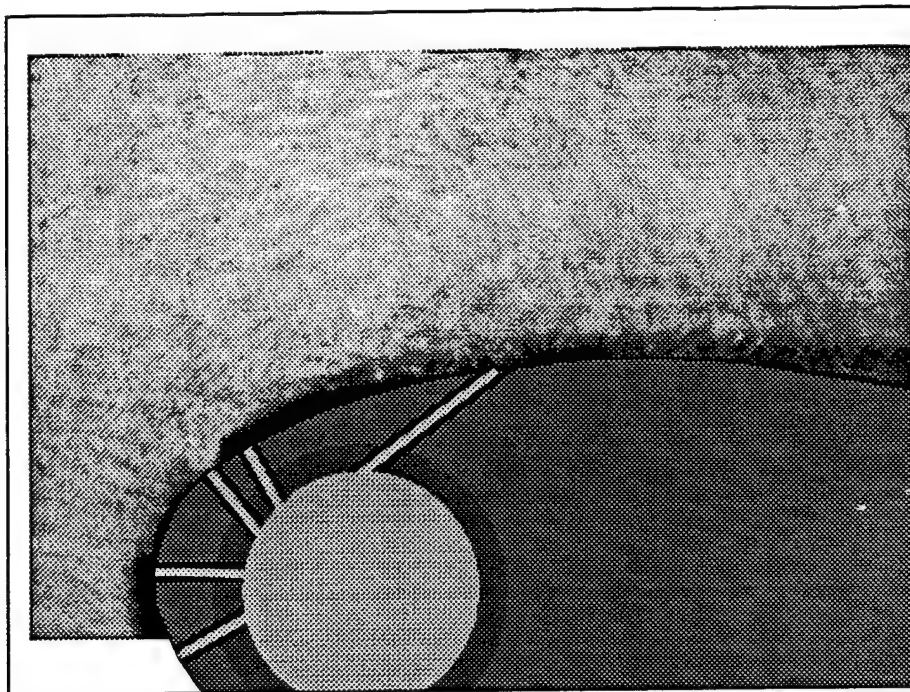


Figure A.1: Shock Progression: Still # 1, time $\approx 450\mu s$.

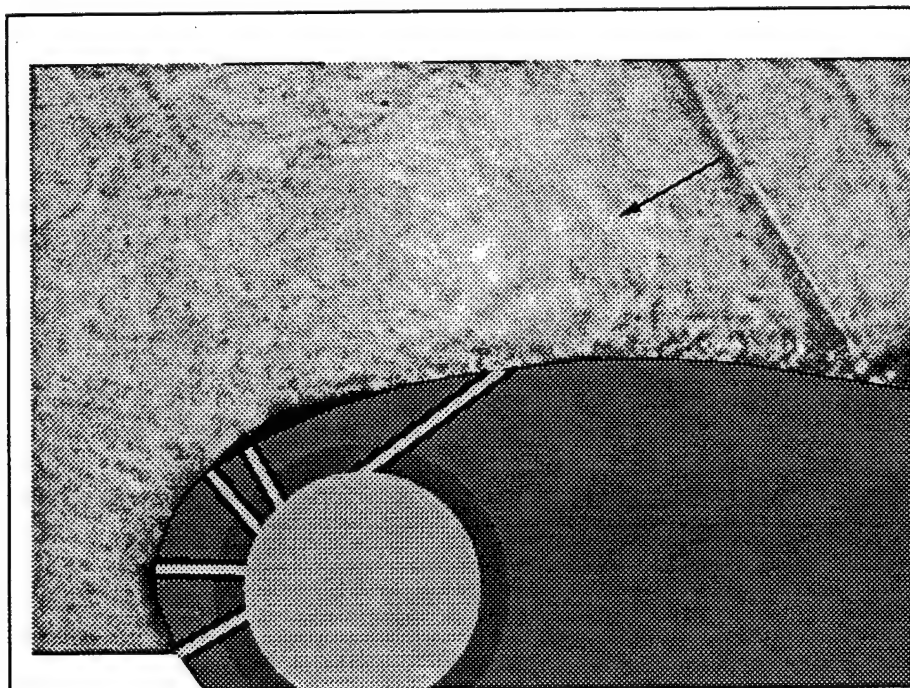


Figure A.2: Shock Progression: Still # 2, time $\approx 520\mu s$.

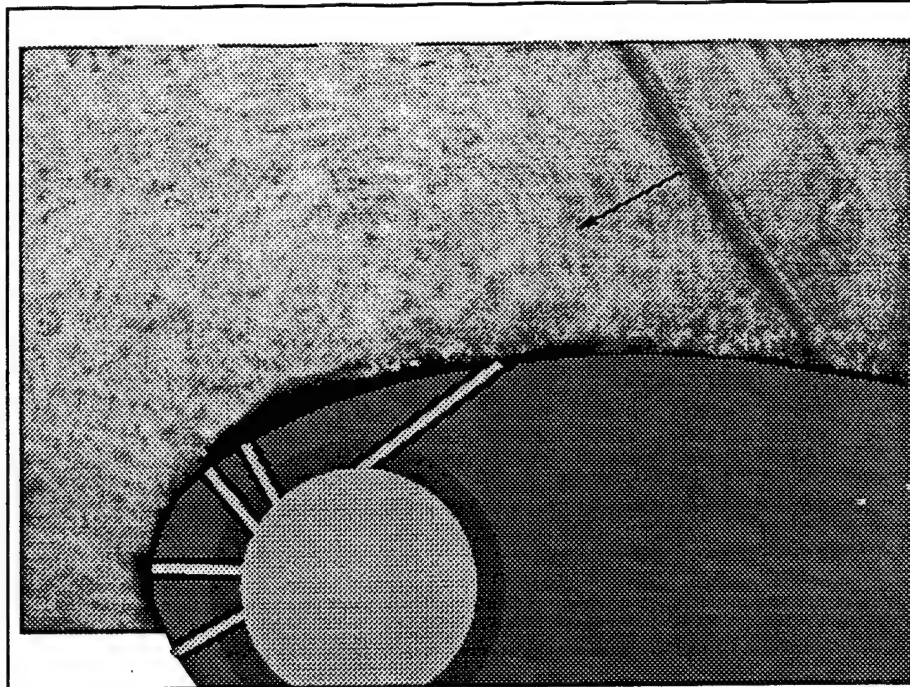


Figure A.3: Shock Progression: Still # 3, time $\approx 525 \mu s$.

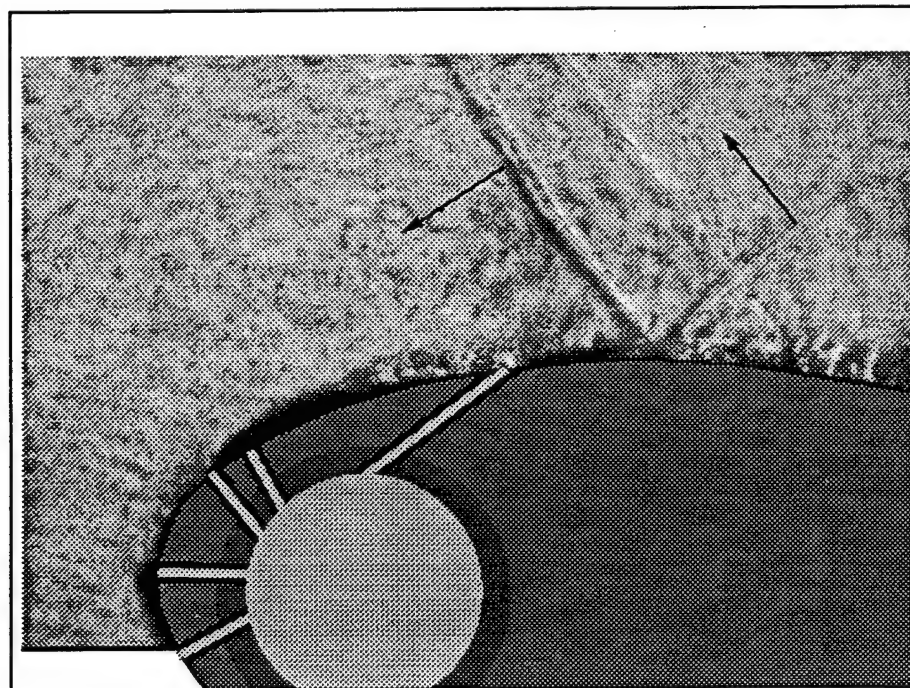


Figure A.4: Shock Progression: Still # 4, time $\approx 562 \mu s$.

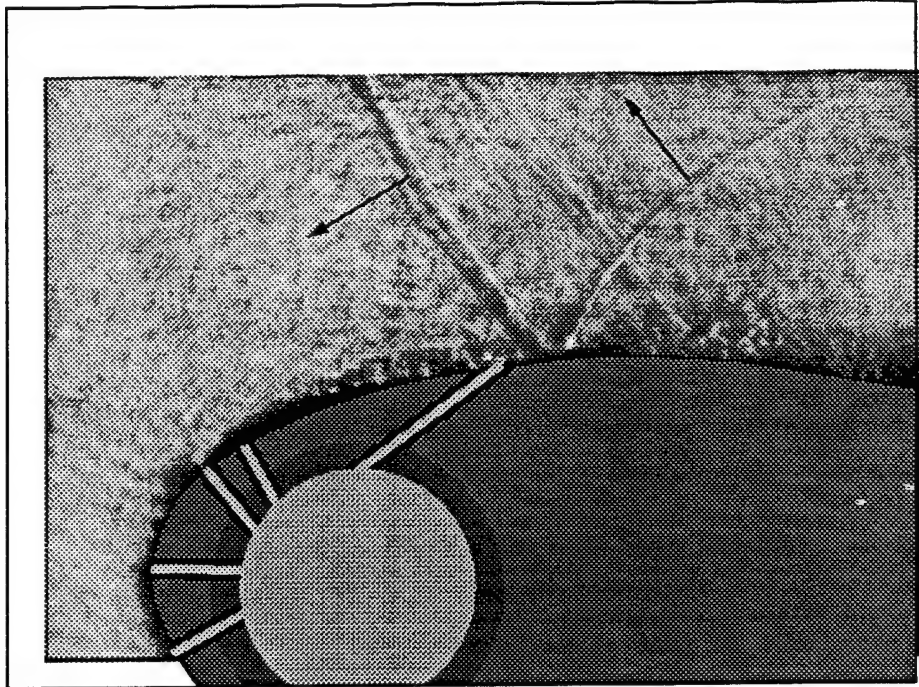


Figure A.5: Shock Progression: Still # 5, time $\approx 585 \mu s$.

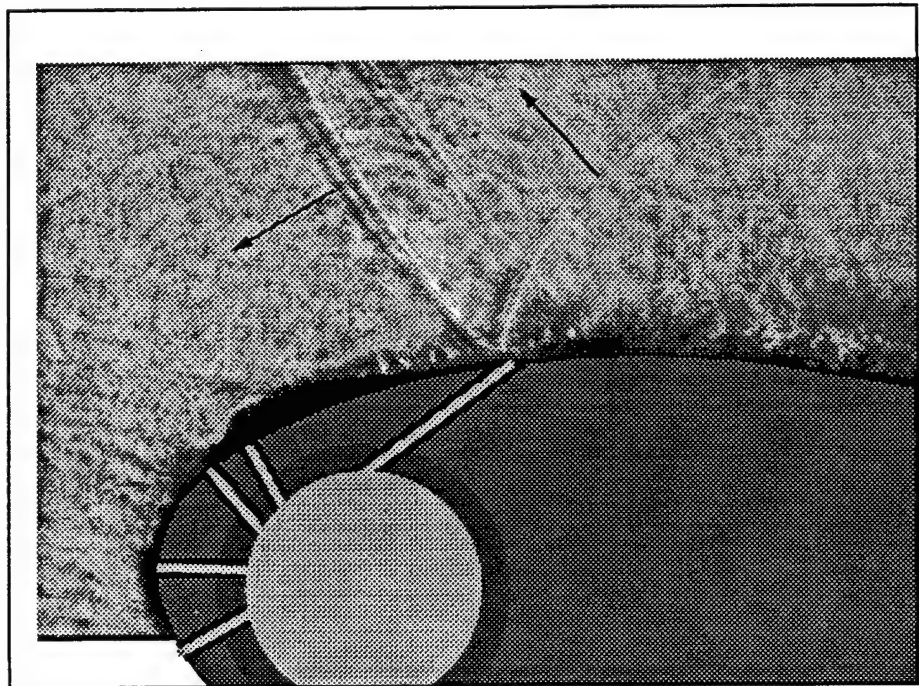


Figure A.6: Shock Progression: Still # 6, time $\approx 600 \mu s$.

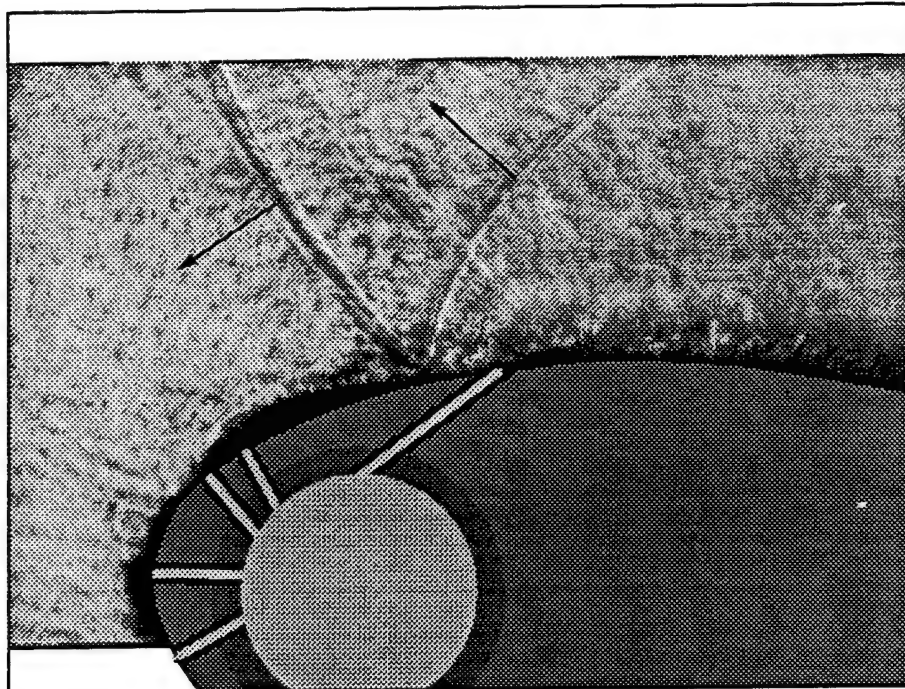


Figure A.7: Shock Progression: Still # 7, time $\approx 622 \mu s$.

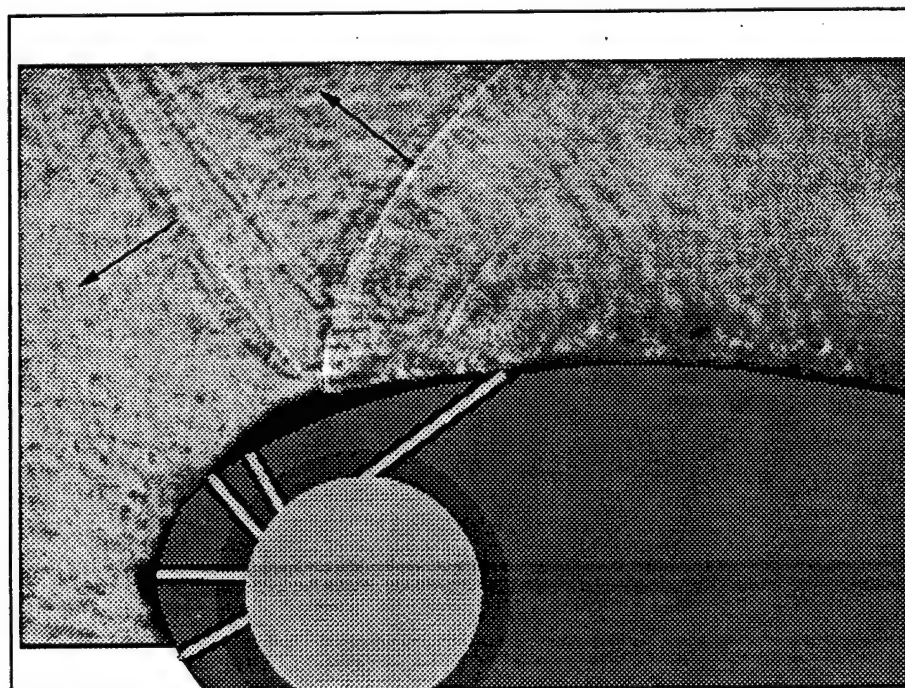


Figure A.8: Shock Progression: Still # 8, time $\approx 640 \mu s$.

Appendix B

Investigation of the Transfer Function of Different *Kulite* Pressure Transducers

B.1 Problem Statement and Approach

In Experimental High Speed Aerodynamics one is often faced with the task of obtaining a good representation of moving shock waves in terms of pressure, temperature, velocity, etc. Since shock waves are represented mathematically by discontinuities, their frequency content is theoretically infinitely wide. The problem is then to decide on transducers that are capable of tracing "adequately" high frequencies. This investigation is aimed at helping with this decision. The dynamic behavior of two *Kulite* transducers *XCQ-062-50a* is investigated. The sensing surface of one of them is exposed to the flow while the second sensor is protected by a "B-Screen" supplied by *Kulite*. Both of them are exposed to a "known" input of pressure in a modified

shock tube in order to determine their transfer functions.

B.2 Experimental Setup

Modified Shock Tube

Figure B.1 shows the shock tube design. A 3/4 inch test pipe is connected to the end of the driven section of a 3 inch shock tube. The shock is triggered by the burst of a plastic diaphragm between driven section and driver section. As the shock reaches the end of the driven section, it propagates into the test tube, growing in strength in the transition. Two *Kulite XCQ-062-50a* transducers are flush mounted to the wall in the middle of the test pipe. While the sensing surface of one of them is exposed to the passing shock, the second transducer is protected by a "B-Screen." The passing shock will be assumed to be an ideal step of pressure in this investigation.

Measurement Chain

Transducer Excitation and Amplification

In order to excite the *Kulite* sensors and to amplify the signals two *Measurements Group 2310 Strain Gauge Conditioner and Signal Amplifiers* were used. The transfer function of these amplifiers was determined by simple sine sweeps for different gain settings. It became clear that significant roll-offs in the frequency range of interest had to be taken into account. Even at a nominal gain of 1, the signal is diminished and phase shifted in the frequency range below 1 MHz as can be seen in

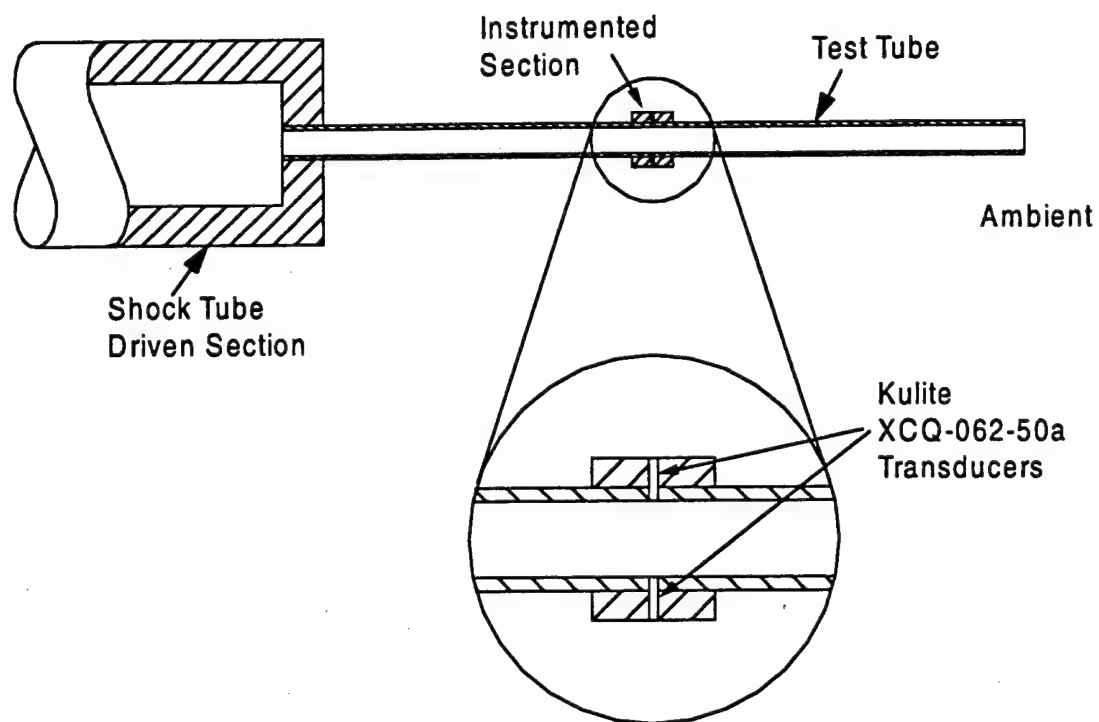


Figure B.1: Shock Tube with *Kulite* Pressure Sensors.

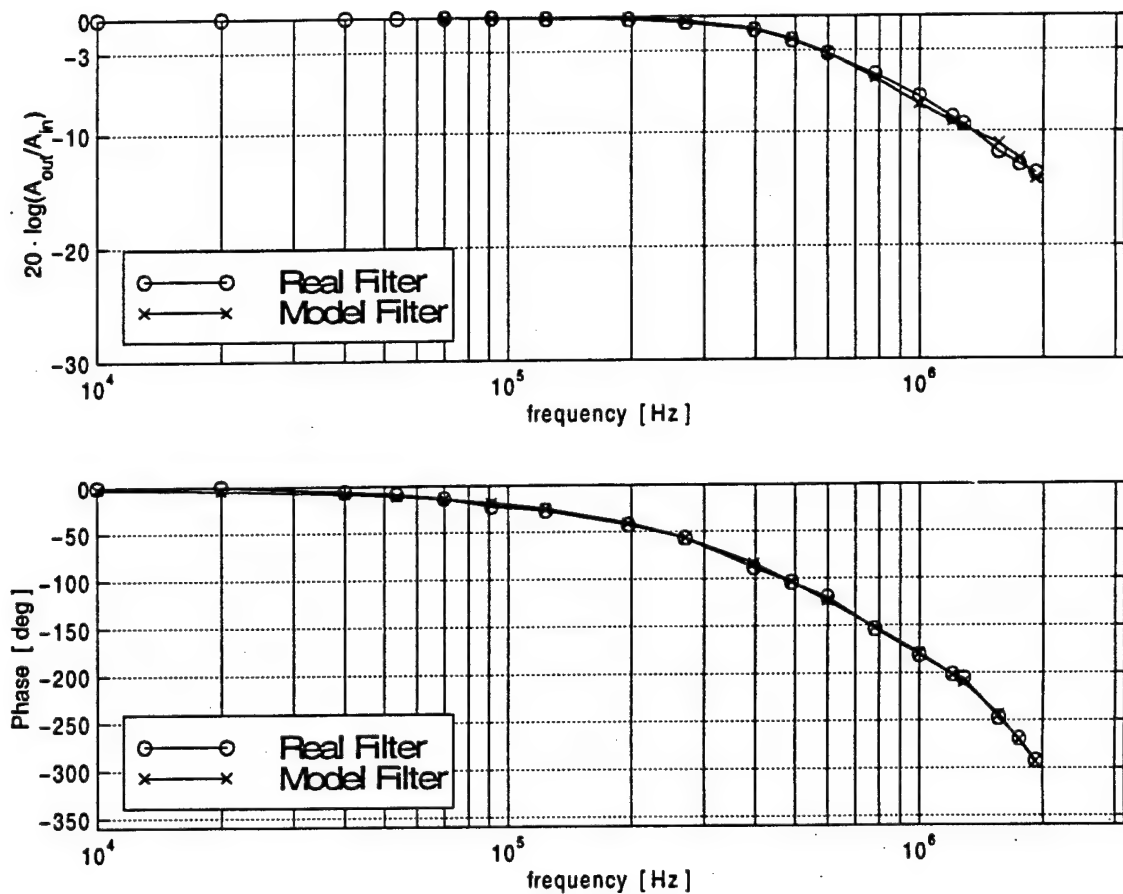


Figure B.2: Transfer Function of the *Measurements Group 2310 Strain Gauge Conditioner and Signal Amplifier* at a gain of 1.

Figure B.2. The measured transfer function was modeled as a filter with one zero and 4 poles using a *Matlab* routine. The experimental and modeled transfer functions are shown on the same axes in Figure B.2.

Anti-Aliassing Filter

In this investigation it was desirable to obtain data over the widest possible range of frequencies. The limiting factor was the cut-off frequency of the filters

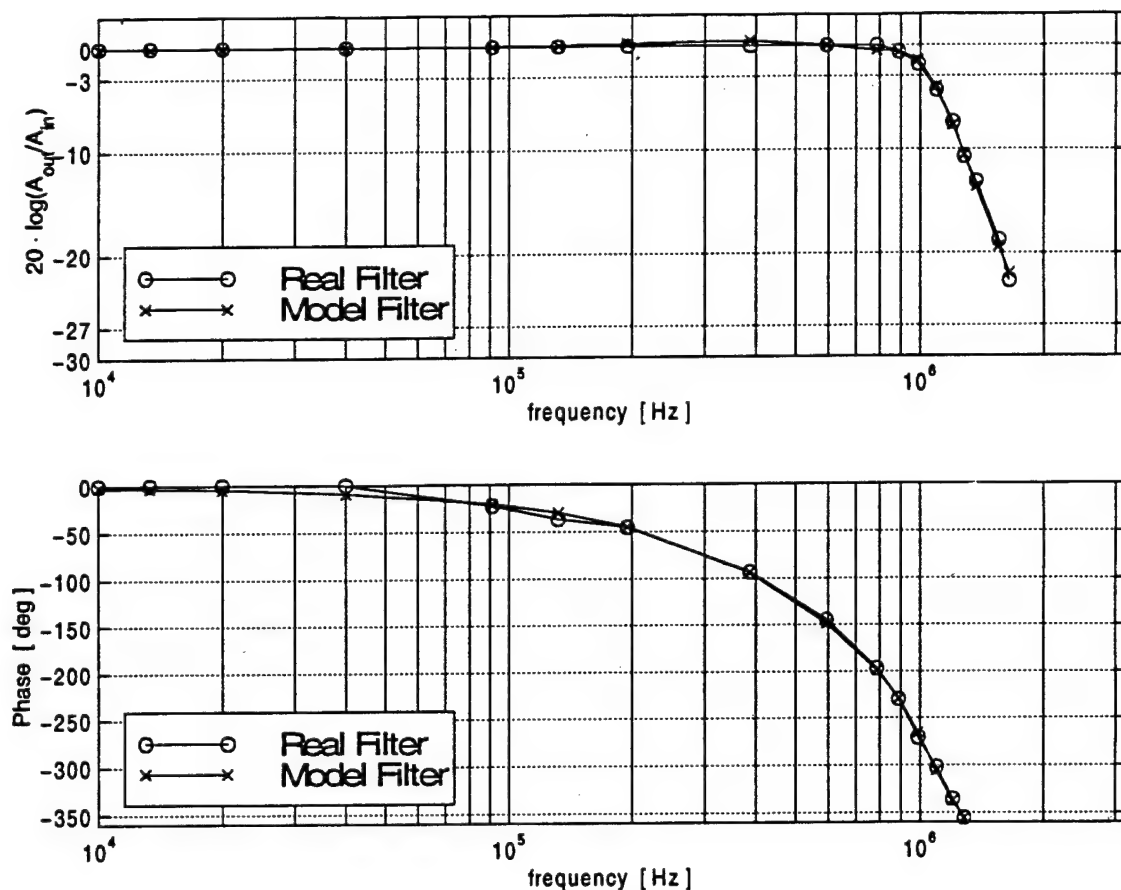


Figure B.3: Transfer Function of the *Ithaco 4302* low-pass filter at a cut-off frequency of 1 MHz.

available. Two *Ithaco 4302* filters were used at a cut-off frequency of 1 MHz. They show a Butterworth characteristic with a 24 dB/octave roll-off as shown in Figure B.3. The filter was modeled assuming 4 zeroes and 4 poles. The measured and modeled filter characteristics are shown on the same axes in Figure B.3. Combining the two transfer functions of the amplifier and the filter, one obtains the measured and modeled transfer function of the measurement chain without the actual transducer, shown in Figure B.4.

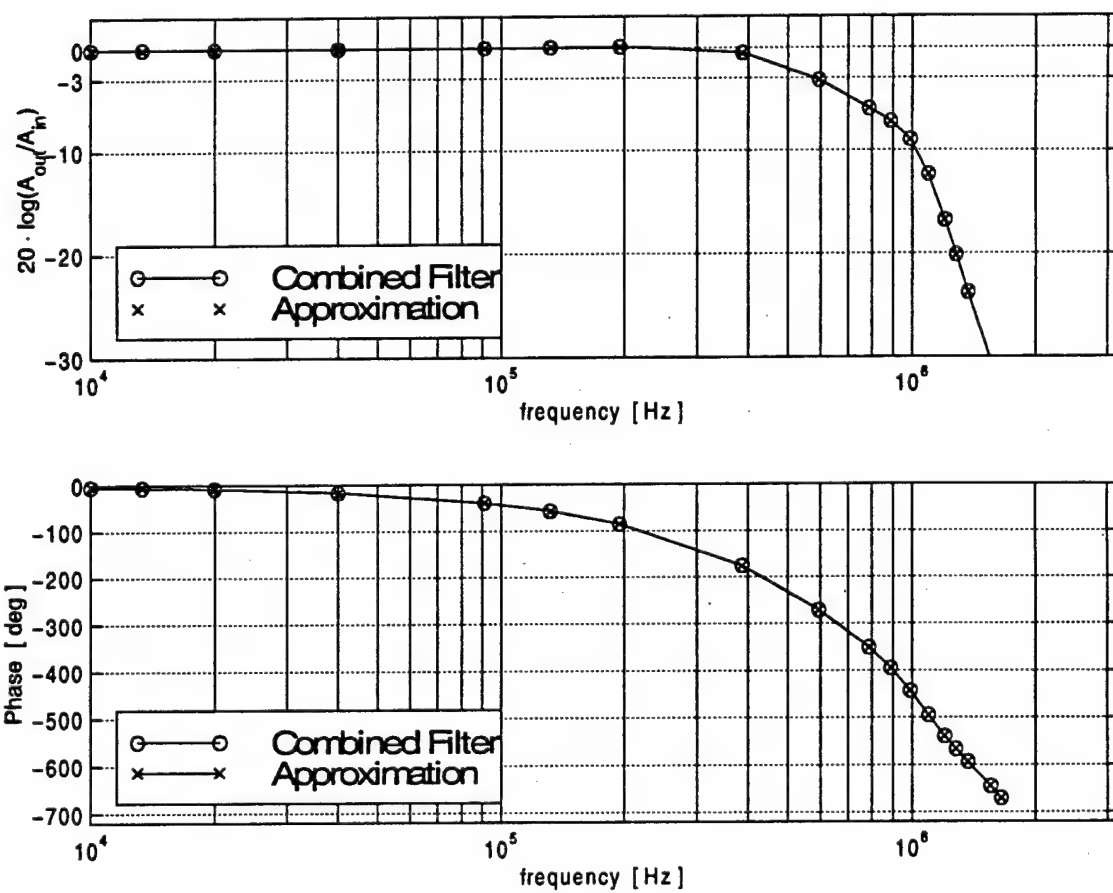


Figure B.4: Combined Transfer Function of *Measurements Group 2310* Strain Gauge Conditioner and Signal Amplifier at a gain of 1 and the *Ithaco 4302* low-pass filter at a cut-off frequency of 1 MHz.

Data Acquisition

The data from the two transducers was acquired using a *LeCroy 6810 Waveform Analyzer* at a sampling frequency of 2 MHz. The system is controlled by a PC using the software *catalyst* via a *GPIB* interface.

B.3 Results and Discussion

The chosen method to obtain the transfer functions will be presented using only one experiment as an example. The raw data will be prepared for treatment in the frequency domain. Then it will be corrected for the influence of the measurement chain. The transfer functions of both transducers will finally be determined in the frequency domain.

Preparation of Data in the Time Domain

A typical result from a shock passing is shown in Figure B.5. Three observations:

- The "real" forcing function is not an ideal step input. There are pressure fluctuations present after the initial shock impact
- There is more data than needed for the determination of the transfer function.
- The signal is not periodic.

Therefore, the signal will be conditioned in the following manner:

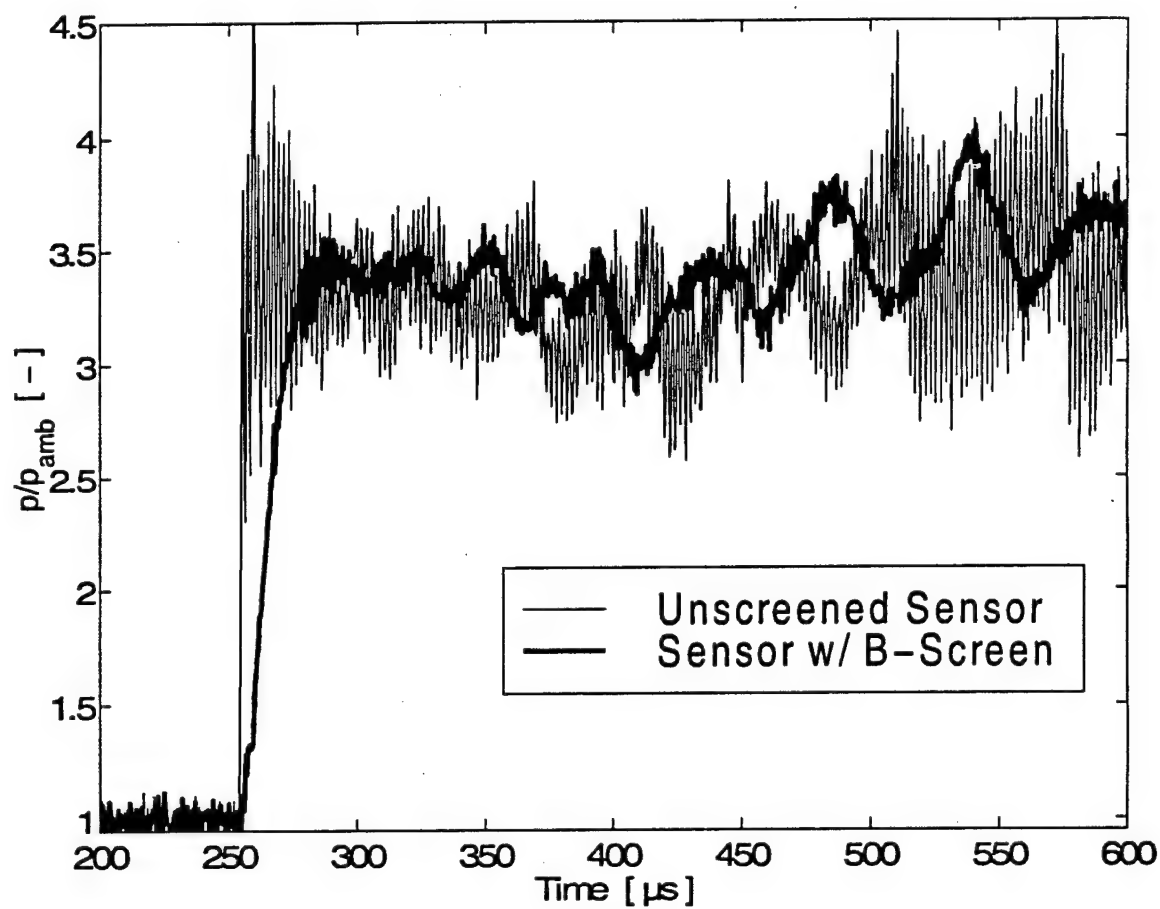


Figure B.5: Raw Data from Both Transducers.

- The data will be truncated very shortly after the initial shock impact to reduce the effect of the shock not being an ideal step input.
- A very slow downslope will be padded at the end of the time window chosen for data analysis. The goal is to make the data periodic without changing the dynamic characteristics of the system.
- An ideal step input is created. This ideal forcing function will be assumed to be the real input for the purpose of the analysis.
- The initial value will be set to zero to make the numerical analysis simpler

The result of these manipulations is shown in Figure B.6. The upper graph in Figure B.6 shows the entire trace. The lower graph shows the time window around the actual shock impact. As the last step in the signal preparation, the time histories are corrected for the influence of the amplifier and filter. The combined transfer function of these instruments was described in Section B.2 and shown in Figure B.4. The signals are corrected according to:

$$S_c(\omega) = \frac{S(\omega)}{H_c(\omega)} \quad (B.1)$$

Where S is the measured signal, S_c is the corrected signal and H is the combined transfer function of the amplifier and filter up to 1 MHz. Capital letters refer to the Fourier Transforms of the signal. The result of this operation is shown in the time domain in Figure B.7. The upper graph in Figure B.7 shows the original and corrected signal from the unscreened sensor while the lower graph shows the effect of the correction on the sensor with the B-Screen. The data resulting from the manipulations described in this Section will be used for the determination of the transfer functions.

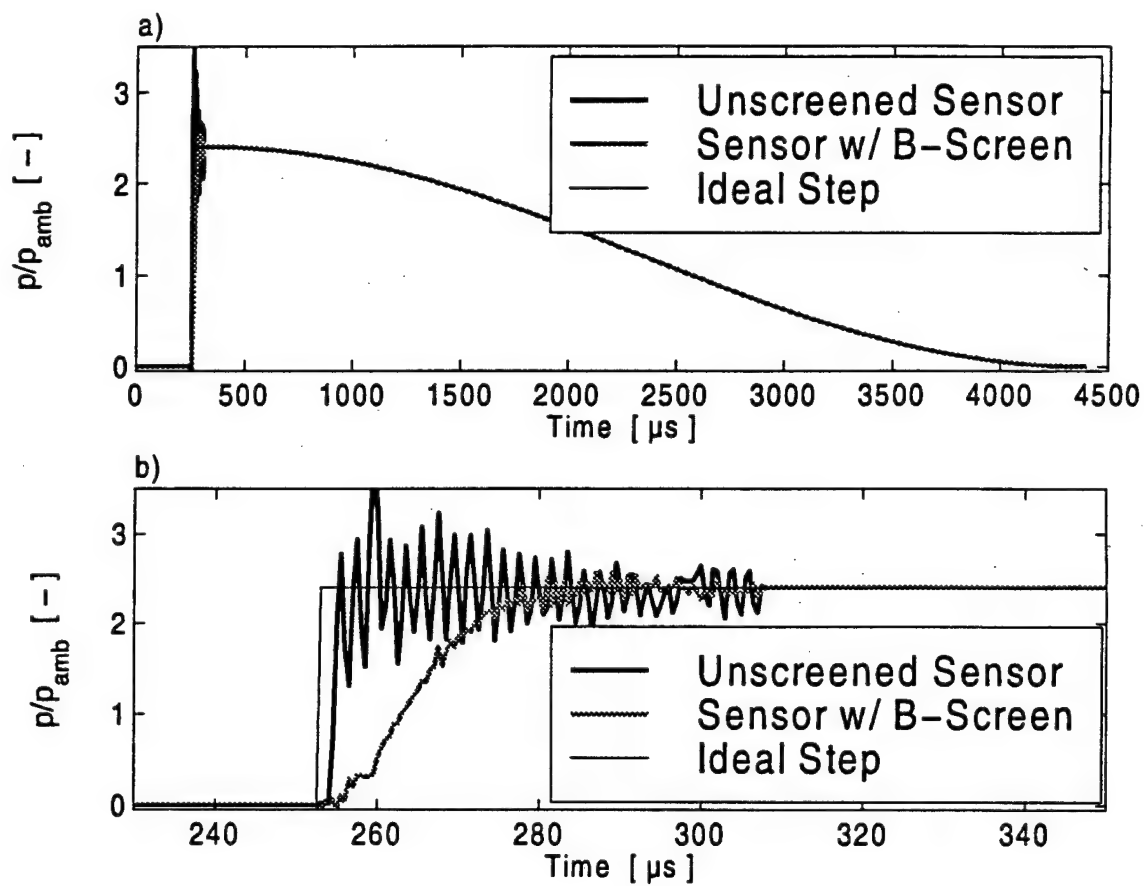


Figure B6: Traces after Truncation, Padding of Downslope, Zeroing of Initial Value. Also Shown is the "Ideal" Step Input. Upper Graph a): Entire Traces. Lower Graph b): Time Window Around Shock Event.

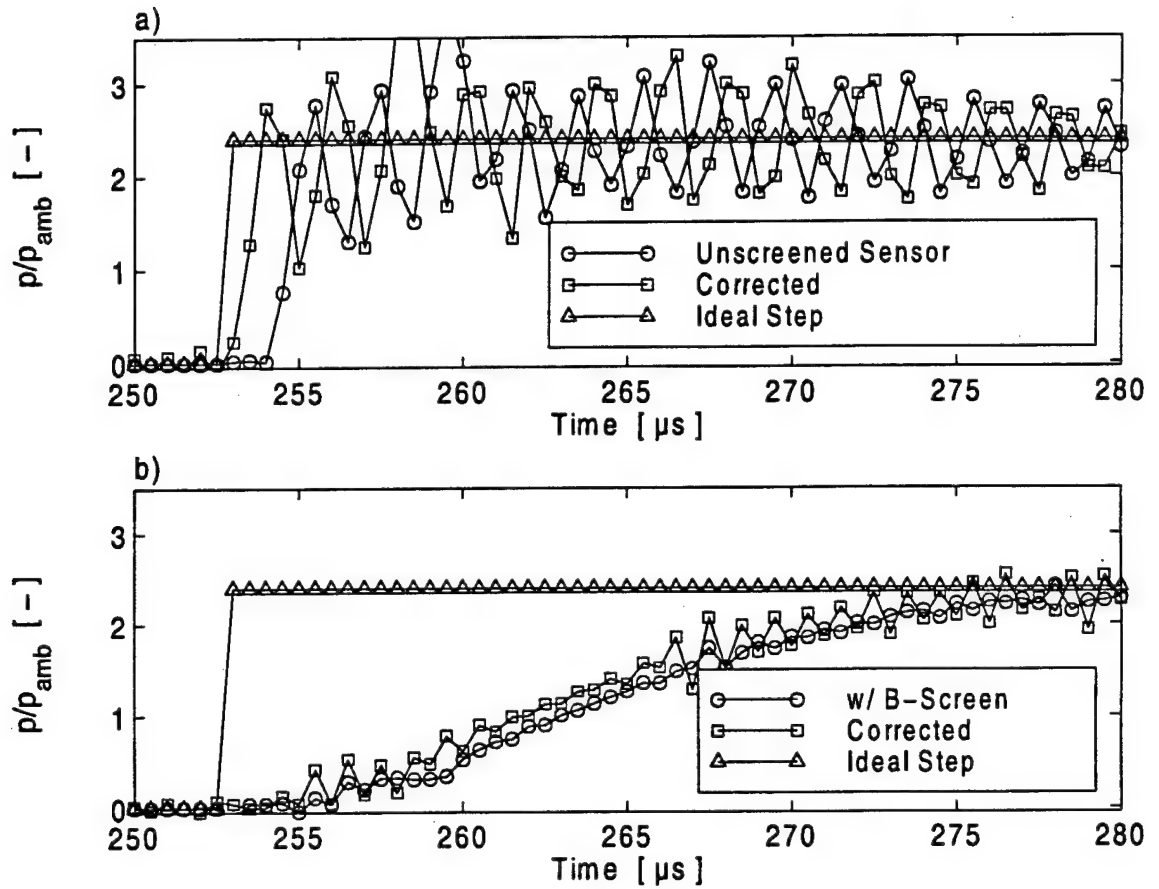


Figure B.7: Data Corrected for the Influence of the Amplifier and the Filter. Upper Graph a): Unscreened Sensor: Raw Signal, Corrected Signal and Ideal Step. Lower Graph b): Sensor with B-Screen: Raw Signal, Corrected Signal and Ideal Step.

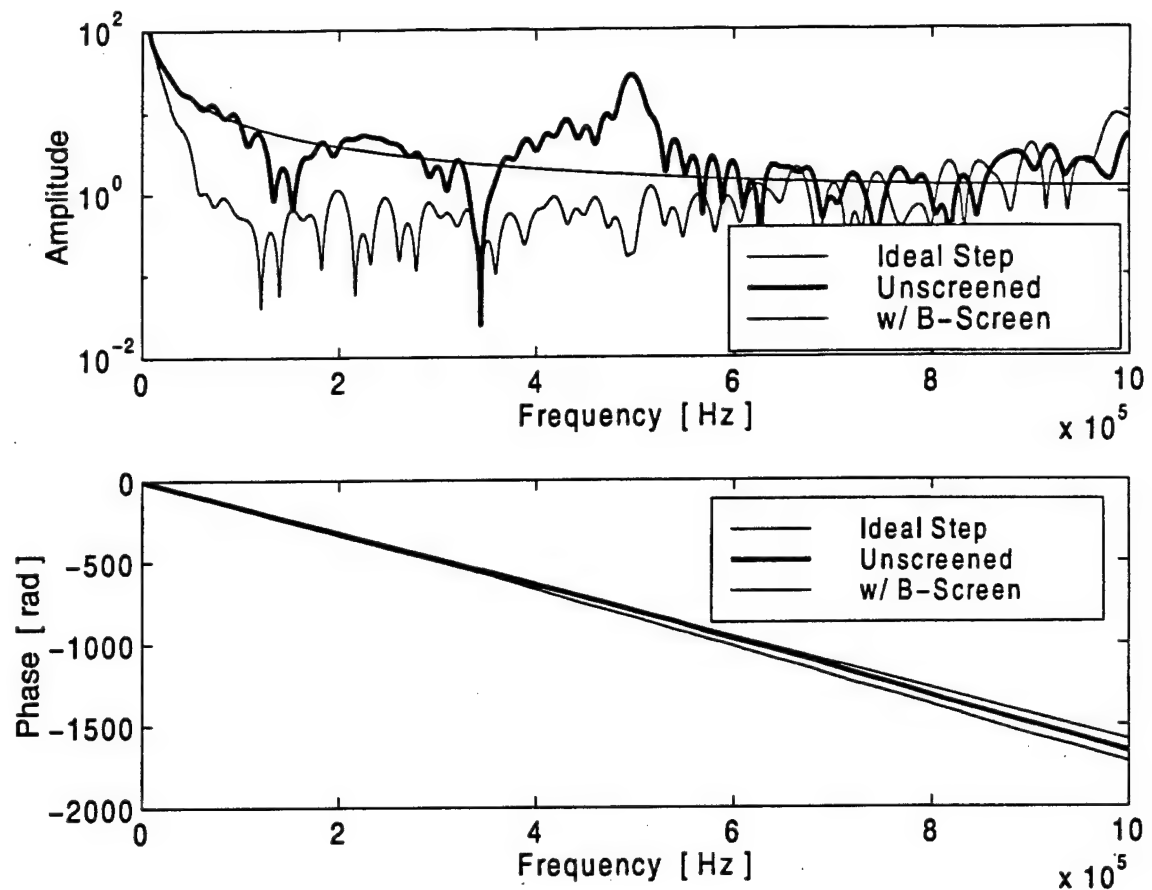


Figure B.8: Bode Plot of Fourier Transforms of the Ideal Step Input, the Unscreened Sensor and the Sensor with the B-Screen.

B.3.1 Determination of Transfer Functions

The signals prepared in the manner described in Section B.3 are now transformed into the frequency domain. The results are shown in Figure B.8. It seems clear from Figure B.8 that the noise level of the signals lies below the 10^0 line in the upper graph in Figure B.8. The amplitude of the FFT of the sensor with B-Screen drops rapidly to this level and does not change for higher frequencies. The input level of the ideal step reaches the noise level at frequencies higher than about 600 kHz. This implies that it is not possible to extract the transfer functions beyond that frequency since the signal to noise ratio becomes too small. The amplitude of the DFT of the

screened *Kulite* sensor shows a very strong roll-off reaching the noise level around 100 kHz. Beyond this point the amplitude seems to stay in the noise level. Therefore, the transfer function of the screened sensor will only be determined up to 100 kHz.

The unscreened sensor shows two significant dips in the amplitude below 500 kHz. The reason for this lies in the fact that the sensor cannot be mounted perfectly flush to the wall. A small cavity of about 6/1000 in. remains in front of the sensing surface due to the geometry of the sensor provided by *Kulite*. Several tests were performed with the sensor mounted recessed from the wall. The frequency range and the magnitude of the dip correspond to different depths of the recess. The transfer function of the unscreened sensor shows a strong peak at about 500 kHz. *Kulite* reports the natural frequency of the sensing element at this frequency.

The transfer functions of the two sensors can now be calculated according to:

$$H(\omega) = \frac{S_{out}(\omega)}{S_{in}(\omega)} \quad (B.2)$$

In this Equation H is the transfer function of either one of the *Kulite* transducers. S_{out} is the sensor signal and S_{in} is the ideal step input.

The transfer functions will be modeled as a second-order system, in the hope to capture the physical behaviour better than with a purely numerical fit. The results are plotted in Figures B.9 and B.10. Along with the data presented in this paper and the second order approximation, another original transfer function from another experiment is added to demonstrate the degree of repeatability in these experiments.

The transfer function of the unscreened *Kulite* can only be modeled poorly by

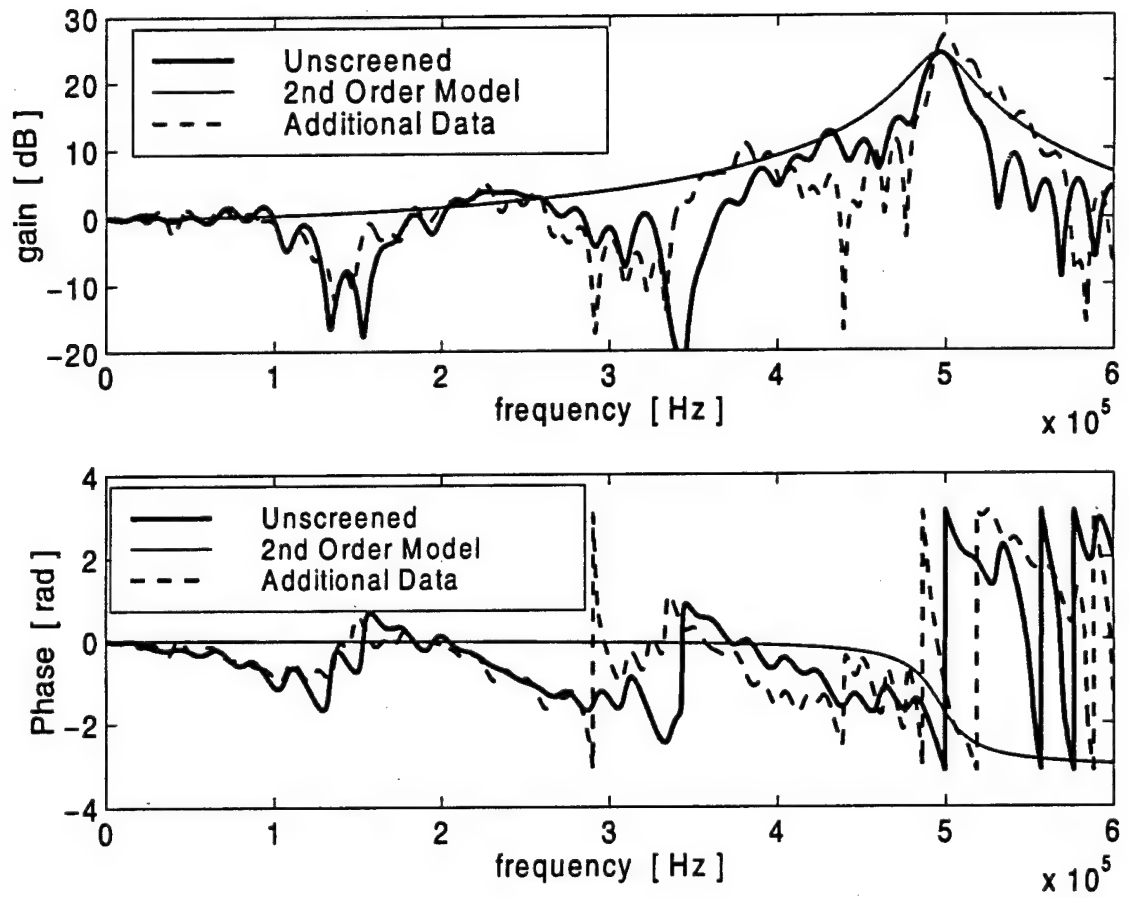


Figure B.9: Bode Plot of Transfer Function of Unscreened Sensor.

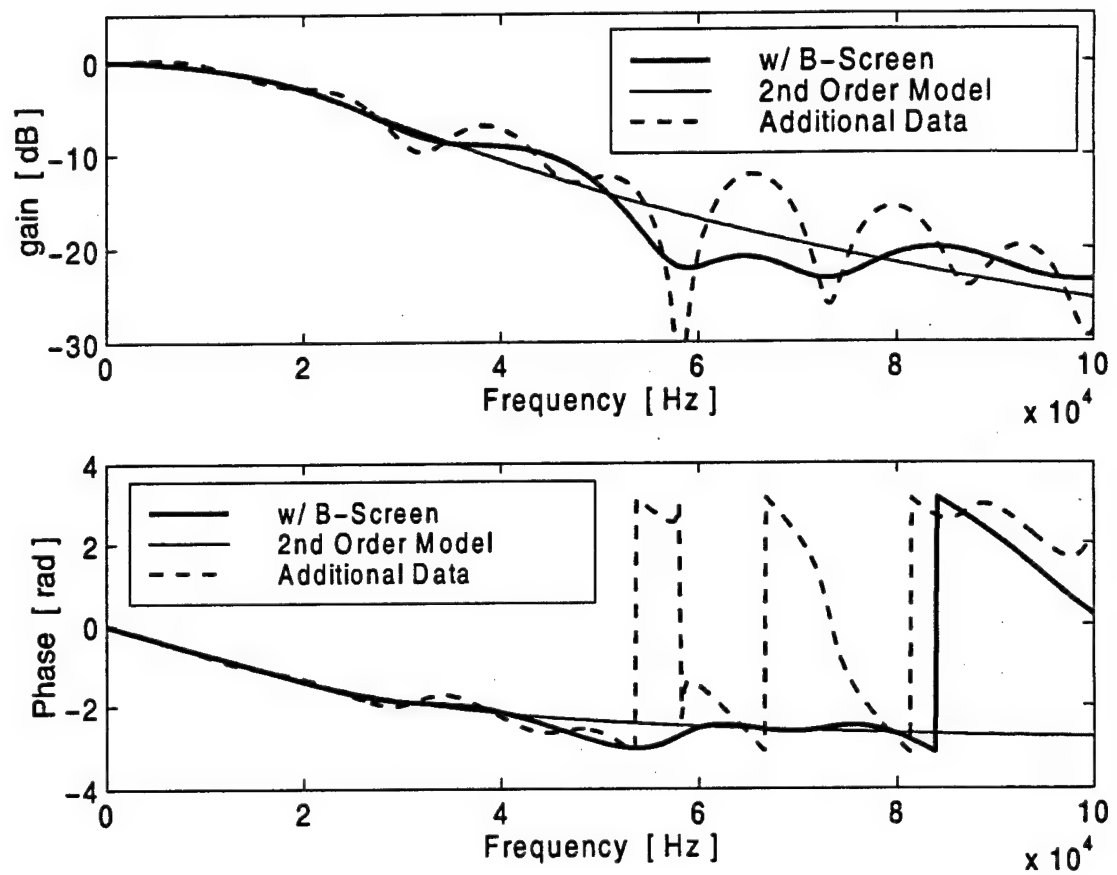


Figure B.10: Bode Plot of Transfer Function of Sensor with B-Screen.

the second order system for two reasons:

- The effect of the cavity seriously degenerates the transfer function in the frequency range below the natural frequency
- The signal to noise ratio decreases strongly in the frequency range beyond the natural frequency

The transfer function of the Sensor with the B-Screen can be modeled with very good agreement up to about 60 kHz. Beyond this frequency the signal seems to consist primarily of noise.

The influence of the B-Screen on the signal phase is unexpectedly strong, especially at rather low frequencies. When modeling the sensor with the B-screen as a second order system and approximating the experimental data up to about 60 kHz shown in Figure B.10, one obtains the coefficients of the transfer function expressed in the frequency domain:

$$H(j\omega) = \frac{B_1}{A_1 \cdot (j\omega)^2 + A_2 \cdot j\omega + A_3} \quad (\text{B.3})$$

The coefficients B_1 and A_1 through A_3 obtained from the two experiments are listed in Table B.1.

Table B.1: Coefficients A_i and B_i Describing the Transfer Function of the Kulite Pressure Transducer XCQ-062-50a with B-screen

Test	$\frac{B_1}{10^{10}}$	A_1	$\frac{A_2}{10^5}$	$\frac{A_3}{10^{10}}$
1	2.2097	1.0000	2.4773	2.1879
2	2.1739	1.0000	2.3290	2.1690

B.4 Conclusions

Two *Kulite* pressure sensors *XCQ-062-50a* were investigated. Their dynamic behavior was determined in terms of their transfer functions. The transfer functions were approximated using a second-order model. The influence of the B-Screen on the frequency response of the *Kulite* sensors is very strong even at rather low frequencies.

It is recommended not to use the screened *Kulite* sensors above a frequency of 60 to 80 kHz. Also, they should not be used in high speed measurements without an appropriate correction, e.g. the second order model proposed in this report.

Appendix C

Investigation of the Transfer Function of a *Vatell HFM-7/L* Heat Flux Sensor

C.1 Problem Statement and Approach

The transfer function of a *Vatell* Heat Flux Microsensor *HFM-7/L* is to be determined. The gauge is exposed to a "known" input of heat flux in a shock tube. The gauge is modeled as a first order system. The theoretical response of a first order system and the actual gauge response are compared to find the time constant.

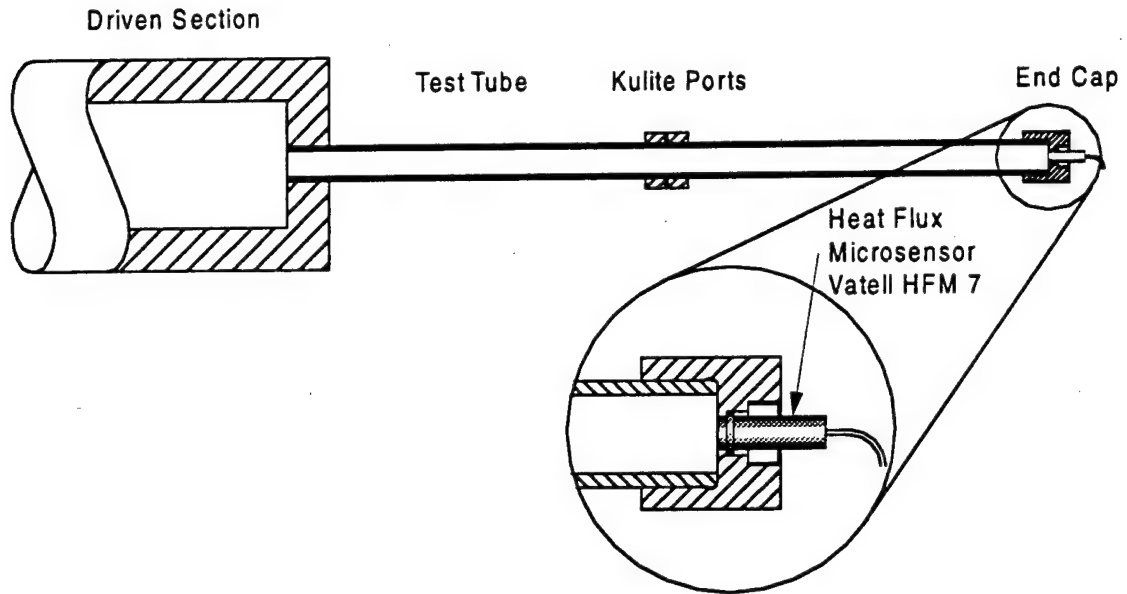


Figure C.1: Shock Tube with *Vatell* Heat Flux Sensor.

C.2 Experimental Setup

Modified Shock Tube

Figure C.1 shows the shock tube design. A 3/4 inch test pipe is connected to the end of the driven section of a 3 inch shock tube. The shock is triggered by the burst of a plastic diaphragm between driven section and driver section. As the shock reaches the end of the driven section, it propagates into the test tube, growing in strength in the transition. The shock then reaches the endcap of the test tube and is reflected. Flush mounted in the end cap is a *Vatell HFM 7* Heat Flux Sensor (serial # 588).

Measurement Chain

Vatell Amplifier

The *Analog Devices* Operational Amplifiers used to amplify the signal voltage from the heat flux sensor are specified to have a -3dB gain at 1 MHz for a gain setting of unity. For the preliminary results presented in this investigation this gain was chosen to get a good idea of the order of the time constant before any further experiments were conducted.

Filtering

A first test that included an anti-aliasing filter showed that the gauge has a time constant of the order of 20μ sec. It was therefore determined that with a sampling frequency of 5 MHz it was not necessary to filter to obtain clean data in the range up to 1MHz since the gauge itself acts as a strong filter. The frequency content above the Nyquist frequency is so small that aliasing can be neglected, and no filter was used.

C.3 Theoretical Heat Flux and Gauge Response

As the shock travels through the test tube it increases the temperature and the pressure according to the normal shock relations. The shock strength of the shock traveling toward the endcap has been measured by *Kulite* pressure transducers to be about 3.4 in terms of the ratio of static pressures before and after the shock (see the *Kulite* locations in Figure C.1). With the shock strength known, the strength of the

shock reflected off the endcap that is housing the heat flux sensor can be calculated. The combination of the impacting and the reflected shock determines the temperature increase from the fluid at rest to the temperature of the fluid after the passing of the reflected shock to be about 313°C.

The following assumptions will be made:

1. The fluid and the surrounding walls of the test tube are at thermal equilibrium before the shock comes by.
2. The fluid just after the reflection of the shock is at rest.
3. The fluid just after the reflection of the shock is at a constant temperature corresponding to the temperature increase due to the normal shock.

Accepting these assumptions, the situation can be viewed as follows:

A fluid at rest at a high temperature level (the level corresponding to the temperature after the shock reflection) is exposed to a sudden change of its boundary temperature, which is the test tube wall temperature. Instead of rapidly changing the fluid temperature by a traveling shock wave, it is assumed that the fluid was always at the higher temperature, and the wall temperature is suddenly dropped to the level before the shock interaction. Assuming the fluid to be a semi-infinite continuum with the test tube axis going into the medium and the end cap wall with the sensor to be its limit, one finds the heat flux at that boundary from the Greens function solution for a shock impact at time $t = 0$:

$$q = \frac{\beta_a \cdot \Delta T}{\sqrt{\pi \cdot t}} \quad (C.1)$$

In Equation C.1 q is the heat flux in $\frac{W}{m^2}$, β_a is the square root of the product of thermal conductivity, density and specific heat of air or the thermal product evaluated at the conditions after the reflected shock. The following conditions were calculated from the knowledge of the incoming shock strength:

$$\begin{aligned}k &= 0.05 \frac{W}{m \cdot K} \\ \rho &= 5.17 \frac{kg}{m^3} \\ c_p &= 1005 \frac{J}{kg \cdot K} \\ \beta_a &= 16.13 \frac{kg}{s^{2.5} \cdot K} \\ \Delta T &= 312.4K\end{aligned}\tag{C.2}$$

From this point on, Equation C.1 with the numerical values shown in this Table will be considered the theoretical heat flux.

The response of the gauge to this theoretical heat flux will be determined next. It has been determined from earlier experiments that the *HFM-7/L* behaves like a first order system with the transfer function in the Laplace Domain:

$$H_g = \frac{\frac{1}{\tau}}{\frac{1}{\tau} + s}\tag{C.3}$$

The s in Equation C.3 is the variable in the Laplace Domain. The time constant τ is the time constant of the gauge. It determines the frequency response and is the parameter looked for in this investigation.

The theoretical heat flux in the Laplace Domain can be expressed as:

$$\bar{q}_t = \beta_a \cdot \Delta T \cdot \frac{1}{\sqrt{s}} \quad (\text{C.4})$$

With Equation C.3 and Equation C.4 one can express the gauge response as:

$$\bar{q}_g = \beta \cdot \Delta T \cdot \frac{1}{\tau \cdot \sqrt{s} \cdot (s + \frac{1}{\tau})} \quad (\text{C.5})$$

One can transform Equation C.5 into the time domain to obtain:

$$q_g = \frac{2 \cdot \beta \cdot \Delta T}{\sqrt{\pi \cdot \tau}} \cdot e^{-\frac{t}{\tau}} \cdot \int_0^{\sqrt{\frac{t}{\tau}}} e^{a^2} \cdot da \quad (\text{C.6})$$

Unfortunately, Equation C.6 cannot be further simplified and has to be integrated numerically. From this point on this time function will be referred to as the theoretical gauge response.

C.4 Results and Discussion

In this preliminary study the objective is to find a good estimate of the time constant τ in order to characterize the transfer function of the gauge. This is accomplished by varying τ in Equation C.6 until good agreement with the experimental data is obtained. Figure C.2 shows very good agreement between the theoretical and the measured gauge response for a time constant of $17 \mu s$. Even though the agree-

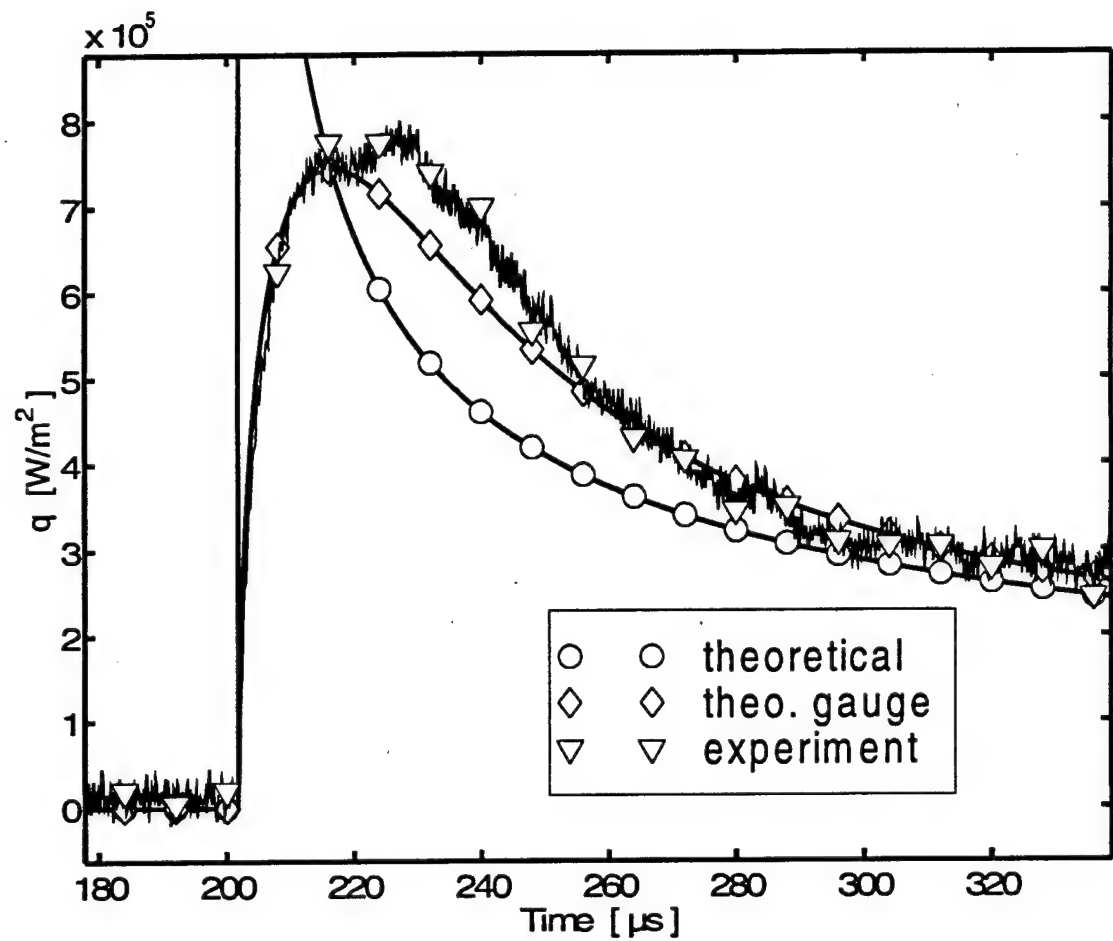


Figure C.2: Comparison of theoretical heat flux, theoretical gauge response and experimental data.

ment is very good for the rising portion of the trace, there seems to be some kind of disturbance after the peak. The reasons for this are being considered and possible modifications to the test setup will be implemented as needed.

Appendix D

Transfer Functions of the *Measurements Group 2310 Strain Gauge Conditioner and Signal Amplifier* at Different Gain Settings

The *Measurements Group 2310 Strain Gauge Conditioner and Signal Amplifier* has been used widely at Virginia Tech as a power supply and signal amplifier in connection with different *Kulite* transducers. The built-in filter unit is usually set to "Wide-Band". The gain settings, however, varied for different experiments. The only information given by the manufacturer concerning the transfer function of the amplifier at this setting is that it supposedly shows -3dB at 75 kHz. There is no mention of the dependency of this Figure on the gain setting.

For the present study this dynamic behavior had to be known in detail in order to obtain realistic representations of the very high frequency shock passing event. Therefore, the transfer functions were determined experimentally using the method called "sine sweep". A sine wave of known frequency and amplitude is fed into the input port of the amplifier. The resulting output signal is compared to the input signal in terms of phase shift and signal attenuation and/or gain. This is repeated for different frequencies and for different gain settings. The experimental data was then approximated assuming a "one zero, four pole" system. This combination seemed to represent the data best. The amplifier can then be treated mathematically in the following way:

$$H(j\omega) = \frac{B_1 \cdot j\omega + B_2}{A_1 \cdot (j\omega)^4 + A_2 \cdot (j\omega)^3 + A_3 \cdot (j\omega)^2 + A_4 \cdot (j\omega) + A_5} \quad (\text{D.1})$$

This Equation describes the transfer function $H(j\omega)$ in the frequency domain. The coefficients A_i and B_i are shown for the different gain settings in Table D.1. The

Table D.1: Coefficients A_i and B_i Describing the Transfer Function of the Measurements Group 2310 Strain Gauge Conditioner and Signal Amplifier according to Equation D.1

Gain	$\frac{B_1}{10^{20}}$	$\frac{B_2}{10^{27}}$	A_1	$\frac{A_2}{10^7}$	$\frac{A_3}{10^{14}}$	$\frac{A_4}{10^{20}}$	$\frac{A_5}{10^{27}}$
1	-1.4586	1.7702	1.0000	1.2607	1.9082	8.6212	1.7666
10	-2.5731	2.6934	1.0000	1.4670	1.6318	5.3787	0.2690
100	-5.8882	5.0545	1.0000	0.8025	0.5753	1.1604	0.0500
1000	-4.2997	4.3428	1.0000	0.5264	0.2098	0.1738	0.0042

experimental data is shown along with the approximation according to Equation D.1 and Table D.1 in Figure D.1 through D.4.

These graphs show that the transfer function of the amplifier is strongly dependent on the gain setting. Great care has to be taken when setting up a measurement

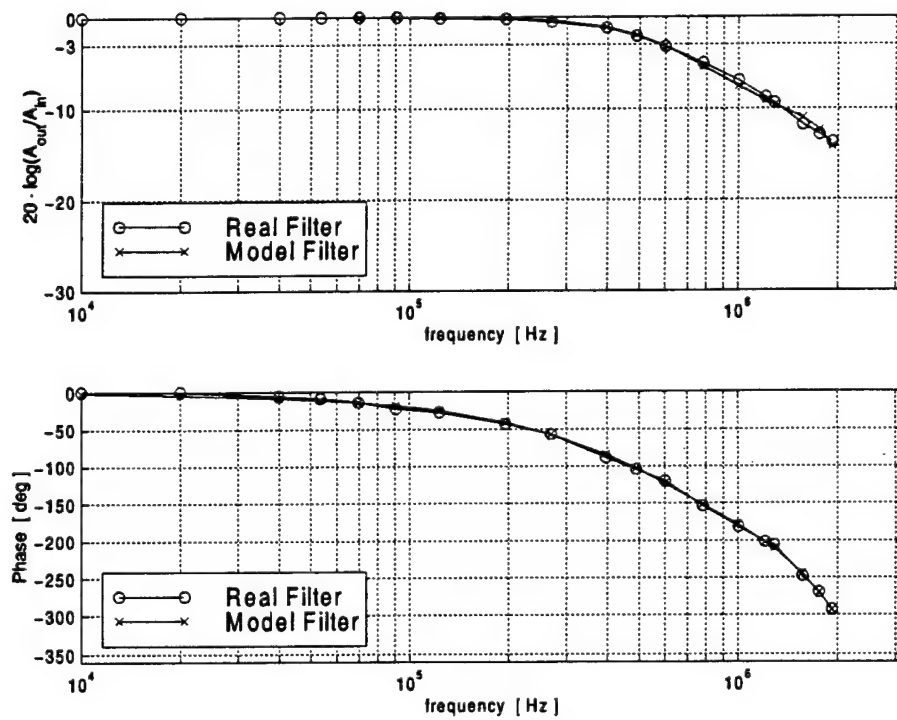


Figure D.1: Experimental and Approximated Transfer Function of the 2310 Amplifier at a Gain of 1.

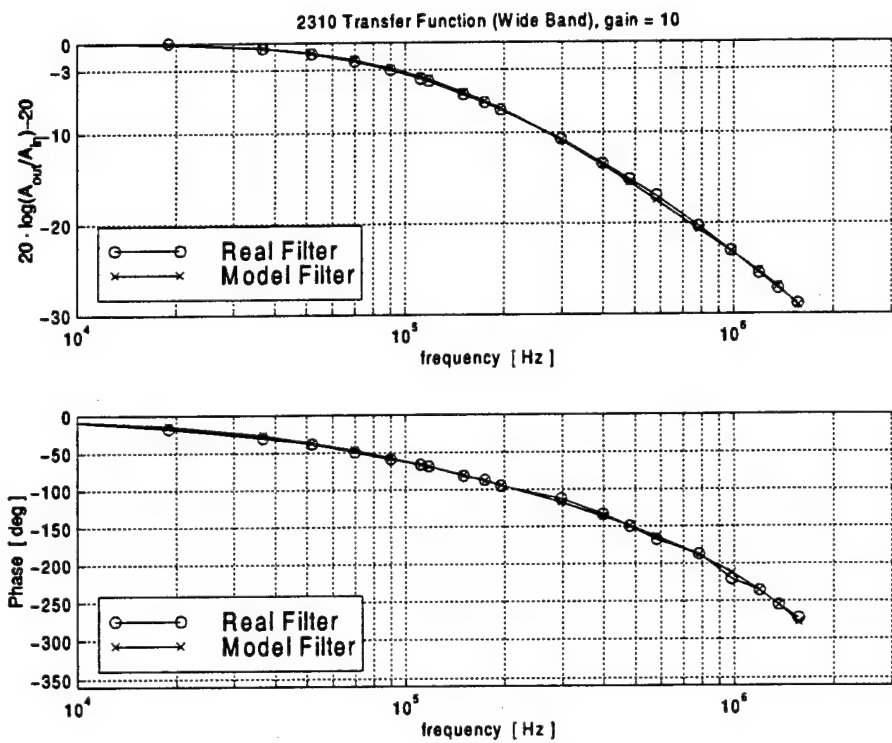


Figure D.2: Experimental and Approximated Transfer Function of the 2310 Amplifier at a Gain of 10.

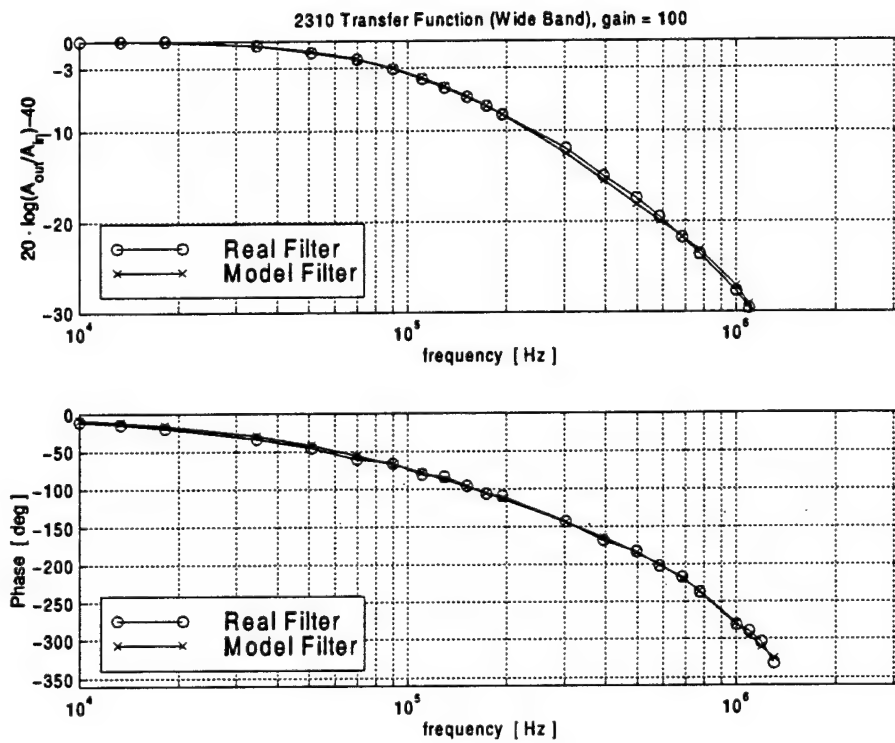


Figure D.3: Experimental and Approximated Transfer Function of the 2310 Amplifier at a Gain of 100.

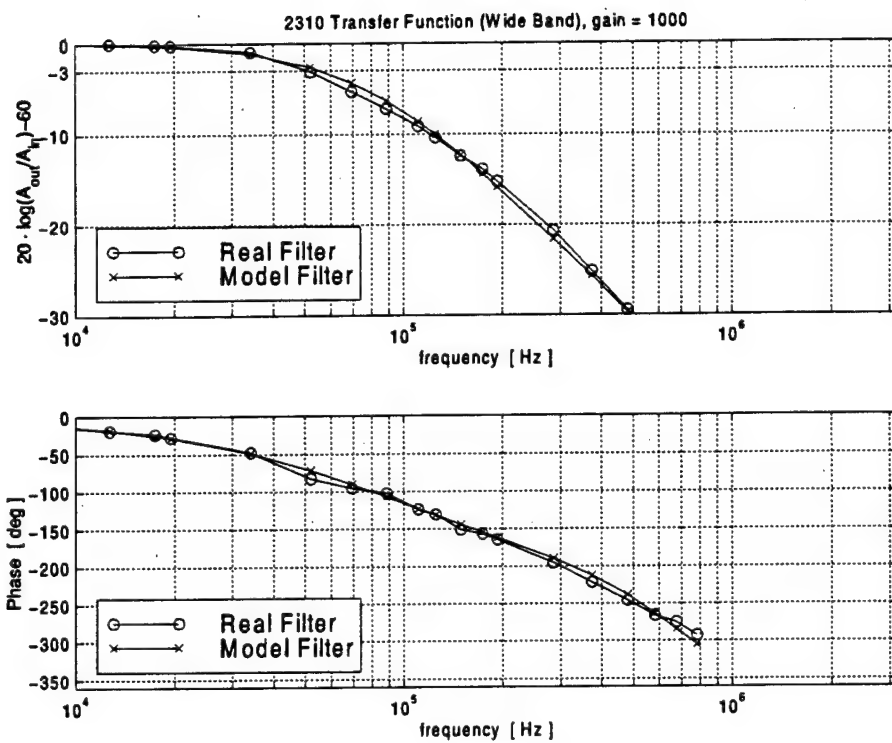


Figure D.4: Experimental and Approximated Transfer Function of the 2310 Amplifier at a Gain of 1000.

chain for high speed measurements. A wrong setting of the amplifier will significantly deteriorate the quality and credibility of the data.

Appendix E

Measurement Error

There are two issues in measurement error that are important to consider: measurement uncertainty and measurement repeatability. Measurement uncertainty refers to how close the measurements are to the true physical properties. Measurement repeatability, on the other hand, is a measure of how repeatable the tests can be reproduced from run to run and day to day. The first of these obstacles to tackle is measurement uncertainty.

E.1 Measurement Uncertainty

Within measurement uncertainty there are two categories, bias uncertainty and precision. A bias uncertainty refers to an error that is made consistently from measurement to measurement. These sorts of errors are typically associated with calibration of the transducers or consistent errors in an acquisition scheme. The precision uncertainty is associated with random errors that vary from measurement to measurement. The first area of uncertainty to address is the bias uncertainty.

Bias Uncertainty

For these experiments, The HFM sensors are the main component of bias uncertainty. Reliable measurements of heat flux are directly dependent on the calibrated sensitivity of each sensor. The sensors went through an extensive calibration procedure summarized by Smith et al. (1999). In this study, the gauges were calibrated with both convective and radiative heat flux. At the conclusion of the study, values for the uncertainty for each of the gauges sensitivities are given. These uncertainties are specific for each of the gauges installed in the blade, and are based on several of the convective tests and a 90% confidence interval assuming a Student-t distribution. These uncertainties are listed in Table E.1. The next question to answer is how do

Gauge	Uncertainty
1	17.0%
2	3.7%
3	5.2%
4	15.2%
5	8.8%
6	10.7%

Table E.1: HFM Gauge Uncertainties

these bias errors in heat flux measurements affect the bias of h , h_c , T_d and η .

Uncooled Runs: Bias Errors in h and T_d

The heat transfer coefficient is the slope of a linear fit to the independent variable, $(T_t - T_w)$, and the dependent variable q . Therefore, the bias error in q will directly translate into the heat transfer coefficient. The difference between total temperature and recovery temperature T_d is determined from the x-axis intercept, where $q = 0$. The bias error in q is a scaling factor and not an offset. Therefore, T_d is not affected by the bias error in q .

Cooled Runs: Bias Errors in h_c and η

Since the value of h_c is the slope of the linearized data, and q is plotted on the y-axis, these q uncertainties go directly into the h_c values, so that the values in Table E.1 can be understood directly as bias uncertainties in h_c . Also, the uncertainty of η is unaffected by uncertainties in the scale of q since η is derived from the x-axis intercept of the linearized data. The value of η is solely dependent upon temperature measurements and is unbiased using this data reduction method.

Precision Uncertainty

The next area of uncertainty is the precision uncertainty. The thermocouple measurements constitute this type of uncertainty. The kinds of errors that go into precision uncertainty are thermocouple wire difference from junction to junction, acquisition inconsistencies from channel to channel, or a wandering electronic ice point.

Uncooled Runs: Precision of h and T_d

Any uncertainty in the measurements of T_i and T_w cannot affect the slope of the linear fit for q and $T_i - T_w$, but will only shift the curve in the direction of the x-axis. The heat transfer coefficient is, therefore, free of precision error. The precision in the difference between T_i and T_w , on the other hand, will directly translate in a precision error in the result of T_d . Temperature measurements are made with K-Type thermocouples and the AMUX-64T multiplexer board. From the *National Instruments* literature the uncertainty of any individual temperature measurement is estimated to be $\pm 1.1^\circ\text{C}$ with respect to the "true" temperature recorded on the same data acquisition system with a perfect thermocouple. Therefore, the precision

on a temperature difference is $\sqrt{2} \cdot \pm 1.1^\circ\text{C} = \pm 1.56^\circ\text{C}$. This is at the same time the precision in the result for T_d .

Cooled Runs: Precision of h_c and η

The three thermocouple measurements that go into the h_c and η calculations are T_w , T_c , and T_r . For T_w and T_c the value of $\pm 1.1^\circ\text{C}$ was used as the precision (see paragraph above). The value used for T_r is 1.56°C since it is a derived value from two thermocouple measurements (square root of the sum of the squares).

In order to translate the individual thermocouple precision uncertainties to h_c and η precision uncertainties, a method was taken similar to that suggested by Moffat (1988). The first step of this approach is re-apply the h_c and η analysis using the nominal values of two of the temperature measurements and an "errored" third temperature measurement consisting of the measurement added to its uncertainty. The addition or subtraction of this individual uncertainty is done such that it has the greatest influence on the h_c and η values. Next, this procedure is repeated for each of the other two measurements individually and the influence of each measurement is computed. Knowing each individual contribution, the total uncertainty, δ , can be calculated as the sum of the squares of all three uncertainties,

$$\delta = \sqrt{\delta_{T_r}^2 + \delta_{T_w}^2 + \delta_{T_c}^2} \quad (\text{E1})$$

The results vary slightly from gauge to gauge and from run to run. A number of runs over different operating ranges were subjected to this uncertainty analysis and the maximum uncertainty for each gauge is listed in Table E.2.

Gauge	h_c Precision	η Precision
	[W / m ² °C], [%]	[-], [%]
1	43.5, 5.9%	0.040, 18.5%
2	49.2, 6.1%	0.041, 21.0%
3	35.0, 5.6%	0.036, 13.9%
4	42.5, 5.9%	0.040, 21.3%
5	48.3, 6.0%	0.040, 17.0%
6	49.4, 5.7%	0.034, 11.5%

Table E.2: Precision Uncertainties

E.2 Measurement Repeatability

Another indication of measurement error is measurement repeatability. This refers to the repeatability of runs conditions from run to run. Measurement repeatability is an experimental number that reflects the same ideas contained in the more theoretical value of precision uncertainty (from Sec. E.1). Measurement repeatability, however, also takes into account the real variations from run to run (e.g. variation of aerodynamic conditions, variations of humidity levels, coolant supply leakage, etc.). These sorts of errors have not been accounted for in the data reduction scheme and perhaps some of the sources of variation probably have not been even conceived. Because of this, it is important to get this experimental value of measurement repeatability.

Repeatability for Uncooled Runs

Using the six uncooled experiments used in this dissertation (see Tables in Section 2.3.1) one can obtain the repeatabilities listed in Table E.3 using a 90% confidence interval from a Student-t distribution with six degrees of freedom:

Gauge	h 90% Confidence Interval [W / m ² °C], [%]	T_i 90% Confidence Interval [°C]
1	± 26.0, ± 2.4%	± 1.48
2	± 20.4, ± 2.6%	± 1.22
3	± 14.3, ± 2.0%	± 0.76
4	± 22.2, ± 2.4%	± 0.60
5	± 28.3, ± 3.2%	± 0.64
6	± 50.9, ± 4.6%	± 0.88

Table E.3: Measurement Repeatability For Uncooled Runs

Repeatability for Cooled Runs

In order to quantify the measurement repeatability, a number of runs at approximately the same conditions were compared. There were the greatest number of runs performed near the cooling design point of a pressure ratio of 1.04. All of the runs for this pressure ratio were compared in Figure E.1 and E.2.

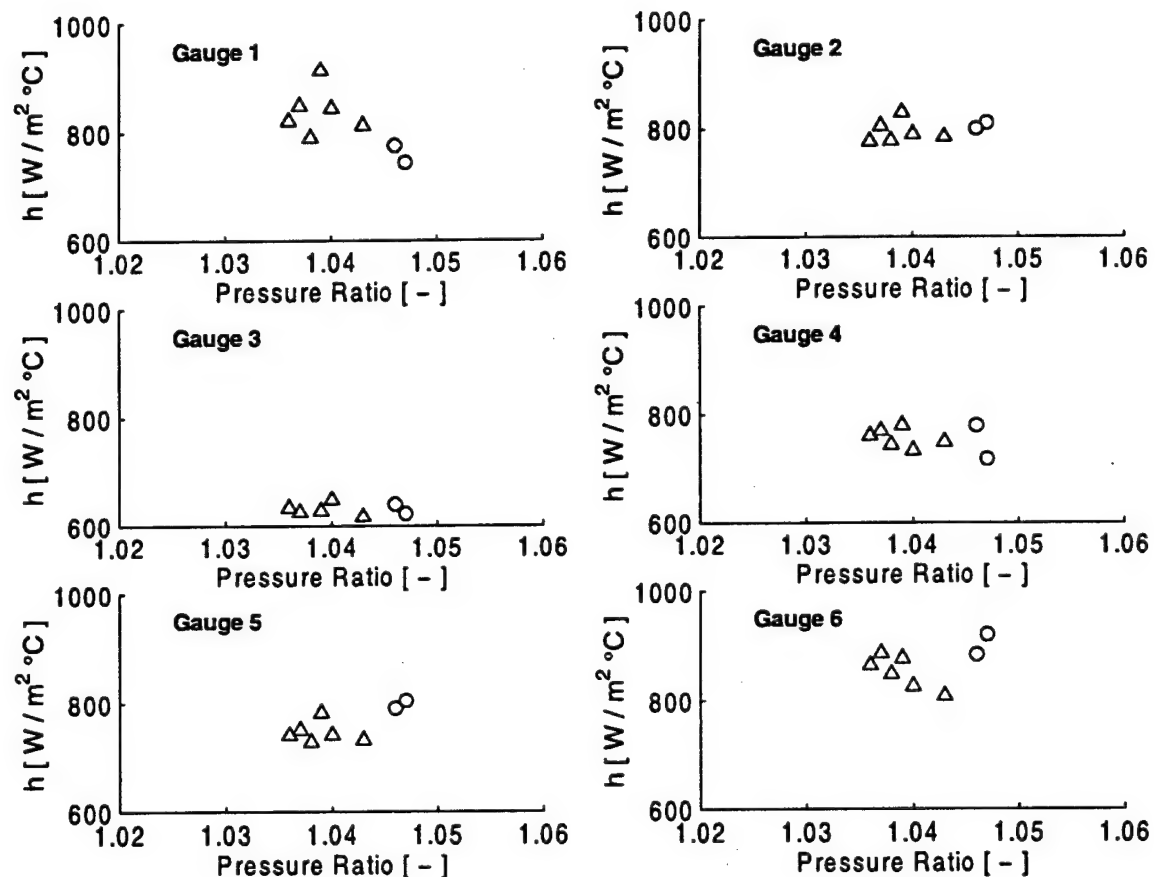


Figure E.1: Measurement Repeatability of Heat Transfer Coefficient at $PR=1.04$

These measurements were taken from eight different runs on two different days. There was considerable variation noticed from day to day. The different day's runs are shown with different symbols. With these runs, a Student-t distribution with a

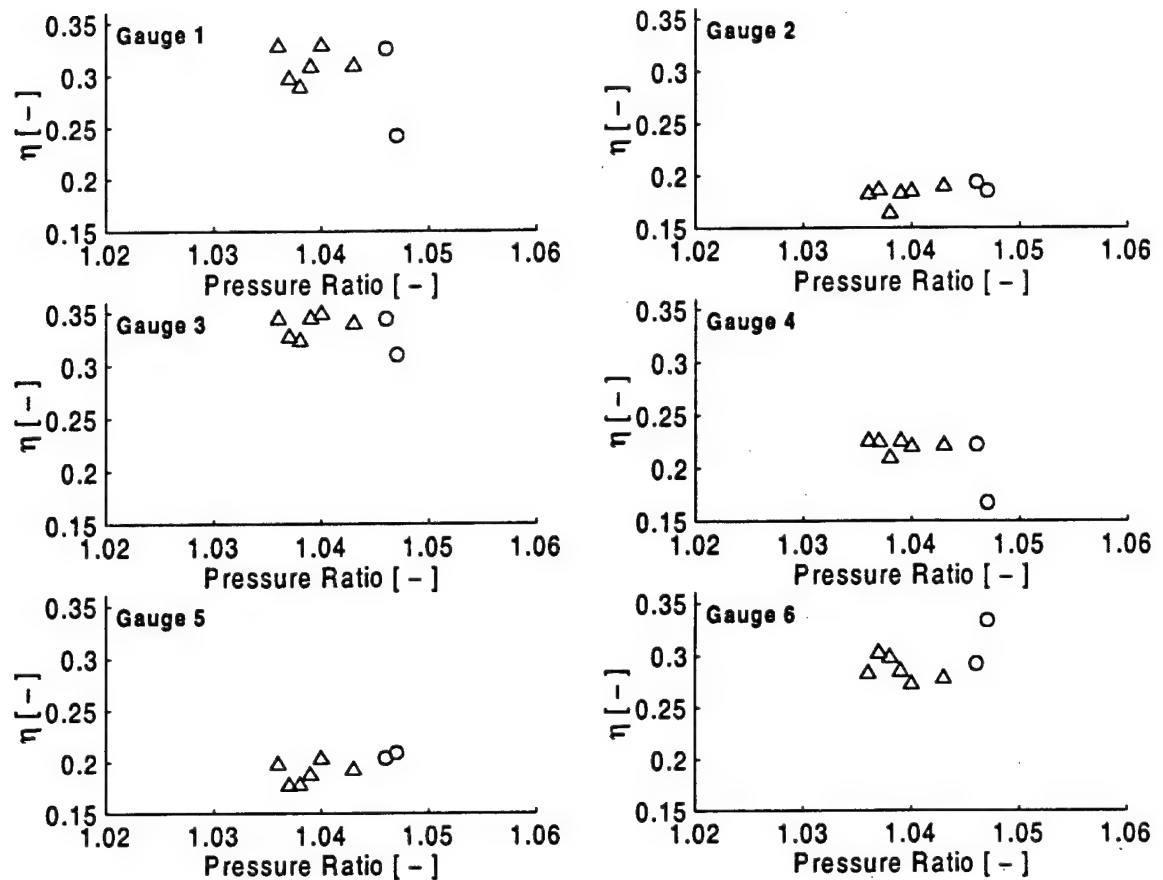


Figure E.2: Measurement Repeatability of Effectiveness at PR=1.04.

90% confidence interval is used. These confidence intervals are shown in Table E.4.

A consistency check can be observed that the observed measurement repeatability is of approximately the same size as at theoretical precision uncertainty. Gauge one is an exception to this generalization as its observed repeatability is higher than its predicted precision. I believe this is due to the fact that the flow physics around gauge one are extremely unstable as it is so close to the last coolant exit.

Gauge	h_c 90% Confidence Interval	η 90% Confidence Interval
	[W / m ² °C], [%]	[-], [%]
1	± 90, ± 11.1%	± 0.049, ± 16.4%
2	± 32, ± 4.0%	± 0.015 ± 8.2%
3	± 34, ± 5.5%	± 0.024, ± 7.1%
4	± 38, ± 5.1%	± 0.034, ± 15.8%
5	± 51, ± 6.7%	± 0.023, ± 12.1%
6	± 63, ± 7.3%	± 0.034, ± 11.4%

Table E.4: Measurement Repeatability for Cooled Runs

Appendix F

Discussion of the Surface Heat Flux Equations and their Discretization

It is often of interest to predict the heat flux to a surface from the surface temperature history recorded digitally in discretized form. Cook and Feldermann (1966) and Cook (1970) as well as Oldfield et al. (1978) and Diller (1996) developed numerical methods to perform this evaluation.

Johnson et al. (1988) and Rigby et al. (1989) showed that the same basic equation applies to the problem of heat transfer between a fluid and a surface in the presence of pressure perturbations in the flowfield. They used a numerical method developed by Oldfield et al. (1978) to obtain the heat flux to the surface.

In this Section the basic equation will be derived for the case of the semi-infinite solid. The same basic equation was derived in Section 3.5.3.3 for the case of pressure disturbances in the flow over a surface. Different discretization schemes

will be reported or developed in order to give an overview of the different options available.

F.1 Derivation of the Basic Equation

Semi-infinite Solid

Let x denote the distance into a semi-infinite solid with the surface at $x=0$. $T(x, t)$ be the temperature at a certain depth and time. Let α be:

$$\alpha = \frac{k}{\rho \cdot c} \quad (\text{F.1})$$

k be the thermal conductivity of the solid, ρ its density and c the specific heat. The differential heat conduction equation for one-dimensional heat transfer is then:

$$\frac{\partial^2 T(x, t)}{\partial x^2} = \frac{1}{\alpha} \cdot \frac{\partial T(x, t)}{\partial t} \quad (\text{F.2})$$

Transforming from the time domain into the Laplace domain:

$$\frac{\partial^2 \bar{T}(x, s)}{\partial x^2} = \frac{s}{\alpha} \cdot \bar{T}(x, s) \quad (\text{F.3})$$

Use was made of the fact that $\overline{\frac{\partial T(x,t)}{\partial t}} = s \cdot \bar{T}(x, s)$. The symbol \bar{T} denotes the Laplace transformed function of x . s is the Laplace variable. Equation F.3 is a differential equation in only one variable (x). The general solution of this equation is:

$$\bar{T}(x, s) = A \cdot e^{\sqrt{\frac{s}{\alpha}} x} + B \cdot e^{-\sqrt{\frac{s}{\alpha}} x} \quad (\text{F.4})$$

The first boundary condition is that at infinite depth the temperature change will always be zero:

$$T(\infty, t) = 0 \quad (\text{F.5})$$

Or transformed into the Laplace domain:

$$\bar{T}(\infty, s) = 0 \quad (\text{F.6})$$

Therefore, A in Equation F.4 has to be zero. The second boundary condition is the heat flux on the surface:

$$-k \cdot \left. \frac{\partial T(x, t)}{\partial x} \right|_{x=0} = q_s \quad (\text{F.7})$$

q_s is the heat flux per unit surface area at the surface of the solid. Transforming F.7 into the Laplace domain yields:

$$-k \cdot \frac{\partial \bar{T}(x, s)}{\partial x} \Big|_{x=0} = \bar{q}_s \quad (\text{F.8})$$

Taking the derivative of Equation F.4 with respect to x at $x = 0$ (noting that A is zero) and replacing in F.8 yields the solution for B . After rearranging:

$$B = \frac{\bar{q}_s}{\sqrt{s} \cdot \sqrt{k \cdot \rho \cdot c}} \quad (\text{F.9})$$

Replacing this solution into Equation F.4 yields the general solution of the temperature in a semi-infinite solid with a heat flux boundary condition:

$$\bar{T}(x, s) = \frac{\bar{q}_s}{\sqrt{s} \cdot \sqrt{k \cdot \rho \cdot c}} \cdot e^{-\sqrt{\frac{k}{c}} \cdot x} \quad (\text{F.10})$$

For the surface temperature at $x = 0$:

$$\bar{T}(0, s) = \frac{\bar{q}_s}{\sqrt{s} \cdot \sqrt{k \cdot \rho \cdot c}} \quad (\text{F.11})$$

And rearranged to yield the surface heat flux as a function of the surface temperature:

$$\bar{q}_s = \sqrt{k \cdot \rho \cdot c} \cdot \sqrt{s} \cdot \bar{T}(0, s) \quad (\text{F.12})$$

This Equation is useful in many applications that involve surface temperature measurements on a thick substrate or a substrate of low conductivity, where the assumption of a semi-infinite assumption is valid over a sufficiently long time.

The same equation can also be applied to a very different problem (Johnson et al. (1988) and Rigby et al. (1989)) as shown in the next paragraph.

Flow over a Surface with Pressure Perturbations

Rigby et al. (1989) derived equations to predict the heat transfer caused by pressure disturbances in the flow over a surface (see Section 3.5.3.3. One component of the unsteady heat flux due was attributed to the transient one-dimensional conduction in the fluid. The equation expressing this component of heat flux was shown to be: F.12:

$$\bar{q}_h(s) = \sqrt{k \cdot \rho \cdot c_p} \cdot T_w \cdot \overline{(1 - \Pi(t))} \cdot \sqrt{s} \quad (\text{F.13})$$

With the following definition

$$T_g(t) \equiv T_w \cdot (1 - \Pi(t)) \quad (\text{F.14})$$

Equation F.13 can be restated:

$$\bar{q}_h(s) = \sqrt{k \cdot \rho \cdot c_p} \cdot \bar{T}_g(s) \cdot \sqrt{s} \quad (\text{F.15})$$

This Equation is similar to Equation F.12. The following parameters correspond to each other: Both equations are derived from very different assumptions and for very

Table F.1: Corresponding Variables in Equations F.12 and F.15

Eq. F.12	Eq. F.15
\bar{q}_s = surface heat flux	$\bar{q}_h(s)$ = surface heat flux
$\sqrt{k \cdot \rho \cdot c}$ = Substrate Properties	$\sqrt{k \cdot \rho \cdot c_p}$ = Fluid Properties
$\bar{T}(0, s)$ = Substrate Surface Temperature	$\bar{T}_g(s)$ = Induced Fluid Temperature

different situations. For both problems (surface heat flux from surface temperature and surface heat flux from fluid temperature variation) the respective equation usually has to be evaluated numerically since the temperature data is recorded digitally. While some researchers use Equation F.12 or Equation F.15 to implement a numerical scheme others first invert to the time domain. For the purpose of this overview the basic equation is stated in the most general way:

$$\bar{q}(s) = \sqrt{k \cdot \rho \cdot c} \cdot \bar{T}(s) \cdot \sqrt{s} \quad (\text{F.16})$$

Expanding yields:

$$\bar{q}(s) = \sqrt{k \cdot \rho \cdot c} \cdot \bar{T}(s) \cdot s \cdot \frac{1}{\sqrt{s}} \quad (\text{F.17})$$

Note that $s \cdot \bar{T}(s) = \overline{\frac{\partial T}{\partial t}}$. Replacing into the above Equation yields:

$$\bar{q}(s) = \sqrt{k \cdot \rho \cdot c} \cdot \frac{\partial \bar{T}}{\partial t} \cdot \frac{1}{\sqrt{s}} \quad (\text{F.18})$$

From the rules of Laplace transforms:

$$\overline{\int_0^t f_1(t-\tau) \cdot f_2(\tau) \cdot d\tau} = \overline{f_1(t)} \cdot \overline{f_2(t)} \quad (\text{F.19})$$

The following replacement will be done:

$$\frac{1}{\sqrt{s}} = \overline{f_1(t)} \Rightarrow f_1(t) = \frac{1}{\sqrt{\pi \cdot t}} \quad (\text{F.20})$$

$$\frac{\partial T}{\partial t} = \overline{f_2(t)} \Rightarrow f_2(t) = \frac{\partial T}{\partial t} \quad (\text{F.21})$$

Replacing this substitution in F.16 yields:

$$\overline{q} = \frac{\sqrt{k \cdot \rho \cdot c}}{\sqrt{\pi}} \cdot \overline{\int_0^t \frac{1}{\sqrt{t-\tau}} \cdot \frac{\partial T}{\partial \tau} \cdot d\tau} \quad (\text{F.22})$$

This can easily be transformed into the time domain:

$$q = \frac{\sqrt{k \cdot \rho c}}{\sqrt{\pi}} \cdot \int_0^t \frac{\frac{\partial T}{\partial \tau}}{\sqrt{t-\tau}} \cdot d\tau \quad (\text{F.23})$$

The following substitution will simplify the integration and eliminate the temperature derivative:

$$z = T(t) - T(\tau) \quad \frac{\partial z}{\partial \tau} = -\frac{\partial T}{\partial \tau} \quad (\text{F.24})$$

With this substitution one can integrate F.23 by parts to obtain:

$$q(t) = \frac{\sqrt{k \cdot \rho \cdot c}}{\sqrt{\pi}} \left[\left[\frac{-z}{\sqrt{t-\tau}} \right]_0^t + \frac{1}{2} \cdot \int_0^t \frac{z}{(t-\tau)^{\frac{3}{2}}} \cdot d\tau \right] \quad (\text{F.25})$$

And resubstituting $z = T(t) - T(\tau)$ into Equation F.25 with $T(0) = 0$ finally yields:

$$q(t) = \frac{\sqrt{k \cdot \rho \cdot c}}{\sqrt{\pi}} \left[\frac{T(t)}{\sqrt{t}} + \frac{1}{2} \cdot \int_0^t \frac{T(t) - T(\tau)}{(t-\tau)^{\frac{3}{2}}} \cdot d\tau \right] \quad (\text{F.26})$$

This is the second form of Equation F.16 that is often used as the starting point for a numerical analysis. A third form was used by Vidall (1962). It will not be discussed here but only stated for completeness:

$$q(t) = \frac{\sqrt{k \cdot \rho \cdot c}}{\pi} \cdot \frac{\partial}{\partial t} \cdot \int_0^t \frac{T(\tau)}{\sqrt{t-\tau}} \cdot d\tau \quad (\text{F.27})$$

He uses an integrated form of Equation F.27:

$$q(t) = \frac{1}{2} \cdot \sqrt{k \cdot \rho \cdot c \cdot \pi} \cdot \left[\frac{T(t)}{\sqrt{t}} + \frac{1}{\pi \cdot \sqrt{t}} \cdot \int_0^t \frac{\sqrt{\tau} \cdot T(t) - \sqrt{t} \cdot T(\tau)}{(t-\tau)^{\frac{3}{2}}} \cdot d\tau \right] \quad (\text{F.28})$$

F.2 Comparison of Different Ways to Obtain Heat Flux from Discrete Temperature Data

Since temperature data is usually recorded digitally, only discrete data points are available. Therefore, Equation F.16 or F.26 have to be evaluated numerically. To do this, one has to interpolate the temperature data between the discrete samples. In the literature three different interpolation schemes have been used:

1. The temperature between two samples is constant. The change from T_{i-1} to T_i takes places at time t_i . This method will be denoted "Late Step" in the discussion to follow.
2. The temperature between two samples is constant. The change from T_i to T_{i+1} takes place at time t_i . This interpolation will be denoted "Early Step" for further discussion.
3. The temperature history between two samples is linear:

$$T(\tau) = T_{i-1} + \frac{T_i - T_{i-1}}{\Delta t} \cdot (\tau - t_{i-1}) \quad t_{i-1} \leq \tau \leq t_i \quad (\text{F.29})$$

This interpolation will be referred to as "Linear Interpolation".

Each of these interpolation schemes will be used with each of the two basic equations:

1. The original Equation in the Laplace domain F.16

$$\bar{q}(s) = \sqrt{k \cdot \rho \cdot c} \cdot \bar{T}(s) \cdot \sqrt{s} \quad (\text{F.30})$$

will be referred to as "Laplace-Equation".

2. The integrated Equation F.26

$$q(t) = \frac{\sqrt{k \cdot \rho \cdot c}}{\sqrt{\pi}} \left[\frac{T(t)}{\sqrt{t}} + \frac{1}{2} \cdot \int_0^t \frac{T(t) - T(\tau)}{(t - \tau)^{\frac{3}{2}}} \cdot d\tau \right] \quad (\text{F.31})$$

will be referred to as "Integral Equation".

The three different interpolation schemes combined with the two equations result in six different combinations. These combinations will be developed in the following six paragraphs.

The following form of the time series will be assumed:

$$\begin{aligned} t_i &= t_1, t_2, \dots, t_N & t_1 &= 0 \\ T_i &= T_1, T_2, \dots, T_N & T_1 &= T_2 = 0 \\ \Delta t &= \text{time step between two samples} \end{aligned} \quad (\text{F.32})$$

With N being the overall number of samples.

"Late Step" into "Laplace Equation"

The interpolated temperature time history for the case of the "Late Step" is:

$$T(t) = \sum_{i=2}^n (T_i - T_{i-1}) \cdot \langle t - t_i \rangle^0 \quad n: t_n < t \quad (\text{F.33})$$

Here $\langle x \rangle$ are the Lagrange operators. Transformed into the Laplace Domain:

$$\overline{T(t)} = \sum_{i=2}^n (T_i - T_{i-1}) \cdot \frac{1}{s} \cdot e^{-t_i \cdot s} \quad n: t_n < t \quad (\text{F.34})$$

Substituted into the "Laplace-Equation":

$$\overline{q(t)} = \sqrt{k \cdot \rho \cdot c} \cdot \sum_{i=2}^n (T_i - T_{i-1}) \cdot \frac{1}{\sqrt{s}} \cdot e^{-t_i \cdot s} \quad n: t_n < t \quad (\text{F.35})$$

Transformed into the time domain:

$$q(t) = \frac{\sqrt{k \cdot \rho \cdot c}}{\sqrt{\pi}} \cdot \sum_{i=2}^n (T_i - T_{i-1}) \cdot \frac{1}{\sqrt{t - t_i}} \quad n: t_n < t \quad (\text{F.36})$$

Applied to discrete time steps:

$$q(t_m) = \frac{\sqrt{k \cdot \rho \cdot c}}{\sqrt{\pi}} \cdot \sum_{i=2}^{m-1} (T_i - T_{i-1}) \cdot \frac{1}{\sqrt{t_m - t_i}} \quad (\text{F.37})$$

And simplified:

$$q(t_m) = \frac{\sqrt{k \cdot \rho \cdot c}}{\sqrt{\pi \cdot \Delta t}} \cdot \sum_{i=2}^{m-1} (T_i - T_{i-1}) \cdot \frac{1}{\sqrt{m - i}} \quad (\text{F.38})$$

For $m=1$ and $m=2$ no values of $q(t_m)$ are found. Note that the summation stops at $m-1$. The reason lies in the way the steps were defined. At the time step m the temperature is still T_{m-1} . Assumed the temperature history would have been defined as such:

$$T(t) = \sum_{i=2}^n (T_i - T_{i-1}) \cdot (t - t_i)^0 \quad n: t_n \leq t \quad (\text{F.39})$$

Then the final equation for $q(t_m)$ would have been:

$$q(t_m) = \frac{\sqrt{k \cdot \rho \cdot c}}{\sqrt{\pi \cdot \Delta t}} \cdot \sum_{i=2}^m (T_i - T_{i-1}) \cdot \frac{1}{\sqrt{m-i}} \quad (\text{F.40})$$

The last term of this series is indeterminate. The last element would have to be fixed by somehow assuming a different interpolation, e.g. a linear ramp.

“Early Step” into “Laplace-Equation”

For the case of an “Early Step” the interpolation for temperature is the following:

$$T(t) = \sum_{i=2}^n (T_i - T_{i-1}) \cdot (t - t_{i-1})^0 \quad n: t_{n-1} < t \quad (\text{F.41})$$

Transformed into the Laplace domain:

$$\overline{T(t)} = \sum_{i=2}^n (T_i - T_{i-1}) \cdot \frac{1}{s} \cdot e^{-t_{i-1} \cdot s} \quad n: t_{n-1} < t \quad (\text{F.42})$$

Substituted into the "Laplace-Equation":

$$\overline{q(t)} = \sqrt{k \cdot \rho \cdot c} \cdot \sum_{i=2}^n (T_i - T_{i-1}) \cdot \frac{1}{\sqrt{s}} \cdot e^{-t_{i-1} \cdot s} \quad n: t_{n-1} < t \quad (\text{F.43})$$

Transformed into the time domain:

$$q(t) = \frac{\sqrt{k \cdot \rho \cdot c}}{\sqrt{\pi}} \cdot \sum_{i=2}^n (T_i - T_{i-1}) \cdot \frac{1}{\sqrt{t - t_{i-1}}} \quad n: t_{n-1} < t \quad (\text{F.44})$$

Applied to discrete time steps:

$$q(t_m) = \frac{\sqrt{k \cdot \rho \cdot c}}{\sqrt{\pi}} \cdot \sum_{i=2}^m (T_i - T_{i-1}) \cdot \frac{1}{\sqrt{t_m - t_{i-1}}} \quad (\text{F.45})$$

And simplified:

$$q(t_m) = \frac{\sqrt{k \cdot \rho \cdot c}}{\sqrt{\pi \cdot \Delta t}} \cdot \sum_{i=2}^m (T_i - T_{i-1}) \cdot \frac{1}{\sqrt{m - i + 1}} \quad (\text{F.46})$$

For $m=1$ no value of $q(t_m)$ can be found. This time history is identical to Equation F.38 shifted one time step to the left. This equation was first published and compared to other schemes by Diller (1996). Note again that the definition of the time history is crucial for the stability of the scheme. Assume the time history was defined as:

$$T(t) = \sum_{i=2}^n (T_i - T_{i-1}) \cdot \langle t - t_{i-1} \rangle^0 \quad n: t_{n-1} \leq t \quad (\text{F.47})$$

Then the equation for $q(t_m)$ would have been:

$$q(t_m) = \frac{\sqrt{k \cdot \rho \cdot c}}{\sqrt{\pi \cdot \Delta t}} \cdot \sum_{i=2}^{m+1} (T_i - T_{i-1}) \cdot \frac{1}{\sqrt{m-i+1}} \quad (\text{F.48})$$

The last term of this series is indeterminate. A different interpolation needs to be used for the last time interval.

“Linear Interpolation” into “Laplace-Equation”

The time function of temperature is composed of linear ramps between data points:

$$T(t) = \sum_{i=2}^n \frac{T_{i+1} - 2 \cdot T_i + T_{i-1}}{\Delta t} \cdot (t - t_i) \quad n: t_n < t \quad (\text{F.49})$$

Transformed into the Laplace domain:

$$\overline{T(t)} = \sum_{i=2}^n \frac{T_{i+1} - 2 \cdot T_i + T_{i-1}}{\Delta t} \cdot \frac{1}{s^2} \cdot e^{-t_i \cdot s} \quad (\text{F.50})$$

Substituted into the "Laplace-Equation":

$$\overline{q(t)} = \sqrt{k \cdot \rho \cdot c} \cdot \sum_{i=2}^n \frac{T_{i+1} - 2 \cdot T_i + T_{i-1}}{\Delta t} \cdot \frac{1}{s \cdot \sqrt{s}} \cdot e^{-t_i \cdot s} \quad (\text{F.51})$$

Transformed into the time domain:

$$q(t) = \frac{2 \cdot \sqrt{k \cdot \rho \cdot c}}{\sqrt{\pi}} \cdot \sum_{i=2}^n \frac{T_{i+1} - 2 \cdot T_i + T_{i-1}}{\Delta t} \cdot \sqrt{t - t_i} \quad n: t_n < t \quad (\text{F.52})$$

Applied to discrete time steps:

$$q(t_m) = \frac{2 \cdot \sqrt{k \cdot \rho \cdot c}}{\sqrt{\pi}} \cdot \sum_{i=2}^{m-1} \frac{T_{i+1} - 2 \cdot T_i + T_{i-1}}{\Delta t} \cdot \sqrt{t_m - t_i} \quad n: t_n < t \quad (\text{F.53})$$

And simplified:

$$q(t_m) = \frac{2 \cdot \sqrt{k \cdot \rho \cdot c}}{\sqrt{\pi} \cdot \Delta t} \cdot \sum_{i=2}^{m-1} (T_{i+1} - 2 \cdot T_i + T_{i-1}) \cdot \sqrt{m - i} \quad (\text{F.54})$$

Note that for $m = 1$ and $m = 2$ no values $q(t_m)$ are found. This Equation was first published by Oldfield et al. (1978) and used by Johnson et al. (1988). An alternative form of Equation F.54 can be obtained by defining the temperature history as follows:

$$T(t) = \sum_{i=3}^n \frac{T_i - 2 \cdot T_{i-1} + T_{i-2}}{\Delta t} \cdot (t - t_{i-1}) \quad n: t_n < t \quad (\text{F.55})$$

This results in the following solution for $q(t_m)$ which gives the exact same result but is slightly easier to program:

$$q(t_m) = \frac{2 \cdot \sqrt{k \cdot \rho \cdot c}}{\sqrt{\pi} \cdot \Delta t} \cdot \sum_{i=3}^m (T_i - 2 \cdot T_{i-1} + T_{i-2}) \cdot \sqrt{m - i + 1} \quad (\text{F.56})$$

“Late Step” into “Integral Equation”

The temperature history for the “Late Step” can be defined as:

$$T(t) = T_{i-1} \quad \text{for} \quad t_{i-1} < t < t_i \quad (\text{F.57})$$

Replacing this interpolation into the “Integral Equation” and performing the integration over each element results in:

$$q(t_m) = \frac{\sqrt{k \cdot \rho \cdot c}}{\sqrt{\pi}} \cdot \left[\frac{T_m}{\sqrt{t_m}} + \frac{1}{2} \cdot \sum_{i=2}^m \int_{t_{i-1}}^{t_i} \frac{T_m - T_{i-1}}{(t_m - \tau)^{\frac{3}{2}}} \cdot d\tau \right] \quad (\text{F.58})$$

Performing the integration yields:

$$q(t_m) = \frac{\sqrt{k \cdot \rho \cdot c}}{\sqrt{\pi}} \cdot \left[\frac{T_m}{\sqrt{t_m}} + \sum_{i=2}^m \left[\frac{T_m - T_{i-1}}{(t_m - \tau)^{\frac{1}{2}}} \right]_{t_{i-1}}^{t_i} \right] \quad (\text{F.59})$$

And using the limits of integration:

$$q(t_m) = \frac{\sqrt{k \cdot \rho \cdot c}}{\sqrt{\pi}} \cdot \left[\frac{T_m}{\sqrt{t_m}} + \sum_{i=2}^m (T_m - T_{i-1}) \cdot \left[\frac{1}{(t_m - t_i)^{\frac{1}{2}}} - \frac{1}{(t_m - t_{i-1})^{\frac{1}{2}}} \right] \right] \quad (\text{F.60})$$

The last element of this series is indeterminate. One way to overcome this problem is to use a linear interpolation for the last time step. This yields the following result:

$$q(t_m) = \frac{\sqrt{k \cdot \rho \cdot c}}{\sqrt{\pi}} \cdot \left[\frac{T_m}{\sqrt{t_m}} + \sum_{i=2}^{m-1} (T_m - T_{i-1}) \cdot \left[\frac{1}{(t_m - t_i)^{\frac{1}{2}}} - \frac{1}{(t_m - t_{i-1})^{\frac{1}{2}}} \right] + \frac{T_m - T_{m-1}}{\sqrt{\Delta t}} \right] \quad (\text{F.61})$$

“Early Step” into “Integral Equation”

The temperature time history for the assumption of an “Early Step” can be defined as such:

$$T(t) = T_i \quad \text{for} \quad t_{i-1} < t < t_i \quad (\text{F.62})$$

The integration is the same as in the previous Section only T_i is used instead of T_{i-1} .
The result of the integration is:

$$q(t_m) = \frac{\sqrt{k \cdot \rho \cdot c}}{\sqrt{\pi}} \cdot \left[\frac{T_m}{\sqrt{t_m}} + \sum_{i=2}^m (T_m - T_i) \cdot \left[\frac{1}{(t_m - t_i)^{\frac{1}{2}}} - \frac{1}{(t_m - t_{i-1})^{\frac{1}{2}}} \right] \right] \quad (\text{F.63})$$

The last term of the summation is again indeterminate. Using a linear interpolation for the last element yields:

$$q(t_m) = \frac{\sqrt{k \cdot \rho \cdot c}}{\sqrt{\pi}} \cdot \left[\frac{T_m}{\sqrt{t_m}} + \sum_{i=2}^{m-1} (T_m - T_i) \cdot \left[\frac{1}{(t_m - t_i)^{\frac{1}{2}}} - \frac{1}{(t_m - t_{i-1})^{\frac{1}{2}}} \right] + \frac{T_m - T_{m-1}}{\sqrt{\Delta t}} \right] \quad (\text{F.64})$$

“Linear Interpolation” into “Integral Equation”

The linear temperature time history over a sample interval can be written as:

$$T(t) = T_{i-1} + \frac{T_i - T_{i-1}}{\Delta t} \cdot (t - t_{i-1}) \quad \text{for} \quad t_{i-1} < t < t_i \quad (\text{F.65})$$

The piecewise integration and summation was done in detail in Schultz et al. (1973). It is not going to be repeated here. The result of the integration is:

$$q(t_m) = \frac{\sqrt{k \cdot \rho \cdot c}}{\sqrt{\pi}} \cdot \left[\frac{T_m}{\sqrt{t_m}} + \frac{T_m - T_{m-1}}{\sqrt{\Delta t}} \right] + \frac{\sqrt{k \cdot \rho \cdot c}}{\sqrt{\pi}} \cdot \sum_{i=2}^{m-1} \left[\frac{T_m - T_i}{(t_m - t_i)^{\frac{1}{2}}} - \frac{T_m - T_{i-1}}{(t_m - t_{i-1})^{\frac{1}{2}}} + 2 \cdot \frac{T_i - T_{i-1}}{(t_m - t_i)^{\frac{1}{2}} + (t_m - t_{i-1})^{\frac{1}{2}}} \right] \quad (\text{F.66})$$

This expression was first presented by Cook et al. (1966). A simplified form of this equation was given by Schultz et al. (1973) and Cook (1970) without derivation (The factor of 2 was omitted by mistake in Schultz et al. (1973)):

$$q(t_m) = \frac{2 \cdot \sqrt{k \cdot \rho \cdot c}}{\sqrt{\pi}} \cdot \sum_{i=2}^m \frac{T_i - T_{i-1}}{(t_m - t_i)^{\frac{1}{2}} + (t_m - t_{i-1})^{\frac{1}{2}}} = \frac{2 \cdot \sqrt{k \cdot \rho \cdot c}}{\sqrt{\pi} \cdot \Delta t} \cdot \sum_{i=2}^m \frac{T_i - T_{i-1}}{(m-i)^{\frac{1}{2}} + (m-i+1)^{\frac{1}{2}}} \quad (\text{F.67})$$

For values $m=1$ and $m=2$ no values of $q(t_m)$ are obtained.

One Additional Equation

The linear interpolation gives a constant slope of temperature for each time interval:

$$T(t) = T_{i-1} + \frac{T_i - T_{i-1}}{\Delta t} \cdot t \quad t_{i-1} < t < t_i$$

$$\frac{\partial T}{\partial \tau} = \frac{T_i - T_{i-1}}{\Delta t} \quad (\text{F.68})$$

Replacing this constant derivative in F.23 and integrating piecewise:

$$\begin{aligned}
 q(t_m) &= \frac{\sqrt{k \cdot \rho \cdot c}}{\sqrt{\pi} \cdot \Delta t} \cdot \sum_{i=2}^m \int_{t_{i-1}}^{t_i} \frac{T_i - T_{i-1}}{\sqrt{t_m - \tau}} \\
 &= \frac{-2 \cdot \sqrt{k \cdot \rho \cdot c}}{\sqrt{\pi} \cdot \Delta t} \cdot \sum_{i=2}^m (T_i - T_{i-1}) \cdot [\sqrt{t_m - \tau}]_{t_{i-1}}^{t_i} \\
 &= \frac{2 \cdot \sqrt{k \cdot \rho \cdot c}}{\sqrt{\pi} \cdot \Delta t} \cdot \sum_{i=2}^m (T_i - T_{i-1}) \cdot (\sqrt{m-i+1} - \sqrt{m-i})
 \end{aligned} \tag{F.69}$$

Unlike any other scheme employing the linear interpolation, this Equation gives a result for $q(t_m)$ at $m=2$. This numerical scheme was first shown by Diller (1996).

Appendix G

Steady and Unsteady Heat Transfer in a Transonic Film Cooled Turbine Cascade

Presented at the 44th ASME Gas Turbine and Aeroengine Technical Congress,
Exposition and Users Symposium as Paper Number ASME 99-GT-259.

STEADY AND UNSTEADY HEAT TRANSFER IN A TRANSONIC FILM COOLED TURBINE CASCADE

Q. Popp, D. E. Smith, J. V. Bubb, H. C. Grabowski III, T.E. Diller, J. A. Schetz, Wing-Fai Ng
Virginia Polytechnic Institute and State University
Blacksburg, VA 24061

ABSTRACT

This paper reports on an investigation of the heat transfer on the suction side of a transonic film cooled turbine rotor blade in a linear cascade. Heat transfer coefficient and film effectiveness are first determined for steady conditions. The unsteady effects of a passing shock on the heat transfer are then investigated. The film cooling pattern used is a showerhead design with three rows on the suction side, one row at the stagnation point and two rows on the pressure side. The experiments were performed at engine representative temperature and pressure ratios using air as coolant. Heat transfer measurements are obtained using a Heat Flux Microsensor, and surface temperature is monitored with a surface thermocouple. Static pressure is monitored with a Kulite pressure transducer. The shock emerging from the trailing edge of the NGV and impinging on the rotor blades is modeled by passing a shock wave along the leading edges of the cascade blades. The steady-state heat transfer coefficient is 8% higher with film cooling than without film cooling. Shock heating of the freestream flow is determined to be the major contribution to the unsteady variation of heat flux, leading to an increase of about 30°C to 35°C in recovery temperature and adiabatic wall temperature.

NOMENCLATURE

Symbols

B	blowing ratio $(pu)_c/(pu)_f$
d	cooling hole diameter (1 mm)
c_p	specific heat of air, 1005 J/(kg K) in Eq.(3)
h	heat transfer coefficient w/o film cooling
h_c	heat transfer coefficient w/ film cooling
I	momentum ratio $(pu^2)_c/(pu^2)_f$
M	density ratio ρ_c/ρ_f
p	static pressure
Pr	Prandtl Number (0.71 in Eq.(9))
q	heat flux per unit area
q_{max}	peak value of the unsteady component of heat flux

q_e	bias in heat flux measurement (Eq.(8))
r	recovery factor in Eq.(3) and Eq.(6)
T_{aw}	local adiabatic wall temperature
T_c	coolant exit temperature
T_d	$T_t - T_r$, Eq.(3)
T_d^*	real value of measured T_d
T_p	coolant temperature in the cooling plenum
T_r	local recovery temperature
T_t	freestream total temperature
T_w	local wall or blade temperature
T_e	bias in temperature measurement $(T_r - T_w)$ (Eq.(5))
u	local freestream velocity in Eq.(3)
η	film effectiveness defined in Eq.(7)

Superscripts

unsteady variation

Subscripts

c	coolant or w/ film cooling
f	freestream

INTRODUCTION

The efficiency of a gas turbine engine increases with turbine inlet temperature. In the ongoing effort to raise the turbine inlet temperature the gas stream temperature is made to greatly exceed the operating temperatures of blade materials, requiring elaborate blade cooling techniques to be developed. One of these methods is to spread a thin layer of cold air between the hot gas and the surface to be protected, referred to as film cooling. The quest for higher thrust to weight ratios in the development of aero-engines has led to the design of nozzle guide vanes (NGV) with supersonic exit velocities. The rotor blades consequently are not only subject to wake but also shock impingement as they pass behind the NGV's at very high speed. The effect of this unsteady process on the heat transfer to the rotor blade has been the topic of a variety of research programs.

The vast majority of results have been presented by the research team led by Schultz and Jones at the University of Oxford. Johnson et

al. (1990) investigated the unsteady heat flux on rotor blades in a linear cascade simulating the wake and shock with a rotating bar mechanism upstream of the cascade. They found a turbulent spot forming on the leading edge produced after the collapse of the shock induced separation. Travelling along the suction side, this turbulent spot increases the heat transfer. Boundary layer transition due to wake impingement was observed to further enhance unsteady heat flux. Moss et al. (1997) performed tests in a rotating annular cascade indicating that the unsteady disturbances caused by the NGV's have little influence on the heat transfer coefficient and the time averaged heat flux. They indicate that the unsteady heat flux is caused mostly by the time variation in relative total temperature. The mean heat transfer level therefore is not strongly affected by the presence of the NGV's. None of these experiments involved rotor blade film cooling. Film cooling experiments have been done on the same blade geometry (Horton et al. 1985) but did not include unsteady effects.

Hilditch et al. (1995) performed time resolved heat transfer measurements on an axial turbine rotor and compared his results with data from the University of Oxford and MIT. The rotor blades were not cooled and no analysis was done to discriminate shock and wake effects.

Similarly, Abhari and Epstein (1992) measured unsteady heat flux on a film cooled rotor in a rotating transonic turbine stage. They observed large fluctuations of heat transfer over a blade passing period but did not distinguish between the effects of shocks and wakes.

Heidmann et al. (1997) experimentally and numerically investigated the effect of wake passing on the time-averaged heat flux in a film cooled annular cascade, modeling the wake using a rotating bar mechanism.

Hale et al. (1997) modeled the effect of wake passing in a quasi-steady way using a stationary strut. Increases in heat transfer coefficient were measured for a number of locations on the blade, particularly on the pressure side.

Nix et al. (1997) analyzed in detail the progression of a shock through the same cascade and its effect on the unsteady heat transfer. When averaged over a 200 μ s blade passing event, a maximum increase of heat flux of 60% was measured due to shock passing.

The intent in the present study is to measure and interpret the unsteady heat transfer due to an isolated shock, as opposed to a combination of wake and shock. The focus of the research has been extended to film cooled blades.

EXPERIMENTAL APPARATUS

Wind Tunnel Facility, Cascade and Shock Apparatus

The experiments necessary for this investigation were performed in the transonic blowdown wind tunnel at Virginia Tech. A passive heating device is available to achieve high (120°C) inlet temperatures to the cascade. It consists of many copper tubes that are preheated prior to running the tunnel. Fig. 1 shows the wind tunnel with the heating loop. With the present cascade, the facility allows run times of up to 35 seconds with the inlet pressure controlled. The test-section and cascade built for this investigation are shown in Fig. 2. The cascade consists of four full and two half blades forming five passages (see Fig. 2). The blade design is a generic, high-turning, first stage rotor geometry. It is scaled up three times to accommodate the cooling scheme and instrumentation. The span is 15.3 cm (6") and the aerodynamic chord is 13.6 cm (5.4"). Pitch and axial chord are 11.4 cm (4.5"). The Reynolds Number based on aerodynamic chord and exit conditions is about $6 \cdot 10^6$. The Mach Number distribution was shown to correspond to design conditions. To simulate the shock emerging from the trailing edge of a NGV, a shock tube creates a

shock wave which is sent along the leading edges of the cascade (see Fig. 2). The shock strength can be varied to obtain realistic pressure ratios. For the present investigation a shock strength of 1.08 (ratio of local static pressure behind shock and local static pressure before shock impact) was chosen. Accordingly, the shock Mach number is about 1.03 relative to the freestream flow.

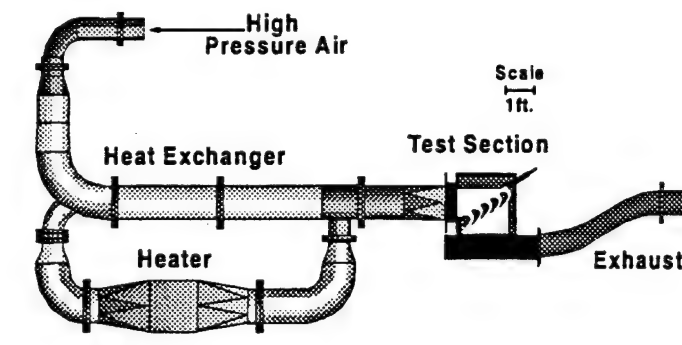


Figure 1: Wind Tunnel Facility

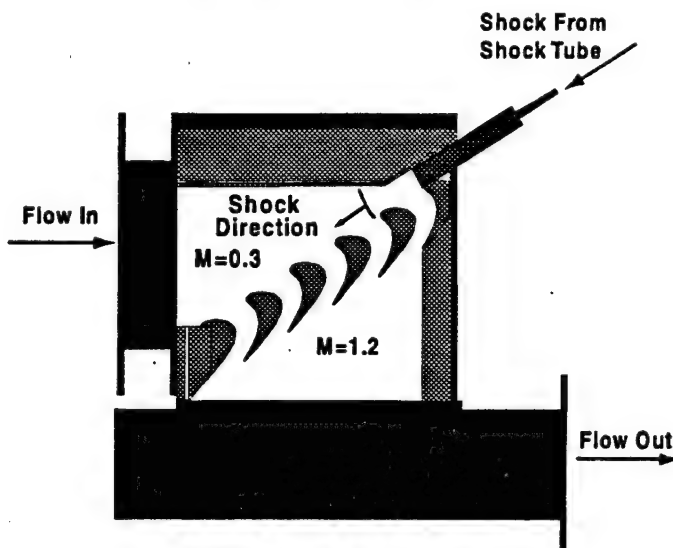


Figure 2: Cascade and Shock Apparatus

Cooling Pattern

A schematic of the showerhead film cooling design is shown in Fig. 3. All coolant holes are cylindrical and straight. The pressure and suction side gill holes form angles with the local chordwise tangent of 45° and 30°, respectively, and have no inclination in the radial direction. All other rows of holes are normal to the local chordwise tangent but angled 60° in the radial direction. Each row consists of 14 holes with a diameter of 1.04 mm (0.041") and a spacing of 9.14 mm (0.360"). The rows are staggered half the spacing with respect to the neighboring rows, yielding an overall pitch/diameter ratio of 4.39. Length/diameter ratios vary from 11.5 for the suction side gills to 4.4 for the suction side nose #2 row. Only the suction side gills and the suction side rows #1 and #2 actually affect the suction side heat transfer. The coolant ejected through the stagnation point row actually flows along the pressure side as observed from shadowgraph pictures. That means that in spite of pressure measurements locating the stagnation point right at the stagnation point row exit, it must be shifted towards the suction side.

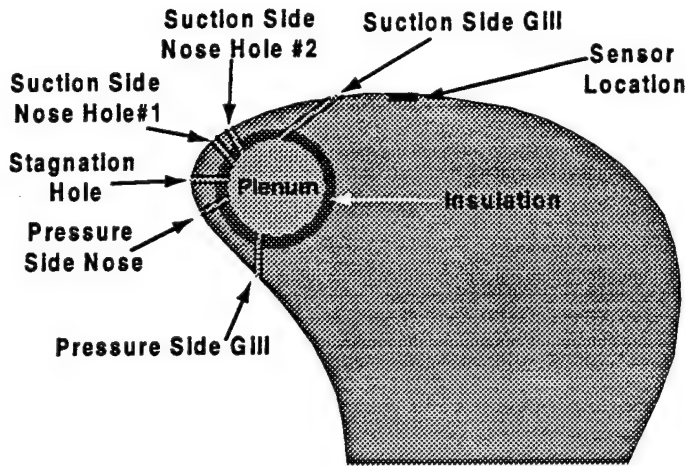


Figure 3: Blade Cooling Scheme

The nominal ratio of coolant to freestream total pressure for these experiments is 1.04. Therefore, the Momentum Ratio for each row of holes is kept constant while Density Ratio and Blowing Ratio vary with coolant temperature as shown later in section 'Steady-State Data Analysis and Results, With Film Cooling'. The temperature ratio T_t/T_c decreases from about 1.9 early in the experiment to about 1.5 late in the run. Homogeneous blowing through the cooling holes was checked by traversing a total and static pressure probe along the centerline of the cooling plenum. The resulting linear velocity distribution indicated uniform blowing. Coolant exit temperatures are measured with very small exposed junction thermocouples protruding into the exit of the last set of cooling holes. Conduction errors in those measurements were investigated experimentally. It was determined that these errors were negligible for the application in the blade. For the experiments without film cooling the plenum is fully plugged with a tightly fitting Nylon rod. The coolant supply is shown in Fig. 4. The two stage reciprocating compressor provides pressurized air at 12 bar (160 psig) to the storage tank. The dryer lowers the humidity to below three percent relative humidity.

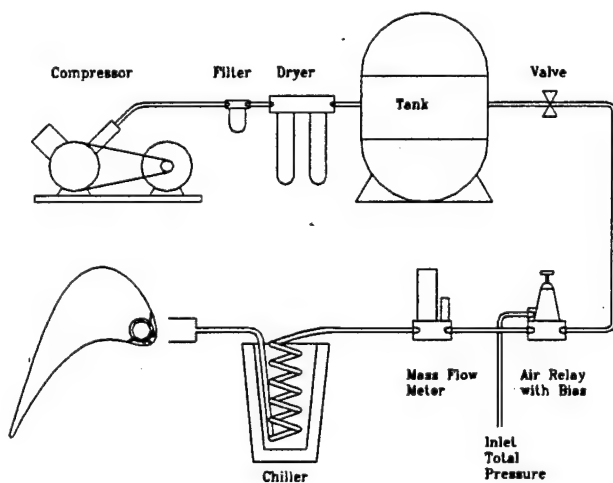


Figure 4: Coolant Supply

In order to control the difference between coolant and freestream total pressure, an air relay is used with the freestream total pressure as the signal and an adjustable bias. The chiller is a copper tube heat exchanger immersed in liquid nitrogen. It provides coolant temperatures down to -100°C in the plenum.

Sensors

The measurement location in this investigation is indicated in Fig. 5. Three different sensors are placed staggered in the spanwise direction. A surface thermocouple monitors the local blade temperature. It was designed to have thermal properties similar to the surrounding blade material (aluminum), and it is press fit to provide good thermal contact. The surface static pressure is measured with a Kulite pressure transducer, so that pressure variations due to the shock passing can be captured. Heat flux is measured using a heat flux microsensor. This sensor is described in detail in Diller (1993).

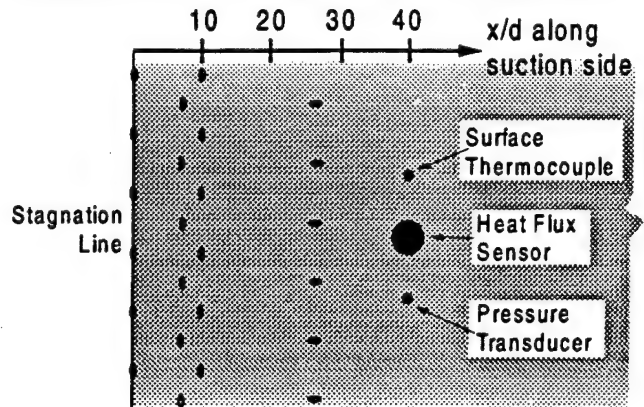


Figure 5: Plan View of a Section of the Suction Side Showing Sensor Locations and Coolant Exits

It behaves similar to a first-order system with a time constant of about $6\mu\text{s}$. Therefore, it is capable of tracing rapid changes like a shock passing with sufficient accuracy. The substrate material of the sensor is aluminum nitride which has thermal properties similar to aluminum but is electrically insulating. Consequently, the temperature history of the gauge should closely follow the local blade temperature. The active diameter of the gage is 5.3 mm (0.21"). Accordingly the gauge extends from 10 to 15 cooling hole diameters downstream of the suction side gills. The relative size and location of the sensor are expected to provide a spatially averaged value of heat flux. For the steady-state investigation, all signals are sampled at 100 Hz and filtered at 50 Hz. Both pressure and heat flux signal are sampled at 1 MHz and filtered at 40 kHz for the unsteady investigation.

Optical Access

To monitor the state of the cooling film and to visualize the shock passing process, shadowgraph pictures were taken either using Polaroid film (steady-state) or a high speed digital camera (shock passing). The digital camera is capable of taking four successive pictures with a frequency of up to 1 MHz. The high speed capability is necessary to investigate in detail the effect of the passing shock.

STEADY-STATE DATA ANALYSIS AND RESULTS

Without Film Cooling

The general definition of the heat transfer coefficient used here is

$$q = h \cdot (T_w - T_\infty) \quad (1)$$

With no cooling film present, the adiabatic wall temperature is the recovery temperature. Therefore

$$q = h \cdot (T_r - T_\infty) \quad (2)$$

The difference between the freestream total temperature and the recovery temperature is a function of the freestream velocity and the recovery factor

$$T_d = T_t - T_r = (1-r) \cdot \frac{u^2}{2 \cdot c_p} \quad (3)$$

This difference T_d is a constant throughout the run. Therefore Eq. (2) can be written as

$$q = h \cdot (T_t - T_\infty) - h \cdot T_d \quad (4)$$

Eq. (4) is a linear equation with the independent variable $(T_t - T_\infty)$ and the dependent variable q . The slope is the heat transfer coefficient h , and T_d is the intercept at $q=0$ as illustrated in Fig. 6. The temperatures T_t , T_∞ , and the heat flux q vary during the experiment, since the passive heating device is cooling down as the freestream air is drawing heat from the copper tubes. The blade temperature is increasing during the tunnel run, so the overall temperature difference $(T_t - T_\infty)$ and the heat flux q decrease (see Fig. 7). Assuming that h is not a function of the temperatures involved, one can obtain the heat transfer coefficient and T_d by fitting Eq. (4) to the data. A typical graph illustrating this technique is shown in Fig. 6. The data shows linear behavior as expected. The difference between the freestream total and wall temperatures never actually reaches zero. It typically spans the range from 70°C down to 10°C. The intercept at $q=0$ is, therefore, an extrapolation which seems justified. The corresponding time history of heat transfer coefficient (h) and recovery temperature obtained using the calculated T_d is shown in Fig. 7 along with the total temperature (T_t), the blade temperature (T_w), and the heat flux (q) during a run.

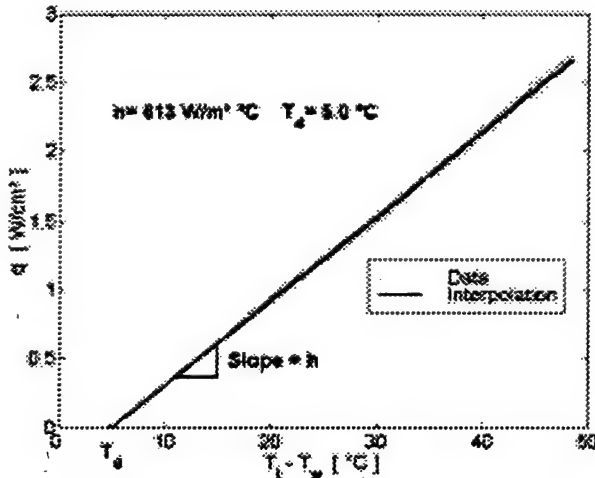


Figure 6: Interpolation for h and T_d (Uncooled Run #6)

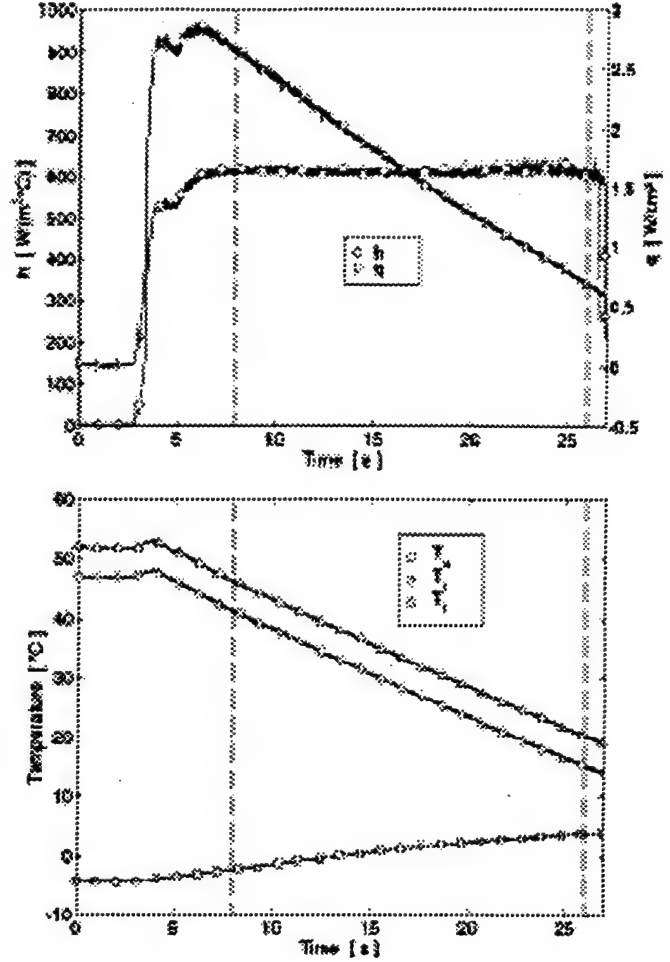


Figure 7: Time History of T_t , T_r , T_w , h , q (Uncooled Run #6)
(Dashed Lines Indicate Range of Useful Data)

An error analysis shows that bias errors in both the heat flux and the temperature measurement do not affect the resulting heat transfer coefficient. This is because an offset of the data in either the x or y-direction ($(T_t - T_w)$ and q respectively) does not change the slope of the curve. Accordingly, the experimental scatter for the heat transfer coefficient is small. T_d on the other hand is more severely affected by measurement uncertainty. A bias error in both temperature and heat flux measurement transfers directly into an error in recovery temperature

$$T_d = T_t^* - T_\infty + \frac{q_\epsilon}{h} \quad (5)$$

Therefore, the scatter is larger. The experimental results for several repeating runs are shown in Table 1. The difference between total and recovery temperature based on

$$r = \sqrt{Pr} \quad (6)$$

and the local Mach Number of 0.6 would yield a value of T_d of 4.2°C, assuming an average T_t . Shadowgraph and Schlieren pictures had

shown that the boundary layer at the blade location of interest is laminar. It needs to be stated that all the experimental results of T_d are higher than the ones based on isothermal flat plate calculations. The reason for this is either in the measurement accuracy (Eq.(5)) or in the steep pressure gradient.

Run #	1	2	3	4	5	6	7	8	9
h [W/m ² °C]	635	620	639	654	664	613	625	623	637
T_d [°C]	6.9	8.6	7.0	7.7	8.8	5.0	6.9	7.3	4.7

Table 1: Run-to-Run Variation of h and T_d

With Film Cooling

To indicate the state of the cooling film, shadowgraphs and Schlieren pictures are taken both with Polaroid film and the high-speed digital camera. The shadowgraph in Fig. 8 shows that the film is attached to the surface showing turbulent structures. The pressure side is hidden by instrumentation outside of the cascade.

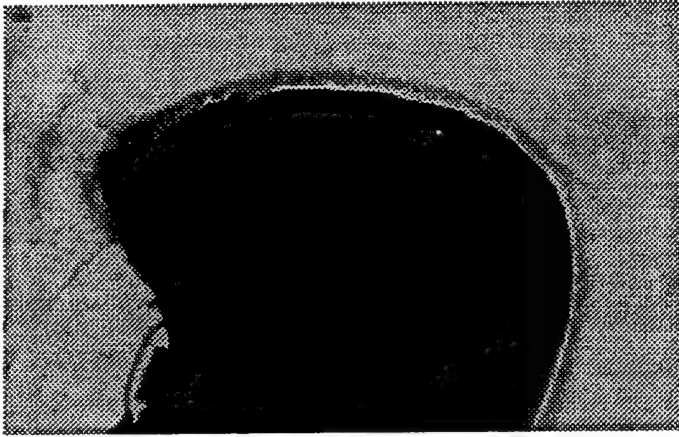


Figure 8: Shadowgraph Showing Attached Film

With film cooling, the adiabatic wall temperature is usually expressed in terms of the film effectiveness.

$$\eta = \frac{T_{aw} - T_r}{T_c - T_r} \quad \text{or} \quad T_{aw} = T_r - \eta \cdot (T_r - T_c) \quad (7)$$

Substituting Eq. (5) into Eq. (1) yields

$$q = h_c \cdot (T_r - T_{aw} - \eta \cdot (T_r - T_c)) \quad (8)$$

Dividing by $(T_r - T_c)$ yields

$$\frac{q}{T_r - T_c} = h_c \cdot \frac{T_r - T_{aw}}{T_r - T_c} - h_c \cdot \eta \quad (9)$$

Since the temperatures and heat flux levels change considerably during the experiment, a wide range of values is obtained, as illustrated in Fig. 9. Assuming that h_c and η are not functions of temperatures, Eq. (9) is a linear relation between the fraction on the left hand side and the temperature ratio on the right hand side. The slope is the heat transfer coefficient, and the intercept at $q=0$ is the film effectiveness.

The recovery temperature is calculated by subtracting the average T_d of 6.9°C from the freestream total temperature. The coolant temperature is determined using the mass flow averaged exit coolant temperatures from the three rows of cooling holes affecting the suction side. A representative example is shown in Fig. 9. Since the data follows the linear interpolation closely, it can be stated that the assumptions leading up to this interpretation of the data are correct. Specifically, the heat transfer coefficient and the film effectiveness do not vary significantly throughout the run.

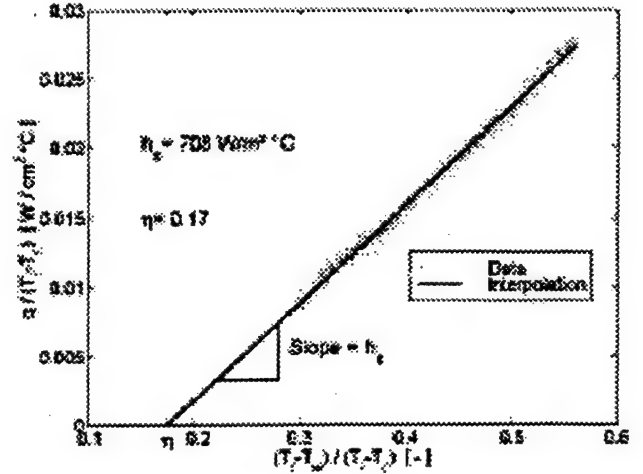


Figure 9: Interpolation for h_c and η (Run #5)

Fig. 10 a) shows the time history of the heat transfer coefficient calculated using the film effectiveness in Fig. 9. The heat transfer coefficient determined this way is very uniform throughout the time window used for the data analysis. In Fig. 10 b) all temperatures involved during this particular experiment are shown. T_{aw} is based on the film effectiveness determined in Fig. 9. It is evident that the coolant exit temperature is significantly higher than the coolant total temperature in the plenum indicating high heat transfer rates in the cooling holes. Fig. 10 c) gives the Density Ratio, Blowing Ratios and Momentum Ratios for all three cooling hole locations of interest. Since the Density Ratio is not a function of the local freestream Mach Number it is the same for all coolant exit locations. Since the total pressure ratio is kept relatively constant throughout the run, the Momentum Ratios are close to uniform. Even though the Momentum Ratios are repeatable, the coolant total temperature varies somewhat from run to run, since there was no physical control for this parameter. As shown in Fig. 10 b) the freestream total temperature changes with time. That causes the decrease of Density Ratio and Blowing Ratio shown in Fig. 10 c). All Ratios are based on isentropic flow through the holes. Realistically, it would be hard to analyze the flow through the cooling holes since not only frictional effects but also high heat transfer rates (see Fig. 10 b)) would have to be taken into account. Based on coolant mass flow measurements an average discharge coefficient of 0.66 for all cooling holes was determined.

The average heat transfer coefficient with film cooling (686 W/(m²°C)) is 8% higher than h without film cooling (634 W/(m²°C)). Using a thermal conductivity of 0.030 W/mK and the axial chord (0.114 m) to obtain the Nusselt number, yields values of 2410 and 2610 for the experiments without and with film cooling, respectively. The average film effectiveness of 15.3% appears to be rather low.

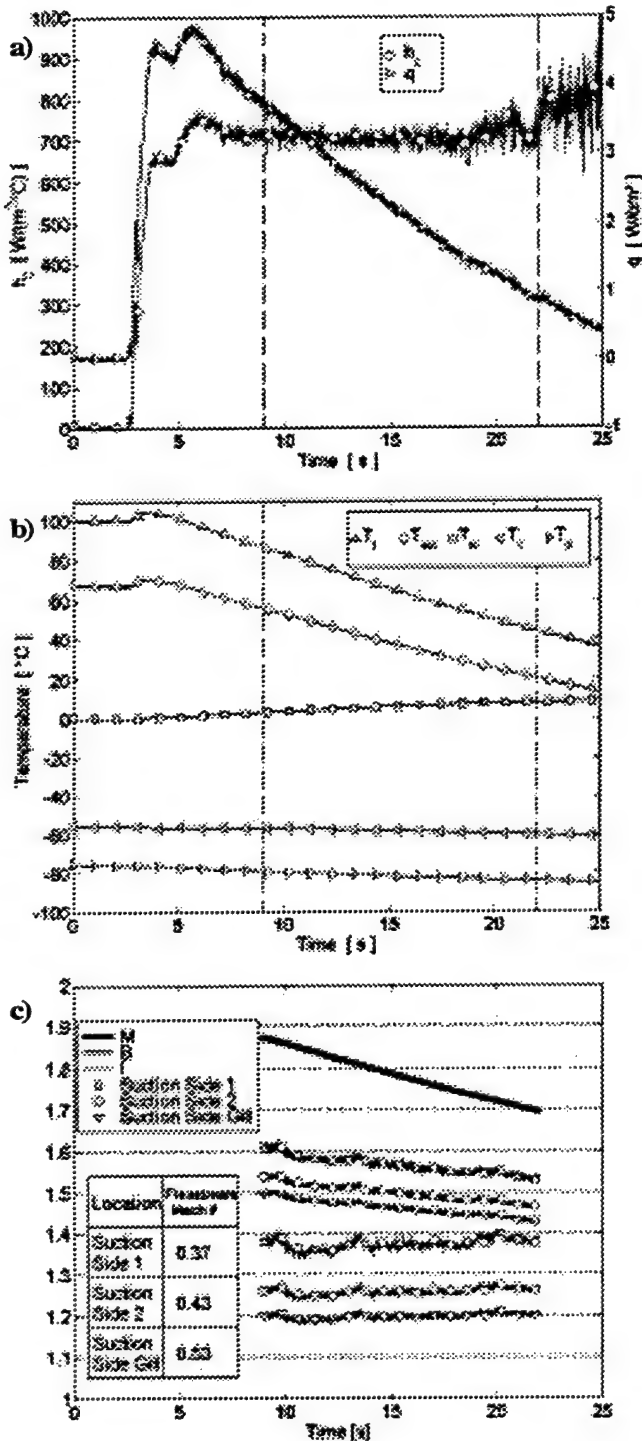


Figure 10: Time Histories from Cooled Run #5

a) Heat Transfer and Heat Transfer Coefficient

b) All Relevant Temperatures

c) Density Ratio, Blowing Ratio, Momentum Ratio
(Dashed Lines Indicate Range of Useful Data)

In low speed cascade tests with one closely spaced row of holes on the suction side of a large scale blade model, Ito et al. (1978) found comparably low values for film effectiveness for similar Momentum

Ratios and gauge locations. Values between about 4% and 17% are found for gauge locations between $x/D=10$ and $x/D=15$ and Momentum Ratios between 1.0 and 2.3.

An error analysis for the method presented shows that the heat transfer coefficient is sensitive to bias errors in temperature and heat transfer measurement. Therefore, a larger scatter in the experimental results can be expected. The film effectiveness is also subject to higher scatter, as it is calculated from the intercept and the heat transfer coefficient. Results for heat transfer coefficient and film effectiveness are shown in Table 2. If the theoretical value for T_d (4.2°C) was used instead of the experimental value (6.9°C) the results for h_c and η would be a few percent higher.

Run #	11	12	13	14	15	16	17	18
h_c [W/m ² °C]	709	623	672	715	708	704	685	675
η [%]	16.6	12.0	17.0	16.6	16.8	14.6	15.1	13.5

Table 2: Run-to-Run Variation of h_c and η

SHOCK PASSING DATA ANALYSIS AND RESULTS

Shock Passing without Film cooling

For the analysis of the passing shock event Eq. (2) will be rewritten in such a way that all properties that are a function of time will be broken down into a mean value before shock impact (no superscript) and a time varying component (superscript \prime). The unsteady heat flux during the event of a passing shock can then be expressed in terms of mean and fluctuating components:

$$q + q' = (h + h') \cdot (T_f + T_f' - T_w) \quad (10)$$

The wall temperature does not change during the short duration of the shock passing. Expanding the right hand side of Eq. (10) yields:

$$q + q' = h \cdot (T_f - T_w) + h' \cdot (T_f - T_w) + h \cdot T_f' + h' \cdot T_f' \quad (11)$$

Subtracting the mean heat flux on both sides yields the fluctuating component of heat transfer:

$$q' = h' \cdot (T_f - T_w) + h \cdot T_f' + h' \cdot T_f' \quad (12)$$

The goal of this investigation is to determine the time variation of heat transfer coefficient (h') and recovery temperature (T_f') during the shock event which constitute the three components of unsteady heat transfer on the right hand side of Eq. (12). In Fig. 11, the traces of heat flux during a shock passing event are shown for different runs. The numbering corresponds to the run numbers in the steady state experiments (Table 1). The different levels of heat flux before the run are due to the fact that the shock is purposely initiated at different times during the run, i.e. at different temperature levels. Run #10 is not listed in Table 1 since the temperature differences were intentionally kept very small for this particular experiment. Therefore h and T_d could not be determined from this run. The time history of heat flux for times later than about $400 \mu\text{s}$ is of no interest since it is dominated by the interaction of shock reflections and later the contact surface emerging from the shock tube. These phenomena are not observed in the engine. Therefore, this investigation focuses on the impact of the first shock front primarily.

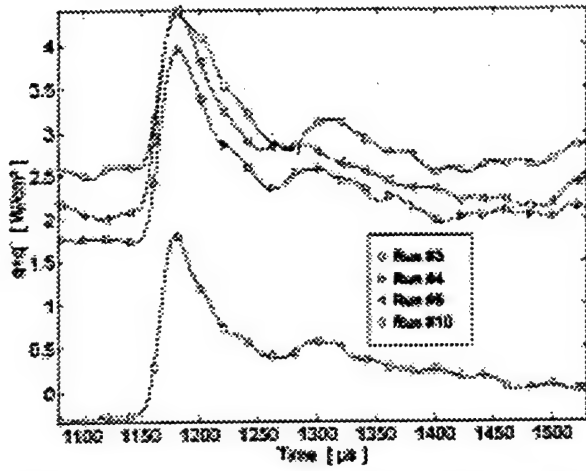


Figure 11: Heat Flux Traces from all Uncooled Experiments

In Fig. 12, the mean components of heat flux have been removed, leaving the traces of q' indicated on the left y-axis. Apparently, all the fluctuating components of heat flux are similar.

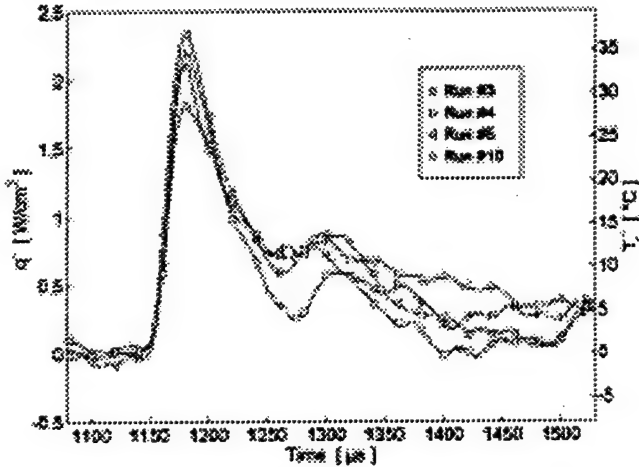


Figure 12: Unsteady Heat Flux and Recovery Temperature from all Uncooled Experiments

The first term on the right hand side of Eq. (12), $h' \cdot (T_r - T_w)$, indicates that the unsteady heat flux (q') is a function of the overall temperature difference ($T_r - T_w$) if h' is significant. If q' is a function of ($T_r - T_w$), then the maximum or peak heat flux (q'_{max}) would also have to be a function of this temperature difference. In Fig. 13 the peak heat flux q'_{max} is plotted versus ($T_r - T_w$).

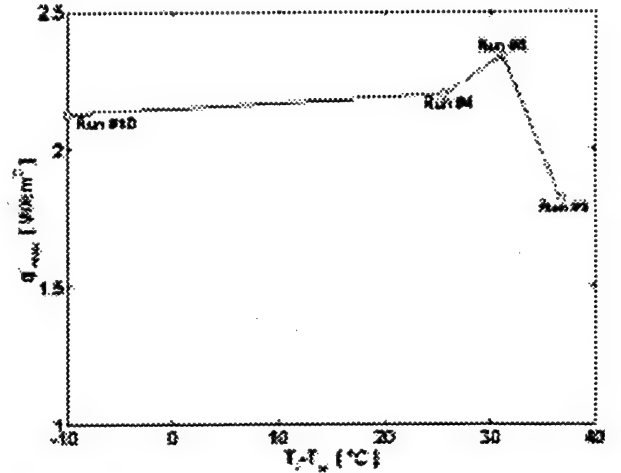


Figure 13: Peak Heat Flux vs. ($T_r - T_w$) from all Uncooled Experiments

There is no clear correlation between the two variables. Hence, q'_{max} does not strongly dependent on ($T_r - T_w$). This can only be the case if h' is much smaller than h . Assuming h' to be negligible and dropping all the terms containing h' on the right hand side of Eq. (12), leaves an equation for the unsteady change of recovery temperature

$$T'_r = \frac{q'}{h} \quad (13)$$

Fig. 12 shows the time histories of this temperature variation indicated on the right y-axis. The heat transfer coefficient used here is the mean of the results of all the steady experiments. Since the scatter is relatively small, an average time variation of recovery temperature is used in the analysis of the experiments with film cooling.

Shock Passing with Film cooling

When film cooling is present, Eq. (12) still applies with the recovery temperature now replaced by the adiabatic wall temperature

$$q' = h'_c \cdot (T_{aw} - T_w) + h'_c \cdot T'_{aw} + h'_c \cdot T'_{aw} \quad (14)$$

Analogous to the analysis for the uncooled case, it is the aim of this investigation to quantify the contribution of T'_{aw} and h'_c to the overall variation of heat flux. T'_{aw} can be expressed in terms of fluctuating components of recovery temperature (T'_r) and film effectiveness (η')

$$T'_{aw} = T'_r \cdot (1 - \eta) - \eta' \cdot (T_r - T_c) - \eta' \cdot T'_r \quad (15)$$

A further question of interest is how much the change in recovery temperature and film effectiveness affect the variation of T'_{aw} . The time variation of recovery temperature is one of the results of the uncooled unsteady investigation. It is the goal of this investigation to determine the contributions of T'_r , h'_c , and η' to the unsteady heat transfer. The coolant temperature is considered to be a constant.

Fig. 14 shows the pressure traces recorded by the blade mounted Kulite pressure transducer for representative experiments with and without film cooling. All the time histories of static pressure are very repeatable, asserting that the comparison of different runs is possible.

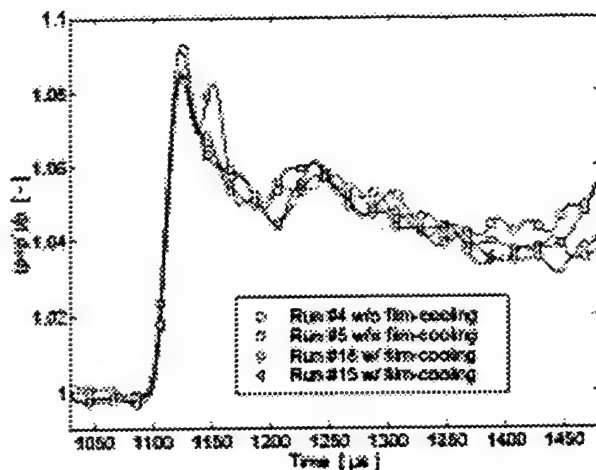


Figure 14: Pressure Traces from Representative Experiments with and without Film cooling

In Fig. 15, all the heat flux traces at shock impact are shown. Again, the differences in heat flux level are due to different temperature levels at the time of the shock release. Run #19 is not listed in Table 2. Intentionally, the temperature differences were kept very small and neither heat transfer coefficient nor film effectiveness could be determined from this experiment.

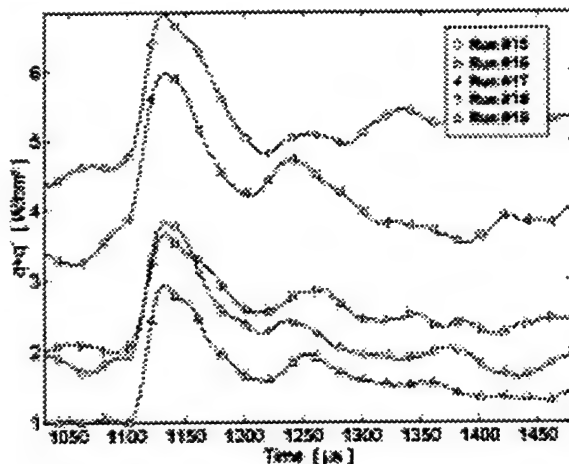


Figure 15: Heat Flux Traces from all Cooled Experiments

In Fig. 16, the same traces are shown after their mean values before shock impact have been removed. The traces of unsteady heat flux with and without film cooling (Figs. 16 and 12, respectively) are very similar in terms of magnitude and shape. Hence, the modes of heat transfer for both cases must be similar. The shock does not seem to influence the heat transfer coefficient or the mixing in the boundary layer (η) in any significant manner, otherwise these time histories would have to appear different for the cases with and without film cooling. Furthermore, pictures taken with the high-speed camera indicate that the cooling-film is not severely affected by the passing shock.

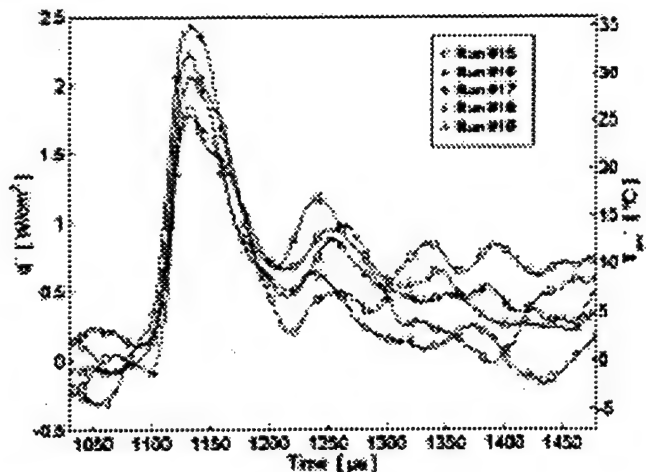


Figure 16: Variation of Heat Flux and Adiabatic Wall Temperature from all Cooled Experiments

The unsteady heat flux as expressed in Eq. (14) contains the term $h'_c(T_{aw}-T_w)$. It represents the first-order term of the contribution of h'_c to the unsteady heat flux. If h'_c is significant, the unsteady heat flux and the peak unsteady heat flux q'_{max} should correlate with $(T_{aw}-T_w)$. In Fig. 17 the peak heat flux is plotted against $(T_{aw}-T_w)$.

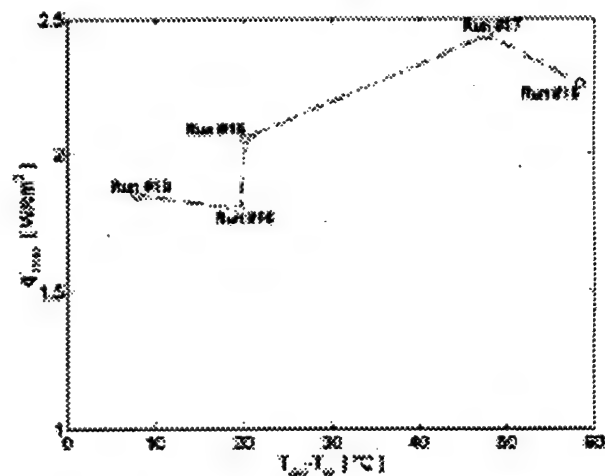


Figure 17: Peak Heat Flux vs. $(T_{aw}-T_w)$ from all Cooled Experiments

There is no strong dependency between q'_{max} and $(T_{aw}-T_w)$ evident. This can only be the case if h'_c is of minor significance. Neglecting all the terms containing h'_c in Eq. (14) yields a relation between the fluctuating components of T_{aw} and q

$$T'_{aw} = \frac{q'}{h_c} \quad (16)$$

The traces of adiabatic wall temperature calculated from Eq. (16) for all the runs are shown in Fig. 16 scaled on the right y-axis. The similarity of the fluctuations seems to allow for an ensemble averaging of the different runs, shown in Fig. 18. Eq. (15) contains an expression for the contribution of T'_r to the variation of the adiabatic wall temperature

$$T'_{aw} = T'_r \cdot (1-\eta) - \eta' \cdot (T_r - T_c) - \eta' \cdot T'_r \quad (15)$$

The averaged time variation of T_{aw} and the first term on the right side of Eq. (14) ($T_r(1-\eta)$) are shown in Fig. 18. For the time variation of recovery temperature, the ensemble average from the uncooled tests are used. The film effectiveness used is the averaged result from the steady film cooled experiments.

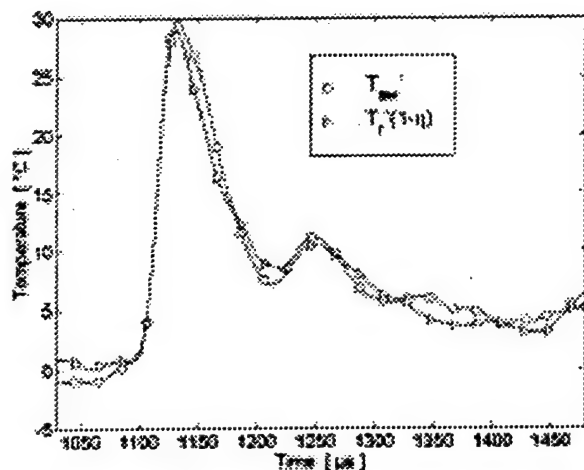


Figure 18: Variation of T_{aw} and the Contribution of T_r

The two traces are of very similar magnitude and shape. This suggests that the remaining terms on the right side of Eq. (14) ($\eta'(T_r - T_c)$ and $\eta'(T_r)$) are small and consequently η' is small. It has to be concluded that the major contribution to the unsteady heat flux is the change of recovery temperature. The variations of h , h_c , and η have to be considered secondary effects. For the uncooled case this has been stated before by Moss et al. (1995). They performed on-rotor measurements of pressure and heat flux. Calculating the change of relative total temperature from the pressure measurement and assuming a constant heat transfer coefficient to calculate heat transfer, they found very good agreement between this calculation and the actual measurement. The present study suggests that this observation is also true for film cooled blades. Extrapolating to engine application, this implies that the time-averaged increase of heat transfer caused by passing shocks is small, since the relative total temperature is by definition varying around its mean value.

CONCLUSIONS

An experimental setup for the investigation of steady and unsteady heat transfer on film cooled transonic turbine blades was designed and built. For uncooled blades, one experiment in the transient facility was shown to be sufficient for the determination of heat transfer coefficient and recovery temperature. For film cooled blades, a method was presented to obtain heat transfer coefficient and film effectiveness from one experiment.

An analysis of the time resolved shock passing event with and without film cooling showed that the major contribution to the unsteady heat transfer is due to the fluctuation of recovery temperature caused by the shock. Heat transfer coefficient and film effectiveness were shown not to vary significantly during the interaction of the shock with the blade surface.

ACKNOWLEDGMENT

This work was supported by the Air Force Office of Scientific Research (AFOSR) under grant F08671-9601062, monitored by Dr. Jim M. McMichael and Dr. Mark Glauser. We would like to thank

Messrs. Scott Hunter, Monty Shelton and Mark Pearson of General Electric Aircraft Engines for their collaboration on this project.

REFERENCES

- Johnson, A.B., Oldfield, M.L.G., Rigby, M.J., Giles, M.B., 1990, "Nozzle Guide Vane Shock Propagation and Bifurcation in a Transonic Turbine Rotor", ASME 90-GT-310
- Moss, R.W., Sheldrake, C.D., Ainsworth, R.W., Smith, A.D., Dancer, S.N., 1995, "Unsteady Pressure and Heat Transfer Measurements on a Rotating Blade Surface in a Transient Flow Facility", AGARD CP-571 pp. 22.1-22.9
- Moss, R.W., Ainsworth, R.W., Garside, T., 1997, "Effects of Rotation on Blade Surface Heat Transfer: An Experimental Investigation", ASME 97-GT-188
- Horton, F.G., Schultz, D.L., Forest A.E., 1985, "Heat Transfer Measurements With Film Cooling on a Turbine Blade Profile Cascade", ASME 85-GT-117
- Hilditch, M.A., Smith, G.C., Anderson, S.J., Chana, K.S., Jones, T.V., Ainsworth, R.W., Oldfield, M.L.G., 1995, "Unsteady Measurements in an Axial Flow Turbine" AGARD CP-571 pp. 24.1-24.8
- Abhari, R.S., Epstein, A.H., 1992, "An Experimental Study of Film Cooling in a Rotating Transonic Turbine", ASME 92-GT-201
- Heidmann, J.D., Lucci, B.L., Reshotko, E., 1997, "An Experimental Study of the Effect of Wake Passing on Turbine Blade Film Cooling", ASME 97-GT-255
- Hale, J.H., Diller, T.E., Ng, W.F., 1997, "Effects of Wake on Turbine Blade Heat Transfer in a Transonic Cascade", ASME 97-GT-130
- Nix, A.C., Reid, T., Peabody, H., Ng, W.F., Diller, T.E., Schetz, J.A., 1997, "Effects of Shock Wave Passing on Turbine Blade Heat Transfer in a Transonic Cascade", AIAA-97-0160
- Diller, T.E., 1993, "Advances in Heat Flux Measurement", Advances in Heat Transfer, Vol. 23, Ads, J.P., Hartnett et al., Academic Press, Boston, 1993, pp. 279-368
- Ito, S., Goldstein, R.J., Eckert, E.R.G., "Film Cooling on a Gas Turbine Blade", Journal of Engineering for Power, 1978, Vol. 100, pp. 476-481

Appendix H

Comparison of Radiation versus Convection Calibration of Thin-Film Heat Flux Gauges

Submitted to the ASME ad-hoc Committee on Heat Transfer

A COMPARISON OF RADIATION VERSUS CONVECTION CALIBRATION OF THIN-FILM HEAT FLUX GAUGES

D. E. Smith, J. V. Bubb, O. Popp, T.E. Diller
Virginia Polytechnic Institute and State University
Blacksburg, VA 24061

Stephen J. Hevey
Vatell Corporation
Christiansburg, VA 24073

ABSTRACT

A transient, in-situ method was examined for calibrating thin-film heat flux gauges using experimental data generated from both convection and radiation tests. Also, a comparison is made between this transient method and the standard radiation substitution calibration technique. Six Vatell Corporation HFM-7 type heat flux gauges were mounted on the surface of a 2-D, first-stage turbine rotor blade. These gauges were subjected to radiation from a heat lamp and in a separate experiment to a convective heat flux generated by flow in a transonic cascade wind tunnel. A second set of convective tests were performed using jets of cooled air impinging on the surface of the gauges. Direct measurements were simultaneously taken of both the time-resolved heat flux and surface temperature on the blade. The heat flux input was used to predict a surface temperature response using a one-dimensional, semi-infinite conduction model into a substrate with known thermal properties. The sensitivities of the gauges were determined by correlating the semi-infinite predicted temperature response to the measured temperature response. A finite-difference code was used to model the penetration of the heat flux into the substrate in order to estimate the time for which the semi-infinite assumption was valid. The results from these tests showed that the gauges accurately record both the convection and radiation modes of heat transfer. The radiation and convection tests yielded gauge sensitivities which agreed to within $\pm 11\%$.

NOMENCLATURE

Symbols

C	specific heat of substrate (J/kg. $^{\circ}$ C)
HFM	heat flux microsensor (temperature and heat flux)
HFS	heat flux sensor
RTS	resistance temperature sensor

S_{conv}	convection tests gauge sensitivity (μ V/W/cm 2)
S_{sub}	standard substitution gauge sensitivity (μ V/W/cm 2)
$S_{rad, blade}$	radiation tests gauge sensitivity (μ V/W/cm 2)
$S_{rad, bench}$	transient tests gauge sensitivity (μ V/W/cm 2)
S_{jet}	impinging jet tests gauge sensitivity (μ V/W/cm 2)
$S_{in-situ}$	in-situ tests gauge sensitivity (μ V/W/cm 2)
T_{calc}	calculated temperature ($^{\circ}$ C)
T_{exp}	experimental temperature ($^{\circ}$ C)
k	thermal conductivity of substrate (W/m. $^{\circ}$ C)
q_{calc}	calculated heat flux (W/cm 2)
q_{exp}	experimental heat flux (W/cm 2)
t	time (s)
ϵ	emissivity of coating applied to gauges
ρ	density of the substrate (kg/m 3)
τ	time allowance for semi-infinite assumption (s)

INTRODUCTION

The accurate measurement of heat flux into a surface is very important to researchers concerned with thermal systems. For example, information about the steady and unsteady heat transfer into turbine blades is in high demand by the turbine industry and its thermal designers. However, the difficulties involved in measuring high-speed thermal phenomena limit the available information. Another area where heat flux measurements are necessary is in the determination of material properties. If the incident heat flux on a material and the corresponding temperature rise are known, the thermal properties of that material may be determined. These are only two of the many areas in which heat flux measurements are critical. The accurate measurement of heat flux is usually a challenge, however.

One difficulty is that the installation of a gauge on a surface will always result in a disturbance to the thermal system being investigated. This disturbance can be minimized if the thermal resistance of the gauge is similar to that of the material in which it is embedded, and if the area to thickness ratio of the gauge is large enough to promote one-dimensional conduction through the gauge. Another difficulty in measuring heat flux is the calibration of the gauges. Moffatt (1995) said that errors in the estimate of gauge sensitivities on the order of $\pm 10\%$ are reasonable due to the difficulties involved with calibration. Moreover, it is often difficult or impossible to calibrate a gauge once it has been mounted in an experimental setup.

One of the present methods for calibrating heat flux gauges consists of a substitution technique where a reference gauge is subjected to an incident radiation heat flux. The gauge to be calibrated is then put in its place and subjected to matched conditions and a calibration is made by comparison with the known gauge. In addition to the substitution calibration, a transient in-situ technique can be used with gauges which have a fast response time provided the temperature is known as well [Hager et al., 1994]. It has been shown (Baker and Diller, 1993) that the surface temperature time history can be calculated from the time history of the measured heat flux. This calculated temperature can then be compared with the transient measured surface temperature to calibrate the heat flux gauges.

For this study, six heat flux microsensor (HFM) thin-film gauges, produced by Vatel, Inc., were mounted on the surface of a first-stage turbine rotor blade made of aluminum. The gauges were used to measure, simultaneously, the local time-resolved heat flux and surface temperature. Because it is difficult to use the substitution technique on these gauges while they are in the blade, the transient calibration method was used. A different set of free-standing gauges were exposed to a radiative flux and the data was used to perform calibrations using both the substitution and the transient techniques. A comparison was then made between the two calibration methods for both convection and radiation.

INSTRUMENTATION

Heat Flux Microsensors

The HFM is composed of two separate sensors, a resistance temperature sensor (RTS) and a heat flux sensor (HFS). The HFS uses a passive differential thermopile made up of 280 thermocouple pairs to generate a voltage proportional to the incident heat flux. The active area of the HFM is 4mm in diameter, two microns thick, and is deposited on an aluminum-nitride substrate, an electrically insulating material with thermal properties close to those of the aluminum blade. The heat flux gauge has been shown to have a time response on the order of 10 μ s [Holmberg, 1995]. The small thickness-to-area ratio and the thermal properties of the substrate ensure that the thermal disruption caused by the gauge will be minimal.

Two different types of HFM's were used in this work: HFM-7's and HFM-6's. The difference between the two types is in the material which is used to form the thermocouple pairs. The HFM-6 gauge uses a Nichrome/Platinum thermocouple pair and has a lower sensitivity ($S=30\mu$ V/W/cm²) than the HFM-7 which uses a Nichrome/Constantan pair ($S=150\mu$ V/W/cm²). All of the gauges use the same material for the substrate, however. The six gauges mounted in the aluminum blade are all HFM-7's and will hereafter be referred to as gauges B1 through B6. Of the five gauges used in the substitution experiments, two are HFM-7's and three are HFM-6's. These gauges will hereafter be referred to as gauges G7/1, G7/2, and G6/1 through G6/3, respectively.

Blade Instrumentation

The six HFM gauges were all mounted on the suction side surface of a generic two-dimensional, high-turning, first-stage turbine rotor blade. The gauges were staggered along the chord of the blade as well as along its span. Each of the gauges was press-fitted flush with the surface of the blade. The curvature of the blade made using the substitution technique extremely difficult and the press-fit meant that the gauges could not be removed from the blade without a very high possibility of incurring damage to the gauges. Therefore, the transient technique was used in-situ to calibrate the six HFM's embedded in the blade.

SUBSTITUTION CALIBRATIONS OF UNMOUNTED GAUGES

The substitution calibration is widely used in research and industry for the calibration of heat flux gauges. Its use in the calibration of HFM's was documented by Hager et al. (1994). The known heat flux is applied to the gauge and the voltage output can be directly calibrated using equation (1).

$$S_{HFS} = \frac{V_{HFS}}{Q_{REF}} \quad (1)$$

The reference gauge, a circular-foil gauge, was calibrated by Vatel Corp. using a primary standard gauge which was calibrated by Nist. After calibration, the reference gauge has an expanded uncertainty (95% confidence level) quoted as $\pm 3\%$.

The substitution technique is a steady-state calibration which uses a reference heat flux gauge to measure the incident flux from a heat lamp and then substitutes an un-calibrated gauge for the known assuming the conditions are the same. An accurate calibration using the substitution method cannot be made with the six gauges that were already embedded in the blade. The curvature of the blade makes it difficult to position the heat lamp the same with respect to both the reference gauge and the embedded HFM. Small changes in the relative positions of the two gauges to the lamp can result in large calibration errors, since the incident heat flux differs with the exact orientation of the lamp. Therefore, five HFM gauges which had not been mounted in the blade were tested instead (G7/1-2 and G6/1-3). The sensitivities of three of these gauges (G6/1-3) was smaller due to the different materials used to make the thermocouple pairs for the HFS and RTS, but the accuracy of the sensitivity estimate was unaffected.

The reference gauge, a circular-foil heat flux gauge painted with a high emissivity coating (0.94), was exposed to a heat lamp to determine the amount of heat flux generated by the lamp. Typical heat flux levels were on the order of 14 W/cm². Both the lamp and the circular-foil gauge were mounted in a fixture that maintained their relative orientation and positioning. The five HFM gauges were also coated, mounted in the fixture, and then exposed to the heat lamp as is shown in Fig. 1. Six tests were performed on each gauge. The data generated by each HFM were recorded at 2000Hz. Sensitivities determined using data from this test will be referred to as S_{sub} . Because all gauges, including the reference gauge, were coated with the same paint, the value of the emissivity did not affect the calibrations.

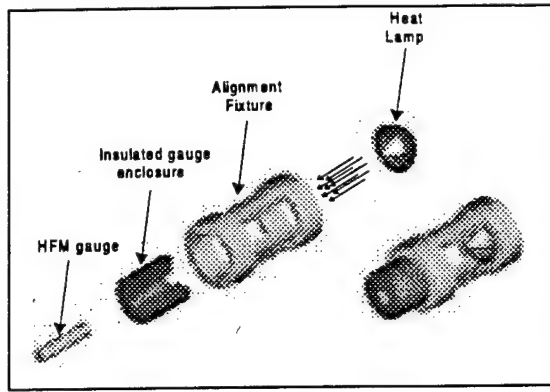


Figure 1: Radiation Tests for Substitution Method

TRANSIENT CALIBRATIONS

Mathematical Model

The transient method of calibrating heat flux gauges was used to analyze the data generated by all of the tests described earlier, including the substitution bench tests. The transient calibration makes use of the fact that for very short time periods, the surface heat flux can be easily calculated from the surface temperature if a one-dimensional, semi-infinite model is assumed [Diller, 1993]. The time period is usually a fraction of a second, and so time-resolved temperature measurements must be taken in order to use this method of calibration. The time response of the HFM gauge is on the order of $10\mu s$, so it is capable of providing these time-resolved measurements for both the surface temperature and the heat flux simultaneously. Baker and Diller (1993) developed a method of determining surface temperature from heat flux using a Green's function approach. By assuming the substrate to be initially at a uniform temperature, T_0 , and treating the series of heat flux data points, q_j , as impulses, the surface temperature time history can be reconstructed using equation (2),

$$T_{calc}(t_n) - T_0 = \frac{2}{\sqrt{\pi k \rho C}} \sum_{j=0}^{n-1} q_j \left[\sqrt{t_n - t_j} - \sqrt{t_n - t_{j+1}} \right] \quad (2)$$

Equation (2) shows that the transient technique requires that the thermal properties of the substrate be known. An algorithm was written to determine the sensitivity of the HFS by minimizing the temperature difference between the measured and calculated temperature histories, $T_{exp} - T_{calc}$.

Validity of 1-D, Semi-Infinite Assumption

The use of the transient method is dependent upon the validity of the one-dimensional, semi-infinite conduction model. Therefore, it is necessary to determine how long this assumption may be considered valid. The active area of the HFM gauge is a circle 4mm in diameter; the HFS (heat flux sensor) occupies the center of that area and the RTS (resistance temperature sensor) is laid down in a ring surrounding it. The HFS and the RTS are located close enough to each other that it might be assumed that they measure the same thermal phenomena. The two-dimensional heat transfer effects, however, are felt first at the edge of the sensor. Therefore, the difference of the temperature at this location from the one-dimensional model is the limiting case for the transient calibration technique. A two-dimensional finite difference conduction code was written to model the penetration of a step input of heat flux into the substrate. The code was used to determine the

maximum time, τ , for which the one-dimensional, semi-infinite assumption was valid.

The parameters used in the code are shown in Fig. 2. The heat flux step input of 10^5 W/m^2 used is typical of the levels measured during heated runs in the transonic blowdown wind tunnel and of the heat lamp used in the radiation bench tests. The step input was applied to a circular area with a diameter approximately four times that of the HFM gauge. This area is the same size as that of the heat lamp, which is the limiting case in this study since the wind tunnel provides a flux over a larger area and two-dimensional heat transfer effects are felt much later in time. The code used cylindrical coordinates to accurately model the gauge, and the thermal properties shown in the figure were used for both the gauge and the surrounding material. The code was discretized in time as well as space; a mesh size of 0.4mm and a time step of 0.005s were chosen.

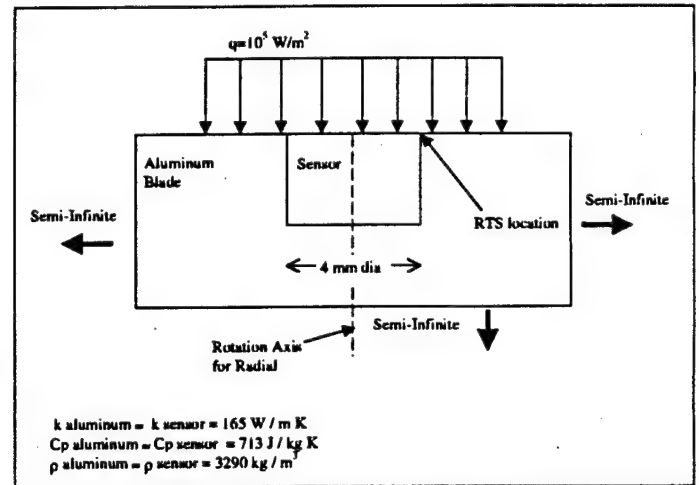


Figure 2: Finite Difference Model

The time history of the RTS surface temperature along with the solution of the one-dimensional, semi-infinite conduction model can be seen in Fig. 3. As time progresses, two-dimensional effects (radial heat transfer) are seen to become more important as the RTS temperature diverges from the one-dimensional model. A time, τ , was chosen such that the error in calculated heat flux from the one-dimensional, semi-infinite model was less than 5%. For the parameters shown in Fig. 2., τ was found to be 125ms.

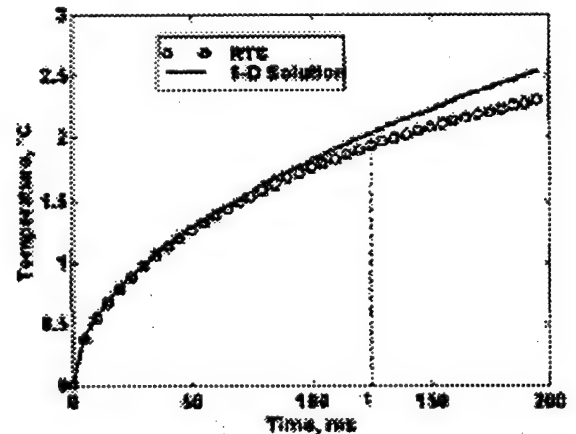


Figure 3: Determination of Time Allowance, τ

Experiments

In-situ Transonic Convection Tests

The mounted HFM's were used to investigate the convective heat transfer into a turbine blade, using the convection experiments performed in the transonic blowdown wind tunnel at Virginia Tech. A set of resistance heaters are used to preheat copper tubes located in the path of the main flow upstream of the test section. The tubes act as a passive heat exchanger and allow the flow to be heated to higher (120°C) temperatures before entering the cascade. Figure 4 shows the wind tunnel with the heating loop and the cascade test section. The cascade test section contains four full blades and two half blades, or five flow passages. Figure 5 shows the location of the instrumented blade in the cascade test section. The heated flow passing over the instrumented blade provides a large convective heat flux to the gauges. Six tunnel runs were made and the data generated by each gauge was recorded simultaneously. The HFM's were sampled at 100Hz and filtered using a low-pass, one-pole filter. The wind tunnel is capable of running for up to 35s with the inlet total pressure controlled, but only a very small fraction of the data recorded by the HFM's is needed for the transient calibration. An important point to note is that the transient calibration technique can be used to perform an in-situ calibration each time a tunnel experiment is performed. The calibration performed at the beginning of an experiment can then be compared to the manufacturer's calibration to determine if the gauge's calibration has drifted. Sensitivities determined using data from this test will be referred to as $S_{in-situ}$.

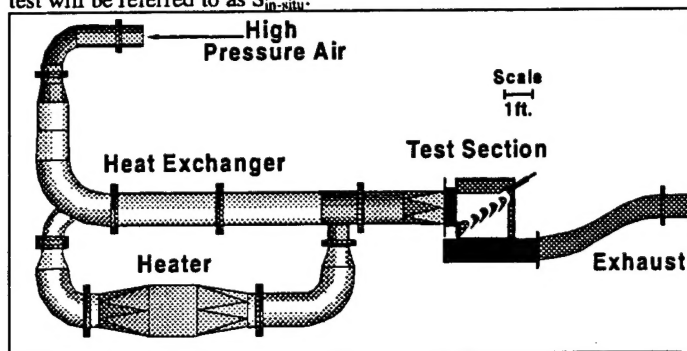


Figure 4: Wind Tunnel Facility

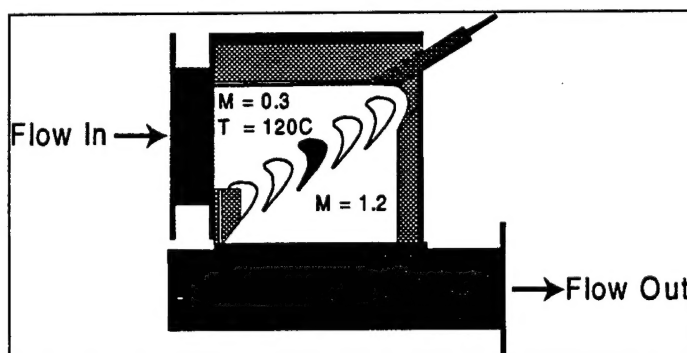


Figure 5: Cascade Test Section

Impinging Jet Bench Tests

In addition to the transonic convection experiments, which were performed in the blowdown wind tunnel, an impinging jet with cold

(-100°C) air was used to provide a large negative incident heat flux to the gauges. These experiments required that the blade be taken out of the cascade test section. The jet was 0.5 inches in diameter and was mounted eight diameters from the blade as is shown in Fig 6. A large tank was loaded to 150 psi and used to supply pressurized air for the impinging jet. For the transient technique, the incident heat flux need not be known if it is assumed to be uniform, so it was not necessary to measure the velocity of the jets. For each test, a shutter placed between the gauge and the jet was manually removed to provide a quick increase in the level of heat flux. The response of the HFM to the jet was recorded at 1000Hz and filtered at 50Hz. Separate tests were performed for each gauge. Sensitivities determined using data from this test will be referred to as S_{jet} .

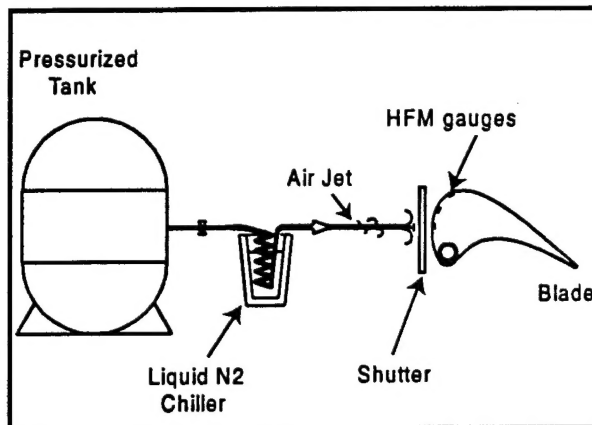


Figure 6: Jet Impingement on Blade

Radiation Bench Tests of Gauges in Blade

Another set of radiation bench tests was performed on the gauges in the instrumented blade after it had been removed from the cascade test section. All of the gauges were painted with a high emissivity coating ($\epsilon = 0.94$), and a heat lamp was used to subject each gauge to an incident heat flux as shown in Fig. 7. The heat lamp was positioned directly over each gauge and the radiative heat flux was made to simulate a step input by using a manual shuttering mechanism; once the lamp had reached its full illumination, the shutter was quickly removed and the gauge was exposed to the incident flux. Again, it should be noted that when using the transient calibration, the incident heat flux does not need to be a known value. It is therefore not necessary to position the lamp in the exact same orientation over each gauge as was required with the substitution method. This test was performed once on each gauge and the data generated by each HFM was recorded at 2000Hz, unfiltered. Sensitivities determined using data from this test will be referred to as S_{rad} .

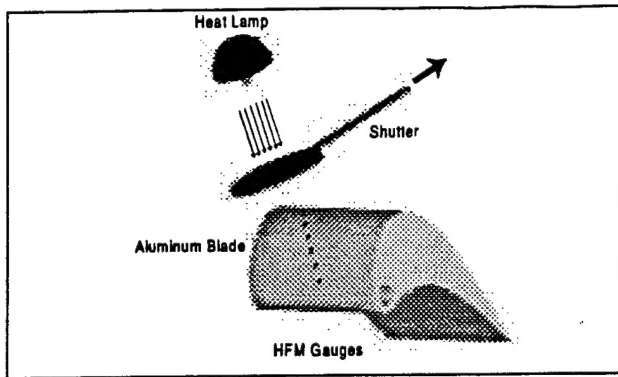


Figure 7: Transient Radiation Tests

Radiation Bench Tests of Unmounted Gauges

The data generated by applying radiative heat flux to the unmounted gauges as described earlier in the substitution experiments section can also be analyzed using the transient method. To do this, data was sampled at 2000Hz, unfiltered, in order to record the initial response of the HFM, the incident heat flux. Sensitivities determined using data from this test will be referred to as S_{trans} .

RESULTS

A comparison of the substitution calibration method with the transient method was done first to determine if the transient method is viable as a calibration technique. The data generated in the substitution experiments were analyzed using both the substitution technique and the transient technique. The material properties ($[k \cdot \rho \cdot C]^{1/2} = 19,670$ in SI units) used in the transient technique are 10% higher than those shown in Fig. 2 due to a change in the aluminum nitride supplier. Six tests were performed for each gauge. The calibration results for both methods can be seen in Table 1. As mentioned earlier, gauges G6-1 through G6-3 are of a different HFM type and so the magnitude of their sensitivities are smaller than those of the other gauges. The difference in the magnitude of sensitivity between HFM-7's and HFM-6's is solely a function of the thermocouple materials used. The percentage difference between the substitution and the transient sensitivities were all less than 13%. Experimental uncertainty for each gauge was calculated by establishing a 90% confidence interval around the mean of the six tests performed using a student-t distribution.

Table 1: Results of Radiation Calibrations

Gauge Number	$S_{\text{sub}} (\mu\text{V/W}\cdot\text{cm}^2)$	$S_{\text{trans}} (\mu\text{V/W}\cdot\text{cm}^2)$
G6-1	18.01	$17.91 \pm 1.3\%$
G6-2	15.33	$16.58 \pm 7.3\%$
G6-3	25.50	$28.72 \pm 5.1\%$
G7-1	108.6	$111.33 \pm 9.7\%$
G7-2	189.05	$191 \pm 9.2\%$

These results show that the transient calibration technique is in excellent agreement with the substitution technique used in most calibrations of heat flux gauges.

Since the convection tests is a viable calibration method, the suitability of convection tests, as opposed to the radiation tests commonly used, was investigated. To do this, two different sets of convection tests were performed and compared to a radiation bench

test. All three sets of tests were performed on the HFM's embedded in the blade. One set of tests was performed in the Virginia Tech transonic cascade wind tunnel. The blade was then removed from the test section and the two bench tests, convection using a cold impinging jet and radiation using a heat lamp, were performed. The data from all three sets of tests were analyzed according to the transient calibration outlined earlier. Figure 8 is a plot of the measured heat flux and surface temperature along with the calculated surface temperature for a sample radiation bench test. The calculated temperature history is a smooth curve underlying the noisier history of the measured surface temperature. The calculated temperature has less noise due to the integration process used to construct it (Baker and Diller, 1993). Figure 8 shows the strength of the transient calibration method; the time histories of the measured surface temperature and the calculated temperature are in excellent agreement, which they should be if an accurate calibration is done.

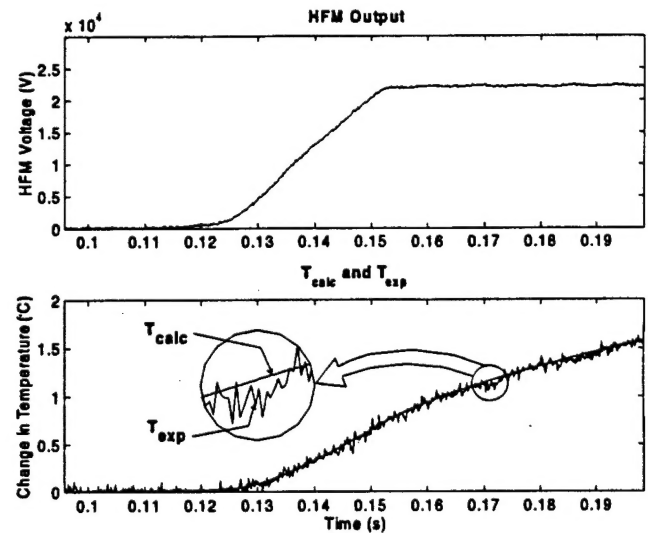


Figure 8: Results of Transient Calibration

The results of the calibrations performed on all three sets of tests can be seen in Table 2. The results for S_{rad} , $S_{\text{in-situ}}$, and S_{jet} are the mean values over all tests for each gauge. A comprehensive method of determining the uncertainty for both the transient radiation and convection calibration was sought. In order to remove the effects of the variations in mean sensitivities of the six gauges, the entire data set for each gauge (S_{rad} , $S_{\text{in-situ}}$, and S_{jet} [$\mu\text{V/W}\cdot\text{cm}^2$]) was divided by the common mean in order to obtain a percentage. This procedure was performed on all six gauges. A normal distribution was assumed, and the uncertainty in the transient calibration at the 95% level of confidence was found to be $\pm 11\%$.

Table 2: Results of Transient Calibration

Gauge	S_{rad}	$S_{\text{in-situ}}$	S_{jet}
B1	264	233	274
B2	114	105	102
B3	148	147	146
B4	150	129	152
B5	177	176	177
B6	155	153	143

CONCLUSIONS

Accurate calibrations are necessary in order to investigate the thermal phenomena reported by heat flux gauges. These calibrations are difficult to make and often impossible to repeat once the gauge has been installed in an experimental setup. A transient method of calibrating thin-film heat flux gauges with fast time responses has been shown to be a viable calibration technique. The strengths of the transient calibration technique are that it can be performed in-situ, the incident heat flux need not be known, and that gauge calibrations can be performed at the start of each run if an appropriate level of heat flux is present. It has been shown that the transient method is capable of using either radiation or convection as the mode of heat transfer.

ACKNOWLEDGMENT

This work was supported by the Air Force Office of Scientific Research (AFOSR) under grant F08671-9601062, monitored by Dr. Jim M. McMichael and Dr. Mark Glauser. We would like to thank Messrs. Scott Hunter, Monty Shelton and Mark Pearson of General Electric Aircraft Engines for their collaboration on this project.

REFERENCES

- Baker, K.I., and Diller, T.E., 1993, "Unsteady Surface Heat Flux and Temperature Measurements." ASME 93-HT-33.
- Diller, T.E., 1996, "Methods of Determining Heat Flux From Temperature Measurements", ISA 0227-7576.
- Hager, J.M., Terrell, J.P., Silverston, E., Diller, T.E., 1994, "In-Situ Calibration of a Heat Flux Microsensor Using Surface Temperature Measurements", ISA 94-1034.
- Holmberg, D.G., Diller, T.E., 1996, "High-Frequency Heat Flux Sensor Calibration and Modeling", ASME *Journal of Fluids Engineering*, Vol. 117, pp. 659-664.
- Johnson, L.P., Diller, T.E., 1995, "Measurements With a Heat Flux Microsensor Deposited on a Transonic Turbine Blade," IEEE 95CH3482-7.
- Moffat, R.J., and Danek, C., 1995, "Calibrating Heat Flux Gauges for Convection Applications", NIST/NSF Workshop on Heat Flux Transducer Calibration.
- Schultz, D.L. and Jones, T.V., 1973, "Heat-Transfer Measurements in Short-Duration Hypersonic Facilities", AGARD AG-165.

Vita

Oliver Popp was born in Offenbach/Main, Germany in 1970. He graduated from high school (Schwäbisch Gmünd, Germany) in 1990. He received his undergraduate degree and his graduate degree in Mechanical Engineering from the Technical University of Darmstadt (Darmstadt, Germany). Fascinated with Fluid Mechanics and Turbomachinery he joined the Von Kármán Institute for Fluid Dynamics in Rhode-Saint-Genèse, Belgium for the 95/96 Diploma Course from which he graduated salutatorian. In the course of his research work there he became aware of the outstanding research done by Dr. Wing-Fai Ng. After consulting with him he joined his research team at Virginia Tech in 1996. Since then he has been pursuing his Ph.D. in Mechanical Engineering and raising son Sebastian Boris with his wife Kerstin. Upon completing his degree Oliver will begin his career with ABB Corporate Research Ltd. in Switzerland as a research engineer in the field of gas turbine cooling.